Miniature Directional Acoustic Sensors: Nature as Inspiration

PhD Thesis

Lara Díaz García

Centre for Ultrasonic Engineering
Electronic and Electrical Engineering
University of Strathclyde, Glasgow

Supervisors:

Prof. James Windmill

Dr Andrew Reid

October 3, 2023

This thesis is the result of the author's original research. It has been composed by the author and has not been previously submitted for examination which has led to the award of a degree.

Signed: Lara Díaz García

Date: October 3, 2023

To Irma and to my parents

"It was a revelation, a liberation. Physicists, mathematicians, astronomers, logicians, biologists, all were here at the University, and they came to him or he went to them, and they talked, and new worlds were born of their talking. It is of the nature of an idea to be communicated: written, spoken, done. The idea is like grass. It craves light, likes crowds, thrives on crossbreeding, grows better for being stepped on."

Ursula K. Le Guin, The Dispossessed

Acknowledgements

I want to thank, in the first place, my supervisors Prof James Windmill and Dr Andrew Reid. Thank you for being supportive, understanding, for guiding me along this journey but also giving me space to grow as a researcher. I believe that supervisors can make or break your PhD experience, which is daunting enough as it is, and I could not have asked for better ones.

Andy, I will never forget my first day ever in the lab, when you showed me a squished moth that had come in an envelope from Florida and made me question every single decision that led me to that day. James, thank you for letting me do a PhD about moths and not once making me be near a moth (other than the Andy incident). I also want to acknowledge and thank Dr Joe Jackson, for being a supervisor at first, and then a mentor and a friend, as well as always being down to go for a nice lunch.

Thank you to everyone that I have been lucky enough to cross paths with in CUE, particularly all my colleagues in the bio group, both the ones that are now gone or just arrived. Thank you to everyone that has attended a Women+ in Engineering meeting, for such a touching reminder that, no matter what it might sometimes feel like, we are not alone in this career path. In particular, thank you to Sophie for agreeing to be on this adventure together, you are a ray of sunshine in rainy Glasgow.

Next, I want to thank my parents for always believing in me, and for telling me that I can do anything I set my mind to. I believe that hearing that consistently since you are a wee kid can make you delusional and excessively self-confident, but fortunately this time it turned out alright. Thank you for all the time you have spent driving me to various classes, for caring for me and loving me, I would not be who I am today if it was not for you. Thank you to the rest of my family, it is not like I could choose, but

I am pretty happy with the hand I was dealt.

Thank you, Diego, for being rock solid, for listening to me, for being an editor and a cheerleader, for being there for the good and the bad and for not once hesitating, you make me want to be a better researcher and person. Thank you to all my friends who have supported me in the distance, for the messages, the video calls, the trips, the birthday gifts that have been mailed, and generally for making me feel you as close as thousands of kilometres allow. Starting anew somewhere far away from home is frightening, and it has been challenging at times, none of it would have been possible without the endless support of all of you.

Finally, thank you to every single person who has made Glasgow feel like home in these years, what a grand time it has been!

Abstract

Miniature directional microphones are desirable for applications ranging from smartphones to hearing aids. The most common technique to achieve directional acoustic sensing is the use of microphone arrays of two or more elements, far from each other, with their inputs then being compared. Nevertheless, this is in conflict with the need to reduce the system or microphones' size. Bigger animals achieve directional hearing in a similar way, with two ears located on opposite sides of the body, an ability known as binaural hearing. Yet smaller animals, like insects, face similar issues to those of miniature microphones. Where inter-ear distance is too short, you cannot rely on comparison for pinpointing the direction of the source. Some small animals have, thus, come up with original solutions to this issue. With bio-inspiration gaining traction in the last few decades, it is not uncommon to look at nature for original design ideas. This Thesis looks at *Achroia grisella*, a small moth capable of seemingly monoaural, i.e. using just one ear, directional hearing. A novel simplified model of the moth's eardrum is developed to explain if the morphology of its eardrum is enough to confer it with directionality. Eigenfrequency and directionality studies are carried out in the model at the moth scale and it is found to have a directivity pattern that reacts more strongly to sounds coming from the front, with eigenfrequencies appearing at a frequency range that the moth is known to detect. A scaled-up model is 3D printed, approximately ten times bigger in length and width, and 50 times thicker depending on the iteration of the model and sample. Its frequency and directional responses are studied through laser Doppler vibrometry, using sound frequencies under 16 kHz for excitation. The 3D printed samples agree with what is predicted by the model, adjusted for the scaling up, and passive structures are found to respond directionally to an acoustic stimulus.

Contents

List of Figures

List of Tables

List of Abbreviations

- 1D: One-dimensional
- 2D: Two-dimensional
- 3D: Three-dimensional
- μCT: Micro-computed tomography
- AMF: Angular Mathieu functions
- CAD: Computer-aided design
- dB: Decibel
- DLP: Digital light processing
- FEA: Finite element analysis
- FEM: Finite element modelling
- HD: High-definition
- ICE: Internally coupled ears
- IID: Interaural intensity difference
- ITD: Interaural time difference
- LCD: Liquid Cristal Display
- LDV: Laser Doppler vibrometry or vibrometer

List of Abbreviations

- LED: Light-emitting diode
- MEMS: Microelectromechanical systems
- mIID: Mechanical interaural intensity difference
- mIPD: Mechanical interaural phase difference
- MSLA: Masked Stereolithography
- PEGDA: Polyethylene glycol diacrylate
- PMN-PT: Lead Magnesium Niobate-Lead Titanate
- PVDF: Polyvinylidene fluoride
- P(VDF-TrFE): Poly(vinylidene fluoride-co-trifluoroethylene)
- RMF: Radial Mathieu functions
- SEM: Scanning electron microscopy
- SLA: Stereolithography
- SPL: Sound pressure level
- TDOA: Time difference of arrival
- UV: Ultraviolet

List of Symbols

- p: Pressure
- p_0: Reference pressure level
- I: Intensity
- W: Power
- r: Distance
- f: Frequency
- T: Period
- n: Refraction index
- ∇: Nabla operator
- c: Wave propagation velocity in a medium for Doppler effect
- E: Young's modulus
- h: Thickness
- D: Flexural rigidity
- ρ: Mass volume density
- ν: Poisson's ratio
- ω: Angular frequency

List of Symbols

- θ: Angular coordinate in polar and spherical coordinates, also known as azimuth, also used for other angles
- φ: Angular coordinate in spherical coordinates, also known as elevation
- λ: Eigenvalue
- ξ: Radial coordinate in elliptical coordinates
- η: Angular coordinate in elliptical coordinates
- z_p: Polymerization depth
- h_a: Characteristic penetration depth
- α: Absorption coefficient
- t_p: Polymerization time
- T_c: Critical time

Chapter 1

Introduction

1.1 Context and motivation

The evolution of technology is, or should be, partly focused on improving people's day-to-day lives and experiences. As science and technology advance, things that seemed impossible a century ago are now widespread. Watching a science fiction film from the last century will show pieces of technology that are currently commonplace as astoundingly advanced. What is more, even in the last 20 years, the size of computers and phones has greatly decreased, making them portable and accessible to more people.

Hearing is a fundamental method of sensing for humans. From a survivalist point of view, hearing greatly facilitates communication with other humans, allows us to detect dangers, etc.; from a purely epicurean point of view, hearing allows us the enjoyment of some of the biggest pleasures in life, like listening to music or the sounds of nature. It is only reasonable that the development of technology is driven by the improvement of comfort and reduction of labour for people.

Microphones are all around us. Without going any further, most of us will carry three or four in our own pockets in our smartphones. These microphones allow sound to be converted into electrical signals that are interpreted in different ways. In phones, this can be recording audio, or voice-to-text dictation; in cochlear implants, a microphone allows the user to receive and interpret sound. Nevertheless, just detecting sound can be insufficient: pinpointing the source of the sound, which people with unimpaired

hearing are able to do naturally, can be desirable as well; this is known as directional hearing [1]. Directional hearing is commonly achieved by comparison of the inputs provided by two or more synchronised sound receivers separated by a certain distance. That way, the time of arrival, intensity, and phase of sound can be compared at each of the receivers and used to calculate the provenance of the sound mathematically [2, 3].

But directionality is not the only aspiration of microphone design; following a general trend in technology in recent years, the demand to miniaturise microphones is pressing. For portable or wearable technology, reduction in size and weight is advantageous, but this brings along challenges that bigger microphones do not face [4]. Picking up from the previous paragraph, the technique of triangularization using two or more microphones is directly in conflict with the desire to make the whole device smaller, so alternative ways to achieve directionality must be sought.

When a novel design is required, we must look at innovative places for inspiration; bio-inspiration consists of gathering insight from biological solutions, with examples of successful bio-inspired design being found in fields like robotics, sensors and material science [5–7]. Many insects present hearing, in fact, a hearing sense is present in at least 9 of the 30 existing orders of insects [8–12]. Some species are further capable of directional hearing, like mosquitoes, crickets, and grasshoppers. Their small body size means that they face similar problems to the ones found in diminutive microphones, making them an ideal inspiration source for small microphone design [13].

Achroia grisella, also known as the lesser wax moth, is just one of many insects capable of hearing in nature. At first glance, it is a small-sized, not very striking moth that inhabits diseased beehives but, upon closer inspection, it is found to be capable of remarkably efficient directional hearing considering its small body size (locates signals six times larger than the distance between their eardrums from up to two metres away in 10-15 seconds [14–16]) and very limited neural processing abilities (four neurons versus the approximately 15000 neurons in the male mosquito's hearing organ) [17–20]. It is for this reason that it was chosen to investigate its hearing sense to better understand its working principles and use it as inspiration for a novel acoustic sensor.

1.2 Novelty of Research and Objectives

There is a knowledge gap on the working principles of the ear of *Achroia grisella* and how it manages to achieve directional hearing. *Achroia grisella* has been investigated in the past mainly with an agricultural interest, due to it being a plague to bee colonies [21, 22]. Biological work has taken place since the 1970s, with a focus on behaviour rather than understanding the mechanism of the hearing. While directionality has been acknowledged and described [14, 23], little work has taken place to explain the achievement of directionality. Some work has been done on the temporal processing of call discrimination [16] and descriptions exist of the vibration mode of the eardrum [19, 24]. Although a model has been developed for the sound field around the moth's body [19], no previous models of the eardrum itself have been published. Furthermore, no attempts to 3D print a structure based on the *Achroia grisella*'s eardrum have been published before. It is to be discovered if *Achroia*'s tympanum would provide a good source of inspiration for acoustic sensor development. The objectives of this Thesis are the following:

- To develop a finite element model of the moth's eardrum that considers the natural resonant frequencies and the air pressure, allowing the investigation of the hearing system of the moth *Achroia grisella*. The model will start from a simplified geometry and evolve in complexity while observing its similarity to the behaviour of the moth's eardrum. The development of such a model will shed light on the working principles of the ear of *Achroia grisella*.

- To examine the working of directional hearing in *Achroia grisella*'s eardrum in simulation. This would allow testing of the hypothesis that directional hearing in *Achroia grisella* is achieved solely due to the morphology of the eardrums, given that no inter-tympanic connection has been found before, unlike the systems of *Ormia ochracea* or the tracheal system found in Orthoptera.

- To apply the findings of the investigation of *Achroia grisella*'s ear to the 3D printing of passive acoustic structures based on the said model that a) replicate the behaviour and natural resonances observed in the model and show similarity

to the behaviour observed for the moth's eardrum and b) show passive acoustic directionality. This will be done by examining different materials and settings of 3D printing techniques encompassed in photopolymerization technologies.

1.3 Contribution to Knowledge

The main work of this Thesis has produced the following contributions to knowledge:

- The development of a novel finite element model for the *Achroia grisella* tympanum that predicts both the resonant frequencies and modes expected for the system and its inherent passive directionality.

- The influence of the value of several parameters (namely Young's modulus, mass-load and mass-load location) on the model developed for the *Achroia grisella* eardrum.

- The 3D printing of passive structures that approximate such a model and replicate the resonant frequencies and modes of the finite element model.

- The 3D printing of structures that show passive acoustic directionality that match those of the finite element model.

1.4 Publications and other outcomes

In this section, the various outcomes of the research carried out for the development of this Thesis are listed.

1.4.1 Peer-reviewed publications

- L. Díaz-García, A. Reid, J. Jackson and J. F. C. Windmill, "Towards a bio-inspired acoustic sensor: *Achroia grisella*'s ear," 2021 IEEE Sensors, Sydney, Australia, 2021, pp. 1-4, doi: 10.1109/SENSORS47087.2021.9639528.

- L. Díaz-García, A. Reid, J. C. Jackson-Camargo and J. F. C. Windmill, "Toward a Bio-Inspired Acoustic Sensor: *Achroia grisella*'s Ear," in IEEE Sensors Journal, vol. 22, no. 18, pp. 17746-17753, 15 Sept.15, 2022, doi: 10.1109/JSEN.2022.3197841.

- L. Díaz-García, A. Reid, J. Jackson-Camargo, J. Windmill; "Directional passive acoustic structures inspired by the ear of *Achroia grisella*". Proc. Mtgs. Acoust 5 December 2022; 50 (1): 032001, doi: 10.1121/2.0001715.

- L. Díaz-García, et al. "Review of the applications of principles of insect hearing to microscale acoustic engineering challenges." Bioinspiration & Biomimetics 18.5 (2023), doi: 10.1088/1748-3190/aceb29.

1.4.2 Conferences

- IEEE Sensors 2021 (virtual). "Towards a bio-inspired acoustic sensor: *Achroia grisella*'s ear" (poster, video, and Q&A session)

- Acoustical Society of America 2021 bi-annual meeting (Seattle, United States). "Finding each other: *Achroia grisella*'s oddly simple directional ear" (poster); "*Achroia grisella*'s ear as inspiration for acoustic sensing" (oral presentation).

- International Workshop on Insect Bio-Inspired Technologies, "3D Printing of directional passive acoustic structures inspired by *Achroia grisella*'s ear" (poster and oral presentation).

- Acoustical Society of America 2022 bi-annual meeting (Nashville, United States). "Directional Passive Acoustic Structures Inspired by the Ear of Achroia grisella" (invited oral presentation).

1.4.3 Prizes

- First prize in Acoustical Society of America (ASA) student challenge 2022 on Acoustics and Additive Manufacturing sponsored by the Technical Committees on Engineering Acoustics and Structural Acoustics and Vibration.

- First prize in the Acoustical Society of America Nashville 2022 meeting POMA student paper competition for "Directional Passive Acoustic Structures Inspired by the Ear of *Achroia grisella*".

- 2022 IEEE Sensors Journal Best Paper Runner-Up Award for "Toward a Bio-Inspired Acoustic Sensor: *Achroia grisella*'s Ear".

1.4.4 Other activities and outreach

- *Inside Science* interview about research in December 2021.

- *Pint of Science 2022* invited talk in May 2022.

- Clydeview Academy talks to S5 pupils in June 2022.

- *IEEE Spectrum* interview about research in September 2022.

- Lay language paper "A moth's ear inspires directional passive acoustic structures" for the Acoustical Society of America in November 2022.

- ASA POMA podcast contribution in May 2023.

1.5 Thesis Organisation

The rest of this Thesis consists of 5 further Chapters and 4 Annexes.

Chapter 2 is a literature review of topics pertinent to the Thesis, namely: an introduction to general acoustics; hearing in humans and in insects; the moth *Achroia grisella* in particular, a moth unusual in its mating call and capable of directional hearing; some of the problems insects face due to their reduced size; microphones, with a focus on MEMS (Microelectromechanical Systems) microphones; and bio-inspired MEMS design. Finally, additive manufacturing is reviewed.

Chapter 3 describes the methodology employed across the Thesis and details the techniques used. Three approaches are considered: an analytical approach, Finite Element Modelling and 3D printing. Further sections are dedicated to micro-computed

tomography and Laser Doppler Vibrometry, which are employed to examine the samples manufactured.

Chapter 4 presents the results of the analytical approach and the Finite Element Modelling. Eigenfrequency, directivity, and damping are all studied in their corresponding sections in an increasingly complex simulated model. Starting from a basic circular plate, the model is progressively improved until it reaches a stage that resembles what is observed in nature. Representation and analysis of the data are provided for each of the subsections.

Chapter 5 contains the results of 3D printing and Laser Doppler Vibrometry, with eigenfrequency and directionality both being studied. Frequency response results are shown for the simplest circular and elliptical plates first 3D printed, compared side-by-side to the ones obtained from simulation, up to the double-thickness elliptical plates that are also compared against simulation. For the latter, the directivity response was also examined.

Finally, Chapter 6 is comprised of two sections. The first one presents a summary of the results and the conclusions of the Thesis. The second section contains information about potential future work and directions where the research might be headed.

Annexes A through D contain copies of the written outcomes outlined in subsection 1.4.1.

Chapter 2

Literature Review

This Chapter contains a review of the fields of knowledge that pertain to the topic of this Thesis. The background is presented for the different areas and the state of the art is also discussed. The bio-inspiration approach followed in this Thesis makes it highly interdisciplinary, so several fields are covered, from acoustics to insect biology and including additive manufacturing.

The first section details some of the fundamentals of acoustics, including the description of waves and the phenomena they experience. The following section is on hearing, both in humans and insects. The section on human hearing describes the parts of the hearing sense and its frequency decomposition mechanism. In the insect section, after a detailed description of *Achroia grisella*, some of the main problems faced by insects due to their reduced body size are discussed.

Next, microphones are reviewed, both standard microphones and smaller micro-electromechanical systems. This is followed by insect-inspired acoustic sensors relating to these three aforementioned problems. Finally, additive manufacturing, the method used for the fabrication of samples in the Thesis, is reviewed.

2.1 Fundamentals of Acoustics

Acoustics is the field of knowledge concerned with the study of sound. Acoustics is approached from diverse disciplines such as physics, engineering, music, psychology,

neuroscience, and architecture, to name a few. Sound is the name given to mechanical pressure waves that propagate through a medium, be it solid, liquid or gas. Acoustical mechanical waves are the product of adiabatic compression and rarefaction, meaning that there's no heat exchange with the medium, which they necessitate to propagate, unlike electromagnetic waves which can propagate through a vacuum. Each infinitesimal point of the medium experiences these compression and rarefaction cycles, which in turn and together make mechanical waves. Mechanical waves are locally characterised by sound pressure, a magnitude that quantifies the deviation of pressure from the equilibrium (atmospheric) pressure. Pressure is commonly denoted as p and it is measured in Pascals (Pa) in the International System of Units.

Sound Pressure Level (SPL) is a quantity that is a logarithmic measure of pressure in comparison with a reference level (p_0). This reference level is often taken to be 20 μPa for air, as it is considered the threshold for human hearing. The unit of sound pressure level most commonly used is the decibel (dB):

$$SPL_{dB} = 20 \cdot log_{10}\left(\frac{p}{p_0}\right) \tag{2.1}$$

Intensity (I), on the other hand, is defined in acoustics as the rate of energy flow (or power, W) per unit area. It is measured in units of watts per surface unit (W/m^2). In a free sound field, its decay follows the inverse square law, where r is the distance from the source:

$$I = \frac{W}{4\pi r^2} \tag{2.2}$$

Mechanical waves can be classified into two groups depending on their direction of propagation and particle motion direction. Longitudinal waves are those where particle motion direction is parallel to the wave propagation direction, which includes sound waves in air. On the other hand, transversal waves are those with particle motion direction perpendicular to the wave propagation direction, like secondary seismic waves (see Figure 2.1 for a representation of both waves). Another possible classification for waves into two alternative categories is according to whether they are confined to a limited

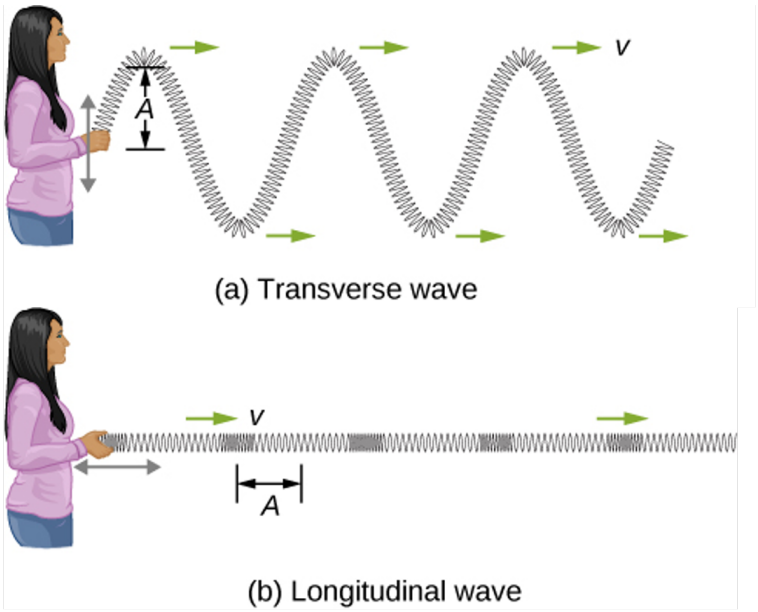

Figure 2.1: Longitudinal and transverse waves. (a) In transverse waves, particle displacement is perpendicular to the direction of travel of the wave, e.g., the spring moves up and down but the wave propagates to the right. (b) In longitudinal waves, particle displacement is parallel to the direction of propagation of the wave, e.g., the spring moves back and forth from left to right, while the wave propagates to the right. [25].

space or not. Unconfined waves are known as travelling waves, and their counterparts receive the name of standing waves. Figure 2.2 shows a schematic representation of travelling waves versus standing waves. Standing waves appear due to the overlap of travelling waves going in opposite directions in a confined space. Standing waves occur in one-dimensional bodies, like a string, but also in two-dimensional bodies, like a membrane. Certain points remain undisturbed, which are known as nodes, and some points reach maximum displacement, antinodes. The waves change over time but the nodes and antinodes are not displaced in space.

Periodical waves are characterised by their frequency (f) and their period (T), both are inherently entwined with each other by definition. The two quantities refer to the repetitions of a certain event: frequency is the number of times that a cycle is completed per unit of time; period, its inverse, is the time it takes to complete a cycle, and therefore its units are time units. Frequency is measured in Hertz (Hz) and in psychoacoustics it relates to pitch, but where frequency is a purely objective physical

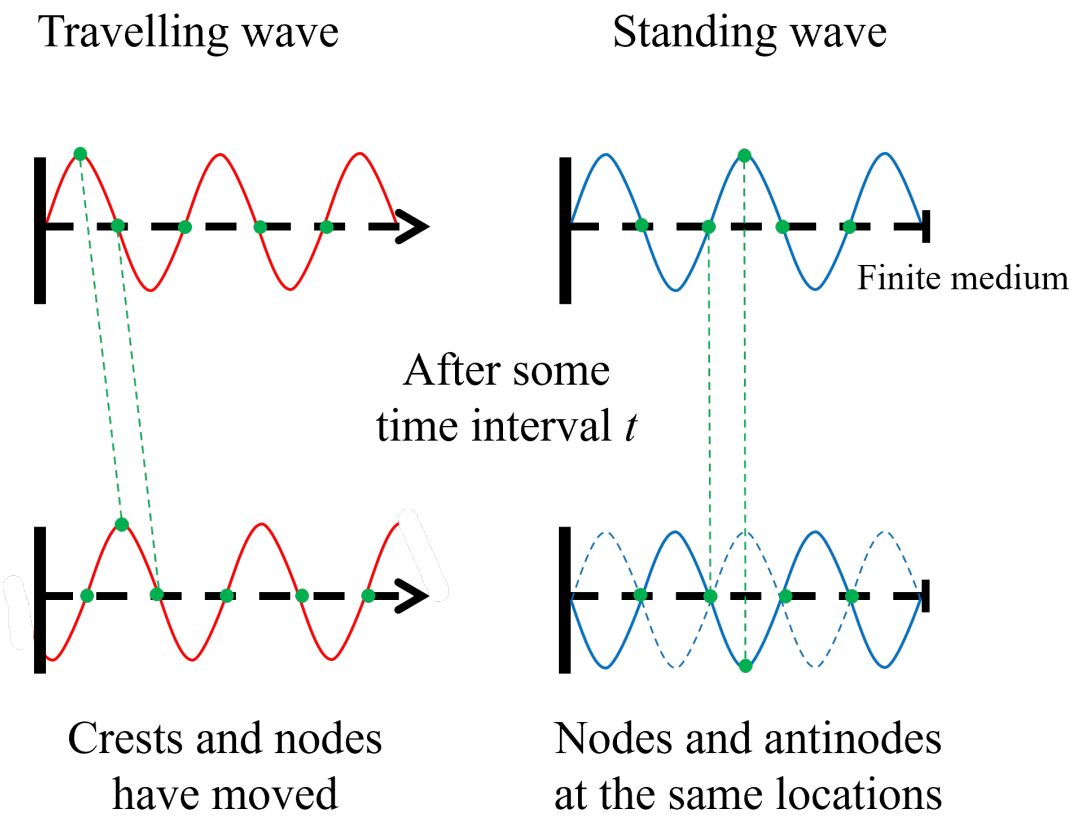

Figure 2.2: Schematic representation of travelling waves and standing waves. In travelling waves, the crests and nodes of the wave are displaced in space as time advances. In standing waves, the nodes and antinodes remain in the same position even when time passes.

magnitude, pitch is affected by perception. In reference to the frequencies that the unimpaired human ear can process, three regimes of sound are differentiated:

- Infrasound: sounds under the human hearing range, below 20 Hz.
- Audio: sounds within the human hearing range, between 20 Hz and 20 kHz.
- Ultrasound: sounds exceeding the human hearing range, above 20 kHz.

Sound, like any other wave, is susceptible to four phenomena, namely reflection, refraction, diffraction, and interference. Reflection happens when sound encounters a boundary that does not absorb or transmit it. Instead, the waves are mirrored back to the same medium that they come from; the reflected angle will be the same as the incident angle of the wave. Reflection only happens if the wavelength of the sound waves is much smaller than the size scale of the boundary. If, instead, they are of similar sizes, diffraction is encountered, where the wave essentially is re-emitted from the edges of the boundary as a new wavefront of diminished intensity. Refraction happens at a boundary between different media or even between layers of the same medium when the characteristics of this medium affect wave propagation speed. The velocity of waves changing will make them deviate from their initial propagation direction. The refractive index of each medium (n) is related to the incident and transmitted angles according to Snell's law. Lastly, interference happens in the overlap of two wavefronts. The pressure at each point will be the sum of two or more different pressure levels. The sum can be constructive (increased pressure level) or destructive (decreased pressure level) depending on the phase of the waves. The resulting wave will be different from the other interfering waves. Figure 2.3 shows a schematic representation of the four phenomena.

2.2 Hearing

Hearing, like the rest of the senses, is a way in which organisms get information from the world that surrounds them. It is an incredibly useful ability to have for many purposes such as finding conspecifics and subsequently engaging in reproduction, hunting prey to

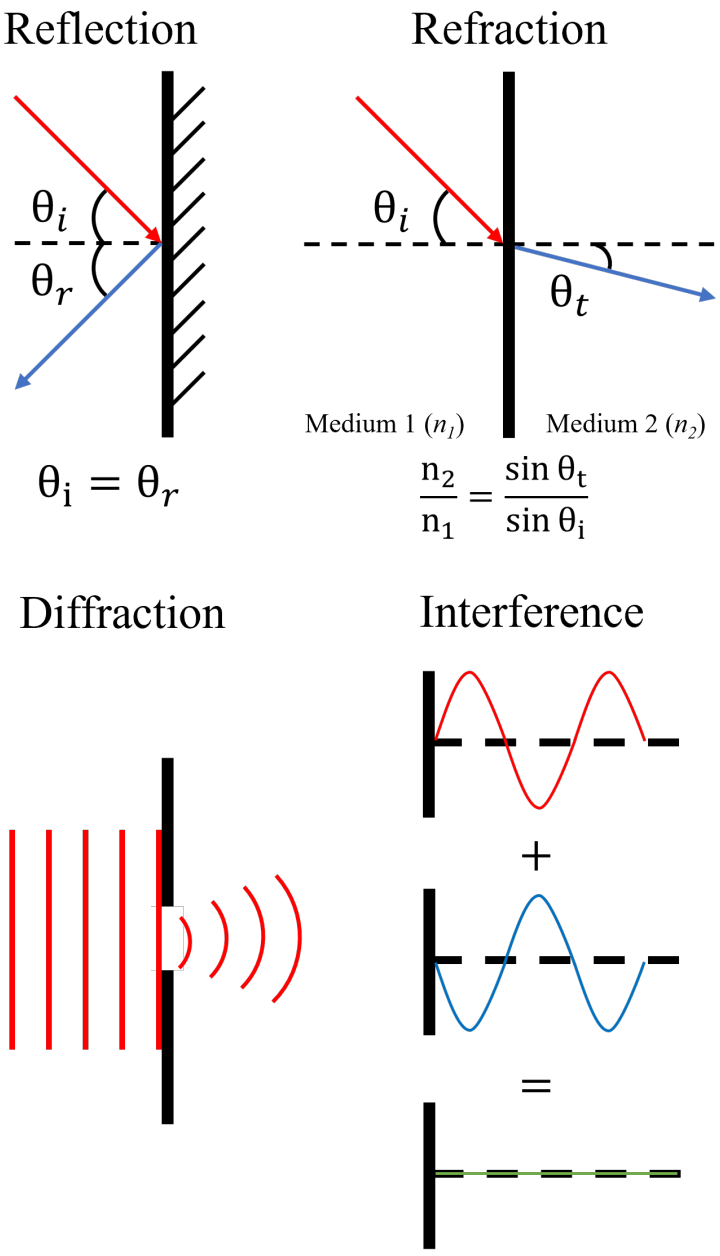

Figure 2.3: Wave phenomena: reflection, refraction, diffraction and interference. In reflection and refraction, the rays represent the propagation direction of the sound wave; in diffraction, the planar and curved lines represent the wavefront; in interference, the red and blue lines represent the waves themselves.

feed upon, fleeing potential predators, and more [1]. Humans in particular use hearing for purposes as varied as complex communication with conspecifics, enjoyment of music or other pleasant sounds, or detecting danger signified by sounds, like sirens or alarms.

Hearing is considered a form of mechanosensation. This means that, through the hearing sense, an individual is able to transform mechanical stimuli into signals for the brain to interpret. This process of transduction takes place in the hearing organ. In vertebrates, the hearing sense is ubiquitous. In mammals in particular, hearing is, in addition, intuitively identified, with the hearing organ being formed by ears or orifices that lead to the rest of the hearing organ inside the head.

2.2.1 Human hearing

The outermost element of the hearing organ in humans, and shared with other mammals, is the pinna or auricle, an appendage mostly made of cartilage that works as an antenna to drive sounds into the ear canal. A notable exception where the pinna is absent or very small in size is cetaceans or water-dwelling mammals, where a cavity opening in the head directly leads to the rest of the ear. From the ear canal, sound is transmitted to the tympanum, more commonly known as the eardrum.

The tympanum is a thin membrane, not unlike a drum skin, that vibrates in response to sound. It comprises two different regions, *pars tensa* and *pars flaccida*, which have different physical characteristics, the first being thinner and tauter and the latter thicker and flaccid. The tympanum is oval in shape and of conic section, with a different thickness across the membrane and an inclined orientation to increase the surface further than the cross-section of the auditory canal in which it is housed. The tympanum is surrounded by an annular ligament and is concave at its deepest point. This point is called the umbo and is roughly at the centre of the membrane [26].

The tympanum leads to the ossicles, three small bones called malleus, incus, and stapes, and it is attached to the malleus at the umbo through the manubrium. See Figure 2.4 for a drawing of the tympanum showing the two sections, the malleus and umbo, and the cone of light, a physical phenomenon visible under examination of the tympanum with an otoscope due to light reflection [27]. The narrowest part of the

cone of light corresponds to the deepest part of the eardrum. The ossicles then drive the vibrations to the cochlea, the element of the hearing organ in charge of frequency discrimination, allowing humans to hear sounds in the range of 20-20000 Hz, although this range changes depending on the individual and throughout the duration of people's lives. Other animals, including other mammals, have very different hearing ranges, being able to perceive sounds outside of human's hearing range. See Figure 2.5 for a schematic of the human hearing mechanism, showing the pinna, ear canal, ossicles and cochlea. The stapes is connected by its annular ligament to the oval window, a membrane found at the entrance of the cochlea [28].

The cochlea is a snail-shaped volume made of bone and filled with two fluids known as endolymph and perilymph. The volume is divided into three parts: the scala vestibuli, scala media or cochlear duct, and scala tympani. The scala media and scala vestibuli are separated by Reissner's membrane; the scala media and scala tympani are separated by a membrane called the basilar membrane, which is naturally frequency selective [29]. The base of the basilar membrane is narrower and stiffer, and it grows wider and less stiff towards the apex, which means different frequencies will excite different regions of the membrane. An acoustic impulse applied to the narrow end of the wedge-shaped structure encounters a stiffness gradient. The wave shoals, increasing in amplitude whilst also slowing down until finally maximal vibration of the basilar membrane is reached at a specific point along the membrane's length; afterwards, the wave rapidly decreases in amplitude. High-frequency stimuli terminate at a point near the narrow end, and those of lower frequency, near the wide end [30, 31].

The organ of Corti, located in the scala media, above the basilar membrane, is where the sensory hair cells protrude from. The hair cells are arranged linearly along the length of the substrate, and they are excited according to their location along the basilar membrane, therefore, as a response to a particular frequency. The cells send impulses to the brain, where sound is finally fully decoded and interpreted [33]. Sitting above the organ of Corti, the tectorial membrane is found. Its role is not fully understood but it is believed to be fundamental for hearing [34]. See Figure 2.6 for a more detailed schematic of the cochlea, showing the basilar and tectorial membranes,

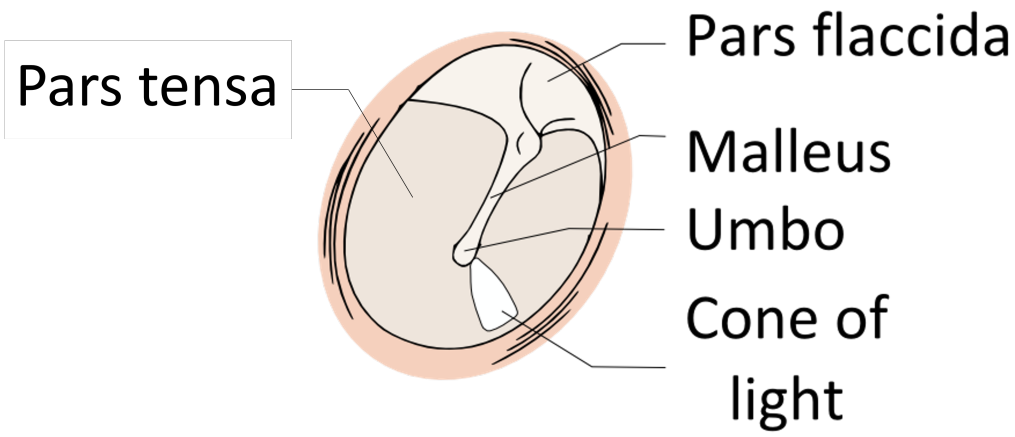

Figure 2.4: Schematic drawing of the tympanum showing the two sections, malleus, umbo and cone of light. Adapted from [32].

the scala vestibuli and scala tympani.

2.2.2 Insect hearing

Hearing in humans has been discussed, but hearing is not alike in all members of the animal kingdom; many of them, in fact, do not even possess a hearing sense. One class within Animalia in which hearing is present and is characterised by notorious biodiversity is insects, also known as Insecta or Ectognatha, within the phylum Arthropoda. They are typified in their adult phase, known as imago, by having an exoskeleton mainly made of chitin, a body divided into three sections (head, thorax, and abdomen), three pairs of jointed legs, compound eyes and one pair of antennae. The cuticle that constitutes the tissue in insect organs is difficult to characterise due to its multiple constituent layers, but its density is roughly that of water or slightly denser; Vincent and Wegst report it to be in the range of 1 to 1.3 g/cm^3 [37]. One of the characteristics shared by many insects is, in general, their reduced body size. This reduced body size occasionates for insects a series of challenges when it comes to hearing. Three of these key challenges will be discussed next: directionality, frequency decomposition and signal amplification. But first, one insect capable of hearing and that overcomes the directionality challenge, the moth *Achroia grisella*, will be reviewed.

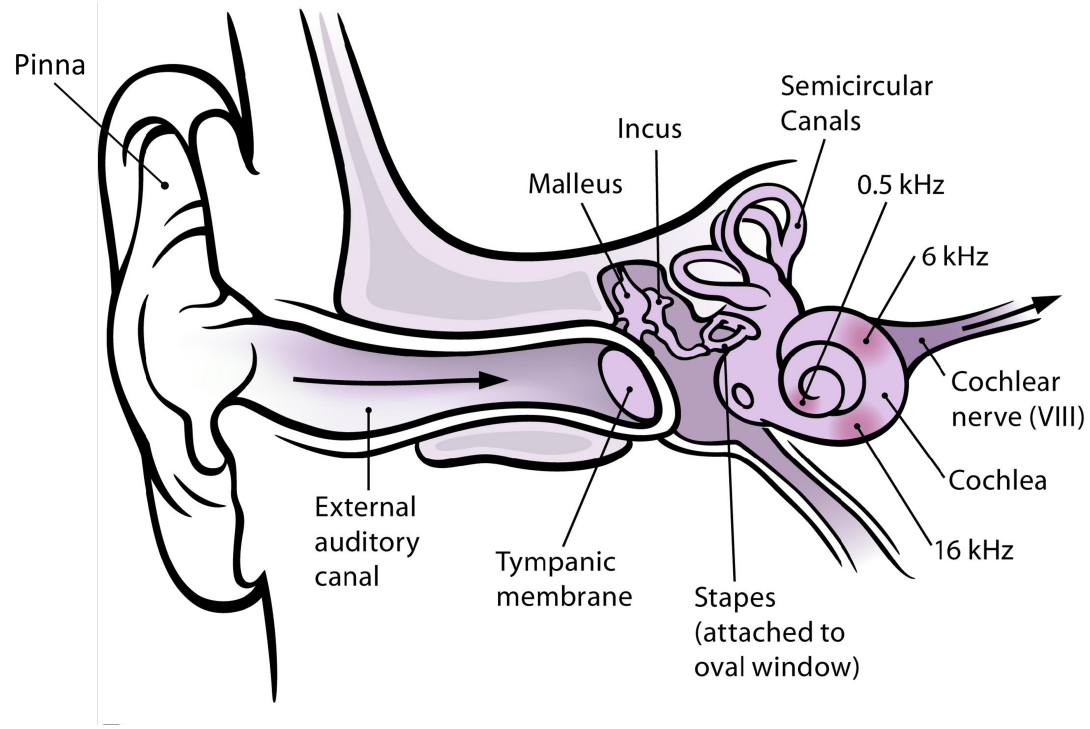

Figure 2.5: The principal parts of the human hearing mechanism. Edited from Chittka and Brockmann's Perception Space [35].

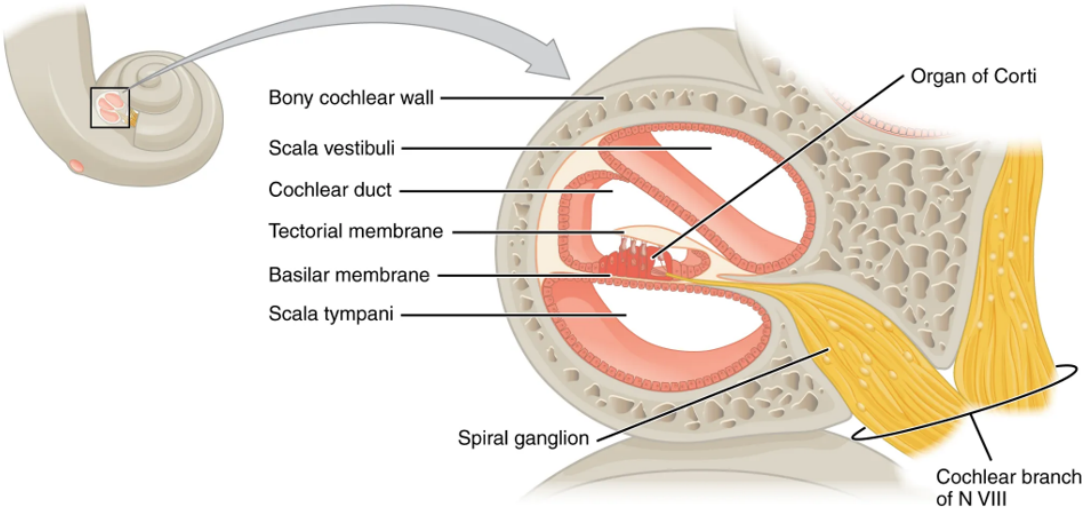

Figure 2.6: Detailed cross-sectional drawing of the cochlea showing the different volumes and membranes inside it [36].

2.2.2.1 *Achroia grisella*

One insect within the Lepidoptera order that bears a central role in this thesis is *Achroia grisella*. Lepidoptera, more commonly known as butterflies and moths, depending on their diurnal or nocturnal habits respectively, are one of the insect orders that present various instances of hearing. It was previously believed that hearing appeared in Lepidoptera later than 65 million years ago, the currently accepted date for the appearance of echolocation in bats [38–41], but more recent studies show that three of the independent origins of hearing in Lepidoptera predate bat echolocation [42]. Therefore, bat hunting pressure has been discarded as the reason pushing lepidopters to develop hearing, although later co-evolution of the two traits might have happened.

The hearing that has evolved in lepidopters is extremely simple, consisting of only 1-4 neurons per tympanum [43], minimum tuning over a broad frequency range (moths are mainly sensitive to sound from 20 kHz to 60 kHz but some go much higher, like *Galleria mellonella*, which shows a sensitivity up to 300 kHz) [24,44,45], and limited or no directionality, yet it remains highly effective for escaping predatory bats [46]. Moths exposed to bat echolocation signals exhibit random evasive movement, diving towards the ground if in flight and freezing behaviour if running on the ground [47]; knowing exactly where the bat is coming from does not change the moth's response.

Achroia grisella is a moth that belongs to the Pyraloidea superfamily. *Achroia grisella* are parasites to beehives, where they deposit their eggs, that later feed on the wax when they become larvae (Figure 2.7 shows an adult specimen). Like most other moths, *Achroia grisella* is mainly predated by bats and is capable of ultrasonic hearing that it uses for escaping them; but they are quite unique among moths because they are known to have a mating call that the females listen to and track, instead of relying exclusively on pheromones [41, 48–50]. Although evasive behaviour from bats might not benefit from directional hearing, finding a mate implicitly involves the need to find the source of the sound, for just detecting that there is a potential mate nearby is not nearly as useful as tracking the calls to their origin [51].

During this mating process, the males fan their wings while remaining stationary [40], producing click trains of main frequency content of approximately 100 kHz [14,49].

Figure 2.7: *Achroia grisella* specimen on a beehive. Picture by Ilia Ustyantsev.

But not only is *Achroia grisella* subversive because of their use of acoustic calling but they also present infrequent female and male roles during courtship. The usual role of females in pair formation is releasing the pheromones for the males to pursue them; *Achroia grisella* reverses this process, with the males being the ones emitting pheromones and calling and the females tracking them [21, 52]. The mechanisms for sound production are a pair of membranes called tymbals located under the forewings of males, buckling and snapping at each upstroke and downstroke of the wings respectively [53]. Their counterparts lack these structures altogether. The females find their way to the calling males, after some zigzagging, but still efficiently [19]. The females have been observed to respond to speakers emitting synthesised sounds like those of the males and to avoid muted males, implying that sound emission is key for pair formation [18].

The female moths' average size is 13 mm, the males being slightly smaller in size [54], with their tympana positioned on their abdomen less than 600 microns apart. The frequency of the male call (100 kHz) corresponds to a wavelength of 3.4 mm, for which the inter-tympanic distance is insufficient to account for any phase, intensity or time of arrival difference. *Achroia grisella* have just four auditory neurons per tympanum [49] and they have no mechanism for frequency discrimination. It is believed that moths can tell bat echolocation calls apart from the males' song through time-encoding [16], deciding on evasive or positive behaviour respectively.

Achroia grisella's tympana are roughly elliptical in shape, approximately 670 μm long in the major axis and 500 μm long in the minor axis in the females ([49], unpublished data by Dr Andrew Reid) and slightly smaller in the males, and located within a cleft of the thorax (see Figure 2.8 for schematic drawing and Figure 2.9 for a μCT scan of a moth's tympanum). They are divided into two visibly different sections: one thicker, called *conjunctivum*, and one thinner known as *tympanum proper* [55]. Connected to the latter is the cluster of four auditory neurons known as *scoloparium*. The two sections of the tympana oscillate in anti-phase when there is no variation in the pressure field across the tympanum (i.e. when the sound wavefronts are planar), with a large peak in displacement near the neuronal attachment point [16, 24, 56]. This vibrational mode remains relatively stable with sound source angle until a 100 kHz sound

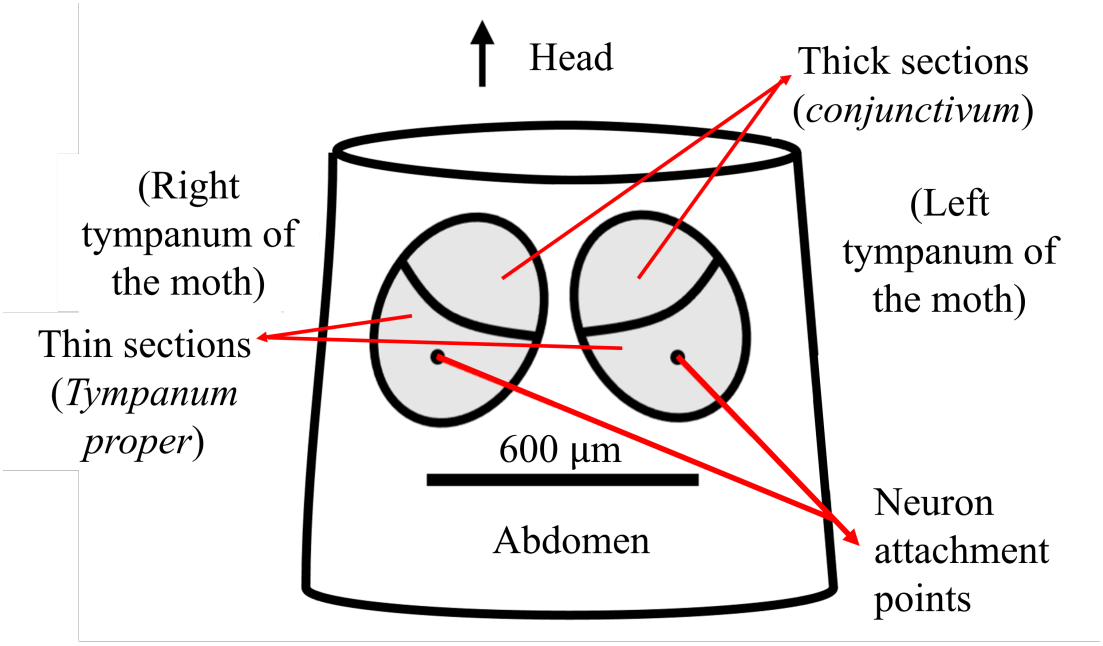

Figure 2.8: Schematic representation of *Achroia grisella*'s abdomen, with the tympana, their sections, and the neural attachment points labelled (adapted from [57]).

source is located along the major axis of the tympanum at which point the peak in displacement near the attachment point grows sharply in magnitude (see Figure 2.10 for a scan of the displacement of a moth's eardrum under excitation of 100 kHz [19]). No connection of any sort has been found between ears and no tracheal system connecting the tympana to the outside has been observed either, discarding some of the mechanisms used in other insects to achieve directional hearing. Diffraction around the body of the moth has been simulated and is not believed to be enough to account for directional hearing [56].

But what is truly baffling about *Achroia grisella* is that females with one tympanum pierced were still able to make their way to a speaker playing male songs [23]. It is therefore believed that *Achroia grisella* moths achieve monoaural directional hearing purely due to the characteristic morphology of their tympanic membranes.

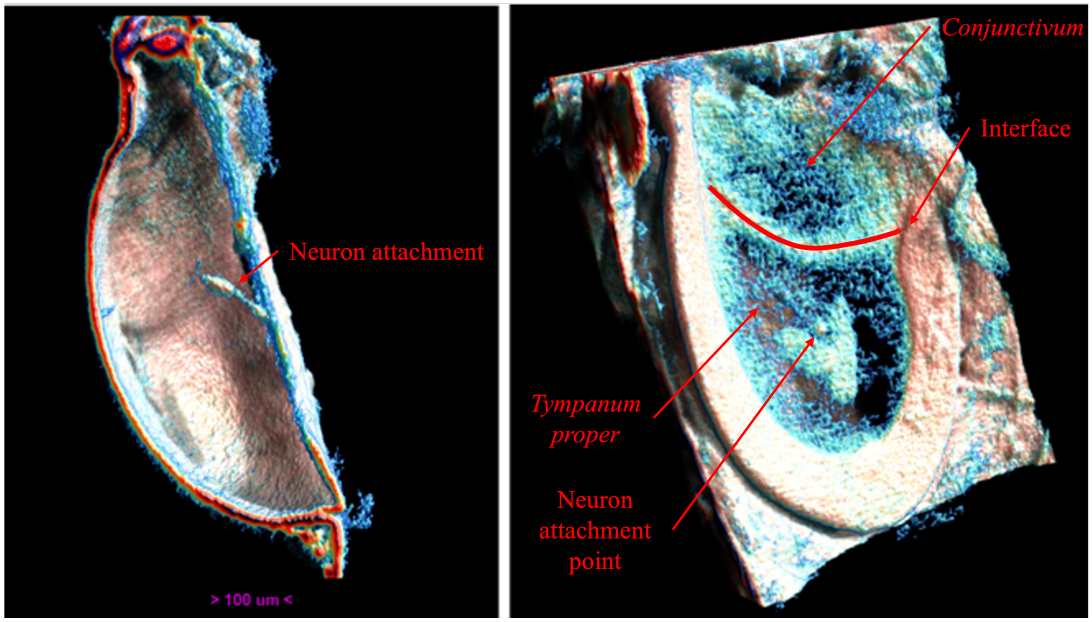

Figure 2.9: μCT scan of *Achroia grisella*'s tympanum showing the thicker ring surrounding the eardrum, the two sections of different thicknesses (*conjunctivum* and *tympanum proper*, as well as the neuron attachment point [57].

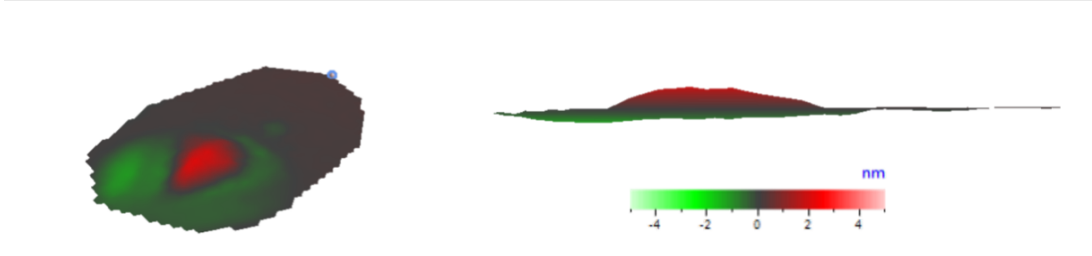

Figure 2.10: LDV measurement taken from a moth specimen showing displacement of the tympanum surface under excitation of 100 kHz. Taken by Dr Andrew Reid [57].

2.2.2.2 Directionality

Directionality is the ability to tell where a sound source is located. Directional hearing can be desirable for animals for several of the tasks they perform during their lives: escaping a predator, finding a potential mate, or locating the host to a parasite. Most animals present bilateral symmetry, including all animals capable of hearing. In biology, bilateral symmetry describes organisms that can be divided by a sagittal plane into two highly similar left and right halves. There are, however, exceptions to this symmetry regarding ears; mantids have one cyclopean ear [58], and owls have asymmetric ears to improve their localization ability [59]. Animals of considerable size, whose ears are separated by a distance, use this bilateral symmetry to their advantage, comparing the signal received by each of their ears, which will be different in time, intensity, and phase of arrival. In these big animals, like most mammals, the differences are processed in the brain to establish which direction the sound is coming from. On the contrary, the localization of sound sources by small animals is a fundamental problem in bioacoustics.

When body size is reduced and the distance between ears is thus small, an animal cannot rely on comparison between the intensity difference or time delay of signals received at either ear. These smaller animals have to find an alternative if they want to achieve directional hearing. For small vertebrates, the solution to the directionality problem is mostly achieved through internally coupled ears (ICE). Some small lizards, frogs, and birds resort to this trick [60, 61], with the directional response being determined mechanically and not neurally [62]. Internally coupled ears have inspired acoustic sensors [63–65]. On the other hand, in the Insecta class, within invertebrates, hearing has evolved separately at least 19 times [11]. Insects have developed diverse solutions to the problem, some of which resemble ICE in vertebrates and some others having little to do with it.

Hearing in insects can be broken down into basically two groups: tympanal and flagellar hearing [44]. The first encompasses many species with big variability between them, both in location and working mechanism. The second consists mainly of mosquitoes and some flies, which have antennae with which they detect particle velocity instead of sound pressure. Particle velocity detectors, given that they measure a vec-

torial quantity, are inherently directional and are instead considered in section 2.2.2.4 for their signal amplification abilities. The tympanal directional hearing in insects of two orders (Orthoptera and Diptera) will be discussed ahead.

Orthoptera, popularly misnamed crickets or grasshoppers, are a widely known insect order that humans are well aware of because the chirping of some of its species happens to fall within the human hearing range. The true crickets are a superfamily (Grylloidea) within one of the two suborders of Orthoptera, Ensifera (the other being Caelifera). Similarly, grasshoppers are one group of insects within the same order. Some of the other insects belonging to this order are bushcrickets (also known as katydids) locusts, and the New Zealand wētā.

All insects in Orthoptera share some characteristics regarding sound production and reception. All of them produce sound by stridulation, which refers to the rubbing of two corrugated body parts against each other. Besides, they all share tympanal ears, even though there is great diversity in their morphology [66]. In Ensifera (the suborder that includes crickets and bushcrickets, among others), the tympana are located in the legs, and may appear as a single tympanum per leg or two depending on species [67]; in Caelifera (the other suborder that includes grasshoppers and similar), the tympana are found in the first abdominal segment. Nevertheless, in both suborders, the tympana are connected through a tracheal system to the outside via spiracles that some species are able to open and close at will [67].

The purpose of hearing in Orthoptera is to listen to both predators and prey, but additionally and most notably, for intraspecific communication [44]. The main purpose of male singing is to attract female mates. Males also chirp to deter other males from entering their territory. For this reason, both female and male specimens are interested in listening to those sounds and being able to tell where the sound is coming from, again resorting to directional hearing.

Hearing systems in Ensifera resemble ICE the most. These insects are known to have several paths through which sound can reach both the outer and inner surfaces of their tympana. They have, besides two asymmetric tympana on each of their two forelegs (four tympana in total), two spiracles, one on each side of the body, that serve

as outputs to the tracheal system consisting of ducts that allow sound to reach the inside surface of the tympana, at the same time adding sound pressure level gain and reducing the speed of sound within the tracheal ducts (see Figure 2.11 for a schematic drawing of the cricket's tracheal system). This way, Ensiferans' ears work as pressure difference receivers [68–70]. Female crickets have been seen to successfully track calling male crickets with one of their tympana impaired, which shows directionality can be achieved monoaurally [71–75]. Orthoptera also present frequency-discriminating hearing, which will be discussed in the next section.

Stepping away from Orthoptera and into the Diptera order (to which flies and mosquitoes belong, among others), one finds what is probably the most known insect in the domain of bio-inspired MEMS, *Ormia ochracea*. *Ormia ochracea* is a tachinid fly, parasitoid of crickets, that locates its host *Gryllus* by phonotaxis to the cricket's mating calls [76]. The auditory system of *Ormia ochracea* has long been of interest to researchers due to the uncanny accuracy with which it can locate the host call, a 5 kHz pure tone with a wavelength of over ten times the body length of *Ormia ochracea* and one hundred times the separation between the insect's tympana. This insect has directionality down to an accuracy of 2^{o} in the azimuthal plane [77].

The system consists of two diaphragms mechanically connected by a bridge and pivot allowing the transfer of energy from the motion of one diaphragm to another (Figure 2.12. When the stiffness of this connecting bridge is correctly tailored to the system, the signals from the stimulating sound wave and the linked companion diaphragm will constructively interfere with the ipsilateral sound source and destructively interfere with the contralateral sound source. The result is what was termed by Miles and Robert [78] mechanical interaural phase difference (mIPD) and mechanical interaural intensity difference (mIID) which can be 40 times higher than the phase difference in the stimulating sound field. Much of the research into *Ormia*-inspired systems targets applications in hearing aids [79]; however, there is an inherent conflict: the *Ormia*'s coupled ears are a resonant system and so single-frequency, while hearing aids, or teleconferencing applications require broadband sound source localization.

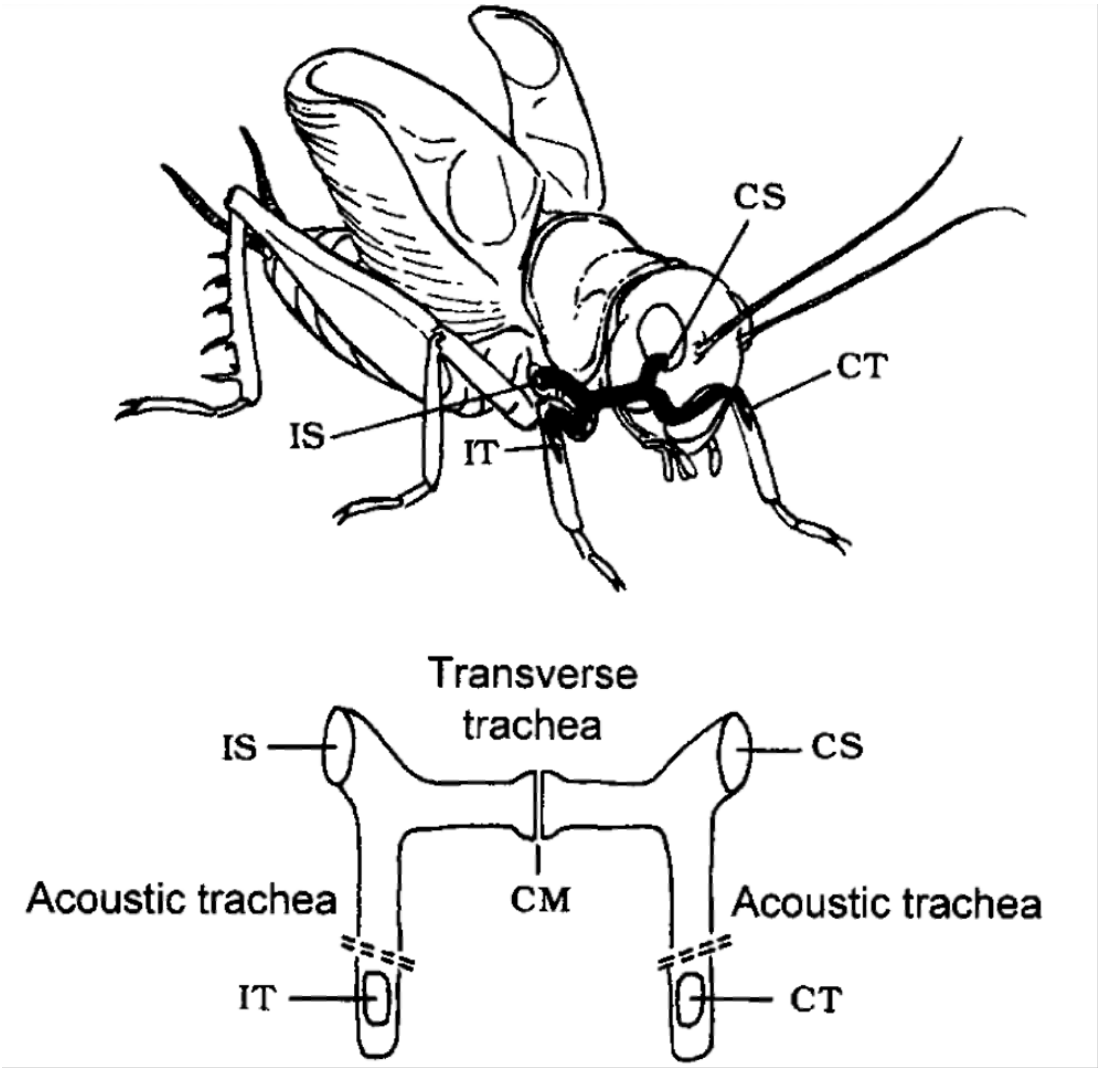

Figure 2.11: Schematic of the cricket's tracheal system, showing the two tympana and spiracles. CM: central membrane; CS: contralateral spiracle; CT: contralateral tympanum; IS: ipsilateral spiracle; IT: ipsilateral tympanum.

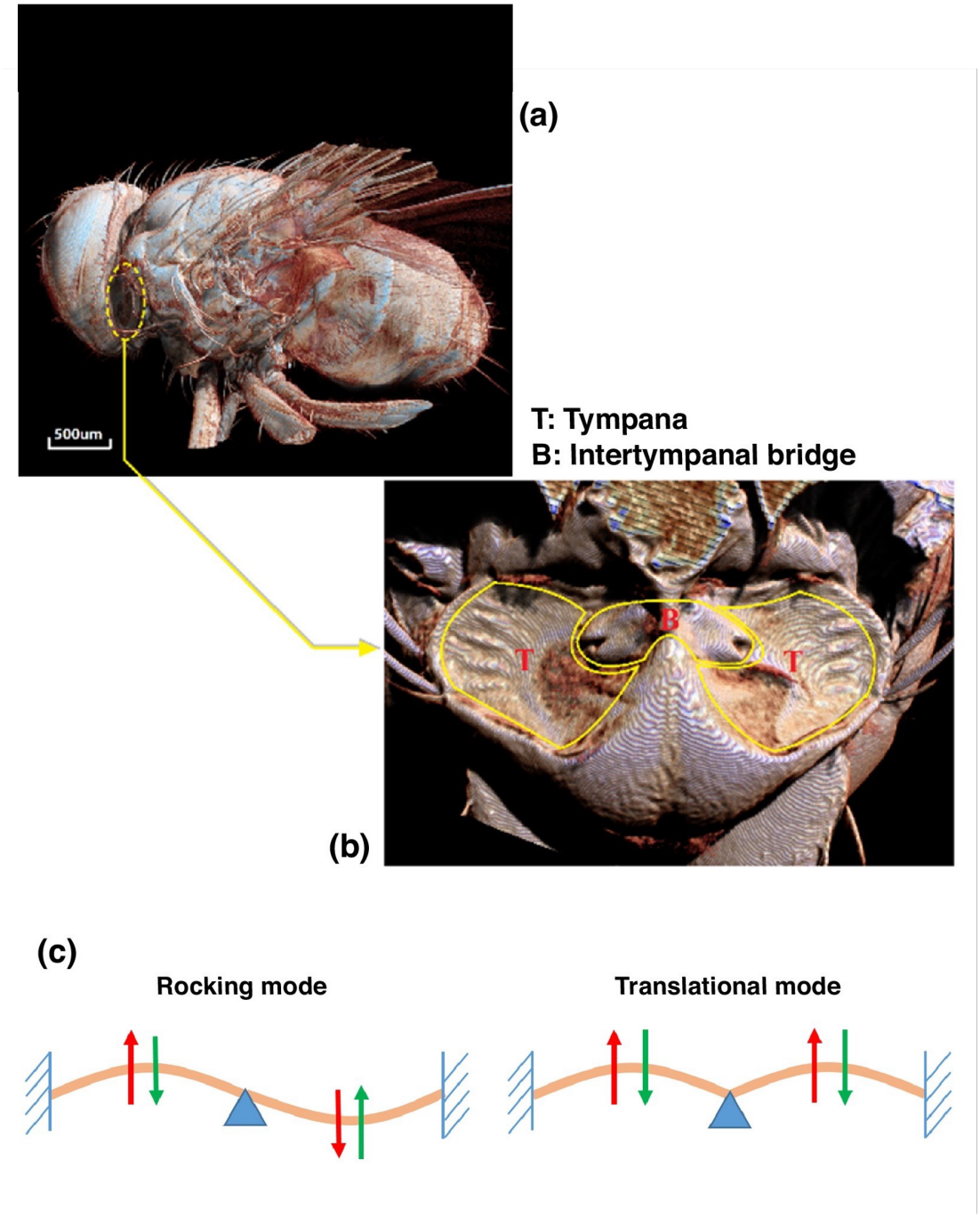

Figure 2.12: μCT images of the tympanal system of *O. ochracea* and schematic showing the mechanical equivalent and the two modes of vibration.

2.2.2.3 Frequency discrimination

As explained in the introductory section on acoustics, frequency is one of the parameters that characterise sounds. Frequency can encode information, therefore there is a reproductive and survival advantage from the ability to distinguish the frequency composition of predators and competing species. All ears must translate acoustic energy travelling through a medium, usually air, into mechanical motion, and then to electrical impulses. Electrical impulses are generated by neurons and, in acoustics specifically, by auditory mechanoreceptor cells, neurons with mechanically gated ion channels that require an acoustic-mechanical stimulus to fire an action potential [80].

To have a means of discriminating frequencies, multiple sensory neurons must be individually tuned to different frequencies [29], which is a problem for simple ears of a small size that presumably want to minimise the number of neurons invested in hearing. Individual tuning of multiple cells can be achieved by the arrangement of the neurons according to a morphological gradient. Morphological variation of a substrate – for example, some areas being thicker, thinner, wider, or narrower – in the cells' proximity can cause different points on the substrate to move differently according to the input frequency [39]. The frequency-specific maximal displacement of the point, if coupled somehow to a sensory neuron, can in turn stimulate that neuron independently, thus tuning the cell to a single frequency. This place-based frequency decomposition is called tonotopy [28].

An additional problem related to the frequency of calling signals is that of the acoustic environment since mating calls must compete with the potentially masking calls of other species without unnecessarily attracting the attention of predators [81]. These mating calls are frequently pure tone signals, reflecting their reliance on resonant structures to transmit the necessary power to attract a mate as well as the need to seek unoccupied space in the locally available acoustic spectrum [82]. This places some constraints on the available communication bandwidth since the resonant frequency is determined by the size of the radiator and, in order to transmit efficiently, the resonant structure should have a diameter approaching half of the signal wavelength [83]. In this section, dispersive frequency decomposition is discussed, where sound travels and

is localized to particular sites based on its frequency.

Dispersive frequency decomposition relies on a travelling wave (a wave that moves throughout a medium); it is typically a flexural mode on a thin medium. The most well-known example of this is the travelling wave associated with the basilar membrane of the mammalian cochlea, discussed in section 2.2.1. In contrast to vertebrates, among invertebrates, tonotopic systems are considerably rarer, and yet invertebrates also showcase the most diversity of system design. Moreover, invertebrate tonotopy is less understood and provides greater scope for novel discovery. Such ears can be categorised into two types, cochlea-type tonotopic systems and tympanal tonotopic systems. Both are exemplified by the bushcricket and the locust, respectively.

The bushcricket ear possesses a well-described insect cochlea, known as *crista acustica* [84]. A *crista acustica* has also been described for the great grig *Cyphoderris monstrosa*, relatives of the bushcricket family [85], and some sort of cochlea analogue has been hypothesised for the cricket [66]. Bushcrickets have two ears, one on each of their two forelegs, located basally in the forelegs' tibiae, consisting of two external tympanal membranes on either side of the leg, making four eardrums in total. Features of the bushcricket ear are reminiscent of the vertebrate peripheral auditory anatomy in terms of function. These include the acoustic trachea that works like an ear canal (outer ear), the tympanal plate (possibly functioning as a middle ear), and the *crista acustica*, enclosed in a fluid-filled cavity (the bushcricket's inner ear or cochlea) [86]. See Figure 2.13 A and B for a picture and schematic drawing of the structure.

The most noticeable characteristic of the bushcricket's *crista acustica* is its tapered shape and orderly arrangement of sensilla (Figure 2.13 A). The sensory neurons, which can range in number from 15 to 116 depending on species [91], are tonotopically arranged from high-frequency tuned cells at the narrowest tip of the organ (up to and above around 50 kHz) to those tuned to lower frequencies at its wider end (tuned from about 6 kHz) [92]. These sensors lie on a thin wall of a cuticular cavity, the anterior tracheal branch. Their dendrites project upwards dorsally, and each connects to a cap cell which is itself attached to a thin sheet that covers the entire organ, the tectorial membrane. Notably, the size gradient of these cap cells is correlated with the tonotopy.

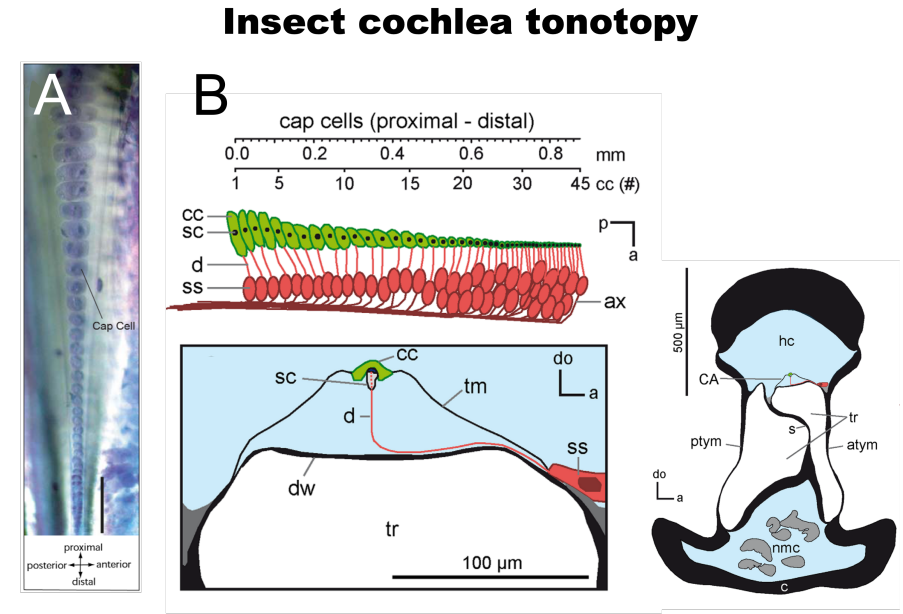

a: anterior; atym: anterior tympanum; ax: axon; c: cuticle; cc: cap cell; d: dendrite; do: dorsal; dw: dorsal wall; hc: hemolymph channel; nmc: nerve muscle channel; p: proximal; ptym: posterior tympanum; sc: scolopale cell; ss: sensory soma; tm: tectorial membrane; tr: trachea.

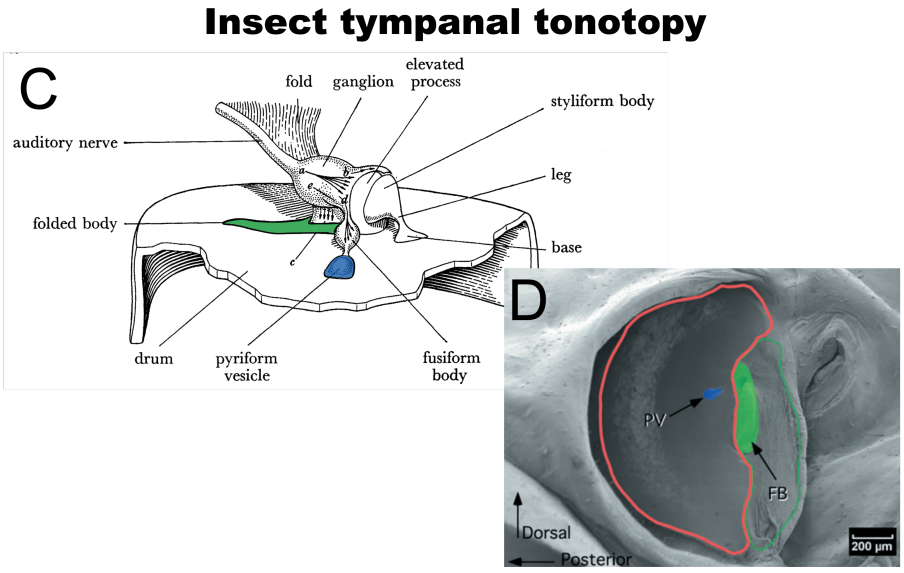

Figure 2.13: Tonotopic insect systems. (A) Bushcricket *crista acustica* stained with methylene blue [87]. (B) Anatomy of the *crista acustica* [88]. (C) Anatomy of the four locust mechanoreceptor attachment points on the underside of the tympanum [89]. Adapted to highlight the same points shown in the adjacent image, D. (D) SEM of the external surface of the locust tympanum [90]. Red outline: thin membrane; green outline: thick membrane; blue feature: attachment point of mechanoreceptors tuned to high frequencies; green highlight: attachment area of low-frequency sensors.

Nevertheless, the correlation is not strong enough to account for the full resolution of frequency representation. Rather, the tonotopy may require another morphological gradient such as features of the sensors themselves [88]. This arrangement appears to enhance a travelling wave across the tectorial membrane, differentially stimulating the sensory cells according to frequency. The wave is initiated at the organ's narrow end and travels along the membrane towards the low-frequency tuned sensors, terminating closer to the wider tip at low-frequency impulses and closer to the point of initiation at higher frequencies [87].

The other type of tonotopic mechanism is not at all like a cochlea and, in fact, has no comparison among the vertebrates. In tympanal tonotopic systems, known in the locust [90], the cicada [93], and more recently in the great grig [85], the tympanum, responsible for sound capture, is also responsible for frequency decomposition; both functions occur at the same substrate. This dual functionality requires the eardrums to be unusually complex, and indeed the locust tympanal membrane may be considered the most sophisticated tympanum yet identified.

Locusts have two tympana, one on each side of their abdomen. Around 70 mechanoreceptor cells attach to the underside of each tympanum, forming Müller's organ, a ganglion of sensilla divided into four groupings. Three of these are tuned to low-frequency bands (3.5 to 4, 4, and 5.5 to 6 kHz) and one to high frequencies (12 to 20 kHz) [89,94]. Each sensory group is secured to its own specific morphologically unique tympanal feature (Figure 2.13 C). In addition, the locust eardrum exhibits further, larger-scale heterogeneity in the form of two parts to the tympanum, a thin membrane, and a smaller thicker membrane (Figure 2.13 D). High-frequency mechanoreceptors attach to a point on the thin region, whereas the others connect to fixtures of the much thicker membrane [90, 95]. Thus, a degree of morphological gradation is provided, enabling travelling waves. When stimulated with sound, a travelling wave is initiated in the thin membrane that maximally vibrates the tympanum at one of the four locations, depending on the stimulus frequency. At frequencies above 10 kHz, no movement of the thick membrane is detected. Rather, the travelling wave terminates at the high-frequency attachment point, rapidly attenuating when reaching the thicker cuticle. As

such, there is a clear spatial frequency decomposition of high and low frequencies [90].

2.2.2.4 Signal amplification

The third central problem for insect hearing is the inherently low energy of a propagating sound wave over the length scales that the insect can hope to capture. This problem is compounded for velocity sensing organs, such as the antenna in mosquitos and fruitflies, where the mechanism for energy capture is through the viscous drag losses in the antennal hairs [96].

Active hearing refers to the ability of the mammalian cochlea to greatly amplify sounds, due to a positive feedback mechanism that takes place in the outer hair cells, which show electromotility [97]. The term active describes the fact that this amplification is not seen on dead cochleae, as opposed to other passive mechanisms such as tonotopy. Active hearing is also seen in some insects.

In order to maximise the capture of these sounds and the transduction into neuronal signals, the mechanoreceptor neurons themselves add energy to the system, resulting in a non-linear response to sound [98]. The existence of active hearing can be inferred from non-linear response characteristics in tympanal systems in insects, such as otoacoustic emissions or self-generated oscillations in tree crickets [99]; nevertheless, the small scale of these systems and the relatively low number of congregated mechanoreceptors compared to Johnson's organ in the mosquito, make these systems harder to study, whereas it can be directly observed in antennal systems.

The champion species for active amplification in flagellar systems is the elephant mosquito, *Toxorhynchites brevipalpis*. The hearing organ consists of an antenna shaft which sits within a pedicel. Mechanically, it acts as a rotational spring, causing the antenna to oscillate in a rigid body motion with a resonant frequency of between 300 to 500 Hz [100]. Within the pedicel is Johnston's organ, a collection of some sixteen thousand mechanosensory cells arranged in a bowl shape along the base of the antenna. These consist of a scolopale rod which connects the antennal structure to the chordotonal neuron, which both senses the motion of the antenna and can inject additional energy into the antenna's oscillations [101]. See Figure 2.14 for a picture, cross-section,

and schematic drawing of the mosquito antenna, with the main elements labelled. If this system is modelled in a sound field as a passive oscillator, it can be approximated as a damped harmonic oscillator [102, 103]. Such a system will have a defined resonant frequency and a Q factor given by the ratio between resonant frequency and damping, which gives the half-power bandwidth of the resonant response.

Mosquitoes use their auditory receptors for mating purposes, detecting the acoustic signature of a female's wing beats. The female creates an extremely weak and brief sound signal, a sound particle displacement of around 3.5 nanometres at 10 centimetres [98]. As the sound intensity varies sharply and quickly with the change in distance between the male and the potential mate, the mosquito requires a sensor with an extremely fast temporal response. Mechanically, this would be a broadband sensor with a low Q factor, allowing the detection of higher frequency transients in the signal. Conversely, to successfully track the female, the male must filter out environmental noise for which a broadband sensor would be a poor choice and a sharply resonant, high Q factor sensor would be preferred. The antenna's frequency selectivity in passive hearing is principally determined by the resonance of the flagellum and spring base, which is well-damped and low Q factor [100]. The mosquito maximises its tracking efficiency by switching from the initial passive response to a sharply resonant response through the generation of force in the neurons at the base of the antenna [100]. These neurons fire at twice the frequency of the antenna's sound field-driven oscillation, sharpening the tuning of the resonant frequency [104].

2.3 Microphones

Microphones are omnipresent, they are used to record the music or the radio programs that people listen to every day, people talk through one when they pick up a telephone to call, and they are an essential component in current smartphones.

Microphone, etymologically, comes from the Greek; from *micro* (μίκρο), which means small, and *fono* (φόνο), which means sound or voice. A microphone's job is to convert mechanical energy in the form of acoustic waves to an electrical signal. In other words, their function is analogous to that of hearing for humans and other ani-

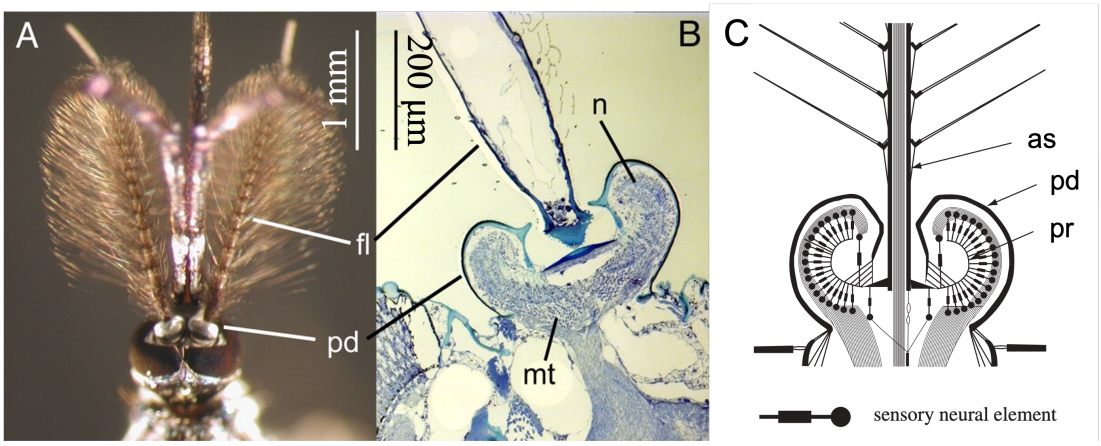

Figure 2.14: The mosquito antenna. (A) Picture of a male mosquito antenna [105]. (B) Cross-section of the antennal pedicel (Picture by H. Kohler and D. Robert) [105]. (C) Schematic of the mosquito antenna [106]. as: antennal shaft; fl: plumose flagella; mt: mitochondria; n: neurons; pd: pedicel; pr: prongs.

mals. The history of microphones goes back to the end of the 19th and beginning of the 20th centuries, with many advances in the quality of performance but the essence of the working mechanism of microphones remaining similar [107].

2.3.1 Standard microphones

There are several types of microphones, usually classified according to the transducing effect they exploit. In condenser microphones, a thin moving membrane known as the diaphragm vibrates in response to incoming sounds. The diaphragm is one of two plates of a condenser, or capacitor, an electronic component that produces a change in capacitance proportional to the change in the distance between the plates. The variation in capacitance is, in time, measured as a voltage difference across the plates. This way, the mechanical movement of the diaphragm produces an electrical current. Condenser microphones presented a disadvantage in their need for external polarization voltage, which was solved in the early 1960s with the inclusion of permanently polarized dielectric materials [108]. This, together with the possibility of reducing their side, makes condenser microphones one of the most used nowadays.

On the other hand, dynamic microphones make the most of electromagnetic induction. A conducting ribbon or coil of small size is placed within a transverse mag-

netic field, meaning that the displacement that the conducting element experiences as a result of the voice's sound pressure produces a voltage, directly proportional to the velocity of the element, which is then measured. Another advantageous effect for microphone manufacturing is piezoelectricity. Piezoelectricity is a phenomenon that certain solid materials exhibit where they accumulate electric charge in response to external mechanical stress (deformation or bending) [2]. In piezoelectric microphones, a diaphragm experiences deflections due to incident sound pressure that will translate to stress on the piezoelectric material, which generates a change in voltage [109].

In the 1930s and 1940s, a new type of microphone was developed and perfected, known as the pressure gradient microphone. It also includes a diaphragm but, in this case, sound can reach the exposed back of the diaphragm as well as its front, causing the diaphragm to respond to the pressure gradient [110]. The pressure gradient is directly proportional to air particle velocity close to the diaphragm at long wavelengths; it also increases with frequency, but only as long as the sensing points' axes are parallel to wave propagation. A sketch of both a pressure microphone and a pressure gradient microphone can be seen in Figure 2.15.

There are several considerations fundamental to microphone design, like frequency range or how to handle noise, still relevant to microphone manufacturers nowadays. Another such aspect is the directionality of microphones. Directionality, or directivity, is, in short, enhanced sensitivity to sounds coming from one direction over others, or the ability to determine the direction of provenance of a sound, echoing the definition of directionality in animals. Depending on its intended use, it is interesting that the microphone picks up sound from mainly one direction, or from the front and back but not the sides, or potentially from all directions equally. These receive the names of cardioid, bidirectional, and omnidirectional patterns respectively. These patterns, together with hypercardioid and shotgun, can be seen in Figure 2.16, and are some of the most common directional patterns in commercial microphones. Some microphones have inherent directionality, for example, the directionality response of the pressure gradient microphone is bidirectional; if sound comes from 90^{o} or 270^{o}, being 0^{o} the front of the microphone and 180^{o} the back, the sound will reach the front and back

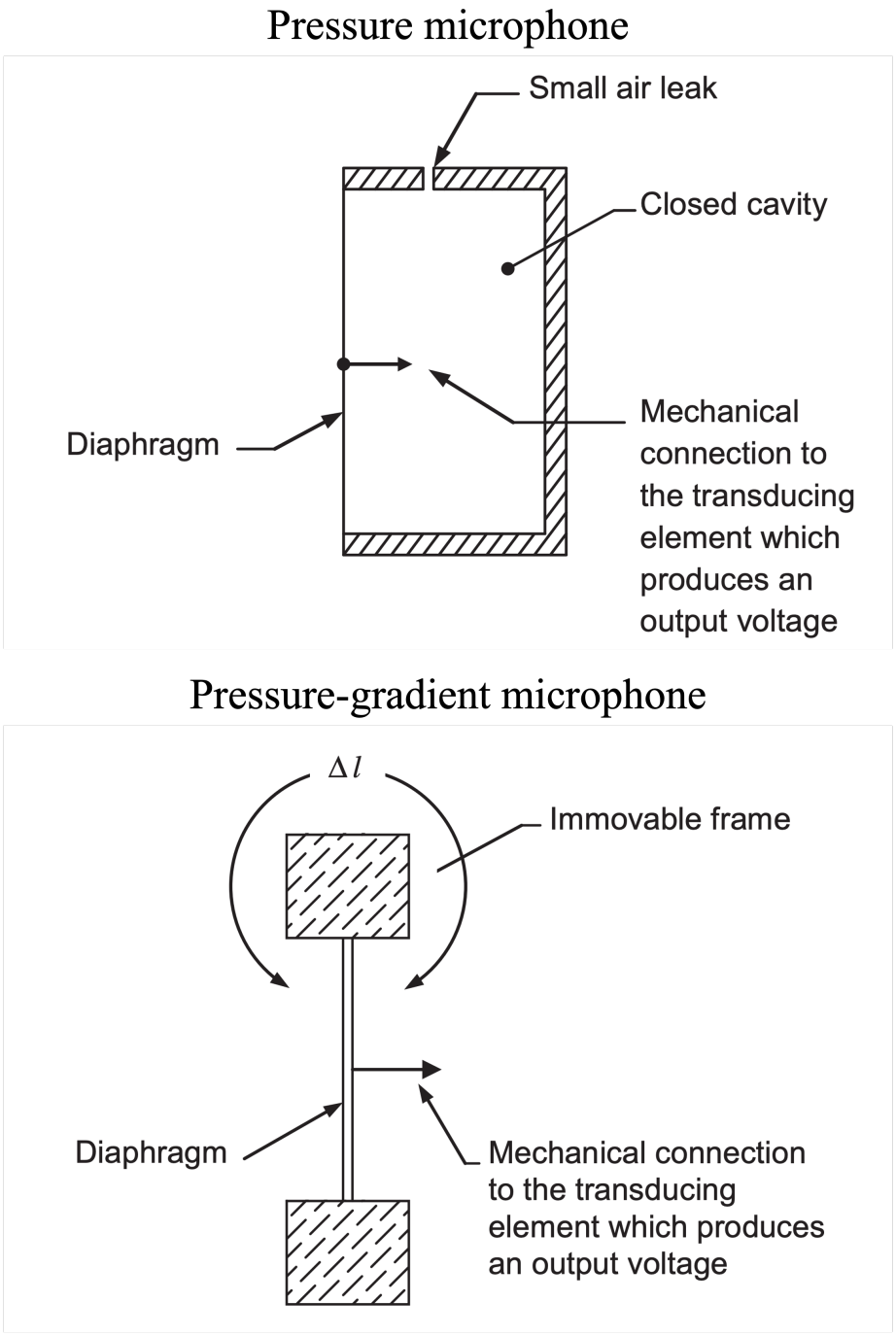

Figure 2.15: Sketches of pressure microphone and pressure-gradient microphone, from Beranek and Mellow's Acoustics: Sound Fields, Transducers and Vibration [111].

of the diaphragm with the same intensity and phase, not eliciting a response from the microphone [111]. Other types of microphones are grouped into arrays to achieve a specific pattern through a combination of the directionality of each element of the array.

2.3.2 MEMS microphones

In the last few decades, a lot of research has been involved in trying to reduce the size of microphones. A small microphone is desirable for many applications, such as smartphones or hearing aids, where a light and portable device is advantageous [113]. Microelectromechanical Systems technology, referred to as MEMS, was established in the 1960s [114]. MEMS technology includes devices like accelerometers, gyroscopes, or microphones among others [115]. A MEMS device is made of some functional components measuring microns and is generally assembled in a total size ranging from a few microns up to a few millimetres [116] (see Figure 2.17 for an example of a MEMS microphone and its relative size). Said functional components are a mix of moving parts and fixed parts.

Some of the most commonly used fabrication techniques for MEMS follow the approach used for semiconductors, similarly pursuing miniaturization of technology [117]. The two most common MEMS fabrication techniques are surface micromachining and bulk micromachining. In surface micromachining, layers of materials are deposited over a base layer. To liberate the space under the moving parts, sacrificial layers are used, i.e. layers that are deposited and later etched away to provide an air gap for the moving parts. In bulk micromachining, on the other hand, all moving elements are selectively etched from an initial block of material [117]. In both techniques, the base material is frequently silicon but can be other materials like polymers or ceramics [118]. Other techniques more precisely aimed towards MEMS fabrication, like Lithography, Electroplating, and Moulding also exist [119, 120].

MEMS microphones can be separated into categories according to their working mechanism, analogously to conventional microphones. Some of them use the same technique that regular condenser microphones employ, with a moving diaphragm that

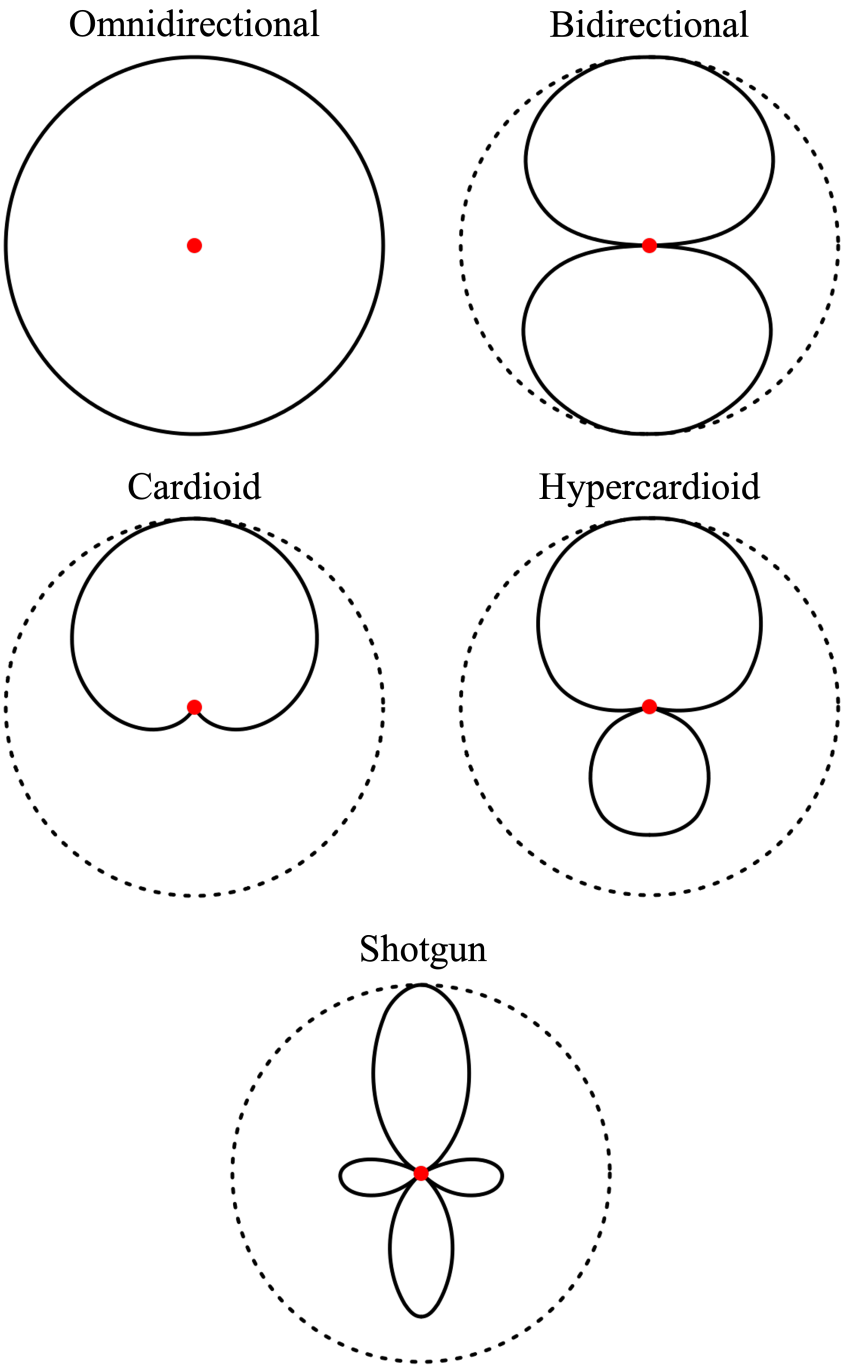

Figure 2.16: Directional patterns of microphones [112]. The top (0^{o}) of each polar plot represents the front of the microphone and the bottom (180^{o}) corresponds to the back.

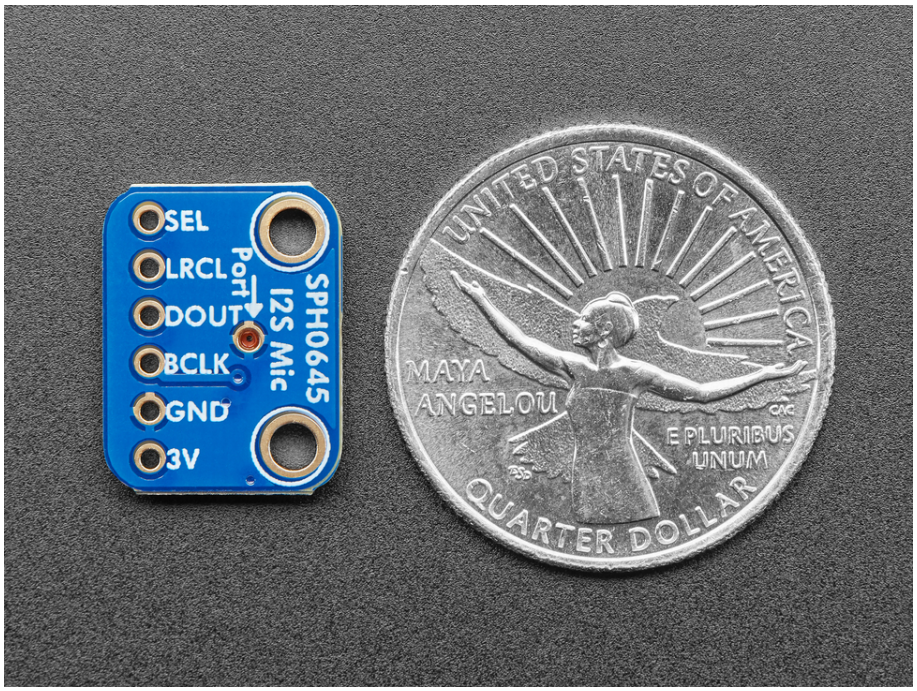

Figure 2.17: Example of MEMS microphone. Adafruit I2S MEMS Microphone Breakout next to a quarter US dollar (diameter of 24.26 mm) [121]. The MEMS microphone itself is the small circular element signalled by the term port.

induces a change in capacitance. The capacitive element can also take the shape of comb fingers [122]. Piezoelectricity is also exploited in MEMS microphones [123]. See Figure 2.18 for a schematic representation of the three types of microphones.

MEMS microphones present great advantages like resilience against temperature change, humidity, or external vibrations [115], but for directionality, it is common for MEMS to relay on microphone arrays to combine omnidirectional patterns, which implies distancing the array elements and going against that quest for size reduction. Furthermore, the fundamental frequency of speech is between 85 and 255 Hz, [124] with corresponding wavelengths of over a metre, which is a scale that no longer corresponds to MEMS; this is the main problem to solve for human voice applications. Bio-inspiration has successfully been exploited in the design of MEMS, with examples of acoustic sensors that achieve directionality, frequency decomposition, and active amplification [125–129]. These examples and more are detailed in section 2.4.

2.4 Insect-inspired acoustic sensors

2.4.1 Directional sensors

Ormia-inspired directional microphones are undoubtedly the largest class of bio-inspired hearing sensors and, consequently, have been subject to several dedicated reviews [125, 126]. The overwhelming direction of design has been towards a single-layer see-saw design realised in a silicon-on-insulator or related MEMS process, either as a single sensor (Figure 2.19 F, G) or an array (Figures 2.19 B, C) [127, 130–132]. This operates similarly to the *Ormiini* system, with each of the "wings" of the device comparable to one tympanum, while the torsional stiffness of the bridge connecting the device to the substrate performs the equivalent function of the raised bridge and fulcrum in *Ormia ochracea*. The system is attractive to researchers as it is easily implemented in a multi-user MEMS process, and it can, with careful tailoring of the relative stiffness of the membrane wings and the torsional stiffness of the bridge, amplify directional cues in a similar manner to *Ormia ochracea*. This design path has several challenges which have not yet been overcome besides the inherent resonant nature of the device. The first is

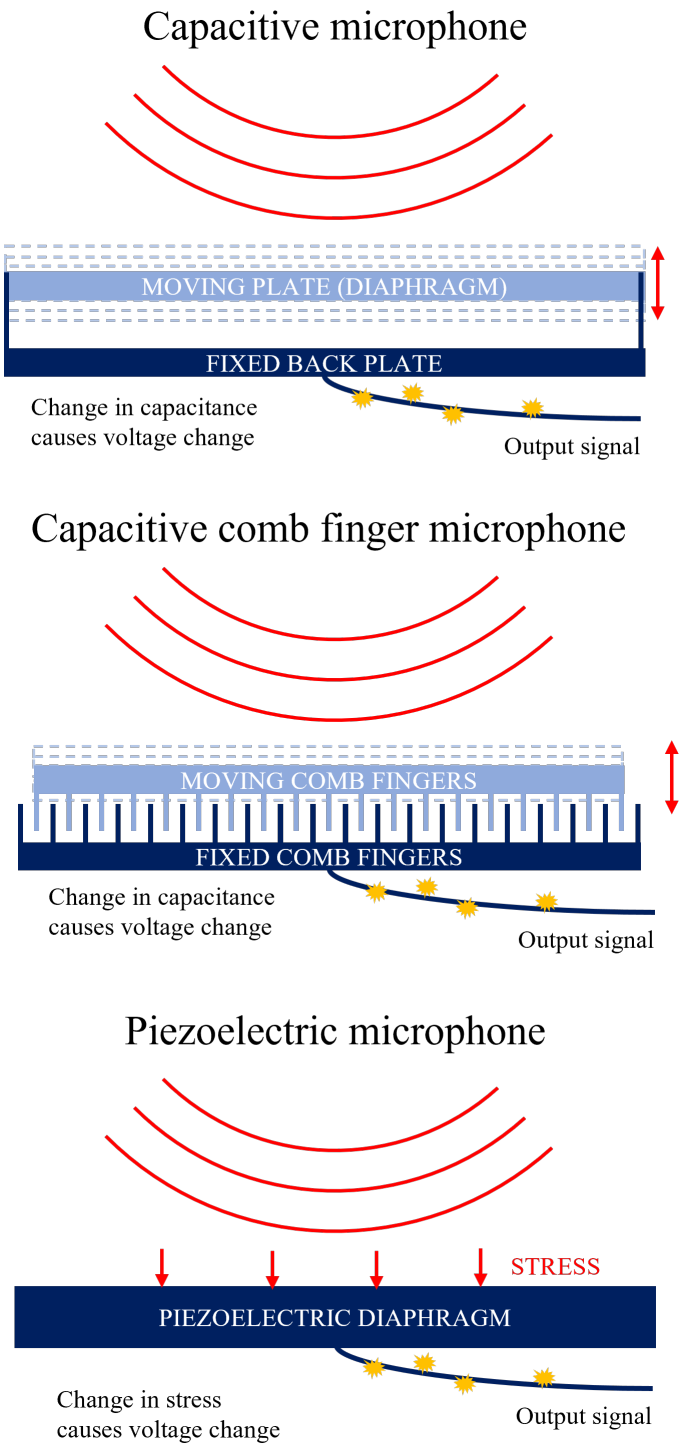

Figure 2.18: Schematic representation of three different types of MEMS microphones: capacitive, capacitive comb fingers and piezoelectric.

the signal-to-noise ratio achievable in this system. As the *Ormia*-inspired microphone relies on the interaction between the resonant modes, a traditional capacitive backplate is generally not used, at least partially because of the thin-film damping such a structure would introduce [133, 134]. Because the system works optimally at the frequency where the in-phase resonance and the out-of-phase resonance are the same power, increasing the bandwidth of these resonances necessarily means increasing the separation between the frequency peaks of the two modes. This has the effect of lowering the amplification of directional cues but does broaden the frequency range over which this is possible [135]. Principally, designers avoid this issue entirely by incorporating optical [133], piezoelectric (Figure 2.19 D) [136], or capacitive comb-based sensing schemes (Figure 2.19 H) [132, 135]. The first of these adds significantly to the design complexity and cost, while both piezoelectric and capacitive comb-based methods in MEMS devices have low sensitivities [131, 137, 138].

The second obstacle to a good signal-to-noise ratio is more fundamental to the design – as the see-saw mechanism must be released from the periphery except at the anchor points, the sound is free to diffract around the device. Since these devices are typically of a maximum size of 1 by 2 mm and the target sound field is in the acoustic range, the pressure difference across the membrane is minimal. This can be solved by making a more direct model of *Ormia*'s hearing system, however, so far, all examples have been demonstrated at the mesoscale due to the complexity of fabricating a true 3D structure using lithographic methods [139, 140].

2.4.2 Frequency discriminating sensors

Engineered systems based on spatial frequency decomposition frequently target sub-Nyquist rate sampling as the value of their system [141]. An analogue-to-digital converter has a maximum sampling rate, and increasing this sampling rate lowers signal-to-noise ratios and increases power requirements [142]. A signal which is already filtered can be captured with lower sampling frequencies, and yet retain a higher effective sampling rate that can be significantly compressed by only retaining content when it is above a threshold. This strategy has been applied using electronic filter banks [143]

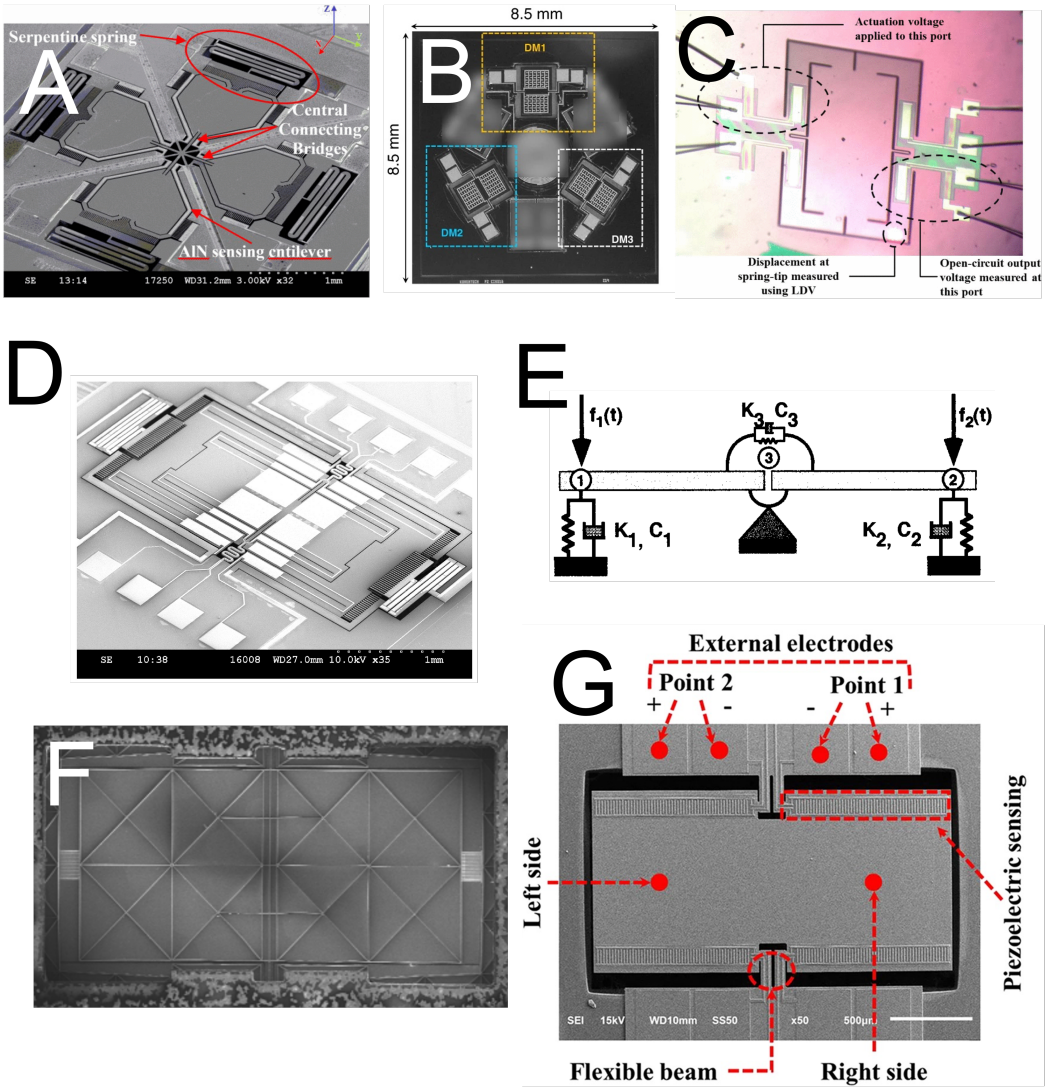

Figure 2.19: Directional insect-inspired acoustic sensors. (A) Arrays of *Ormia*-inspired membranes [126]. (B) four coupled membranes [79] © [2018] IEEE (C) Array of 3 see-saw style *Ormia* membranes [134]. (D) Transduction of membrane motion using piezoelectric sensing and lever arms attached to the central membrane [130] © [2009] IEEE. (E) Illustration of rocking and translational mode along with standard two-degree-of-freedom model of the *Ormia* system [78]. SEM images of *Ormia* membranes targeting low acoustic frequencies using (F) silicon-on-insulator MEMS [126] and (G) Silicon nitride patterning [125]. (H) Transduction of membrane motion using capacitive comb sensing [131].

and even converted to an output spike train to mimic the event-driven format of nerve conduction [144]. Mechanical filtering of the signal can be grouped into solutions using an array of resonators (figures 2.20 A, D) [145, 146] or solutions using a tapered membrane [147]. Resonator arrays perhaps are the most obliquely connected to the natural inspiration, but they are simple to implement on silicon as arrays of cantilevers (Figure 2.20 B) [128] or clamped-clamped beams (Figure 2.20 C) [148]. The resonant frequency of each channel can be adjusted by changing the length of the beam; and transduction of the signal may be accomplished by piezoelectric [150, 151], triboelectric [148] or optical means [152]. While relatively easy to implement, using a beam as a method of acoustic capture is extremely inefficient for lower frequencies due to diffraction around the relatively narrow beam width. The pressure difference between the front and back sides of the cantilever is small, resulting in maximum displacements at resonance in the order of tens of nanometres [153]. The resultant electrical transduction and signal-to-noise level are also prohibitively small since the cantilevers may not rely on capacitive sensing through an electrical backplate, as in a traditional microphone, due to the impact of thin film damping on both the mechanical sensitivity of the device and the resonance frequency [154, 155]. Piezoelectric sensing can be used with the ceramic element implemented either on the upper surface with interdigitated electrodes [145], or by fabricating the cantilever as a bimorph [156]. However, both strategies produce piezoelectric charge sensitivities in the order of femtoCoulombs per nanometre. One strategy to overcome this limitation in MEMS consists of using a thickened or disc-shaped central region in the arrays, maintaining a thin base region for the purposes of keeping a desired resonance frequency while maximising the surface area for acoustic capture (Figure 2.20 E) [149].

Frequency decomposition based on tapered membrane structures is closer to bio-inspired sources, consisting of a single membrane with significant acoustic dispersion to isolate the frequency bands. Such systems have two fundamental requirements: there must be a time-dependent pressure gradient along the membrane to support flexural wave propagation, and the wave velocity must change along the length of the membrane. The support of a travelling flexural wave can be achieved by having a defined, highly

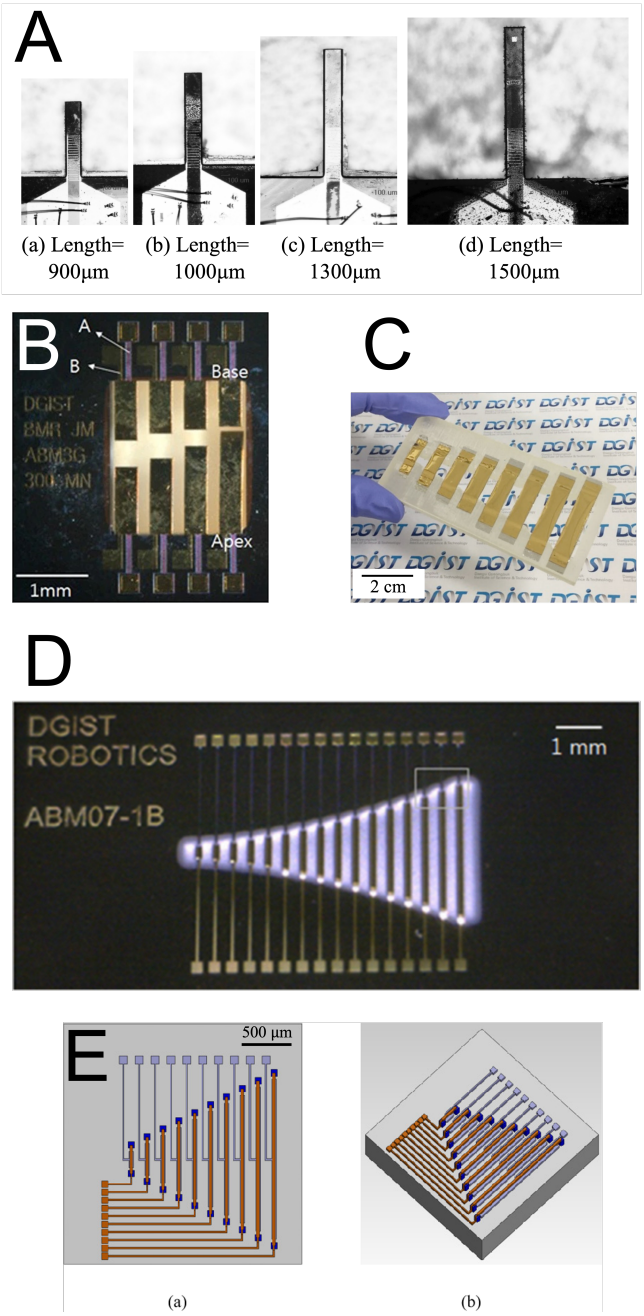

Figure 2.20: Tonotopic array of resonators insect-inspired acoustic sensors. (A) Single crystal PMN-PT cantilevers with interdigitated electrodes [145] (B) Dual-sided cantilever array [128] (C) Clamped-clamped array with triboelectric transduction [148]. The bottom row shows solutions to achieving desired frequency while maximising surface area for mechanical sensitivity (D) Tapered clamped-clamped beam array [146] and (E) COMSOL simulation of centrally supported disc array with clamped-clamped beams [149] © [2016] IEEE.

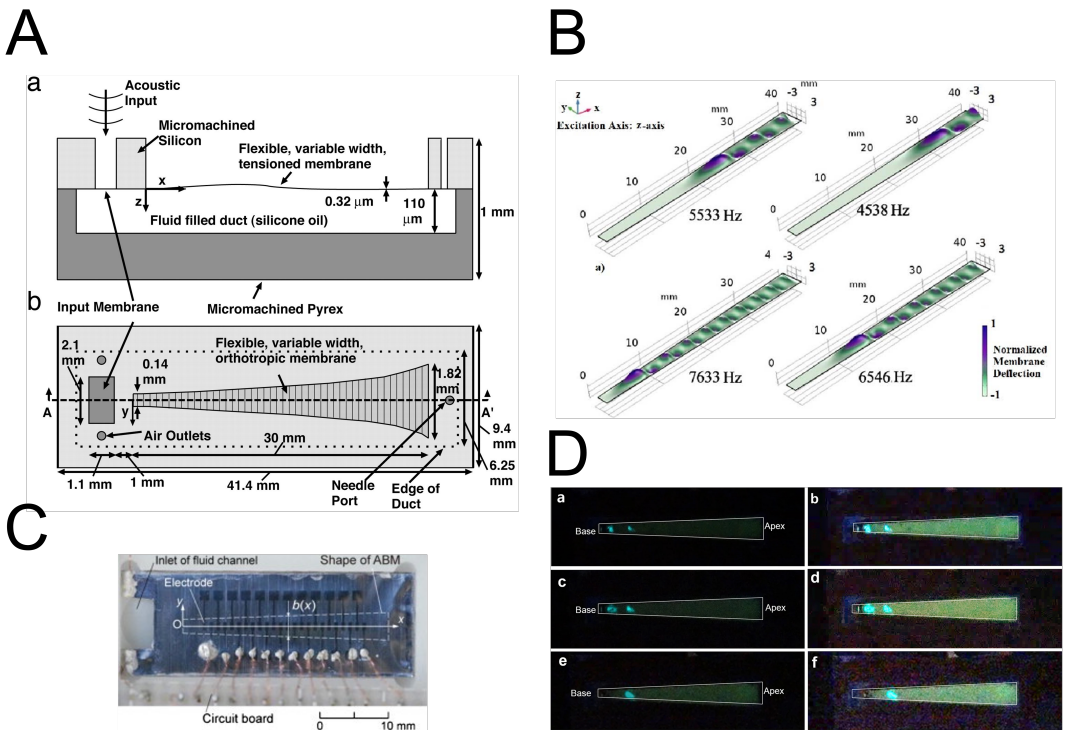

Figure 2.21: Tonotopic continuous membrane insect-inspired acoustic sensors, which have one single graded sensing area with a localized transduction mechanism. (A) Hydromechanical model of the basilar membrane with silicon oil backing with a small input membrane analogous to the oval window in the cochlea [147] © (2005) National Academy of Sciences, U.S.A. (B) COMSOL model of deflection patterns in a tapered membrane at a range of acoustic frequencies [158] © [2020] IEEE. (C) Fluid-backed tonotopic sensor using PVDF as the membrane with individual measurement points [159]. (D) Luminescent tapered membrane showing some frequency separation at very low frequencies (a, b) 110 Hz; (c, d) 80 Hz; (e, f) 40 Hz [150].

localized sound input point, analogous to the oval window in the mammalian cochlea (Figure 2.21 A) [147,157], or by ensuring the membrane length is between 1/6 and 1/4 of the frequency range of interest to ensure a phase difference across the membrane surface (figures 2.21 B, C) [158,159]. Both solutions have limitations since restricting the sound input to a single point restrains the power that may be captured by the device, and tailoring the membrane length to the phase difference in the incoming sound wave either requires prohibitively large membranes or a highly restricted high-frequency range of interest.

The second requirement for acoustic dispersion is equally challenging to meet within

the constraints of MEMS systems. The most obvious source of generating dispersion is through the tapering of the thickness of the membrane, based on an Euler-Bernoulli model of a thin plate where the bending wave speed may be given by [160]:

$$c_b = \left(\frac{E \cdot h(x)^2 \cdot \omega^2}{12\rho \cdot (1 - \nu^2)} \right)^{1/4} \tag{2.3}$$

Where E is Young's modulus, *h(x)* is the thickness profile, ω is the angular frequency, ρ is the density, and ν is the Poisson's ratio. In theory, for every frequency, there is a height below which the wave speed will drop to the point where it is no longer transmitted, or at least may be assumed to be sufficiently attenuated, analogous to the acoustic black hole effect described by Mirinov [161]. In practice, the variation in thickness would need to be two orders of magnitude over the length in order to separate frequency bands in the acoustic range using a common MEMS material such as single-crystal silicon.

The more commonly seen model varies the width of the membrane along its length, which should not result in variation of the phase velocity [162]. Instead, such systems rely on the membrane being placed on a closed channel, or either air or some fluid medium, such as water [163] or silicon oil [159]. The variation of the velocity of fluid flow in this channel generates a variation in the velocity potential [164], and hence the local pressure on the membrane; while the depth of the fluid channel increases, the fluid loading on the membrane reduces the resonance frequency (Figure 2.21 D) [165]. This, in combination with the slight spatial variation of the membrane's first-order resonance peak with frequency, results in some degree of tonotopy. Despite the size of these membranes, over 5 cm in length, they have extremely low mechanical responses at the resonance of less than a micron displacement and are only able to separate a few, widely separated frequency bands with poor spatial confinement compared to examples in nature.

2.4.3 Active feedback sensors

The concept of active Q control has found applications in atomic force microscopy [166, 167] and in optical amplifiers, where it is referred to as parametric amplification. Rather than directly injecting energy, parametric amplification involves changing some properties of the system with a specific phase timing, analogous to a child on a swing. In acoustic systems, the forcing mechanism is usually directly applied to either the membrane or the flagellum through electrostatic actuation, perhaps more analogous to someone pushing a swing.

At root, this is a feedback system where the oscillations of the acoustic receiver are filtered through a leaky integrate and fire stage and recombined. In practice, this has meant generating a pulsed actuation signal controlled by a computational control mechanism, designed to fire in time with the oscillations of the incoming microphone signal. A MEMS microphone directly inspired by this principle was demonstrated by Guerreiro et al. (Figure 2.22 B) [168, 169], using capacitive combs to inject the pulsed feedback signal. This was a unipolar signal, firing only once per oscillation of the membrane as opposed to the 2:1 mode of the mosquito [105]. The Q factor of the MEMS microphone is already high in the absence of strong damping sources such as thin film damping; however, the feedback mechanism demonstrated an increase of the Q factor from 30 to 66 with a consequent amplification of 2.19 [168].

The mechanism has also been used to lower the effective Q factor in *Ormia*-inspired devices. As noted, MEMS devices without backplates will experience very light damping and therefore exhibit sharply resonant behaviour which can be a detriment to sound localization. The introduction of passive damping systems would increase thermal noise and reduce the microphone's fidelity. Miles et al. [173] have demonstrated active Q control aimed to reduce damping, here using a proportional and differential gain and feedback scheme to an electrostatic mesh, successfully broadening the resonant response without noise gain. A similar effect can be achieved with pulse train stimulation, changing the phase timing of the pulse with respect to the diaphragm oscillations [129]. Active control over the damping in this manner relies on separate methods of measurement and feedback; for example, piezoelectric measurement of membrane motion and

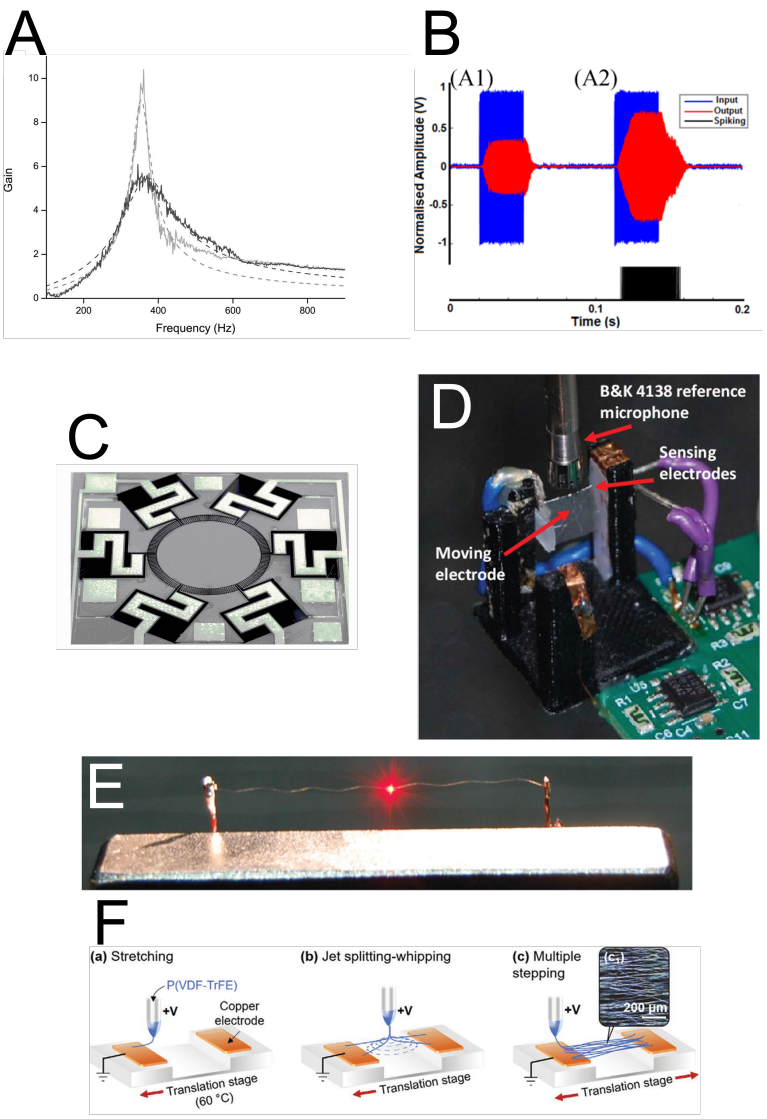

Figure 2.22: Insect-inspired active amplification acoustic sensors. (A) Impact of twice frequency forcing in the mosquito antenna, changing the broadband response of the antenna into a sharp narrowband response [105] © [2009] National Academy of Sciences, U.S.A. Frequency forcing in a MEMS microphone using piezoelectric sensing and capacitive combs to inject the motile force, (B) resultant amplification with forcing [168] © [2018] IEEE, (C) SEM of the membrane design [169] © [2017] IEEE. (D) Hair sensor microphone using electrostatic transduction [170] © [2019] IEEE, and (E) larger scale proof of concept of same using optical sensing [171]. (F) Meshed hair sensing using electrospun PVDF [172].

capacitive comb feedback [174], or laser diffraction-based measurement and actuation through a capacitive backplate [175, 176].

Particle velocity acoustic sensors are relatively rarer, with the majority of the bio-inspired hair sensors being directed towards the detection of fluid flow [177], and there are few examples of hair or flagellum-based sensors that are directly mosquito inspired (for example [178]), although the claimed incorporation of active feedback appears in reality to be a simple directional response. A velocity feedback controller on a cantilever beam was demonstrated by Joyce and Tarazaga [179], the device was constructed at scale, being a 5 cm long aluminium beam with a resonance of 10.8 Hz. Antenna-inspired acoustic sensors should have a large surface area relative to their mass (or moment of inertia) and stiffness [171, 180]. This can be achieved via sub-micron diameter thickness wires, either arranged individually (Figure 2.22 D, E) [180] or in a mesh via electrospinning (Figure 2.22 F) [172]. This leads to a significant challenge with signal transduction since a mechanical element that is sufficiently agile to respond to the drag forces from a sound field will also be driven more powerfully by any electrostatic or capacitive field [181]. Solutions based on electrospun meshes have the convenient electrical transduction mechanism of a piezoelectric polymer [182], in this case, P(VDF-TrFE) however, due to the random orientation of the fibres, the weak reverse piezoelectric effect and the clamped-clamped nature of the mesh the return pathway would be challenging to implement.

2.5 Additive Manufacturing

Additive manufacturing, more commonly known as 3D printing, has revolutionized engineering in the last few decades due to its ease and low cost of prototyping. It is a method for fabricating structures by an increment in material presence by the accumulation of layers, as opposed to subtractive manufacturing [183]. 3D printing has become gradually more accessible, with many people owning 3D printers and using them regularly at home. 3D printing has been chosen as the method for sample fabrication in this Thesis.

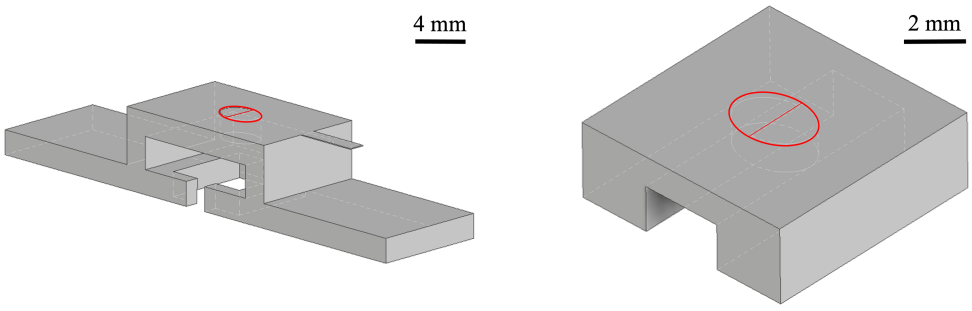

3D printing model made for housing the piezoelectric chip

3D printing model made for acoustic testing in LDV

Figure 2.23: CAD sketches of two designs for 3D printing. The left one corresponds to a design made to house the square piezoelectric vibrating chip; the right one corresponds to the design made to rotate during acoustic testing. Both sketches show the elliptical double-thickness sections highlighted in red.

With Computer-Aided Design (CAD) software, one can quickly develop a personalized prototype with as much detail as one wishes. In Figure 2.23, the CAD sketches of two of the designs used, each one made to accommodate the tools used for measuring in two phases of the research, can be seen. With materials, including the 3D printer itself, being generally cheap, it is possible to produce an efficient prototype in any lab in a short time. The level of customization it achieves together with its low cost in comparison with other fabrication techniques make it advantageous for the development of early prototypes. With the current technology, it is possible to print thin membranes and diaphragms, which are key components in microphone models.

There are several techniques that fall under the umbrella of additive manufacturing like binder jetting, powder bed fusion or material extrusion [183]. All the 3D printers used in this Thesis fall within the branch of photopolymerization and, therefore, it will be the focus of this review. Polymers are long chains of monomers, a smaller molecular unit, bound together in the process of polymerization [184], and more commonly known as plastics. Photopolymerization is the process that produces thermosetting polymers

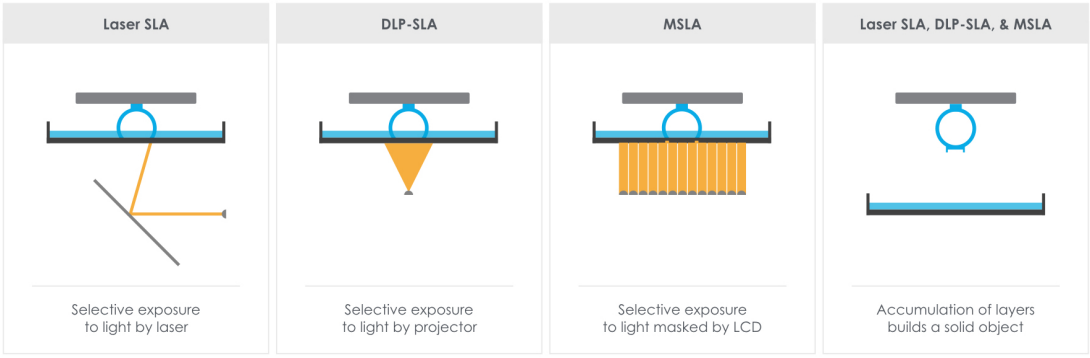

Figure 2.24: SLA (stereolithography) vs. DLP (digital light processing) vs. MSLA (masked stereolithography): Comparison of the three techniques [188].

(i.e. that withstand heat due to significant cross-linking [185]) made of photocurable monomers that are cross-linked together when exposed to light of a certain wavelength [186].

Several techniques satisfy the definition of photopolymerization, all of them sharing a layer-by-layer approach to photocuring. In masked stereolithography (MSLA), a light source shines on an LCD photomask, which is selectively shaded according to the CAD file creating a 2D pixel array of a slice of the design. The resolution in the XY plane in MSLA is determined by the minimum pixel size of the LCD screen [187]. The photomask selectively exposes the photosensitive resin to UV light, solidifying it, and shining over the whole layer at once. A printed layer will normally then fuse to the previously printed layer, however in the case of suspended regions or overhangs the layer thickness will be determined by the UV light exposure.

Digital Light Processing (DLP) is very similar to MSLA, the only difference being that it uses a projector instead of an LCD screen. Lastly, Stereolithography (SLA), sometimes called laser stereolithography, differs from both MSLA and DLP in the light source employed for curing the polymer, in this case, a laser beam of UV light used to selectively pattern each material, with the laser spot size being related to XY precision and making the process altogether a bit slower than the two alternatives [183]. A comparison of the three techniques can be seen in Figure 2.24, where schematic drawings of the three are presented side by side.

Photopolymerization requires post-processing of the printed samples by being washed

in isopropyl alcohol and dried (e.g. using an air gun) to remove the excess resin remaining on the surfaces. The washing of 3D printed parts may cause the apparition of cracks and even the complete collapse of some of the thinner membranes. This is caused by the swelling and shrinking that takes place due to the absorption of solvent and subsequent evaporation. This can be avoided at least partly by limiting the time that the parts are left in the solvent or using water instead of isopropyl alcohol, but water is not as effective in the removal of residue.

It must be noted that 3D printing of small devices is not straightforward, with residual stress gradients affecting the result significantly [189–192]. Other frequent sources of error in 3D printing are film bulging and cross-curing of the horizontal overhangs. An overhang is a region that does not have a pre-existing layer directly underneath. For regular parts without overhangs, the UV light cures the uppermost layer enough to have it stick to the previously printed ones but, when there is no layer underneath, the UV light cures through the layer, causing it to be thicker than expected or to collapse if it cannot sustain itself. Overhangs are frequently dealt with by placing supports under the structure that are meant to be removed afterwards, but when dealing with very thin structures, this will likely damage the printed part. Film bulging, on the other hand, happens while submerging thin layers in the resin pool during the printing process. If the layer is too thin, it will not be strong enough to withstand it, and it may cause bulging or layer separation. Film bulging and cross-curing also prevent the printing of sharp corners under an overhang for similar reasons, and a combination of the two happens in most cases [193–196]. All of these, together with the residual stress gradients and post-processing warping, can make it difficult to achieve repeatability and accuracy when 3D printing small parts.

2.6 Chapter Summary

In this Chapter, information about the topics pertaining to this Thesis is presented. Vertebrate and insect hearing are discussed, including the challenges faced by the latter. More specifically *Achroia grisella*'s hearing system, which inspires the design presented

in this Thesis, is detailed. Microphones, particularly insect-inspired MEMS, are also discussed. Lastly, additive manufacturing, the fabrication technique employed in this Thesis, is reviewed.

Chapter 3

Methodology

This Chapter focuses on the methodology followed, which consists of three different approaches, with results being compared against each other. First, analytical equations that describe the problem were considered; next, simulation software was used for Finite Element Modelling, allowing the inclusion of more complex details into the model; lastly, 3D printing of samples took place, allowing the study of the model's behaviour with the help of micro-computed tomography and Laser Doppler Vibrometry. The shapes examined and later 3D printed are the circular plate, elliptical plate and elliptical with two sections of different thicknesses. Analytically, only the first two are considered; the three of them are considered in both simulation and 3D printing.

The consideration of the analytical equations and the posterior comparison against the simulated results attests to the validity of the model. The 3D printing of samples is also compared against simulations, which provides another layer of confirmation to the simulated results; if something of great importance was being overlooked in the simulation, the disagreement with the experimental results would reveal it. This, together with a similar methodology from simulation to 3D printing having been followed before [197, 198], substantiates the methodology followed.

3.1 Analytical Equations

3.1.1 Stiff Circular Plate

As a first approximation to *Achroia grisella*'s tympanum, the vibrational modes of a circular plate clamped all around will be examined. According to Rao [199], "[a] plate is a solid body bounded by two surfaces". The distance between the two limiting surfaces, known as thickness, is considered to be small in comparison with the other dimensions of the plate. If the ratio between the thickness and the smallest of the other dimensions is less than 1/20, it can be considered a thin plate. Plates are characterised by stiffness rather than tension, in opposition to membranes. In a membrane, unlike a plate, the resistance to shear and bending forces is negligible, and the restoring forces are due to in-plane tension.

A series of assumptions are made for thin plates, in what is called classic plate theory or Kirchhoff-Love theory. By taking them, a three-dimensional plate can be represented and studied as a two-dimensional plane by considering the centre plane of the plate. The kinematic assumptions are the following [200]:

- "Straight lines perpendicular to the mid-surface (i.e., transverse normals) before deformation remain straight after deformation."
- "The transverse normals do not experience elongation (i.e., they are in-extensible)."
- "The transverse normals rotate such that they remain perpendicular to the middle surface after deformation."

See Figure 3.1 for an illustration of the Kirchhoff-Love hypothesis. Now that the definition of a thin plate is clear, the behaviour of any plate experiencing vibrations under no transverse loading will be examined, which is given by equation 3.1 [202].

$$\nabla^2(\nabla^2 W) + \frac{1}{c^2} \cdot \frac{\delta^2 W}{\delta t^2} = 0 \tag{3.1}$$

Where $\nabla^2(\nabla^2)$ is known as the biharmonic operator, $W = W(x, y, t)$ is the displacement

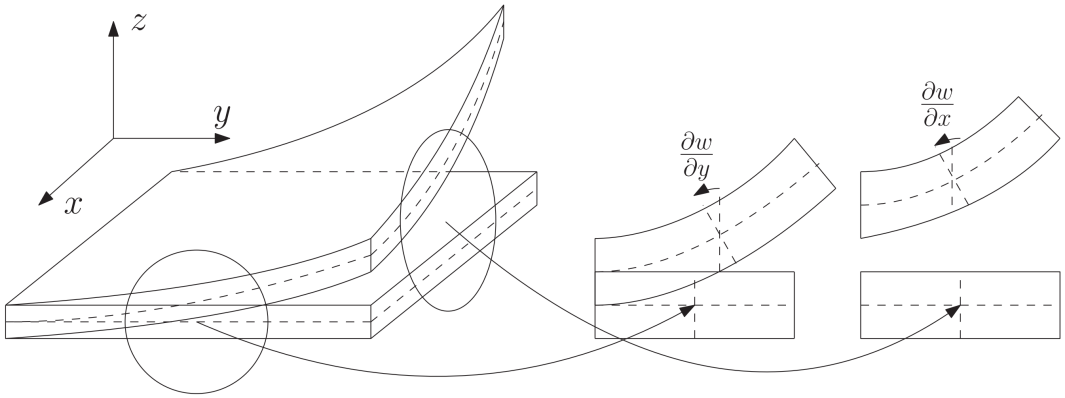

Figure 3.1: Kirchhoff-Love kinematic assumption for thin-plates [201].

of the plate, and the parameter c is [202]:

$$c = \sqrt{\frac{E \cdot h^2}{12 \cdot \rho \cdot (1 - \nu^2)}} \tag{3.2}$$

The parameters being Young's modulus (E), thickness (h), mass volume density (ρ), and Poisson's ratio (ν). In some of the literature, instead of using the parameter c, the flexural rigidity (D) is used, and the equation is instead [202]:

$$\nabla^2(\nabla^2 W) + \frac{\rho \cdot h}{D} \cdot \frac{\delta^2 W}{\delta t^2} = 0 \tag{3.3}$$

Where flexural rigidity is defined as [202]:

$$D = \frac{E \cdot h^3}{12 \cdot \rho \cdot (1 - \nu^2)} \tag{3.4}$$

The first parameter c is chosen, but the result is indistinct.

If a periodical dependence on time is assumed, $W = W(x, y) \cdot T(t)$, and $T(t) = cos(\omega \cdot t)$, being ω the angular frequency, then:

$$\nabla^4 W(x, y) \cdot T(t) - \frac{\omega^2}{c^2} \cdot W(x, y) \cdot T(t) = 0 \tag{3.5}$$

Then, the wavenumber $k^4 = \omega^2/c^2$ is defined, with units of m^-1, and separation of

variables is carried out to focus on the spatial part:

$$(\nabla^4 - k^4) \cdot W(x, y) = 0 \tag{3.6}$$

Which, in turn, can be factored as:

$$(\nabla^2 + k^2) \cdot (\nabla^2 - k^2) \cdot W(x, y) = 0 \tag{3.7}$$

Resulting in two Helmholtz equations of the shape $\nabla^2 f + a \cdot f^2 = 0$, where a^2 is equal to k^2 and $-k^2$ respectively. Equation 3.7 will be satisfied if either of the factors is equal to zero:

$$\begin{cases} \nabla^2 W_1(x, y) + k^2 \cdot W_1(x, y) = 0 \\ \nabla^2 W_2(x, y) - k^2 \cdot W_2(x, y) = 0 \end{cases} \tag{3.8}$$

And, according to the theory of linear differential equations, the sum of W_1 and W_2 provides the general solution $W(x, y)$ [202].

For the circular plate case, it is beneficial to consider a coordinate change to polar coordinates. In the new coordinates, r is the radial coordinate and θ is the angular coordinate or azimuth. The remaining equations are conveniently in the shape of Bessel's equations and their solutions are combinations of Bessel functions, where the boundary conditions will get rid of the constants. The boundary conditions for the solid, clamped circular plate are [203]:

$$\begin{cases} W(R, \theta) = 0 \\ \dfrac{\delta W(R, \theta)}{\delta r} = 0 \end{cases} \tag{3.9}$$

Where R is the radius of the plate.

The theoretical eigenvalues are obtained by solving the following equation [202]:

$$J_n(\lambda) \cdot I_{n+1}(\lambda) + I_n(\lambda) \cdot J_{n+1}(\lambda) = 0 \tag{3.10}$$

Where J and I are the Bessel function of the first kind and the modified Bessel function

Table 3.1: Theoretical eigenvalues obtained from the resolution of equation 3.10. * indicates a degenerate mode.

Eigenmode	**(*n*,*s*)**	**Theoretical Eigenvalue**
1^{st}	(0,1)	3.196
2^{nd} & 3^{rd}	(1,1)*	4.611
4^{th} & 5^{th}	(2,1)*	5.906
6^{th}	(0,2)	6.306

of the first kind respectively, $\lambda = k \cdot R$, and n is the number of the eigenvalue. For each n, there is an infinite number of solutions that will be indexed as s [204]. The solutions to equation 3.10 are calculated numerically in MATLAB and can be seen in Table 3.1. The results match those collected by Arthur Leissa in his Vibrations of Plates, a seminal work on the analytical resolution of the governing equations of the mechanics of plates of different shapes and boundaries [202]. The second and third eigenmodes are degenerate, and the same is true for the fourth and fifth. This means that they share the same frequency but the vibrating modes are orthogonal. From the definition of k, the vibration frequency of a stiff circular plate depends on the parameter (c) and its radius (R). The relationship to the eigenvalues of the system is:

$$\omega_e = \frac{\lambda_e^2}{R^2} \cdot c = \frac{\lambda_e^2}{R^2} \cdot \sqrt{\frac{E \cdot h^2}{12 \cdot \rho \cdot (1 - \nu^2)}} \tag{3.11}$$

The mode shapes for the first three combinations of *(n,s)* solutions can be seen in Figure 3.2. These results can later be compared to the COMSOL simulation to test its accuracy by substituting the same values in the equations as the parameters in the model.

3.1.2 Stiff Elliptical Plate

A second more realistic approximation would be to examine the eigenmodes and eigenfrequencies of an elliptic plate, more similar in shape to the moth's tympana.

The solution of the elliptical plate is far more complex than the circular one. A set of equations and functions arise as a consequence of the geometry called Mathieu's

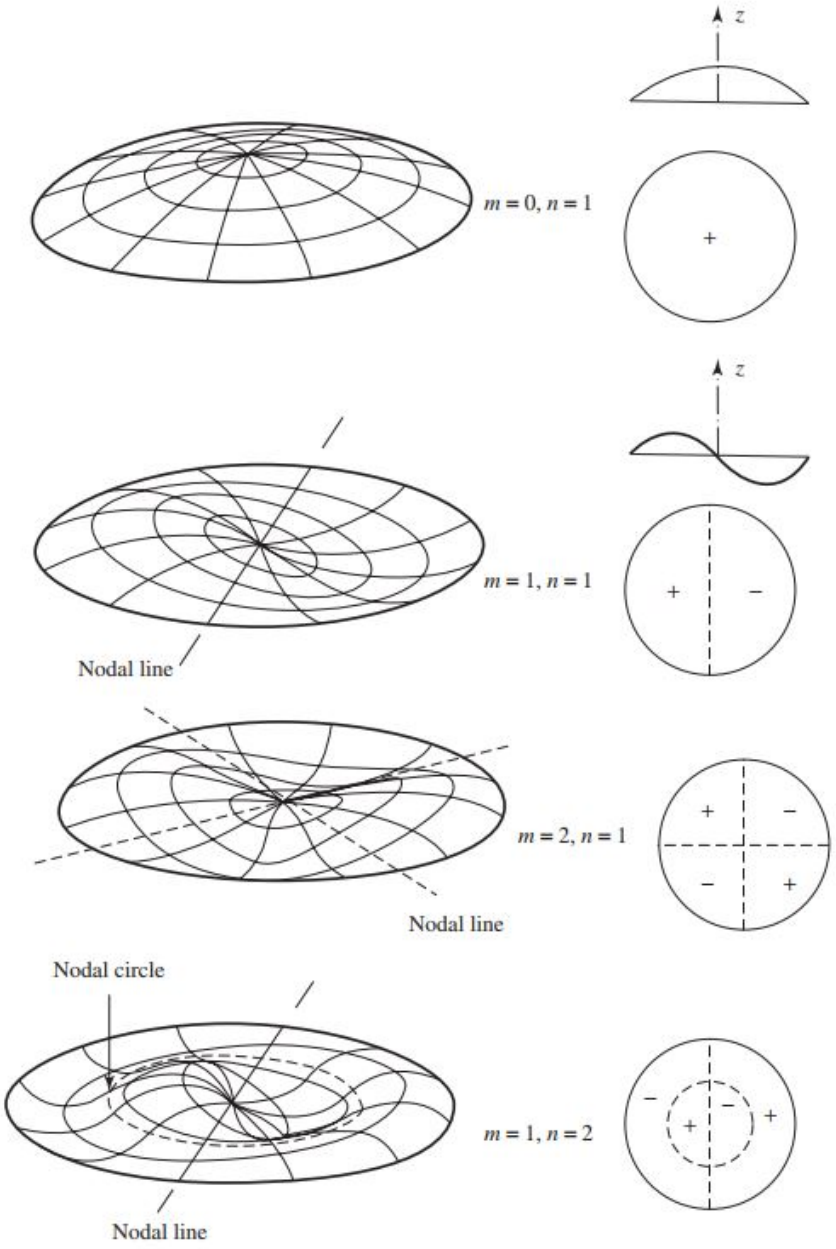

Figure 3.2: Mode shapes of a clamped circular plate. Dashed lines denote nodal lines within the plate. Adapted from Rao's Vibration of Continuous Systems [199].

equations and functions respectively [202, 205–207]. Mathieu's function is of the shape:

$$\frac{\delta^2 x}{\delta y^2} + (a - 2q \cdot \cos 2y) \cdot x = 0 \tag{3.12}$$

The modified Mathieu equation is similar but exchanges the cosine for its hyperbolic counterpart [202, 205–207]:

$$\frac{\delta^2 x}{\delta y^2} + (a - 2q \cdot \cosh 2y) \cdot x = 0 \tag{3.13}$$

Returning to equation 3.1 in the previous section:

$$\nabla^2(\nabla^2 W) + \frac{1}{c^2} \cdot \frac{\delta^2 W}{\delta t^2} = 0 \tag{3.14}$$

Similarly to the procedure in the previous section, a periodical time dependence of the shape $W(x, y, t) = W(x, y) \cdot T(t) = W(x, y) \cdot \cos(\omega \cdot t)$ is assumed, which turns out as:

$$\nabla^4 W(x, y) \cdot T(t) - \frac{\omega^2}{c^2} \cdot W(x, y) \cdot T(t) = 0 \tag{3.15}$$

Then, $k^4 = \omega^2/c^2$ is defined and separate variables to focus on the spatial part:

$$(\nabla^2 + k^2) \cdot (\nabla^2 - k^2) \cdot W(x, y) = 0 \tag{3.16}$$

That turns into two equations whose combined solutions give the general solution for *W(x,y)*. So far, the procedure has been the same as in the previous section, but now, elliptical coordinates will be considered to ease the application of the boundary conditions further down the line. Elliptical coordinates are defined as:

$$\begin{cases} x = f \cdot \cosh \xi \cdot \cos \eta \\ y = f \cdot \sinh \xi \cdot \sin \eta \end{cases} \tag{3.17}$$

Where f is the semi-focal distance i.e., half of the distance between the two foci of the ellipse and can be calculated as $f = \sqrt{a^2 - b^2}$, where a and b are the semimajor and

semiminor axes respectively. If a new constant $2 \cdot K = k \cdot f$ is defined:

$$\begin{cases} \frac{\delta^2 W_1}{\delta \xi^2} + \frac{\delta^2 W_1}{\delta \eta^2} + 2K^2(\cosh 2\xi - \cos 2\eta)W_1 = 0 \\ \frac{\delta^2 W_2}{\delta \xi^2} + \frac{\delta^2 W_2}{\delta \eta^2} - 2K^2(\cosh 2\xi - \cos 2\eta)W_2 = 0 \end{cases} \tag{3.18}$$

If the further assumption $W_1, 2(\xi, \eta) = E(\xi) \cdot N(\eta)$ is taken, it is possible to separate in variables, so, for example, taking the first equation of 3.18:

$$\begin{gathered} \frac{\delta^2 W_1}{\delta \xi^2} + \frac{\delta^2 W_1}{\delta \eta^2} + 2K^2(\cosh 2\xi - \cos 2\eta)W_1 = \\ \frac{\delta^2 E(\xi)}{\delta \xi^2} \cdot N(\eta) + E(\xi) \cdot \frac{\delta^2 N(\eta)}{\delta \eta^2} + 2K^2(\cosh 2\xi - \cos 2\eta)E(\xi) \cdot N(\eta) = 0 \end{gathered} \tag{3.19}$$

$$\left(\frac{\delta^2 E(\xi)}{\delta \xi^2} + 2K^2 \cdot \cosh 2\xi \cdot E(\xi)\right) \cdot N(\eta) = \left(-\frac{\delta^2 N(\eta)}{\delta \eta^2} + 2K^2 \cdot \cos 2\eta \cdot N(\eta)\right) \cdot E(\xi) \tag{3.20}$$

$$\begin{cases} \frac{\delta^2 E(\xi)}{\delta \xi^2} - (C - 2K^2 \cdot \cosh 2\xi) \cdot E(\xi) = 0 \\ \frac{\delta^2 N(\eta)}{\delta \eta^2} + (C - 2K^2 \cdot \cos 2\eta) \cdot N(\eta) = 0 \end{cases} \tag{3.21}$$

Where C is the separation constant. These two equations have the shape of 3.13 and 3.12 respectively, where a is equal to C, and q is equal to K^2. It must be remembered that, so far, only the first equation of 3.18 has been dealt with; for the second equation there are another two equations that correspond to Mathieu radial and angular equations, namely:

$$\begin{cases} \frac{\delta^2 E(\xi)}{\delta \xi^2} - (C + 2K^2 \cdot \cosh 2\xi) \cdot E(\xi) = 0 \\ \frac{\delta^2 N(\eta)}{\delta \eta^2} + (C + 2K^2 \cdot \cos 2\eta) \cdot N(\eta) = 0 \end{cases} \tag{3.22}$$

Since q is real, because its value is $q = f^2/4 \cdot \omega/c$, the solutions to the equations are a combination of the Radial Mathieu Functions (RMF) and Angular Mathieu Functions (AMF). The names arise from the analogy to polar coordinates. The angular variable η takes values from 0 to 2π; on the other hand, ξ behaves as the radial polar coordinate and takes values from 0 to ∞ [205]. The Angular Mathieu Functions are also known as Mathieu functions of the first kind, and they are separated into even (ce_n) and odd

(se_n) families of order n:

$$\begin{cases} ce_n(x,q), & n = 0,1,2... \\ se_n(x,q), & n = 1,2,3... \end{cases} \tag{3.23}$$

The Radial Mathieu Functions are also known as modified Mathieu functions and are related to the angular Mathieu functions through the imaginary unit as follows [208]:

$$\begin{cases} Ce_n(x,q) = ce_n(i \cdot x, q), & n = 0,1,2... \\ Se_n(x,q) = se_n(i \cdot x, q) \cdot (-i), & n = 1,2,3... \end{cases} \tag{3.24}$$

The boundary conditions, analogously to the clamped circular plate, are:

$$\begin{cases} W(\xi_0, \eta) = 0 \\ \dfrac{\delta W(\xi_0, \eta)}{\delta \xi} = 0 \end{cases} \tag{3.25}$$

Where $\xi_0 = \arctan(b/a)$ is the perimeter of the ellipse. This implies that RMF vanish at the boundary:

$$Ce_m(\xi_0, q) = Se_m(\xi_0, q) = 0, \quad m = 0,1,2... \tag{3.26}$$

The functions are then numerically evaluated in Maple to obtain the values of q that satisfy the equations, and, from it, the angular frequency of the solutions can be obtained. The mode shapes that appear on a clamped elliptical membrane can be seen in Figure 3.3, consisting of antinodes both concentrical and elliptical, and symmetric and radial. The mode shapes are numbered following an *(m, n)* nomenclature, where m describes the number of radial valleys and n corresponds to the number of elliptical valleys. Mode shapes for the elliptical plate are similar [209].

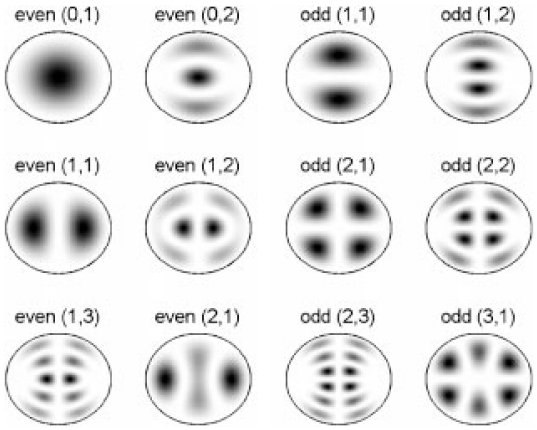

Figure 3.3: Plots of the first even and odd standing modes in an elliptic membrane. The shaded regions represent crests (maxima) or valleys (minima) on the membrane surface. From Gutiérrez-Vega's Mathieu Functions: a visual approach [205].

3.1.3 Beam theory

Beam theory will be used to experimentally determine the Young's modulus of the materials from 3D printed cantilever beams, the results of which are detailed in Chapter 5. According to beam theory [210], Young's modulus (E) of a cantilever beam can be calculated using the following equation:

$$E = \frac{40 \cdot \pi^2 \cdot \rho \cdot f_n^2 \cdot L^4}{\lambda_n^4 \cdot h^2}, n = 1, 2, 3... \tag{3.27}$$

The parameters being mass volume density (ρ), the eigenfrequencies (f_n), the length of the beam (L), the eigenvalues (λ_n), and the thickness (h).

3.2 Finite Element Modelling

For the Finite Element Modelling, the software COMSOL Multiphysics® was used. Finite Element Modelling is a method for numerically solving the governing differential equations in a complex geometry. To do so, the potentially complex geometry is broken down into a mesh of much simpler, smaller finite elements. An approximating function is then derived for each of these finite elements and finally, the solution for the nodes between these finite elements is chosen to satisfy the governing equations [211].

COMSOL is a powerful software that considers many different aspects of physics, being able to compute the interactions between them, as its name suggests. Several steps are followed to set up a model.

After a model from the Model Wizard is chosen, a physics domain is selected. In this case, the Shell interface, from the Structural Mechanics module, is chosen to mimic the tympanum. Shells are appropriate to consider thin structures with considerable bending stiffness, which echoes the definition of thin plates. Other domains can be included in the next steps. A starting study is chosen, with the possibility to add more later; this is the Eigenfrequency study, which will find the natural resonances of the model. Initial results were obtained with only the Shell interface and Eigenfrequencies studies.

Parameters are defined for the main dimensions and properties of the system, so they can be easily adjusted if needed to fit a real 3D printed sample, in a bigger size and the physical characteristics of the printing resin; or the moth tympanum, with much smaller dimensions and estimated values for cuticle tissue (see Figure 3.4 for a list of the parameters and the values chosen for one of the models).

The geometry of the model is constructed next. A circle or ellipse, depending on the model, is defined on a plane using the radius or minor and major semi-axes parameters. Its thickness is later added through the Shell tab. For the double-thickness model, a working plane perpendicular to the shell plane is defined along the minor axis, dividing the geometry into two halves. In the model where a point mass is located in the centre of the thin section, this is added as a point in the geometry tab, the mass load being added later in the Shell interface (see Figure 3.5 top for a close up of the shell). For the models that will include an air domain, a dome is built above the shell. This is half a sphere several orders of magnitude larger than the largest element of the shell (see Figure 3.6).

Materials are chosen next; air is selected from the list of predetermined COMSOL materials and can be adjusted for possibilities other than standard room temperature and humidity. For the tympanum, a new material named “insect cuticle” is built, characterised by its Young’s modulus, Poisson’s ratio and volumetric mass density,

Settings

Parameters

Label: Parameters

Parameters

Name	Expression	Value	Description
mem_th	0.102[mm]	1.02E-4 m	Tympanum thickness
E_mat	52.9 [MPa]	5.29E7 Pa	Young's modulus
nu_mat	0.32	0.32	Poisson's ratio
rho_mat	1183 [kg/m^3]	1183 kg/m^3	Mass density
a	3.35[mm]	0.00335 m	Semimajor axis
b	2.5[mm]	0.0025 m	Semiminor axis
cj_th	0.259[mm]	2.59E-4 m	Conjuctivum thickness
theta	35[deg]	0.61087 rad	polar angle
phi	0[deg]	0 rad	azimuth angle
k1	sin(theta)*cos(phi)	0.57358	x direction vector
k2	sin(theta)*sin(phi)	0	y direction vector
k3	cos(theta)	0.81915	z direction vector

Figure 3.4: COMSOL's Parameters tab within Global Definitions showing the values chosen for one of the iterations of the model.

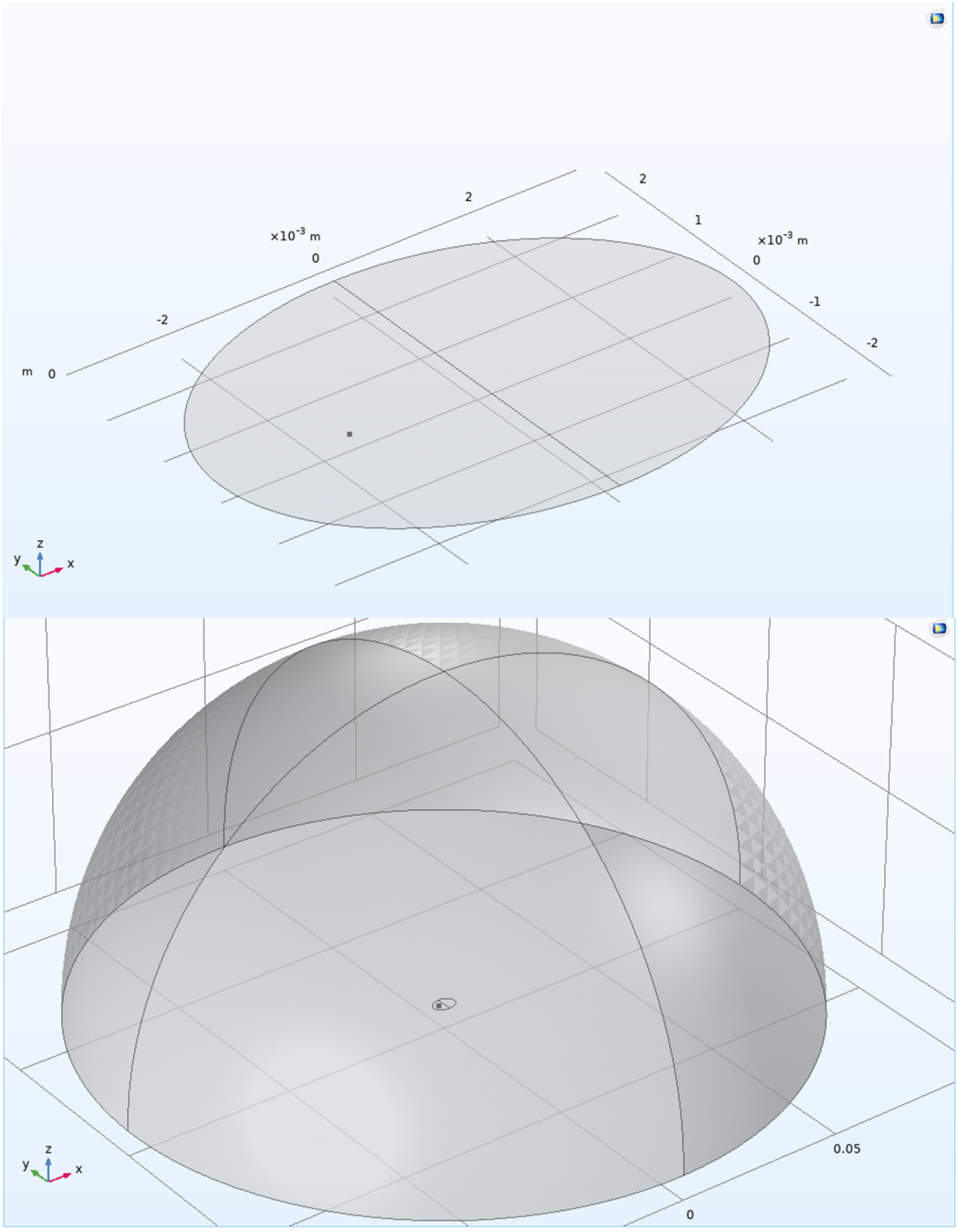

Figure 3.5: COMSOL's Graphics tab showing a close-up of the shell representing the moth tympanum, with the neural attachment point marked (top) and the model within the air environment (bottom).

previously listed in the parameter list, so they can be easily changed. Volumetric mass density for the tympanum is chosen to be within the range of values given for insect cuticle.

The Pressure Acoustics domain was added to the directionality measurements to account for the simulation of the transmission of sound in air and boundaries. Losses can be accounted for in the gas model used for air, which provides the options viscous and ideal, among others, to name the ones used. The tympanum element is assigned to the Shell module and the air dome is assigned to the Pressure Acoustics, Frequency Domain module. A Multiphysics model is set for the simulations containing the air domain pertaining to the boundaries between the two domains. See Figure 3.6 for a full breakdown of the model builder for the simulation.

A mesh is built to break down the complex geometry model into smaller pieces that COMSOL then handles; for a model like this, a predetermined free tetrahedral mesh is suitable. The points between mesh elements are called nodes and the differential equations are solved at each of these nodes, working out a general solution that might be ruled by equations too complicated and time-consuming to deal with analytically.

Then, the studies chosen to evaluate the situations that are interesting to the research are set. In the first place, the eigenfrequencies and eigenmodes of the structure are considered in the aforementioned Eigenfrequency study selected at the beginning of the simulation. Eigenfrequencies, or natural resonances, are key pieces of information about a system. They are the frequencies and the shapes at which a structure is naturally inclined to vibrate.

Secondly, the directivity response of the tympanum is to be examined. A directivity response is a graphical representation of how the system reacts to the same stimulus coming from different points around the system. If the reaction of the system is the same no matter what the direction of the stimulus is, the directivity response will be circular in a polar plot, which is known as *omnidirectional* in microphone design. If the response changes with the angle, the pattern observed in the polar plot will change too. The stimulus is thus consistently displaced around the system in the plane of interest.

Directivity is evaluated through a general Frequency study. For the general Fre-

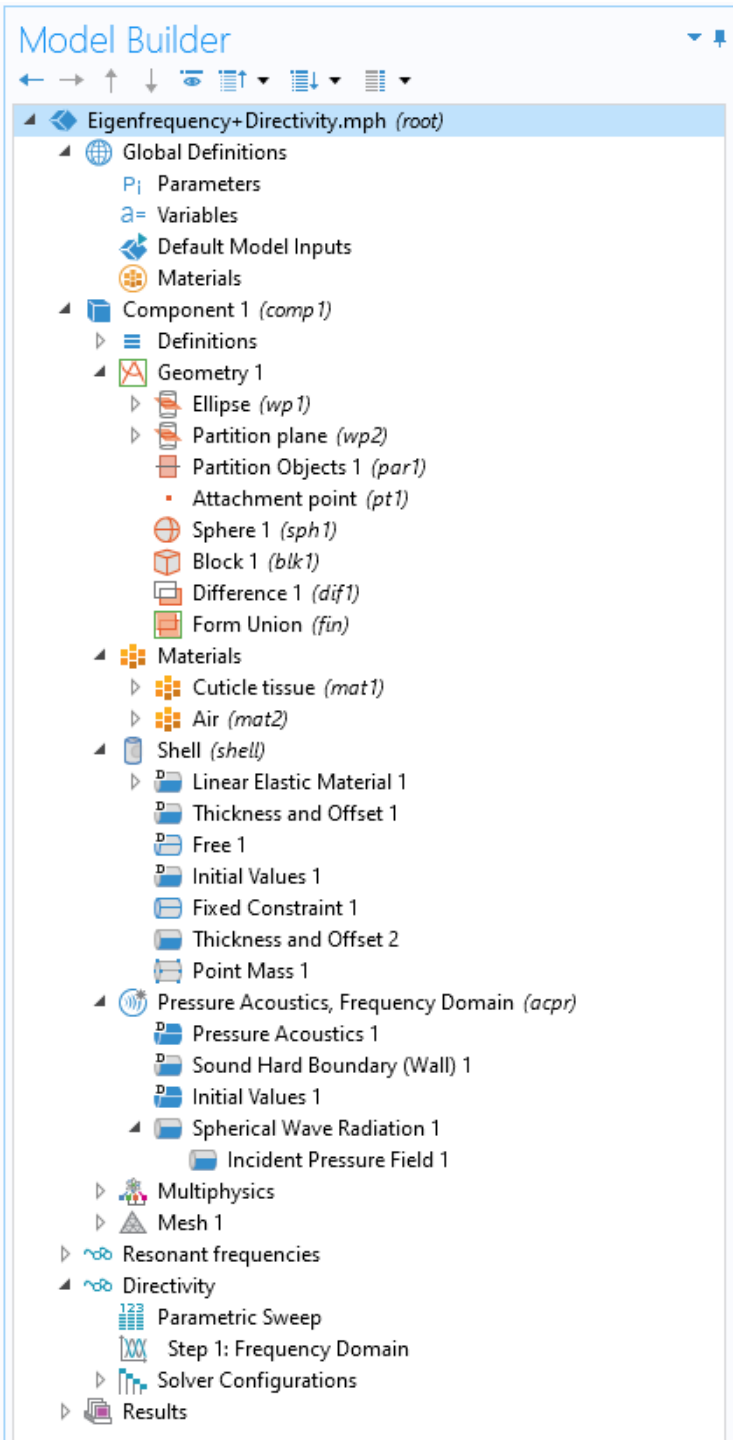

Figure 3.6: COMSOL's Model Builder tab showing the breakdown of the model for the moth tympanum.

quency study, the stimulus used is a spherical wave radiation with an incident pressure field of 1 Pa. The provenance of the stimulus is characterized by two angles, azimuthal and polar. The azimuthal angle may be varied but is kept consistent for each study while a 360^{o} parametric sweep over the polar angle, in intervals of 5^{o}, takes place to produce the directivity plots. The results are shown on COMSOL's visualization window but can also be exported in plain text files that can later be used for plotting in MATLAB.

3.3 3D Printing

3D printing was done using three different machines and two materials, based on two different techniques, both within the photopolymerization branch of additive manufacturing. The structures used to initially determine the frequency responses were produced with an Original Prusa SL1 3D printer (XY-resolution of 47 microns, layer thickness of 25, 50 or 100 microns), which employs masked stereolithography technology. In the Prusa SL1, the light source is an LED array of 405 nanometres. The resin used is a commercial resin from the same manufacturer called Orange Tough, and it is modelled after Acrylonitrile-butadiene-styrene. The properties of the resin are obtained from the literature as a Poisson's ratio of 0.35 and volumetric mass density of 1180 kg/m^3 [212]. Young's modulus was measured in the printed samples using a 3D printed cantilever and beam theory as explained in section 3.1.3.

The second 3D printer used was an Asiga Pico 2/HD 3D printer (resolution of 26 µm, layer thickness of 50 microns). This printer uses the digital light processing technique. The resin chosen is a custom-mixed one composed of a base monomer, a photoinitiator, and a photo absorber. These are, respectively, Polyethylene glycol diacrylate (PEGDA) Mn 250, Phenylbis(2,4,6-trimethylbenzoyl)phosphine oxide at 0.5% weight per cent, and Sudan I at 0.2% weight per cent, all purchased from Merck Life Sciences and used without further modification. The resin is mixed in an ultrasonic bath (Decon FS250) for 20 minutes before use to ensure even distribution. From the literature, the Poisson's ratio and mass density of the resin are taken to be 0.32 and 1183 kg/m^3 respectively [213]. A value for Young's modulus of 52.9 MPa is also provided, but

the 3D printed cantilever method was used to determine it in these samples. These samples were used to determine the frequency response and directional response of the first series of directionality measurements.

The reason for switching printing machines and moving to a custom resin was to achieve a lower Young's modulus, in turn producing lower resonant frequencies that can be more easily excited through sound with a common speaker for the directionality measurements. The size of the vibrating plates was increased for the same reason. The aim was to produce the first three resonance frequencies under 20 kHz, reflecting the human hearing range.

The third and last 3D printer used is a Prusa SL1S Speed (XY-resolution of 49 microns, layer thickness of 25, 50 or 100 microns), a newer version of the first 3D printer mentioned that, as indicated by its name, is capable of curing the same materials faster. The same mix of custom resin was used for this printer. The custom resin was calibrated in the following way: the UV light of the 3D printer was shone directly onto the resin pool without a tray at different exposure times. The subsequent samples produced are stuck to the bottom of the resin pool, which are then carefully removed and their thickness is measured using a digital calliper. The relation between thicknesses and exposure times is adjusted using the model provided by Gong et al. [214], from it:

$$z_p = h_a \cdot \ln \frac{t_p}{T_c} \tag{3.28}$$

Where z_p is the polymerization depth (our dependent variable y when adjusting to a polynomial fit), h_a is the characteristic penetration depth (the inverse of the absorption coefficient α), t_p is the polymerization time (the independent variable x for the polynomial fit), and T_c is the critical time. MATLAB is used to adjust equation 3.28 to an equation of the shape $y = A \cdot \ln x - B$. The relation between exposure times and thicknesses collected for calibration is contained in Table 3.2. The fitting can be seen in Figure 3.7 with a logarithmic scale for time. The samples produced with this printer are yet larger in size and used for the last series of directionality measurements. The post-processing detailed in section 2.5, namely washing in isopropyl alcohol or water and air gun drying, is followed for all 3D printers and material combinations.

Table 3.2: Exposure times and thicknesses used for calibration of the custom-mixed material.

Exposure Time (s)	**Thickness (mm)**
10	0.07
20	0.11
30	0.16
40	0.17
50	0.19
60	0.20

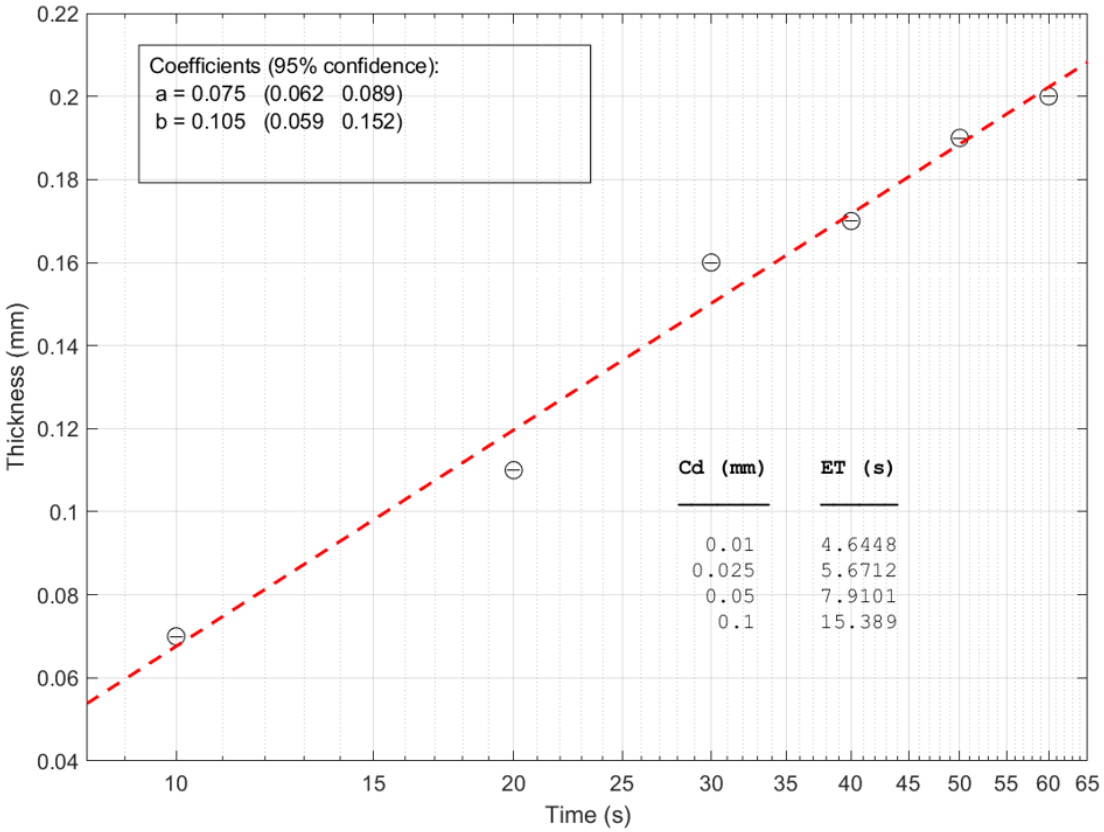

Figure 3.7: Fitting of the data collected for calibration of the custom-mixed printing material.

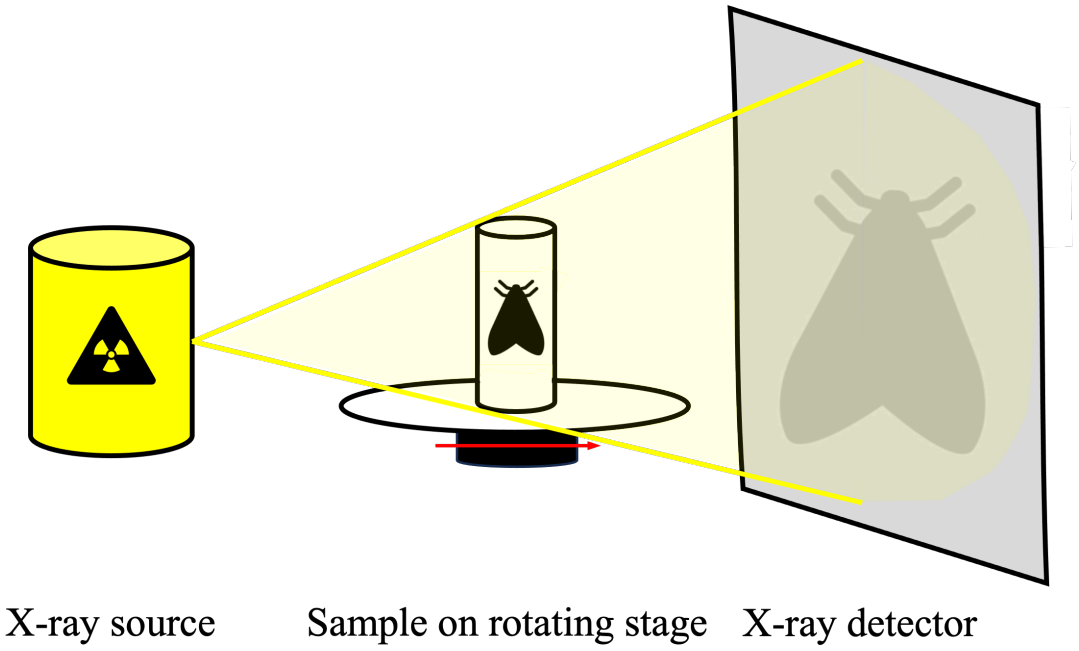

Figure 3.8: Schematic of the Micro-computed tomography with a sample located on a rotating stage. Redrawn from [216]

3.4 Micro-Computed Tomography

Micro-computed tomography (abbreviated as μCT) is a non-destructive technique developed clinically in the early 1970s for 3D imaging throughout a sample; it is used in this Thesis to image and determine the dimensions and thickness of the 3D printed samples. μCT can be used for both live and dead samples, as well as delicate objects, which is why it is employed in subjects ranging from medicine to archaeology. All μCT machines consist of a series of elements: an X-ray source, a rotating stage (either for the sample to be measured or the source), and an X-ray detector (see Figure 3.8 to see a schematic representation of these elements) [215]. This way, it is possible to obtain high-resolution cross-sections of a sample for its posterior 3D reconstruction. Using software, the images can be stacked to generate a 3D volume.

The printed samples were examined using a Bruker Skyscan 1172 with SHT 11-megapixel camera and Mamamatsu 80 kV (100 mA) source to determine their thickness. The images generated were 1332 x 2000 pixels with a resolution of 4.98 microns per

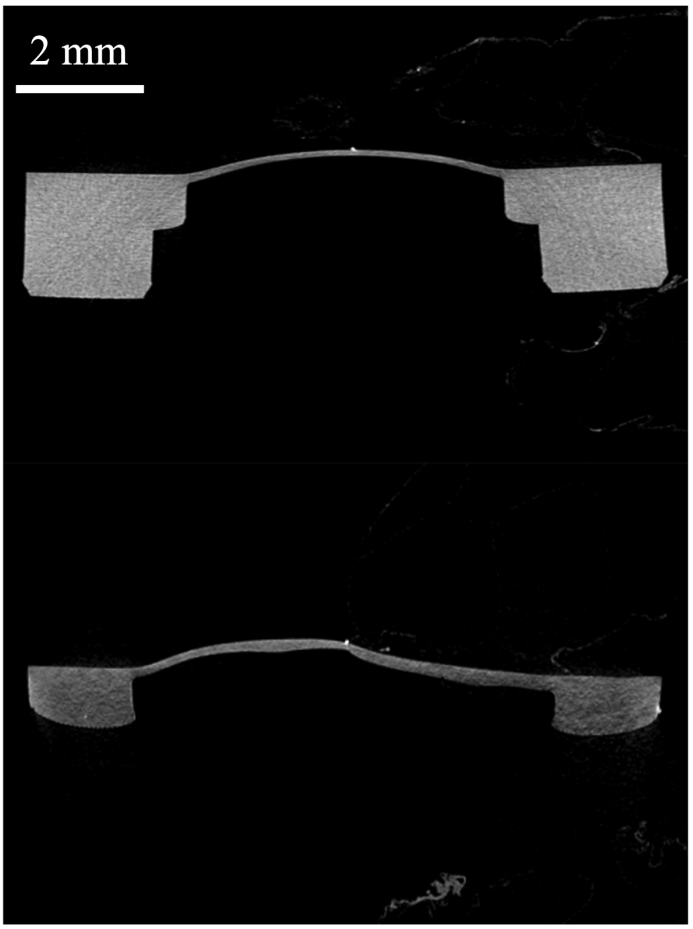

Figure 3.9: Transaxial (above) and coronal (below) perspectives of a μCT scan of a 3D printed sample of double thickness. Pictures courtesy of Dr Andrew Reid.

pixel. The images were collected, and a volumetric reconstruction of the sample was generated by Bruker's CTvol software. The images produced are based on the level of attenuation through the sample, which is dependent on the thickness of the material and its absorption coefficient and is notably less near an object's extremities. The thickness measured is therefore dependent upon this manual thresholding. Figure 3.9 shows an example of the images produced in this process, showing a two-thickness elliptical plate. The figure shows the bowing of the sample's thinnest sections, due to the aforementioned stress gradients in 3D printing, cross-curing, film bulging, and shrinking during the post-processing of the samples.

3.5 Laser Doppler Vibrometry

The printed structures were examined using 3D laser Doppler Vibrometry (3D LDV). Laser Doppler Vibrometry is a technique that exploits the effect of the same name. The Doppler effect takes place when there is a relative movement between the source of the signal and the receiver, and it results in an apparent frequency shift of the signal for the receiver. It can happen both in classical and relativistic physics. The classic example is that of an ambulance with its siren on, approaching the listener. The siren, for the listener, will apparently lower its pitch during this process (see Figure 3.10 for a schematic representation). In classical physics, the shift in frequency can be predicted by the following equation:

$$f = \left(\frac{c \pm v_r}{c \pm v_e}\right) \cdot f_0 \tag{3.29}$$

Where c is the wave propagation velocity in the medium, v_r and v_e are the velocities of the receiver and emitter respectively, and f and f_0 are the perceived and emitted frequency respectively.

In the 3D LDV, a laser beam is pointed at the surface being examined, and the shift in frequency of the beam caused by the velocity of displacement of the surface is recorded and analysed (Figure 3.11). The machine will provide a voltage that is proportional to the velocity of the surface according to the Doppler's effect equation (see equations 3.29 and 3.30). In the 3D LDV, as opposed to a 1D LDV, three laser beams are pointed at the sample to determine the three components of velocity, namely x, y and z. In this Thesis, a 3D LDV was used but only the z component was examined.

In the schematic of Figure 3.11, the signal measured at the detector will have shifted from the original signal emitted by the laser. The backscattering from the moving sample and detected by the LDV will shift the original frequency by f_d, determined as:

$$f_d = 2 \cdot \frac{v_s}{c} \cdot f_0 \tag{3.30}$$

Where v_s is the velocity of the sample, c is the wave propagation velocity, and f_0 is the frequency of the original signal.

The instrument used is an MSA-100-3D scanning head (Polytec, Waldbrom, Ger-

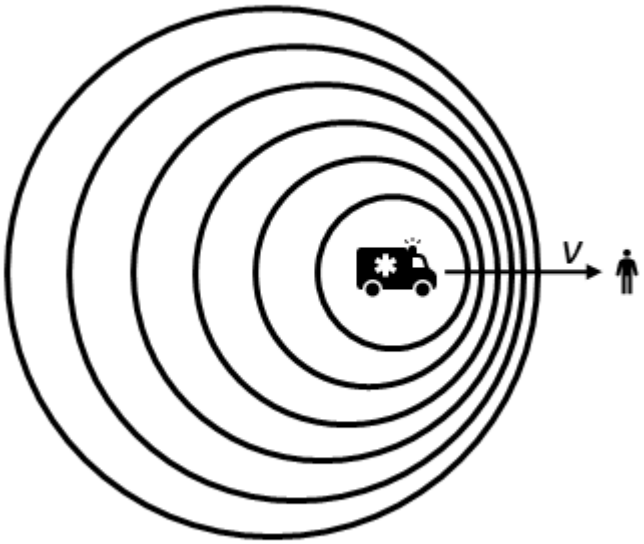

Figure 3.10: Schematic representation of the Doppler shift as perceived by a receiver when a sound source is approaching. The receiver to the right will perceive the wavelength as lower and, conversely, the frequency as higher. The opposite would be true if the receiver was standing on the left.

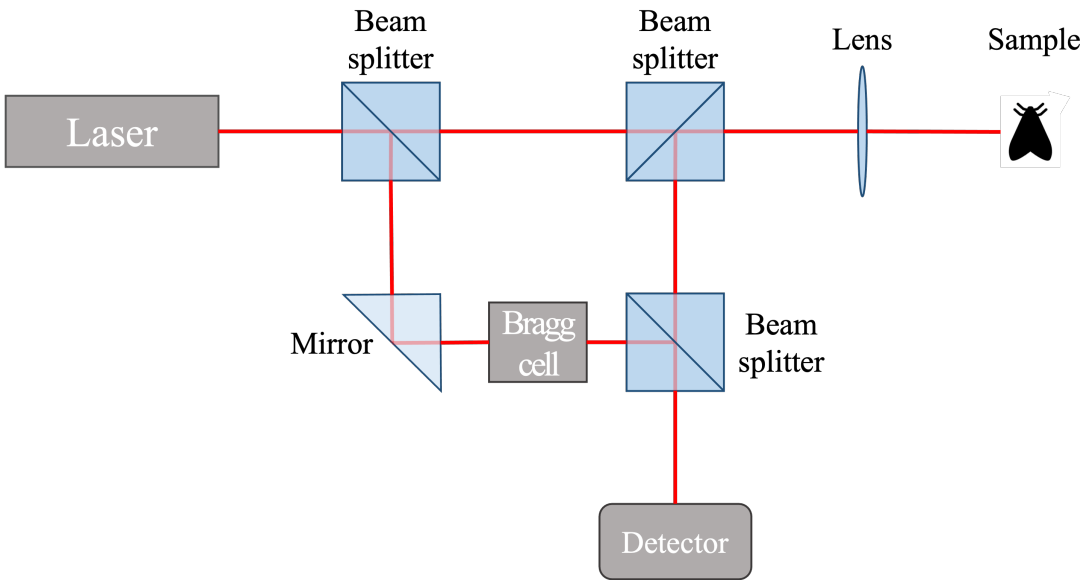

Figure 3.11: Basic measurement principle of vibrometry and setup of a laser Doppler vibrometer.

many). The Polytec head has sub-nanometre amplitude resolution for in-plane and out-of-plane movements (provided by the manufacturer). Measurements taken in the LDV are complex-averaged five times. The structures are stimulated first with a displacement piezoelectric chip (75 V, 2.8 microns, Thorlabs, Newton, New Jersey, see frequency response in Figure 3.12), with wideband periodic chirp signals. The Polytec software-generated periodic chirp corresponds to sinusoidal signals generated at all frequency bins within an indicated frequency range simultaneously, where the phases of each sinusoidal signal are adapted to maximise the resulting signal's energy. The signal generator requires two values: a peak amplitude voltage value and a DC offset value for high-impedance termination. The two are constrained such as the sum of the peak amplitude and the absolute value of the offset must be equal to or lower than 10 volts. This allows examination of the frequency response recorded by the LDV. The resonances can be identified by looking at out-of-plane vibrations and compared with the eigenfrequencies obtained from simulation, readjusted to the new parameters that match those of the 3D printed structures.

Once the resonant frequencies are found, the 3D printed plates are excited with a

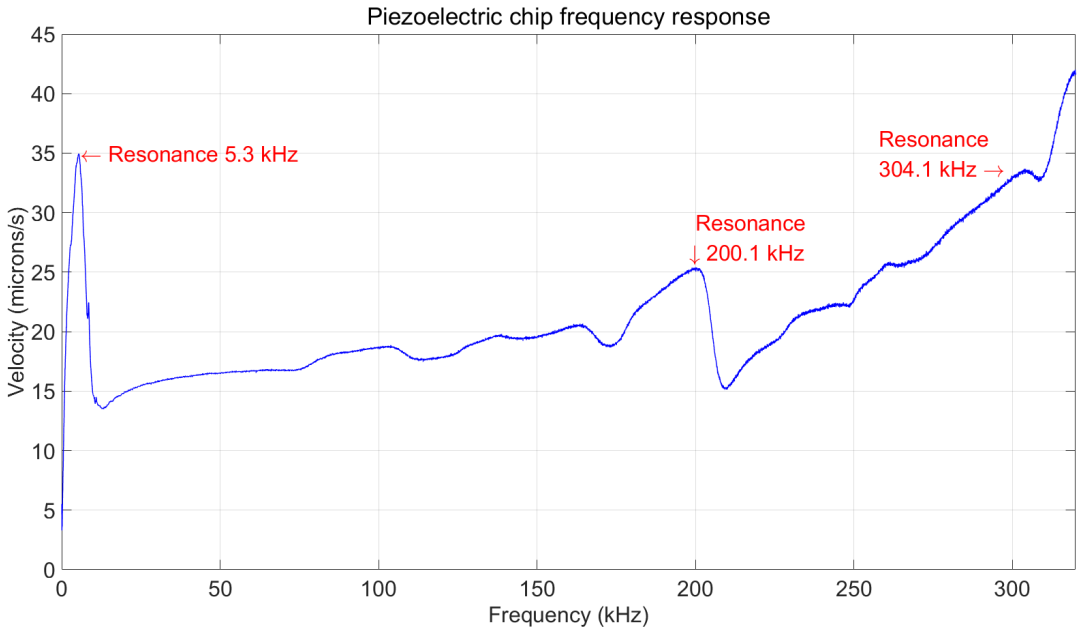

Figure 3.12: Frequency response of the piezoelectric vibrating chip measured with the Laser Doppler Vibrometer, range of excitation between 0 and 320 kHz. Peaks in the frequency response have been labelled. The response of the piezoelectric chip between 13 kHz and 250 kHz is reasonably flat. The results agree with the value provided by the manufacturer, where 310 kHz is indicated as the main resonant frequency.

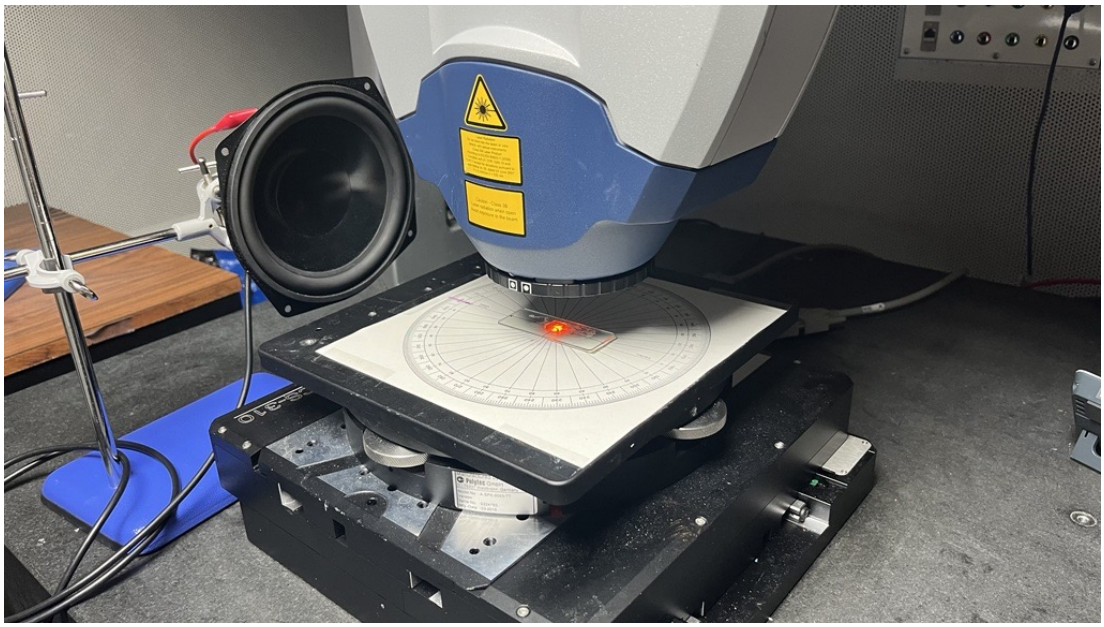

Figure 3.13: Experimental setup for the last set of the directionality measurements.

new setup to get the directionality measurements. Stimulation was with a Labo LB-PS1401D speaker (frequency response of 80 Hz to 20 kHz, maximum output power of 60 W, sensitivity of 88 dB/W/m). The setup can be seen in Figure 3.13 and a schematic representation of its side and bird's-eye views in Figure 3.14. The signals used consist of a series of sine tones at the resonant frequencies. The sample is rotated in increments of 10^{o}, and the displacement is measured at the middle point of the thin half of the two-thickness sample, where the neural attachment point of the moth would be. The experimental data are plotted using MATLAB. The direction taken for the polar plot is on the same plane as the plate and aligned with the major axis, with the thick half being towards the front and corresponding to 0^{o}. This corresponds to where the head of the moth would point to, as was seen in Figure 2.8.

3.6 Chapter Summary

In this Chapter, the author covers the different tools, technologies and techniques used for the development of this Thesis, including the equations used, the Finite Element model developed, additive manufacturing, x-ray scanning, and laser Doppler

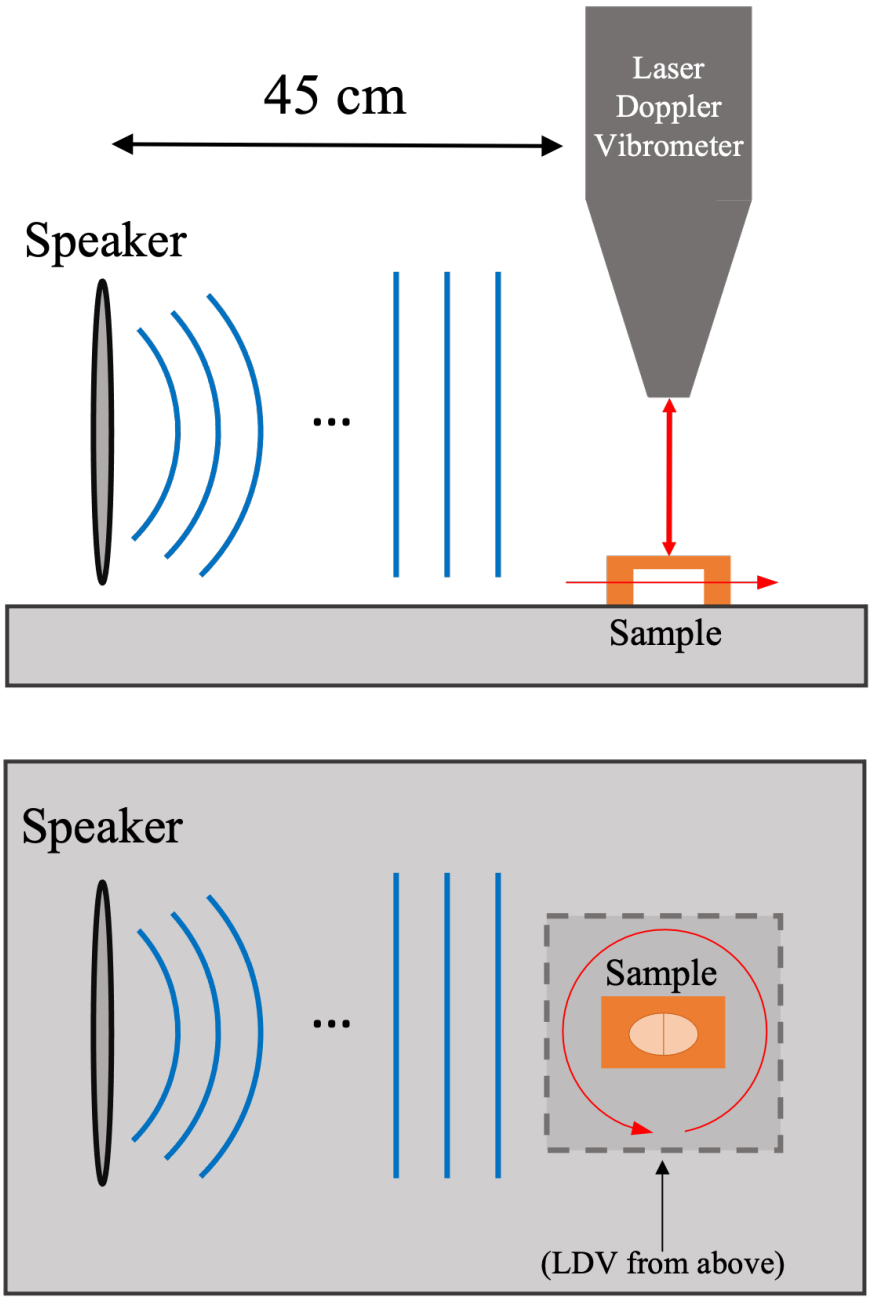

Figure 3.14: Schematic representation of the experimental setup for the last set of the directionality measurements, showing the direction of turning of the samples (not to scale). Side view (above) and bird's-eye view (below).

vibrometry. General details of all equipment are provided as well as a more thorough explanation of the exact purpose and use of them in this Thesis.

Chapter 4

Analytical and Modelling Results

This Chapter contains the results related to the analytical equations and Finite Element Modelling. The simulated model evolved in two distinct directions; one is more closely related to the extent of what can be 3D printed and as a contrasting method for experimental results, which are detailed in Chapter 5. The other direction, which this Chapter concerns, is the model that arose and evolved from trying to explain what is observed in the moth tympanum.

The first section of the chapter serves as validation for the simulated model comparing circular and elliptical homogeneous plates against the analytically obtained results from the resolution of the governing differential equations. Both the mode shape described for the moth eardrum and the seemingly directional hearing, believed to arise from the tympanum's morphology almost exclusively, are examined in sections 4.2 and 4.3. A section detailing the effects of the inclusion of damping follows, with closing remarks for this Chapter making up section 4.5.

4.1 Validation of the model

The first step was the validation of the COMSOL model, and to do so, the results predicted by COMSOL were compared against the outcomes from the equations detailed in section 3.1. The two simplest cases, the circular and elliptical homogeneous plates, were solved through partial differential equations using MATLAB and Maple

Table 4.1: Parameters used for the circular and elliptical plate models.

Parameter	**Circular Plate**	**Elliptical plate**
Plate radius/semi-axes	250 μm	335μm, 250μm
Plate thickness	5 μm	5μm
Young's modulus	250 MPa	250 MPa
Poisson's ratio	0.35	0.35
Volumetric mass density	1183 kg/m^3	1183 kg/m^3
Number of mesh elements	5418	4062

and examined via eigenfrequency study in COMSOL.

Table 4.1 contains the parameters chosen for the circular and elliptical plate simulations. They are chosen to be of biological relevance according to the literature on *Achroia grisella* and insect cuticle. Female *Achroia grisella*'s tympana have a major axis length of approximately 670 μm and minor axis length of approximately 500 μm; regarding thickness, the *conjunctivum* is found to be approximately 8 μm thick and the *tympanum proper* is approximately 3 μm thick (unpublished data by Dr Andrew Reid, [49]). The COMSOL models consist of a Shell interface, and the study used initially is an eigenfrequency study. The first six eigenfrequencies are evaluated and compared against the analytically obtained eigenfrequencies. The results obtained for both as well as the percentage difference between them are contained in tables 4.2 and 4.3.

4.1.1 Circular plate

For the circular plate, the simulation results match the analytical solutions very well, with percentage differences below 0.8% for all cases (see Table 4.2). The determination coefficient R^2 of the regression analysis for the circular plate is 1, indicating an excellent fit between the analytical and simulation data. The clamped circular membrane is a well-known differential equation problem, the clamped circular plate being similarly solved, involving the use of Bessel partial differential equations and functions. The COMSOL model is a simple one, the geometry being one of the easiest and highly symmetrical. The first six simulated eigenmodes can be seen in Figures 4.1 and 4.2. As expected, the second and third modes are degenerate and appear at the same frequency,

Table 4.2: Side-by-side comparison of analytical eigenfrequencies and simulated eigenfrequencies for the homogeneous circular plate clamped all around.

CIRCULAR PLATE		
Analytical eigenfrequencies	**COMSOL eigenfrequencies**	**Difference**
18.4 kHz	18.4 kHz	0%
38.3 kHz	38.2 kHz	0.3%
38.3 kHz	38.2 kHz	0.3%
62.9 kHz	62.4 kHz	0.8%
62.9 kHz	62.4 kHz	0.8%
71.7 kHz	71.2 kHz	0.7%

and, similarly, the fourth and fifth modes can be seen at the same frequency, being degenerate too.

4.1.2 Elliptical plate

The clamped elliptical plate problem has been solved, its resolution involving Mathieu partial differential equations and functions, instead of the Bessel equation and functions involved in the circular case. Mathieu functions are evaluated numerically in Maple, so the results cannot be considered the exact eigenfrequencies of the elliptical plate, introducing some uncertainty to the reference for comparison against the simulation. The coefficient of determination R^2 for the regression analysis of the elliptical plate model is 0.9938, indicating a very good fit between analytical results and simulation (the simulation results are within a 7% difference from the analytical results, see Table 4.3). The first six simulated eigenmodes can be seen in Figures 4.3 and 4.4. It is notable that the degeneracy between modes two and three and the degeneracy of modes four and five for the circular plate have disappeared for the elliptical plate, due to the asymmetry between its major and minor axes.

Once the model is validated against the analytical equations, the next iteration is developed, no longer solved analytically due to how time-consuming it would prove.

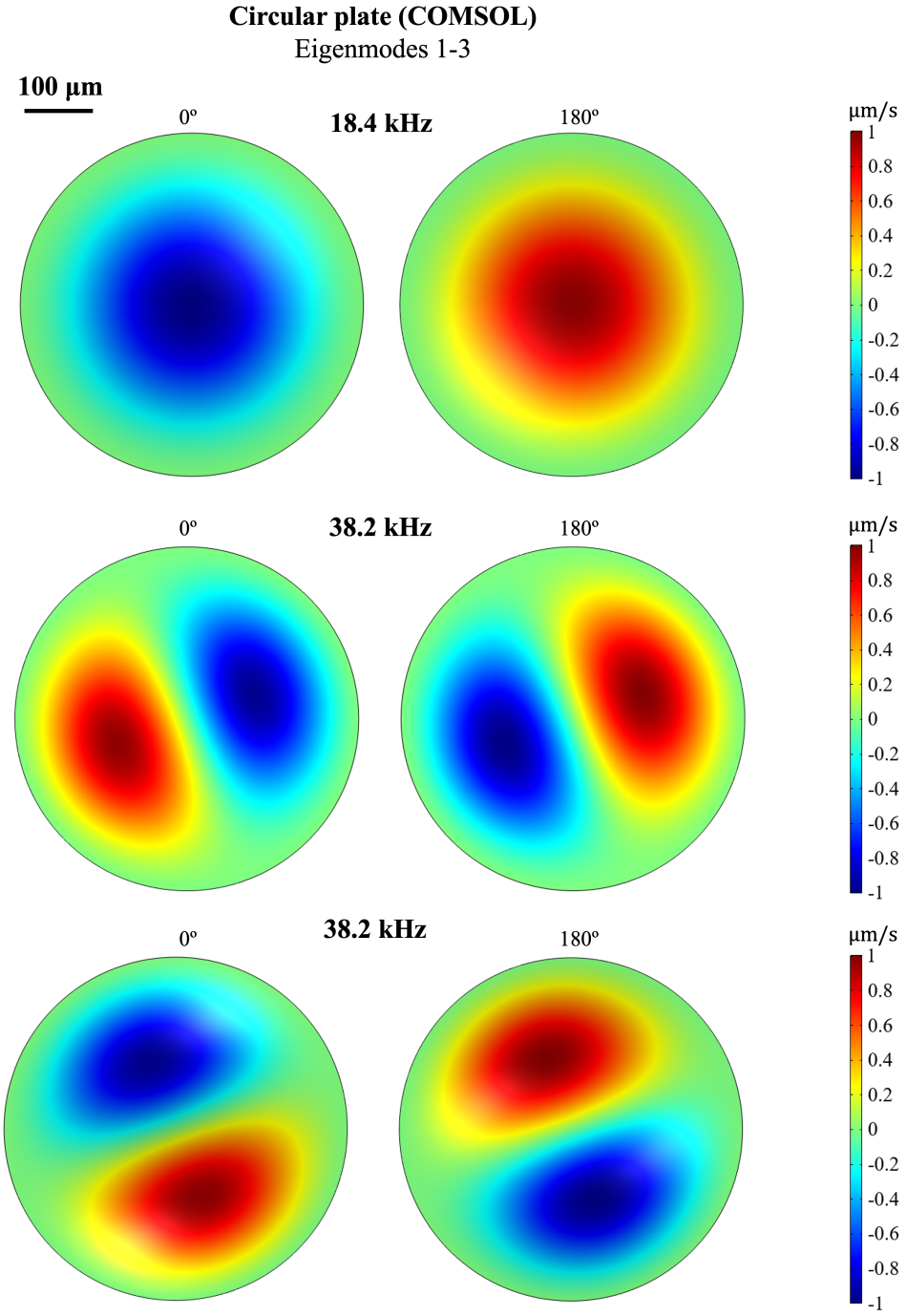

Figure 4.1: COMSOL simulation for the first three eigenmodes of the circular plate clamped all around. Two stills of opposite phases are shown to convey the maximum range of the eigenmode. The second and third modes are degenerate, occurring at the same eigenfrequency.

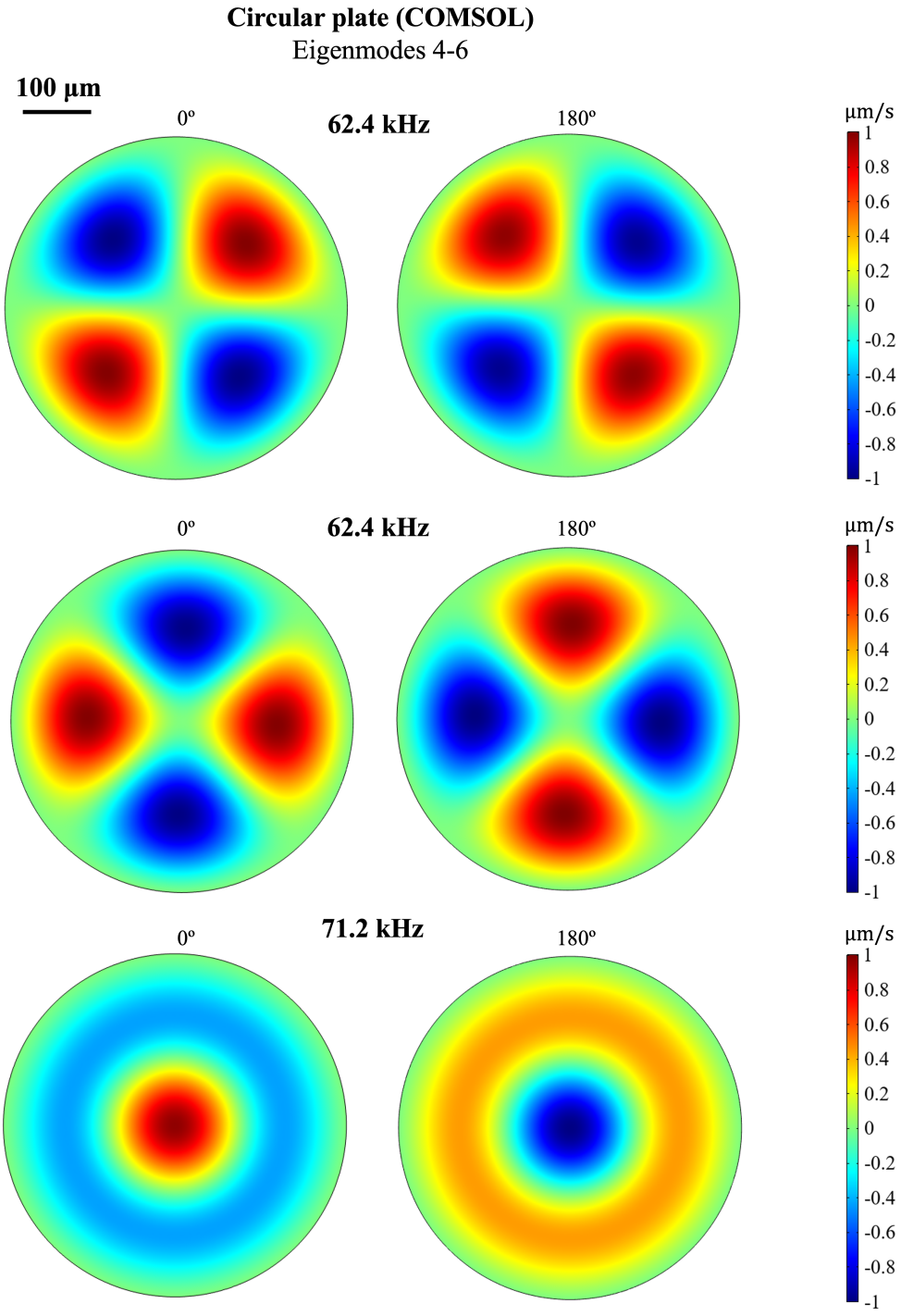

Figure 4.2: COMSOL simulation for eigenmodes four to six of the circular plate clamped all around. Two stills of opposite phases are shown to convey the maximum range of the eigenmode. The fourth and fifth modes are degenerate, occurring at the same eigenfrequency.

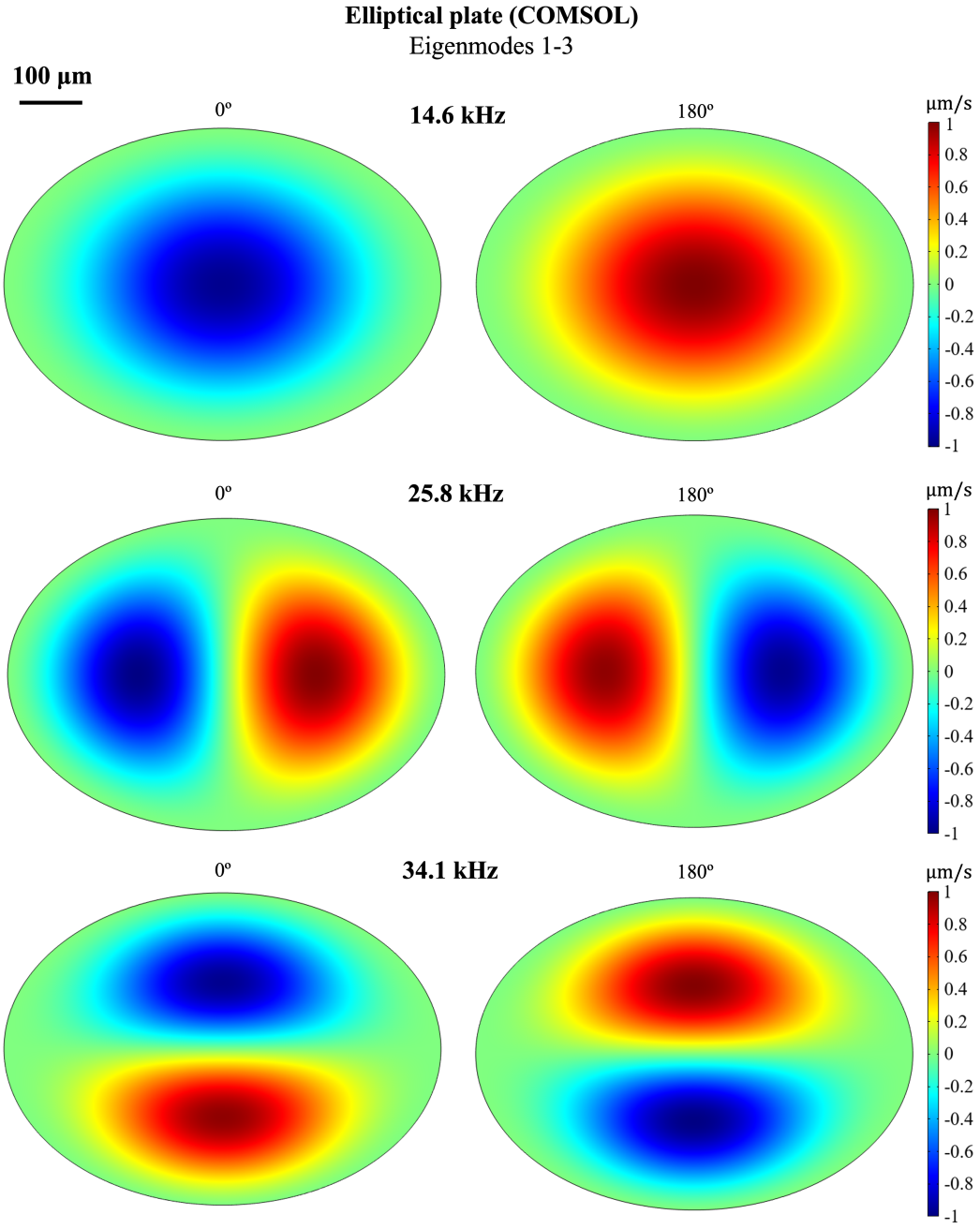

Figure 4.3: COMSOL simulation for the first three eigenmodes of the elliptical plate clamped all around. Two stills of opposite phases are shown to convey the maximum range of the eigenmode.

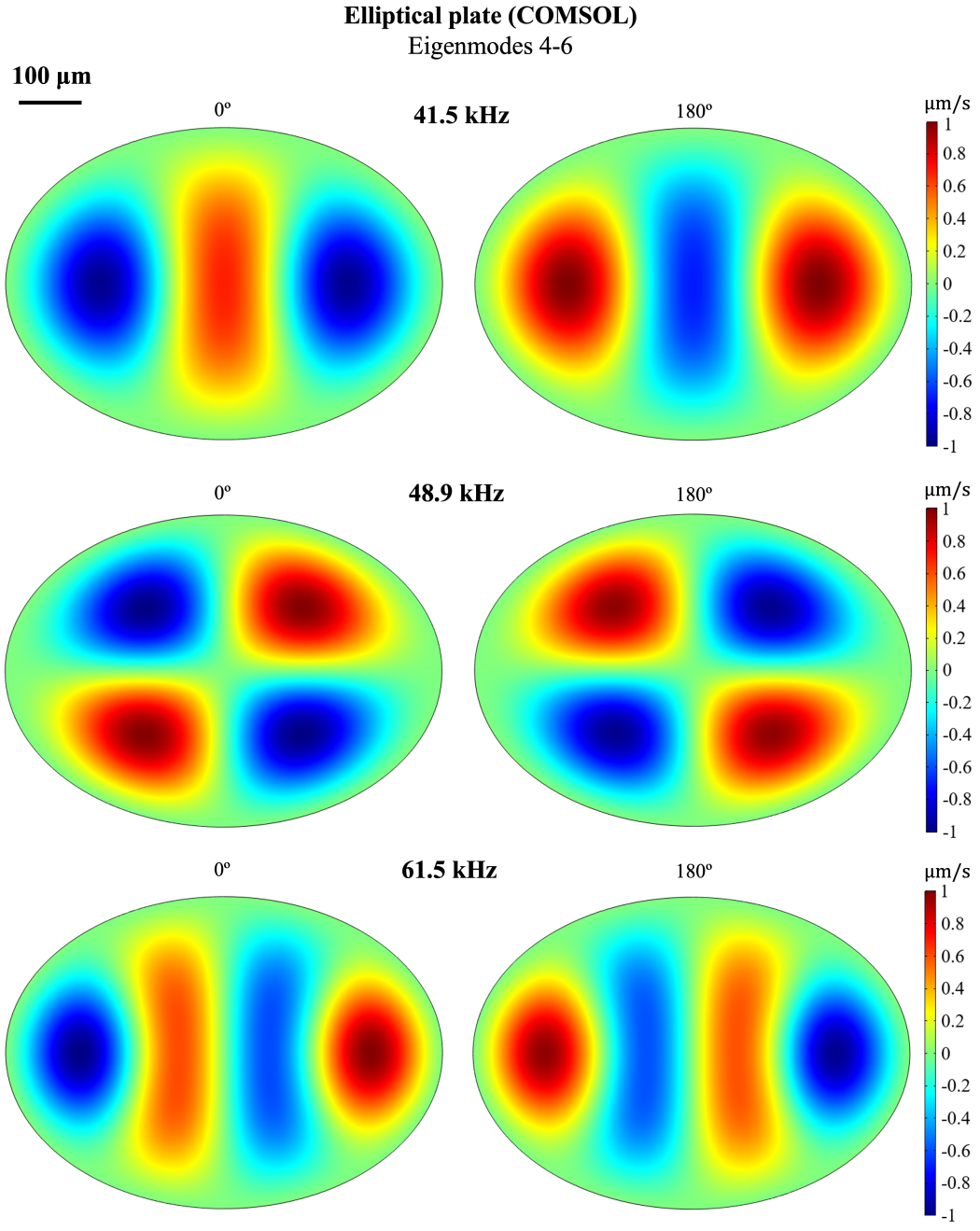

Figure 4.4: COMSOL simulation for eigenmodes four to six of the elliptical plate clamped all around. Two stills of opposite phases are shown to convey the maximum range of the eigenmode.

Table 4.3: Side-by-side comparison of analytical eigenfrequencies and simulated eigenfrequencies for the homogeneous elliptical plate clamped all around.

ELLIPTICAL PLATE

Analytical eigenfrequencies	**COMSOL eigenfrequencies**	**Difference**
15.5 kHz	14.6 kHz	5.8%
26.6 kHz	25.8 kHz	3.0%
34.8 kHz	34.1 kHz	2.0%
40.8 kHz	41.5 kHz	1.7%
50.1 kHz	48.9 kHz	2.4%
66.0 kHz	61.5 kHz	6.8%

4.2 Elliptical double-thickness mass-loaded plate

A new simulation that fits the moth's eardrum morphology better is devised based on the previous COMSOL model. While the outline is still elliptical and the edge is clamped, the new simulation takes into consideration the two sections of different thicknesses (namely *tympanum proper* and *conjunctivum*, the boundary between the two referred to as interface between sections) and includes a point mass to account for the neural attachment. Figure 4.5 shows the geometry with different parts and elements labelled.

In the moth's eardrum, the transition between the thinner and thicker sections is not an abrupt step, but instead a gradient. It is modelled as a step to determine if a simplification of the feature modelled in this way will capture the moth's eardrum behaviour in the simulation. Furthermore, such a gradient is not possible to replicate in 3D printing. Similarly, the point mass accounting for the neural attachment might be better approximated by a spring or stiff connection between the eardrum and substrate underneath it, but the simplification is examined to see if the model approximates the eardrum's behaviour. The mass for the point load is estimated as one of biological relevance, in this case, a value is chosen equal to that of the mass of the entire eardrum concentrated on a single point. The parameters chosen for the simulation, based on the existing literature on *Achroia grisella*, are listed in Table 4.4.

Firstly, mesh size is evaluated while running the eigenfrequency study for 6 different mesh sizes. The last two mesh sizes took significantly longer to draw and compute the

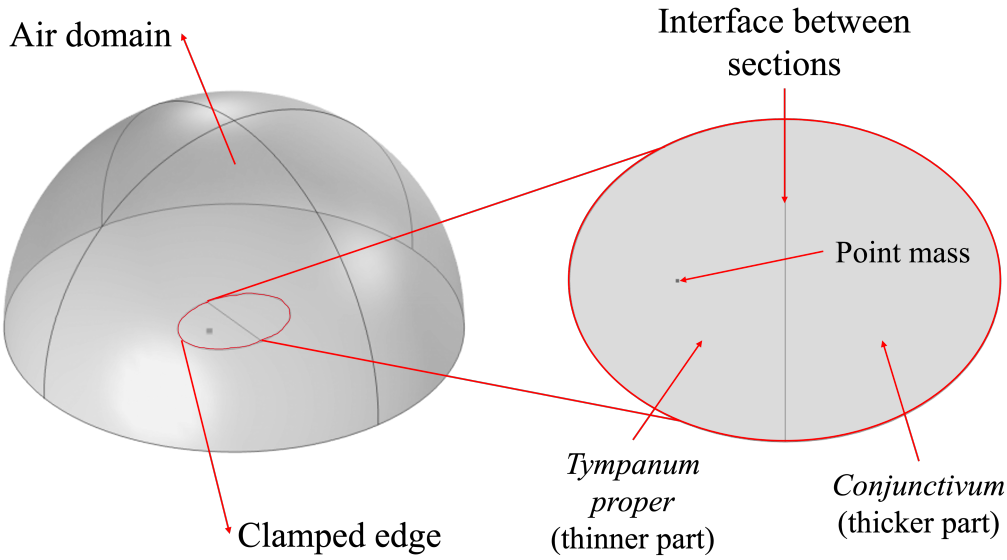

Figure 4.5: COMSOL geometry for the elliptical double-thickness plate with point mass.

Table 4.4: Parameters used for the elliptical double-thickness plate models.

Parameter	**Value**
Major semi-axis	335 μm
Minor semi-axis	250 μm
Tympanum proper thickness	3 μm
Conjunctivum thickness	8 μm
Interface between *ty.* and *conj.*	15 μm from centre (*ty.*> *conj.*)
Point mass	0.778 - 3.113 μg
Point mass location	175 - 145 μm from interface (*ty.*)
Young's modulus	1 MPa - 20 GPa
Poisson's ratio	0.35
Volumetric mass density	1183 kg/m^3

Eigenfrequency study. The eigenfrequency study with Custom 1 mesh took 2.4 times longer to compute than the Extremely Fine mesh and the study with the Custom 2 mesh took 11.4 times longer to compute. There is a trend that can be observed in Table 4.5 and represented in Figure 4.6, with results improving less with the reduction in mesh size. For the two custom meshes, reducing the element size approximately in half brings the results less than 3 Hz closer; this corresponds to multiplying the number of elements by almost 4 between Extremely Fine and Custom 1 and by 5 between Custom 1 and Custom 2. The trade-off between computational efficiency and accuracy for the custom meshes is considered not worth it. The extremely fine mesh is chosen for a balance between computation speed and accuracy.

The mode shapes for the aforementioned model are observed, and it is found that the fifth resonant frequency is the most graphically similar to the mode described for the moth tympanum (see Figures 4.7 and 4.8). This is, a peak with the largest displacement near the attachment point, a surrounding half-ring of lower amplitude and approximately opposite phase to the peak, and a broader lower-amplitude bump in the *conjunctivum*, also of approximate opposite phase to the main peak [19,56]. It is notable that the addition of a point mass and the two sections with different thicknesses approximate the simulation to what is observed on *Achroia grisella* significantly in comparison with the homogeneous elliptical model.

As reflected in Table 4.6, the simulation was run with three different values for Young's modulus, the parameter with the greatest range of values for insect cuticle according to the literature [37]. Two iterations are with Young's modulus values at both ends of the spectrum, 1 MPa for the lower end of the range and 20 GPa for the higher end of the range, and the other one is 1 GPa. This Young's modulus is chosen both because it is somewhat in the middle of the spectrum for sclerotised cuticle [37] and also provides a fifth resonant frequency (the mode shape with the highest similarity to the mode shape described at the moth's eardrum) at a frequency close to that observed for the moth, coincident with that of the male mating call and moth's maximum sensitivity [15,56]. Because just three values for Young's modulus are studied out of a wide range of possibilities, and the rest of the parameters are similarly

Table 4.5: Comparison of the first six eigenfrequencies for the elliptical double-thickness mass-loaded model for different mesh element size (Young's modulus 1 GPa, mass load of 1.556 μg, mass location 160 μm from interface into the tympanum).

Mesh size	Fine	Finer	Extra Fine	Extremely Fine	Custom 1	Custom 2
Maximum element size (m)	$5.36{\cdot}10^{-5}$	$3.68\ {\cdot}10^{-5}$	$2.35{\cdot}10^{-5}$	$1.34{\cdot}10^{-5}$	$7{\cdot}10^{-6}$	$3{\cdot}10^{-6}$
Minimum element size (m)	$6.7{\cdot}10^{-6}$	$2.68{\cdot}10^{-6}$	$1{\cdot}10^{-6}$	$1.34{\cdot}10^{-7}$	$7{\cdot}10^{-8}$	$3{\cdot}10^{-8}$
Number of mesh elements	258	522	1284	3908	13902	74158
1^{st} eigenfrequency (Hz)	6956.6	6986.6	7014	7029.3	7035.8	7037.4
2^{nd} eigenfrequency (Hz)	37914	38002	38098	38138	38153	38159
3^{rd} eigenfrequency (Hz)	57918	58363	58678	58846	58908	58931
4^{th} eigenfrequency (Hz)	68771	69285	69724	69996	70113	70144
5^{th} eigenfrequency (Hz)	85276	86019	86652	87068	87236	87289
6^{th} eigenfrequency (Hz)	90739	91347	91807	92028	92165	92202

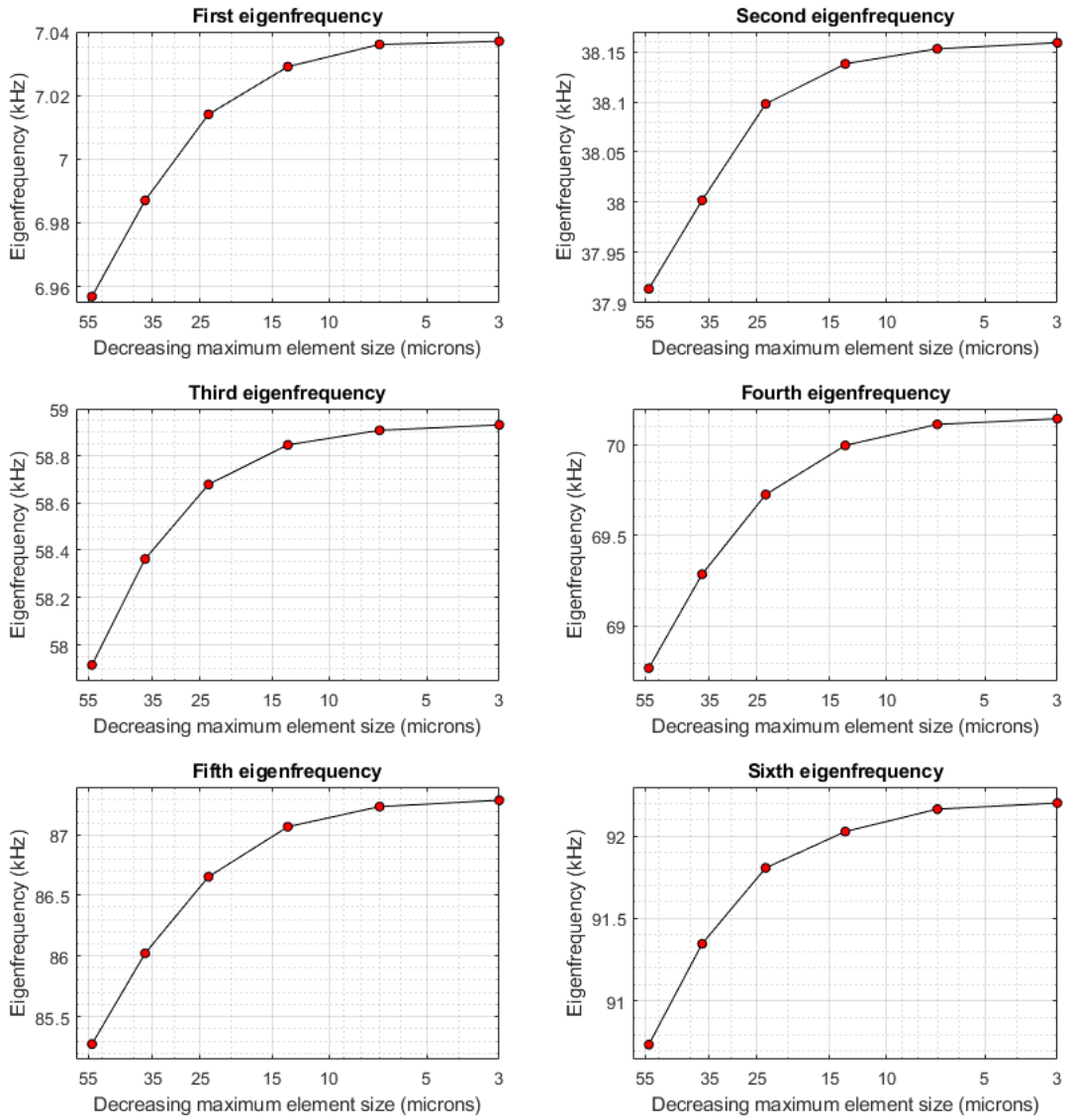

Figure 4.6: Representation of the trend in eigenfrequency value (in kHz) for decreasing mesh element size, and therefore increased computation time.

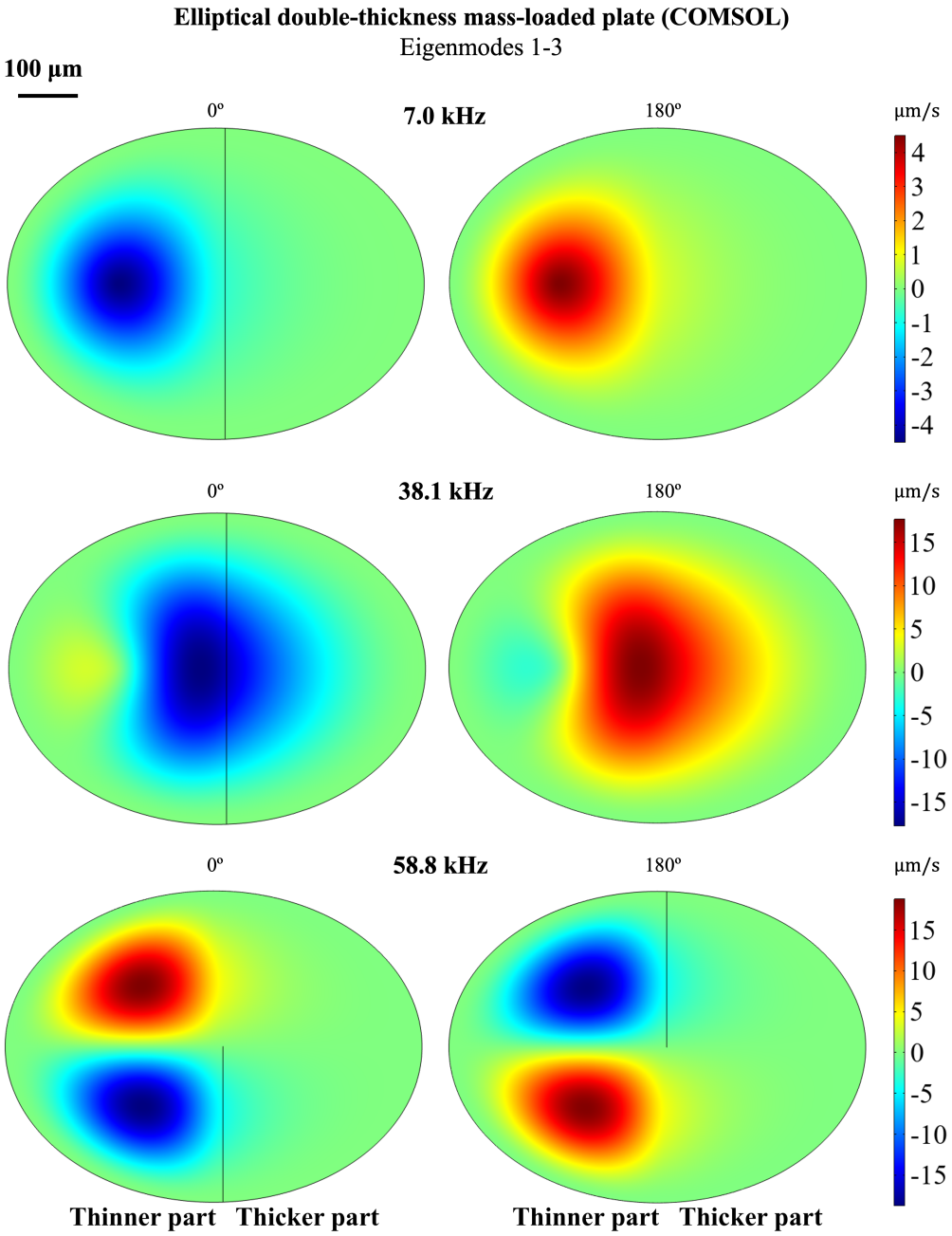

Figure 4.7: COMSOL simulation for the first three eigenmodes of an elliptical double-thickness mass-loaded plate (Young's modulus 1 GPa, mass load of 1.556 μg, mass location 160 μm from interface into the tympanum). Two stills of opposite phases are shown to convey the maximum range of the eigenmode.

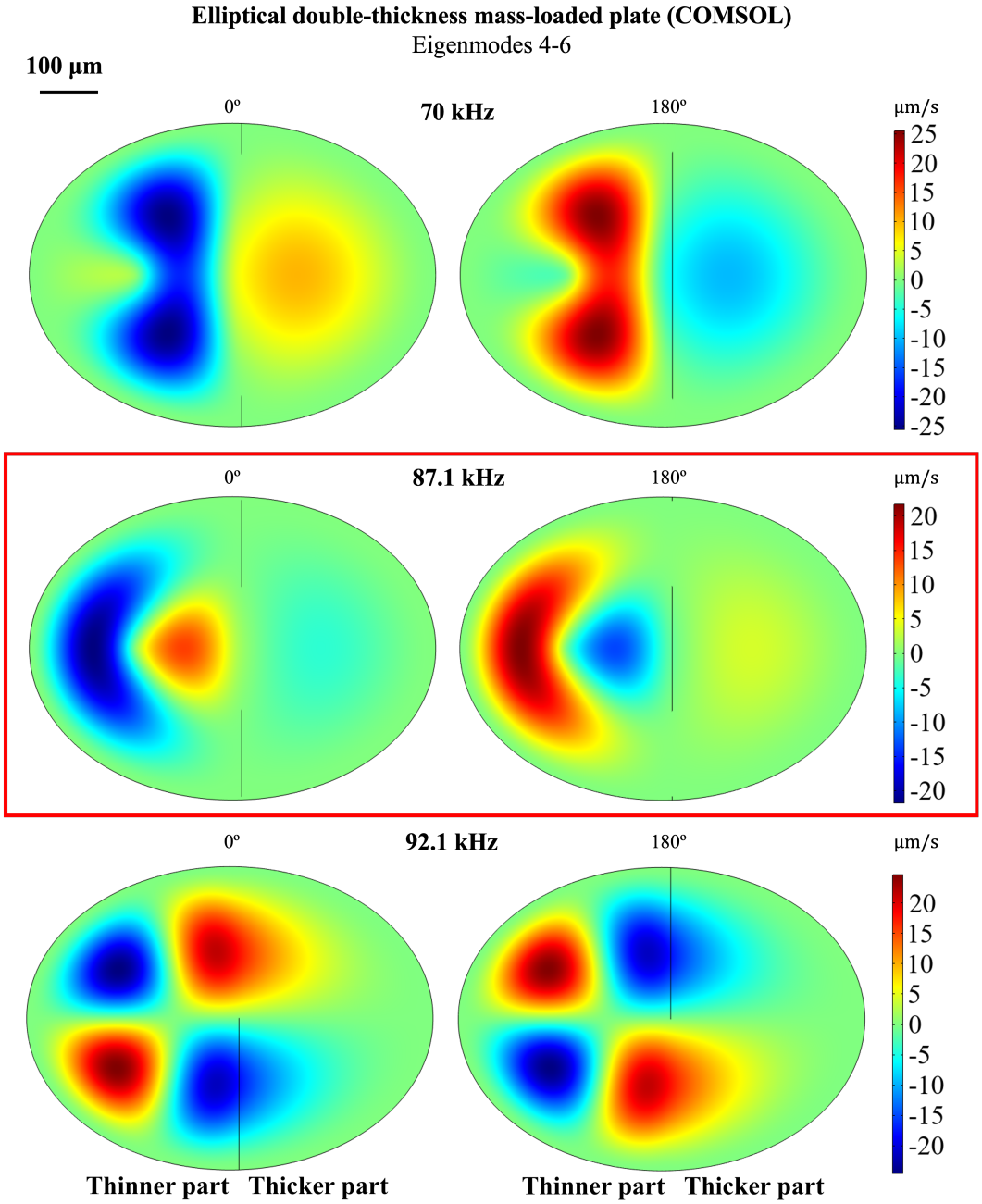

Figure 4.8: COMSOL simulation for eigenmodes four to six of an elliptical double-thickness mass-loaded plate (Young's modulus 1 GPa, mass load of 1.556 μg, mass location 160 μm from interface into the tympanum). Two stills of opposite phases are shown to convey the maximum range of the eigenmode. The fifth mode, the one resembling the moth's eardrum movement the most, is highlighted.

Table 4.6: Simulated eigenfrequencies for the elliptical double-thickness plate clamped all around. Three different values for Young's Modulus (mass load of 1.556 μg, mass location 160 μm from the interface into the *tympanum proper*).

	YOUNG'S MODULUS		
Eigenfrequency	**1 MPa**	**1 GPa**	**20 GPa**
1^{st}	228.5 Hz	7.0 kHz	32.3 kHz
2^{nd}	1.2 kHz	38.1 kHz	165.5 kHz
3^{rd}	1.9 kHz	58.8 kHz	263.2 kHz
4^{th}	2.1 kHz	70.0 kHz	297.4 kHz
5^{th}	2.9 kHz	87.1 kHz	411.7 kHz
6^{th}	3.0 kHz	92.1 kHz	418.4 kHz

estimated, there is a clear limitation to the results. Nevertheless, it is worth observing the effect of the parameter on the eigenfrequencies of the system. The difference in the natural frequencies with the three Young's modulus values can be seen in Table 4.6

Two other parameters were varied and their effect on the simulation was considered. Firstly, the location of the loaded mass point is seen to greatly affect the fourth, fifth and sixth resonant frequencies, eventually exchanging the positions of the fifth and sixth. The mode shapes also see changes with the displacement of the mass point as little as 15 microns closer or further to the frontier between *tympanum* and *conjunctivum* (see results for three positions in Table 4.7). For a location of the neural attachment point mass of 170.95 microns into the tympanum, the fifth and sixth modes become as close as essentially degenerate at 92.07 kHz and 92.08 kHz.

Contrarily, the mass itself doubling or halving does not affect the eigenfrequencies or eigenmodes much (see results for these three cases in Table 4.8). If the mass is removed completely, the resonant frequencies increase significantly, and the fifth and sixth modes are again switched, with the sixth mode in particular changing shape considerably.

4.3 Directivity analysis

The directivity analysis requires the addition of the Pressure Acoustics, Frequency Domain module, as described in the methodology. The directivity of the elliptical two-thickness plate with the mass-loaded point to account for the neural attachment is

Table 4.7: Simulated eigenfrequencies for the elliptical double-thickness plate clamped all around. Three different values for the location of the mass point (Young's modulus 1 GPa, mass load of 1.556 μg).

	POINT MASS LOCATION					
Eigenfrequency	**175 μm**		**160 μm**		**145 μm**	
1^{st}	7.2 kHz		7.0 kHz		6.9 kHz	
2^{nd}	37.0 kHz		38.1 kHz		39.3 kHz	
3^{rd}	58.9 kHz		58.8 kHz		58.8 kHz	
4^{th}	66.5 kHz		70.0 kHz		72.4 kHz	
5^{th}	92.1 kHz		87.1 kHz		80.2 kHz	
6^{th}	93.6 kHz		92.1 kHz		92.1 kHz	

Table 4.8: Simulated eigenfrequencies for the elliptical double-thickness plate clamped all around. Four different values for the point mass accounting for the neural attachment point, including its complete absence (Young's modulus 1 GPa, mass location 160 μm from interface into the *tympanum proper*).

	POINT MASS			
Eigenfrequency	**0.778 μg**	**1.556 μg**	**3.113 μg**	**No mass**
1^{st}	9.7 kHz	7.0 kHz	5.02 kHz	29.2 kHz
2^{nd}	38.3 kHz	38.1 kHz	38.0 kHz	46.4 kHz
3^{rd}	58.8 kHz	58.8 kHz	58.8 kHz	58.8 kHz
4^{th}	70.4 kHz	70.0 kHz	69.8 kHz	78.6 kHz
5^{th}	87.3 kHz	87.1 kHz	86.9 kHz	92.1 kHz
6^{th}	92.1 kHz	92.1 kHz	92.1 kHz	99.0 kHz

Table 4.9: New spherical coordinates parameters added to the COMSOL model for characterisation of the acoustic stimulus.

Parameter	**Value**
Elevation angle (θ)	90^{o}
Azimuth angle (φ)	0^{o} - 360^{o} (in 5^{o} steps)
$k_1 = \sin(\theta) \cdot \cos(\varphi)$	-1 - 1
$k_2 = \sin(\theta) \cdot \sin(\varphi)$	-1 - 1
$k_3 = \cos(\theta)$	0

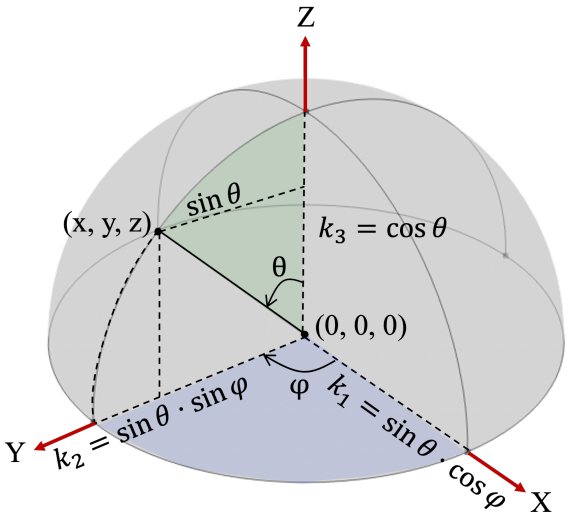

Figure 4.9: Representation of the elevation (θ) and azimuth (φ) angles and the vectors k_1, k_2 and k_3.

evaluated, representing in a polar plot the displacement of the tympanum surface at the precise neural attachment point (centre of the thinner section). Five new parameters are added to the existing model to characterise the acoustic stimulus. Two angles, the elevation and azimuth, and three direction vectors that depend on the aforementioned angles and are expressed in spherical coordinates. These are collected in Table 4.9. The eigenfrequency study is run again to ensure the values are the same, which is found to be the case if the mesh is kept intact using the same minimum and maximum element sizes. The frequency study with the parameter sweep over the azimuth angle (from 0^{o} to 360^{o}, in 5^{o} steps) is then run at the frequency of the fifth resonant mode, 87.1 kHz. Figure 4.9 shows a schematic drawing of these vectors and angles.

The azimuth angle is the one that will be swept over in intervals of five degrees for

producing the polar plots, and therefore its initial value is, to begin with, unimportant. The elevation angle will characterise the angle with which the stimulus reaches the tympanum; it is chosen to be 90^{o} to match the experimental setup of previous work done on *Achroia grisella* specimens. Previous work examined the tympanum response in live moths, the specimens being turned upside down so that their abdomen is facing upwards towards the scanning head of the laser, their legs and ventral clefts removed to leave the tympana exposed. The tympana are then scanned under exposure to an acoustic stimulus, that is rotated around the moth, the speaker perpendicular to the tympanum plane [56]. The stimulus used in the COMSOL simulation is 1 Pa or 94 dB. The polar plot resulting from measuring the displacement of the shell at the neural attachment point (in the middle of the *tympanum proper*) can be observed in Figure 4.10. The displacement is sub-nanometre, and there is a difference of an order of magnitude between the minimum displacement and the maximum. The Figure shows that the neural attachment point experiments the highest displacement when the acoustic stimulus is coming from the 0^{o} angle, equivalent to the head of the moth, minimal at the sides (90^{o} and 270^{o}), and showing lower displacement at 180^{o}, or the back of the moth.

The simulated data is normalised with respect to the maximum displacement and compared against data from existing measurements of deflection on live *Achroia grisella* specimens [56]. The comparison can be seen in Figure 4.11, with the data on live moths more sparsely captured than that simulated in COMSOL (30^{o} intervals for live moth data and 5^{o} intervals for simulations). Despite this disagreement in the sampling, it can be observed that the data collected on the moths also shows the highest displacement when sound comes from the 0^{o} direction, decreases from the left and right, and is larger, but again lower than that from the front, when sound comes from the back of the moth (180^{o}). The main features of the data simulated in COMSOL and those of the data measured on *Achroia* specimens are therefore in agreement.

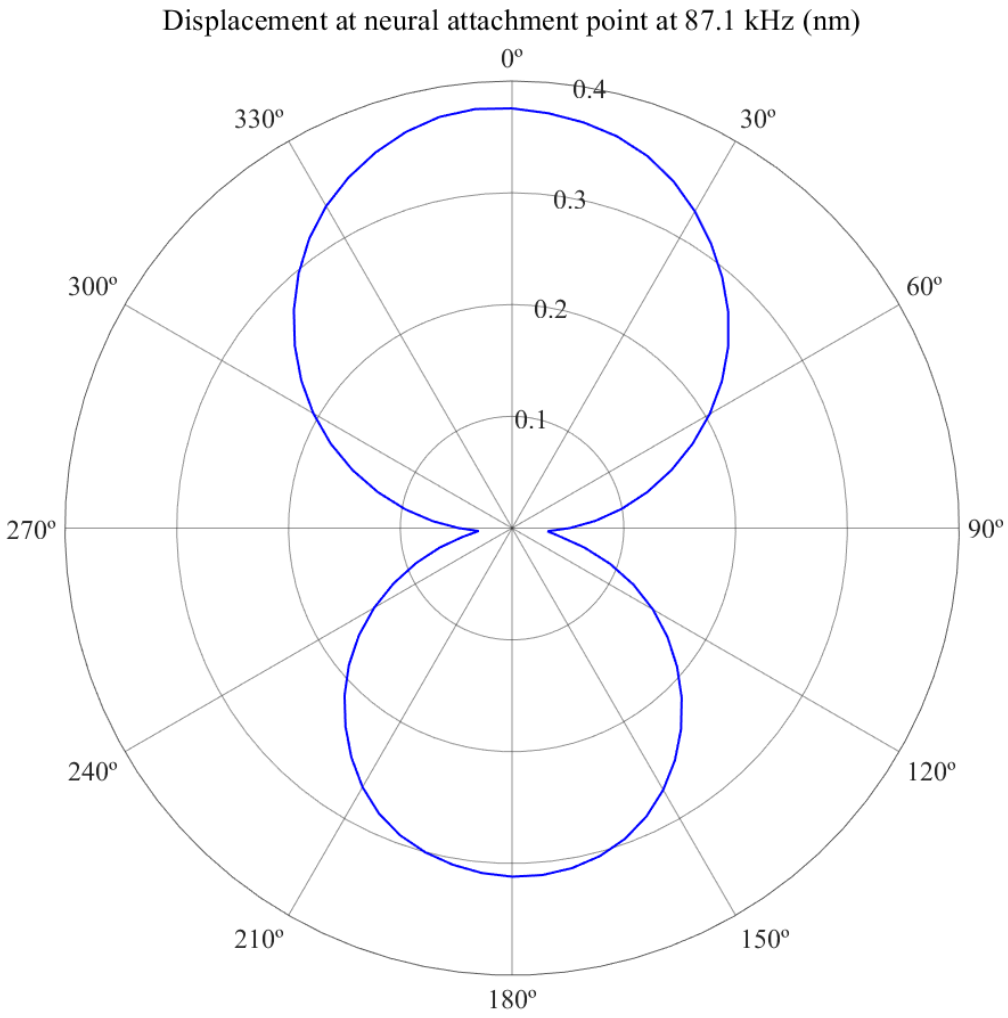

Figure 4.10: Polar plot of the COMSOL simulation of the displacement at the neural attachment point of an elliptical double-thickness mass-loaded plate (Young's modulus 1 GPa, mass load of 1.556 μg, mass location 160 μm from interface into the tympanum) with an acoustic stimulus.

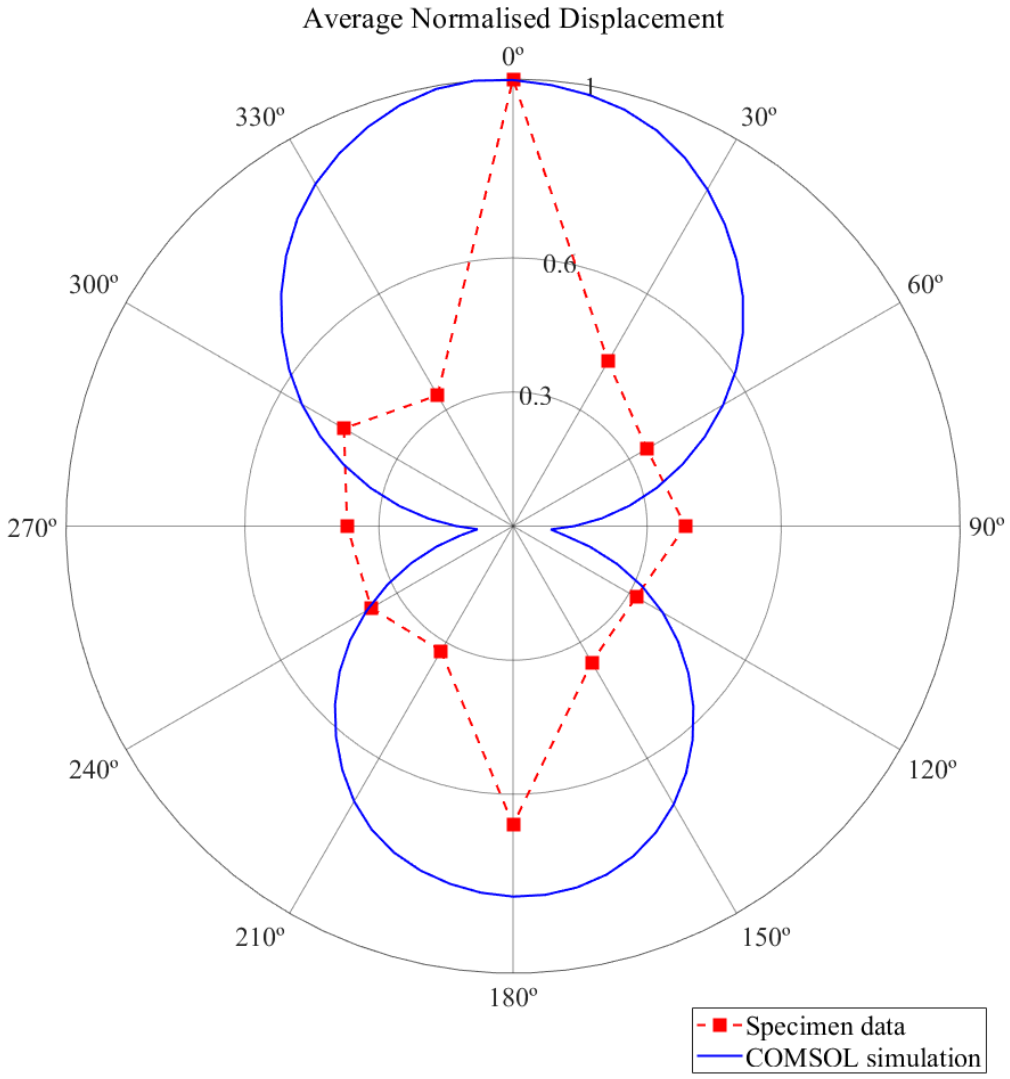

Figure 4.11: Comparison in a polar plot of data points obtained from a real specimen by Dr Andrew Reid and the COMSOL simulation from Figure 4.10, where both have been normalised. *Achroia grisella* data taken from Figure 6.16 in Dr Andrew Reid's thesis [56].

4.4 Damping

The eigenfrequency analyses done so far are a simplification of the real cases, in which no motion would continue without the presence of external forces. Damping accounts for the transfer of energy that results in the decay of the waves travelling through the system. Without damping, maximum displacement and equilibrium position in an eigenmode are synchronised for all parts of the system, but when damping is considered, the peak values for the maxima of the eigenmode and equilibrium positions are no longer reached at the same instant in time and the phase information is contained in the imaginary part of the eigenfrequency, which corresponds to what is observed in the moth eardrum [19, 56].

There are several options for damping that can be modelled in COMSOL; loss factor damping, Rayleigh damping, viscous damping, modal damping or thermoelastic damping are just some of the possibilities. Nevertheless, damping can be difficult to characterise for a particular system; a very small change in, for example, the loss factor, can impact the results greatly. Viscous damping is one of the preferred damping models due to its mathematical expression being simpler than others. It is chosen in this particular case in an attempt to increase the similarity of the model to the moth ear in a qualitative way. Viscous damping is introduced in the equations of motion as a factor multiplying velocity, where D is the damping constant, m is the mass, k is a force constant, and *F(t)* is the time-dependent force:

$$m \cdot \frac{\delta^2 x}{\delta t^2} + D \cdot \frac{\delta x}{\delta t} + k \cdot x = F(t) \tag{4.1}$$

The addition of damping through viscous modelling of air to the considered model results in the apparition of complex solutions, where the imaginary part refers to the decaying part of the solution (see Figures 4.12 and 4.13). In the new fifth eigenfrequency, a peak with maximum displacement is present near the point loaded with mass, surrounded by a series of secondary peaks, out of phase but not in exact opposition of phase, and a broader bump in the thick region, of a similar phase to that of the peak ring. For the considered model, the addition of viscous damping increases the

apparent likeness of the eigenmode to the resonating mode observed in the moth ear (see Figure 4.14 published in reference [57]). The rest of the eigenfrequencies also become complex, and a new eigenfrequency appears, close to the fifth one but not exactly degenerate. The modes of these two frequencies are also similar in shape.

4.5 Chapter summary

This Chapter details the results regarding the behaviour of *Achroia grisella*'s tympanum obtained through COMSOL simulations. It is seen that a simplification from the complex natural morphology to an elliptical double-thickness mass-loaded plate already bears similarities to the eardrum's movements. Different values for some of the parameters are tested in simulation and their effect on the eigenfrequencies and eigenmodes is evaluated (Tables 4.6, 4.7 and 4.8).

A mode shape (the fifth eigenmode at 87.1 kHz) is identified for one model (centred neural attachment point at 160 μm, mass to account for the neural attachment of the same mass as that of the whole plate of 1.556 μg, Young's modulus in the lower end of the range for sclerotised cuticle of 1GPa), seen highlighted in Figure 4.8, that resembles the displacement of the eardrum under exposure to a signal of approximately 100 kHz (that of the male mating signal).

Furthermore, directionality is observed at the neural attachment point for the aforementioned natural resonance mode that resembles the displacement of the moth tympanum (see Figure 4.11), therefore signalling that the morphology of the system is conferring it with directionality. Lastly, viscous damping is added to the model through the gas model for the air domain, which alters the eigenfrequencies, making them complex-valued, and increases the likeness to the observed motion in the real moth tympana.

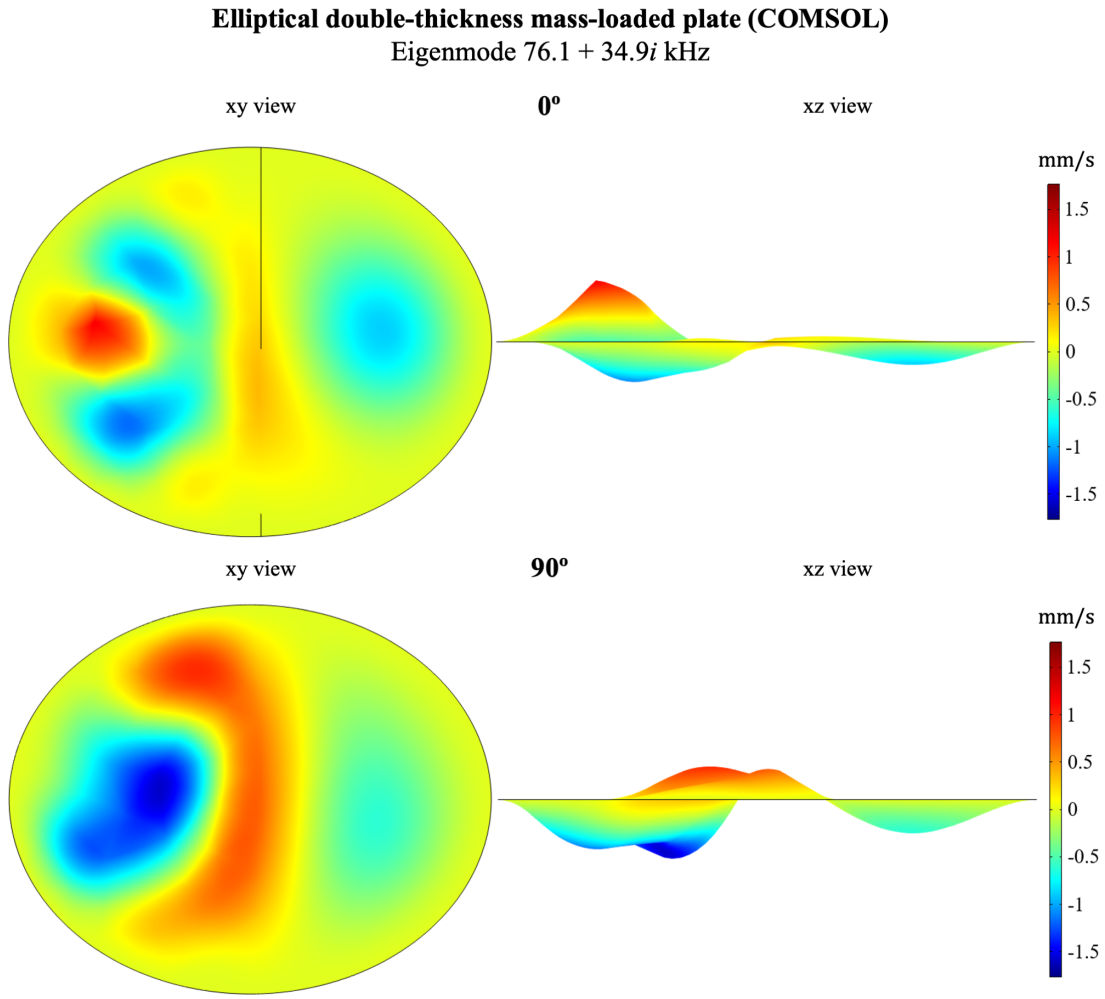

Figure 4.12: Eigenmode for the eigenfrequency found at $76.145+34.941i$ kHz for an elliptical double-thickness plate with a mass-loaded point and damping induced by a viscous model for air. Two stills of different phases (0^{o} and 90^{o}) are shown to convey the range of the eigenmode (see Figure 4.13 for continuation), xy and xz views are provided to evidence the peaks and the phase relation between them.

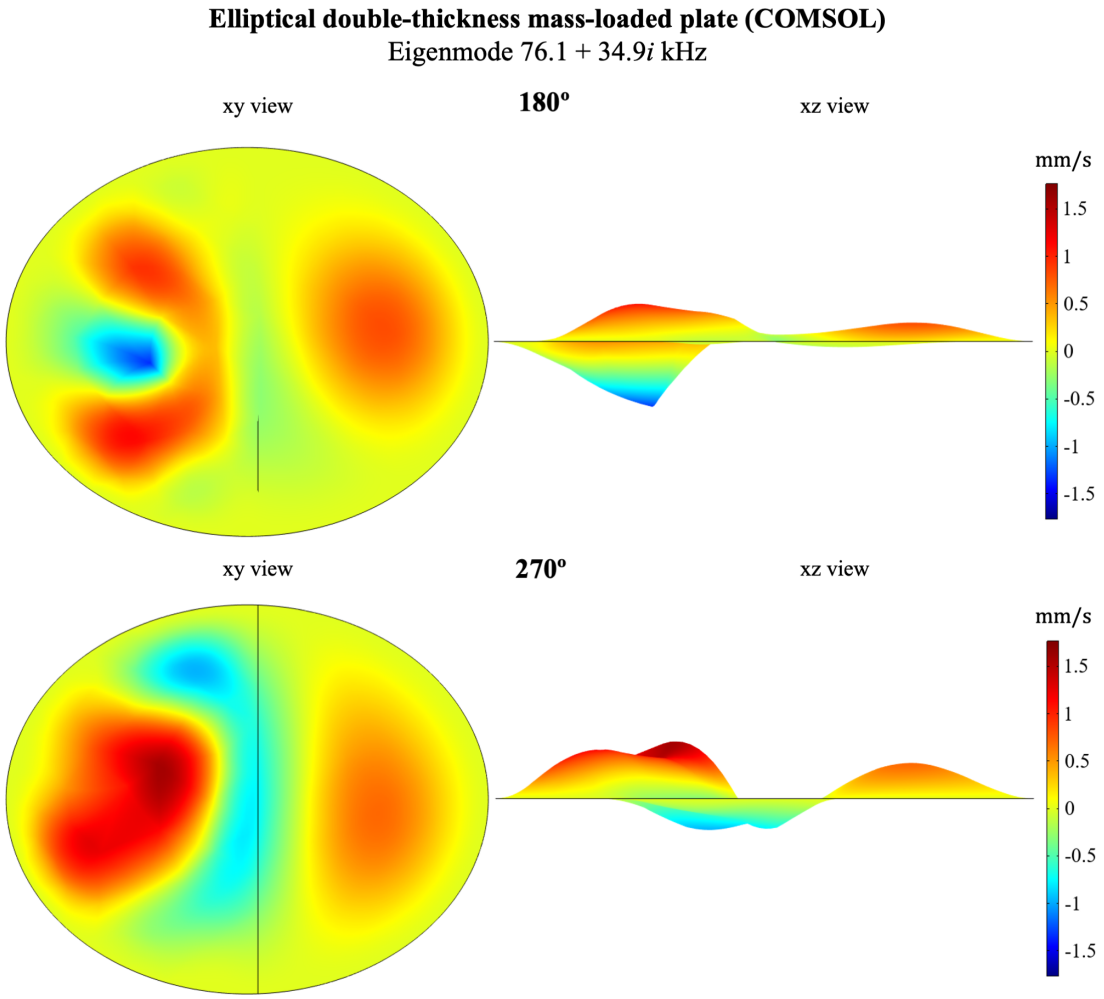

Figure 4.13: Eigenmode for the eigenfrequency found at $76.145+34.941i$ kHz for an elliptical double-thickness plate with a mass-loaded point and damping induced by a viscous model for air. Two stills of different phases (0^{o} and 90^{o}) are shown to convey the range of the eigenmode, XY and XZ views are provided to evidence the peaks and the phase relation between them.

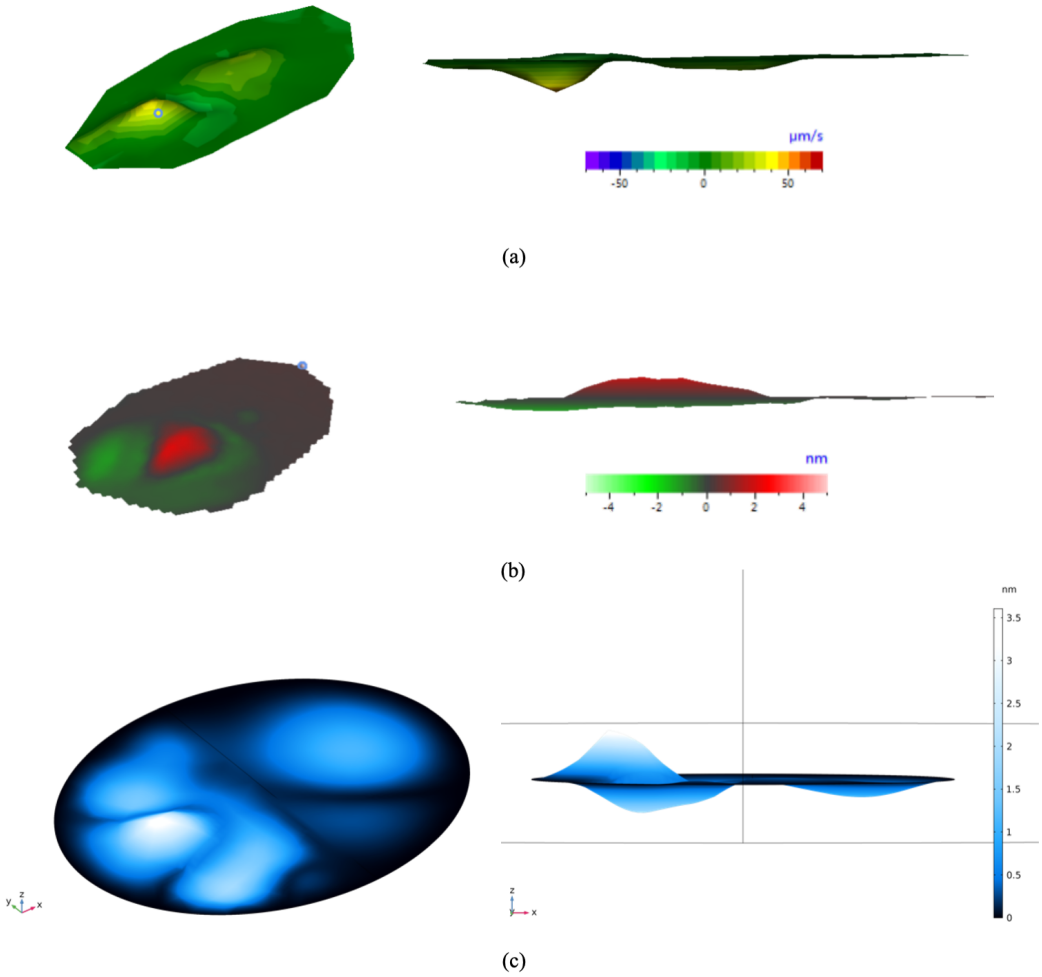

Figure 4.14: LDV measurements for a moth specimen and COMSOL simulation [57]. LDV measurement taken from a moth specimen by Dr Andrew Reid showing (a) the velocity and (b) the displacement at which the tympanum surface moves under excitation of a pure tone of 100 kHz. (c) COMSOL simulation showing displacement of the plate surface at the sixth natural frequency ($76.1 + 34.9i$ kHz) of an elliptical plate divided into two sections of different thicknesses (thin one on the left half of the ellipse and thick one on the right) with an attached mass (perspective view on the left and XZ plane view on the right) .

Chapter 5

3D Printing Results

This Chapter reports on the results of the experiments carried out with scaled-up 3D printed samples and how they compare to the simulated results obtained from COMSOL. The samples printed are of the order of 10 times larger in length and width than the moth's tympanum and about 50 times thicker. The COMSOL model is adapted to match the size of the 3D printed parts. The samples are scaled up for manoeuvrability and to bring the resonant frequencies down. This Chapter consists of two sections, one referring to the frequency analysis of the samples and one regarding the directivity analysis. Each section is divided into subsections. The first one has three subsections, each concerning one of the different shapes in which frequency responses were examined: circular plates, elliptical plates and elliptical double-thickness plates. This section relates to the peer-reviewed conference paper presented at IEEE Sensors 2020, which can be found in Annex A.

The second section is divided into two subsections; the first one refers to the first iteration of a smaller sample, of which the lower resonant frequencies' directionality patterns were explored, and the second one refers to the larger sample of which the higher resonant frequency's directionality was examined. These subsections correspond to a publication each. The first subsection corresponds to the peer-reviewed journal paper published in the IEEE Sensors Journal in 2022, and subsection 5.2.2 relates to the editor-reviewed paper presented at the biannual Acoustical Society of America meeting in 2022 and subsequently published at the Proceedings of Meetings on Acoustics in

2023. These publications can be found in Annexes B and C respectively. Pictures of the 3D printed parts corresponding to the designs used can be seen in Figure 5.1.

5.1 Commercial resin samples for frequency analysis

The first samples produced were manufactured using a Prusa SL1 and Orange Tough resin. The Young's modulus of these samples was determined as explained in section 3.1.3 by 3D printing a cantilever and measuring its resonant frequencies and found to be 1.4293 GPa (standard error 0.0632 GPa, sample size of 5). Three different shapes were produced in Orange Tough; circular plates that have a diameter of 1.50 mm, and uniform thickness and double-thickness elliptical ones that have major and minor axes of 2.10 mm and 1.50 mm respectively. Pictures of the samples can be seen in 5.1 A and B. The thickness of the samples measured through μCT scanning is found to be 162 microns for single-layers and 270 microns for the thicker three-layer regions. As explained in section 2.5, this is thicker than expected, even though the print settings are established as a layer thickness of 50 microns, due to a combination of film bulging and cross-curing of the horizontal overhangs [193–196].

The frequency responses for the three shapes were examined as explained in section 3.5, with the help of a piezoelectric vibrating chip. Knowing their sizes and thicknesses, equivalent COMSOL models were adapted to match these parameters and be compared with them. The range of excitation for each sample is chosen to cover the first few expected resonant frequencies, as predicted from simulations, with some margin on both ends of the range in case the eigenfrequencies are displaced. The eigenfrequencies are identified in the following way: the whole surface of the sample is scanned and the frequency response produced is the average of all points scanned. The maxima of the frequency response are selected and the displacement pattern at each frequency is observed, and then the main features are compared against the eigenfrequencies obtained from the simulation. An experimental resonant frequency is selected if the frequency corresponds to a maximum and there is a similarity between the patterns. Similarly, some of the peaks in the frequency response are discarded if the mode shape observed at these peaks does not match any expected eigenmode. This procedure is

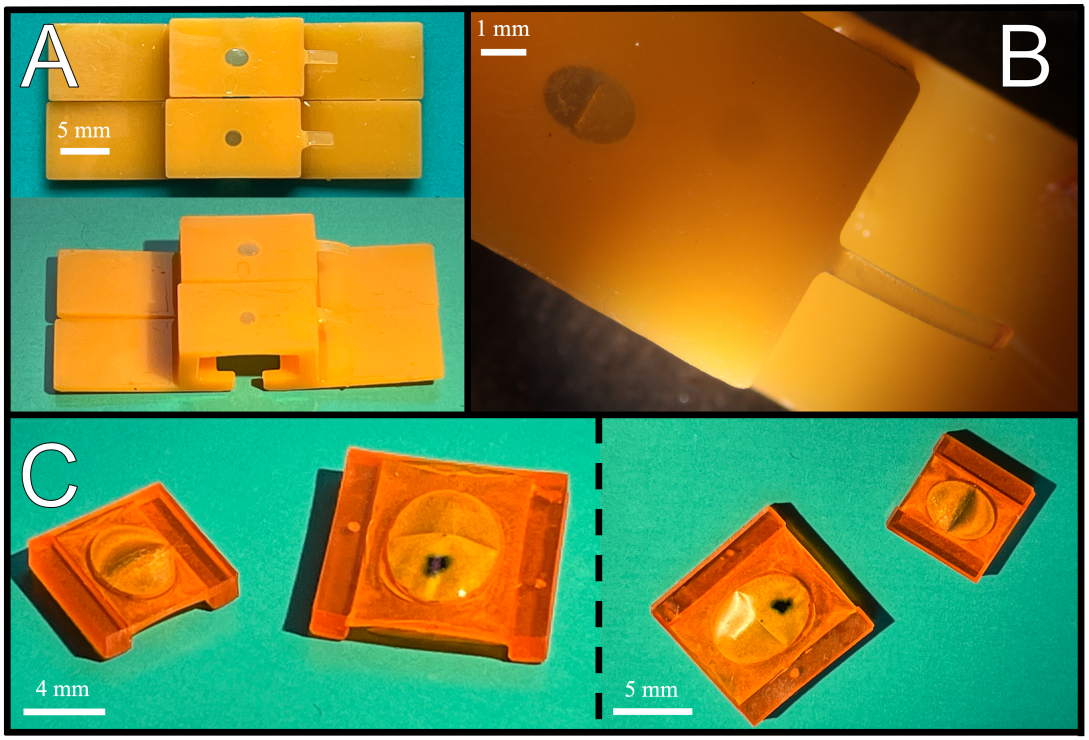

Figure 5.1: 3D printed samples used for experiments. (A) Two different perspectives of the circular and elliptical samples that were used in sections 5.1.1 and 5.1.2. The circular sample has a size of 1.5 mm in diameter, and the elliptical sample measures 2.10 mm by 1.50 mm (major and minor axes respectively). The cantilevers printed for Young's modulus measurement can be seen on the right of each structure. (B) The elliptical double-thickness sample used in section 5.1.3, its measurements are 2.10 mm by 1.50 mm (major and minor axes respectively). The cantilever for Young's modulus measurement can be seen in the lower right of the picture. (C) Two different perspectives of the elliptical double-thickness samples used for measuring directivity in section 5.2. The smaller sample, used in 5.2.1, measures 5.36 mm by 4 mm (major and minor axes respectively); the bigger one, used in section 5.2.2, measures 6.55 mm by 4.95 mm (major and minor axes respectively). The black residue corresponds to where a reference dot was painted to measure the directivity and spread during time.

followed for all shapes of samples. The first few resonant frequencies found for each shape both in COMSOL and experimentally are compiled in Table 5.1. The generally good agreement between the two can be perceived from the low percentage differences.

5.1.1 Circular plates

For the circular samples, there is a good agreement between COMSOL and predicted eigenfrequencies, with differences below 1.5%. The frequency response extracted with the use of the piezoelectric chip and LDV scanning can be seen in Figure 5.2. The intersections of the mesh lines overlaid on all LDV measurements represent the measurement points in the scan. The stimulus used is a periodic chirp excitation from 100 kHz up to 275 kHz. The first two resonant peaks have been tagged in the graph. The patterns of vibration of this model, which are still far from resembling the moth tympanum's movement, can be seen side by side with the corresponding COMSOL predicted eigenmodes for the fundamental mode (Figure 5.3), and second and third degenerate resonant frequencies (Figures 5.4 and 5.5). The patterns clearly resemble each other, with the superposition of the second and third modes being seen in the LDV scans, as expected from the simulation and the literature (see Figure 3.2 in Subsection 3.1.1).

5.1.2 Elliptical plates

For the simple elliptical plates, there is also good agreement between COMSOL and predicted eigenfrequencies, with differences below 13% (the fundamental frequency being an outlier and all the rest of them being less than 5%). The frequency response for the elliptical plate obtained with the use of the piezoelectric chip and LDV scanning can be seen in Figure 5.6, the stimulus used this time is a periodic chirp excitation from 80 kHz up to 280 kHz. The first four resonant peaks located have been tagged in the graph. The patterns of vibration of this model are like those of the circular plate but slightly elongated and have lost the degeneracy of modes two and three, and four and five due to the asymmetry between the major and minor axis of the elliptic shape. Modes one through five can be seen, next to their corresponding COMSOL-predicted eigenmodes, in Figures 5.7 to 5.10.

	Resonance	COMSOL frequency (kHz)	Experimental frequency (kHz)	Difference
Circular	1^{st}	135	137	1.48%
	2^{nd}	257	260	1.17%
	3^{rd}	257	260	1.17%
Elliptical	1^{st}	106	93	12.26%
	2^{nd}	174	167	4.02%
	3^{rd}	228	230	0.88%
	4^{th}	262	258	1.53%
Elliptical double thickness	1^{st}	129	127	1.55%
	2^{nd}	209	202	3.35%
	3^{rd}	266	260	2.26%
	4^{th}	302	305	0.99%

Table 5.1: Comparison between eigenfrequencies obtained from COMSOL and experimentally measured through Laser Doppler Vibrometry for circular, elliptical, and elliptical two-thickness plates 3D printed in Orange Tough.

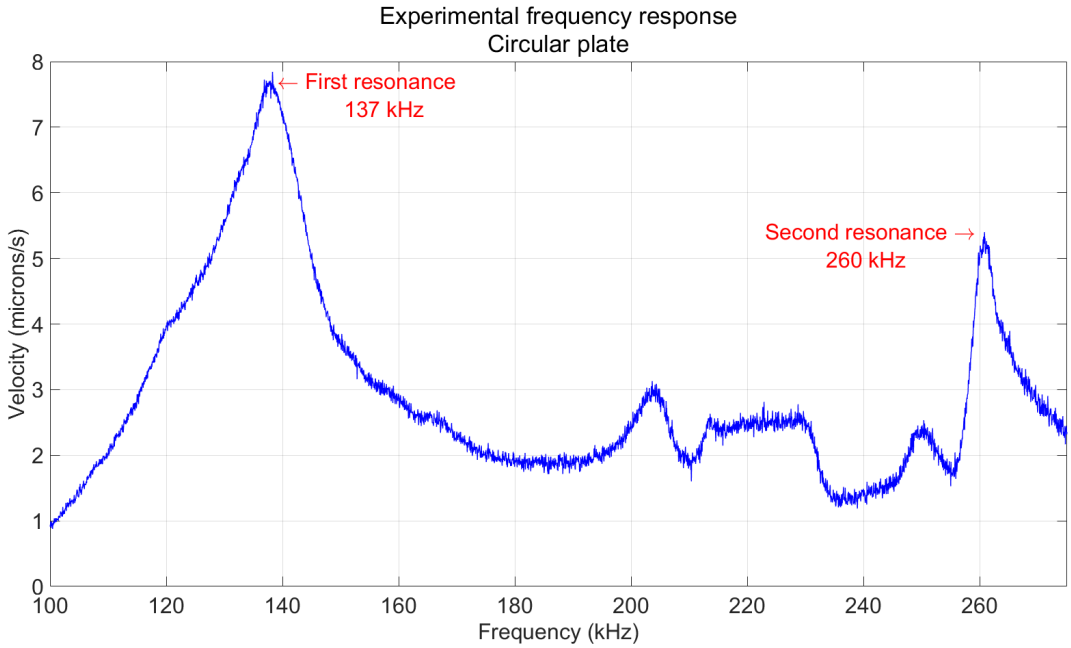

Figure 5.2: Frequency response for the circular plate under periodic chirp excitation from 100 kHz up to 275 kHz. The peak amplitude voltage supplied to piezoelectric chip 3V, offset 5V, velocity setting for the LDV 10 mm/s. The maxima identified as resonant frequencies have been labelled.

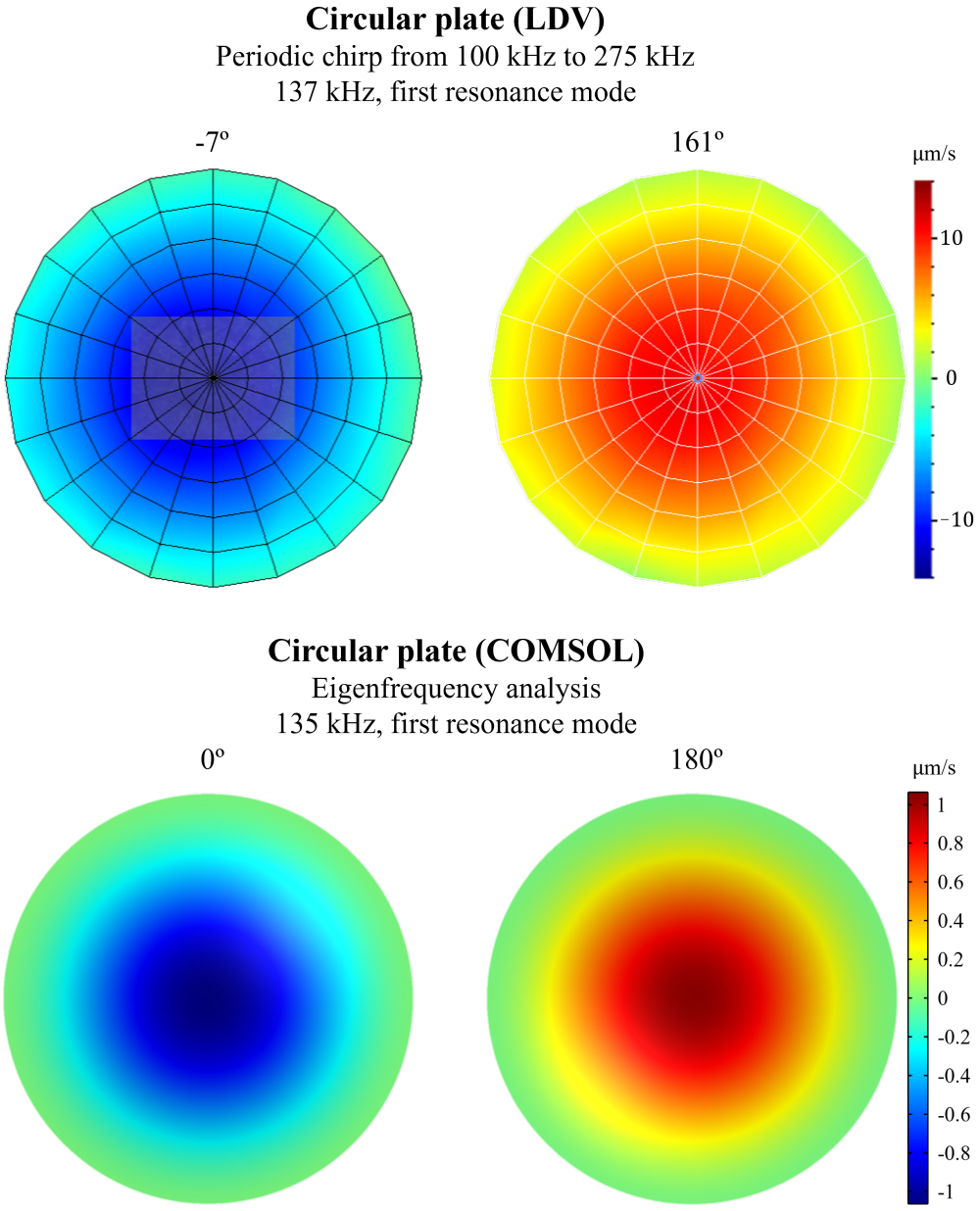

Figure 5.3: Comparison of LDV scans (top, 137 kHz) and COMSOL simulation with settings to match the 3D printed samples measured (bottom, 135 kHz) for the fundamental mode of a circular plate. Two stills of different phases are shown for each case to reflect the range of the eigenmode of the plate.

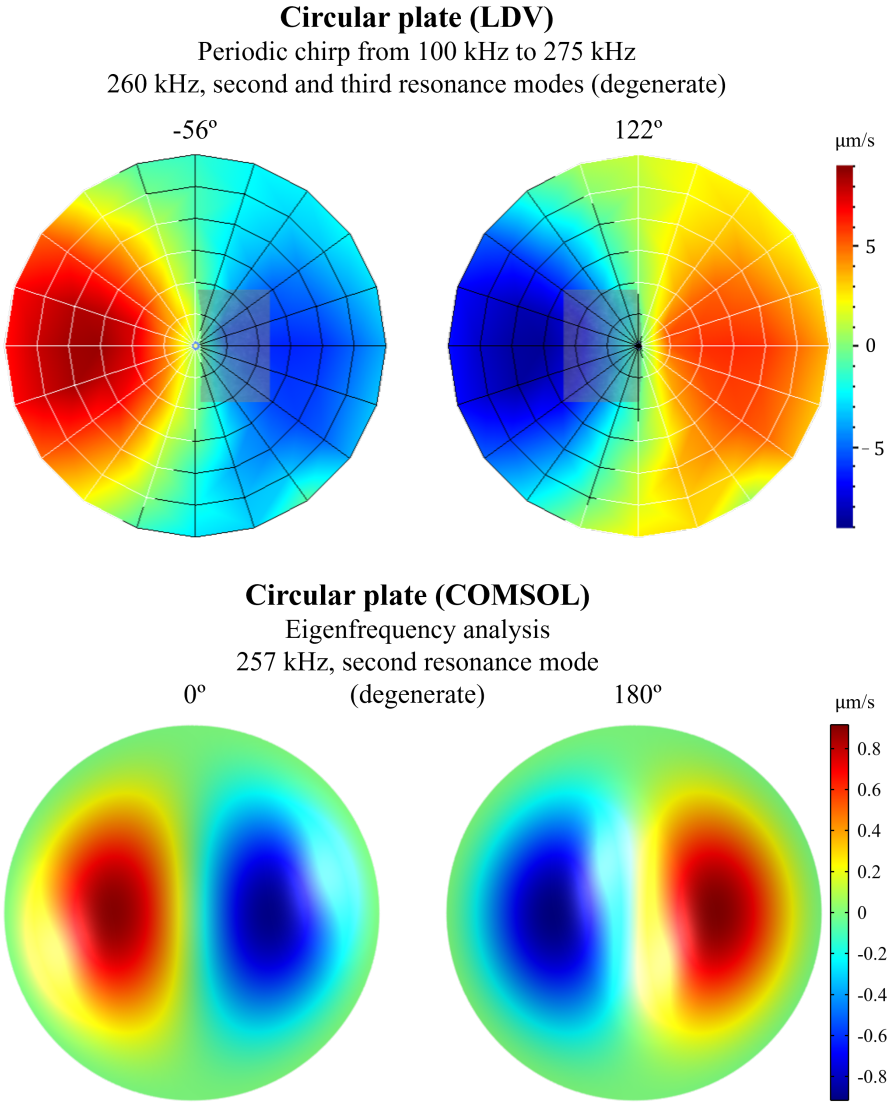

Figure 5.4: Comparison of LDV scans (top, 260 kHz) and COMSOL simulation with settings to match the 3D printed samples measured (bottom, 257 kHz) for the second resonant mode of a circular plate. Two stills of different phases are shown for each case to reflect the range of the eigenmode of the plate.

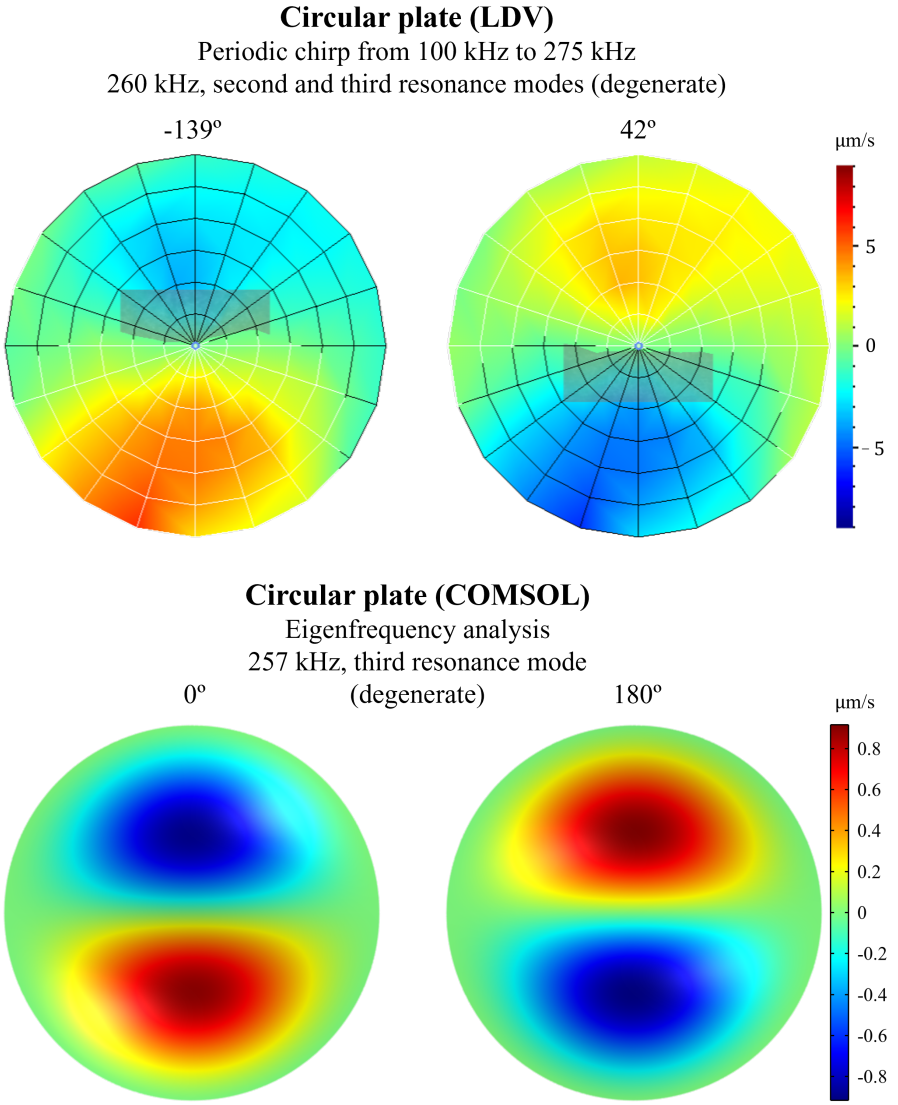

Figure 5.5: Comparison of LDV scans (top, 260 kHz) and COMSOL simulation with settings to match the 3D printed samples measured (bottom, 257 kHz) for the third resonant mode of a circular plate. Two stills of different phases are shown for each case to reflect the range of the eigenmode of the plate.

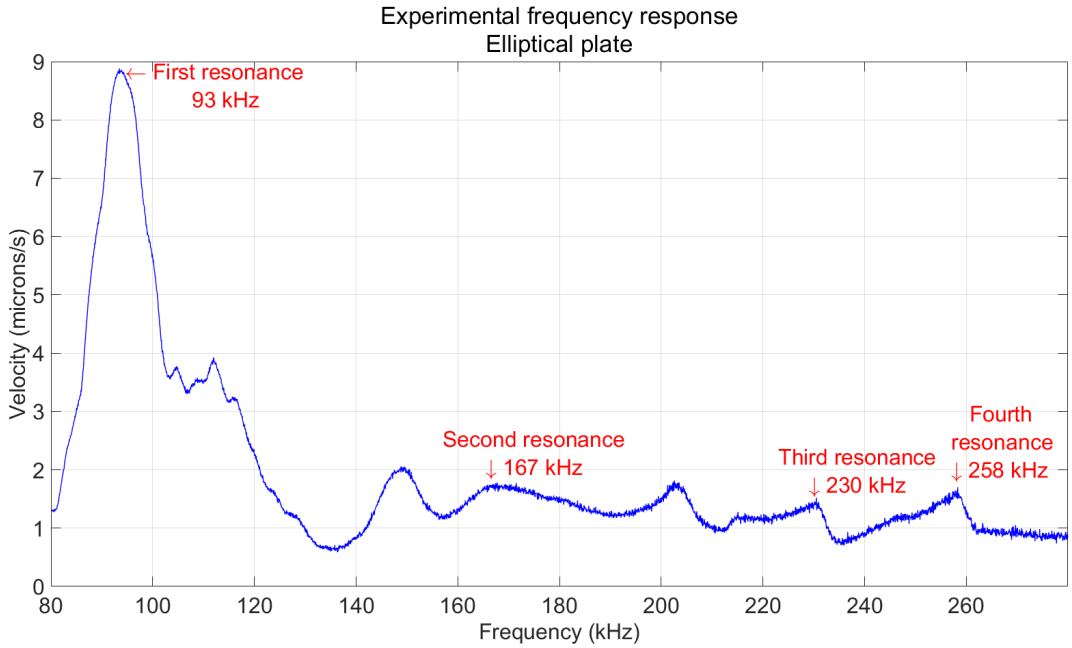

Figure 5.6: Frequency response for the elliptical plate under periodic chirp excitation from 80 kHz up to 280 kHz. The peak amplitude voltage supplied to piezoelectric chip 3V, offset 5V, velocity setting for the LDV 10 mm/s. The maxima identified as resonant frequencies have been labelled.

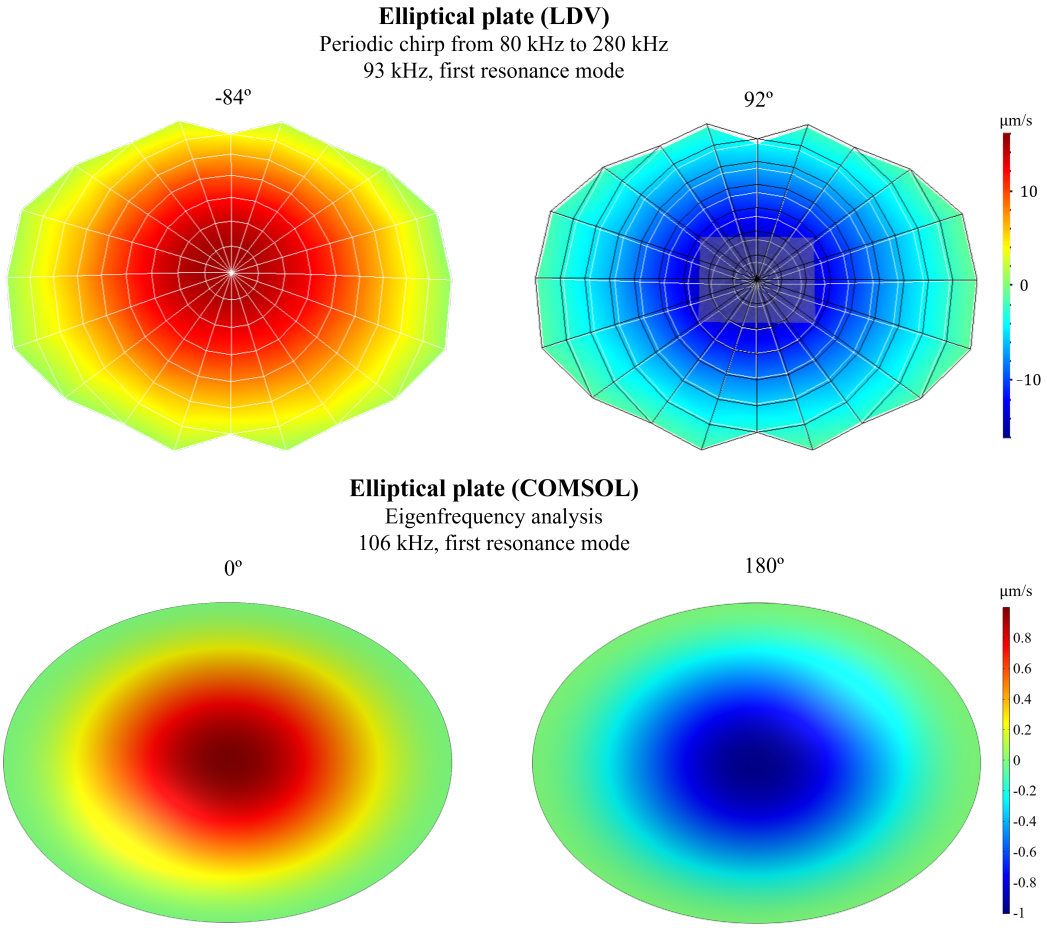

Figure 5.7: Comparison of LDV scans (top, 93 kHz) and COMSOL simulation with settings to match the 3D printed samples measured (bottom, 106 kHz) for the fundamental mode of an elliptical plate. Two stills of different phases are shown for each case to reflect the range of the eigenmode of the plate.

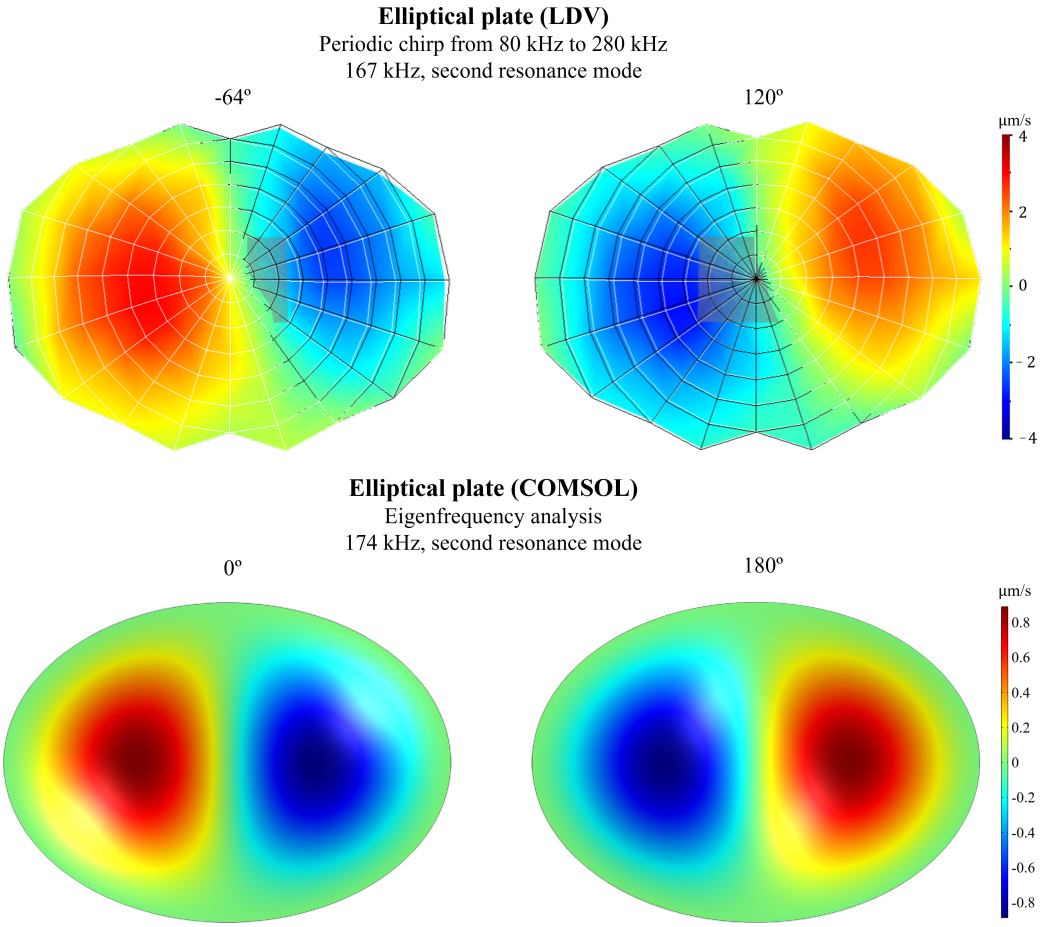

Figure 5.8: Comparison of LDV scans (top, 167 kHz) and COMSOL simulation with settings to match the 3D printed samples measured (bottom, 174 kHz) for the second resonant mode of an elliptical plate. Two stills of different phases are shown for each case to reflect the range of the eigenmode of the plate.

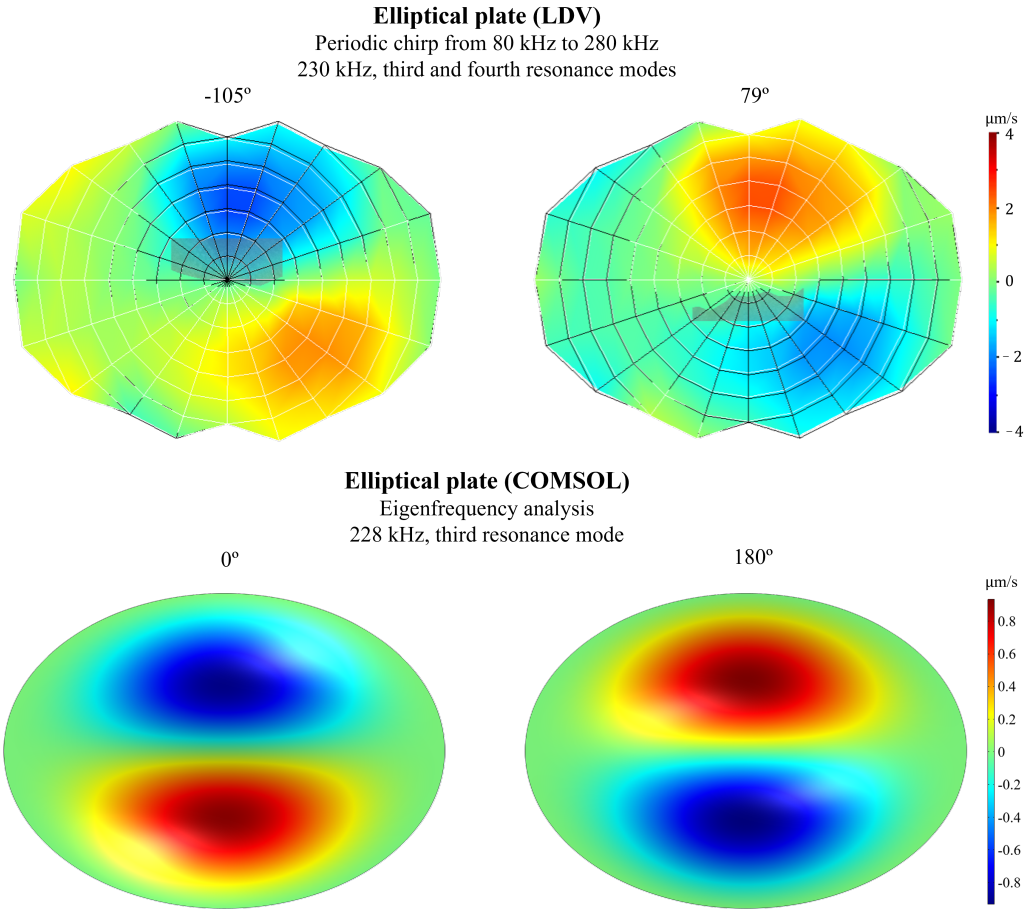

Figure 5.9: Comparison of LDV scans (top, 230 kHz) and COMSOL simulation with settings to match the 3D printed samples measured (bottom, 228 kHz) for the third/fourth resonant mode of an elliptical plate in what seems like a degeneracy or overlap of modes not predicted in simulation. Two stills of different phases are shown for each case to reflect the range of the eigenmode of the plate.

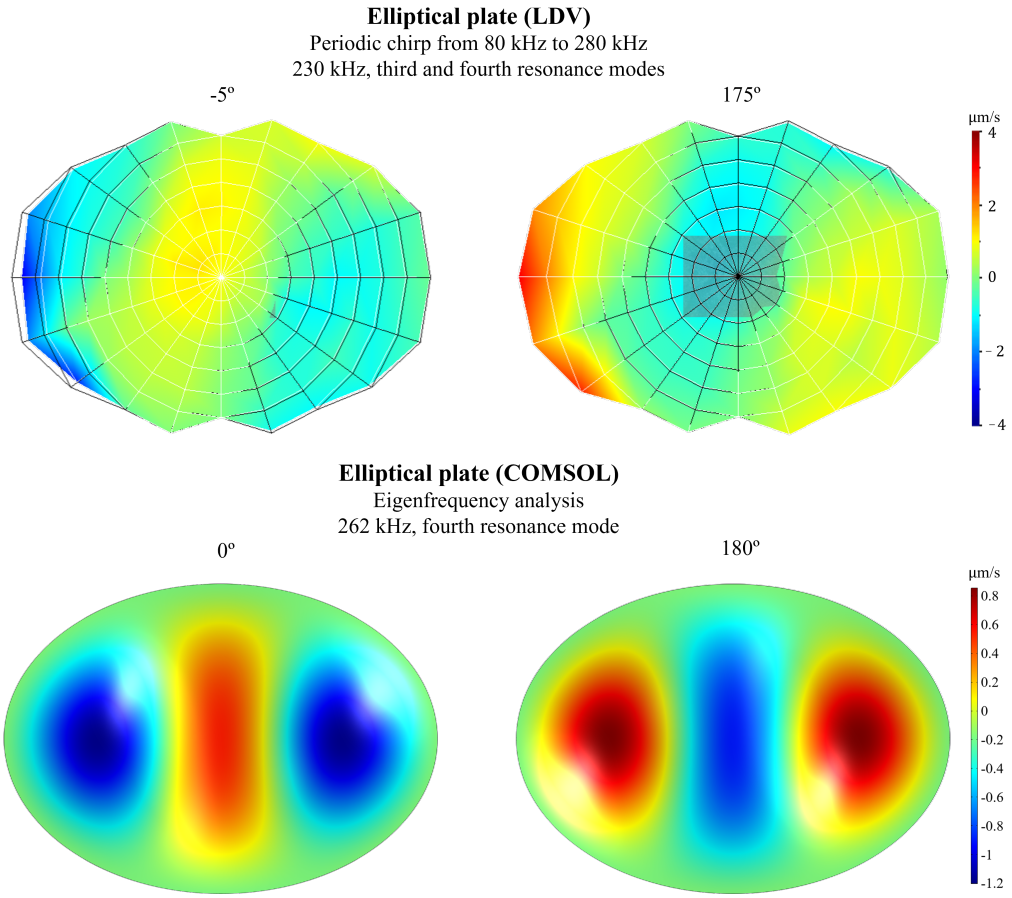

Figure 5.10: Comparison of LDV scans (top, 230 kHz) and COMSOL simulation with settings to match the 3D printed samples measured (bottom, 228 kHz) for the third/fourth resonant mode of an elliptical plate in what seems like a degeneracy or overlap of modes not predicted in simulation. Two stills of different phases are shown for each case to reflect the range of the eigenmode of the plate.

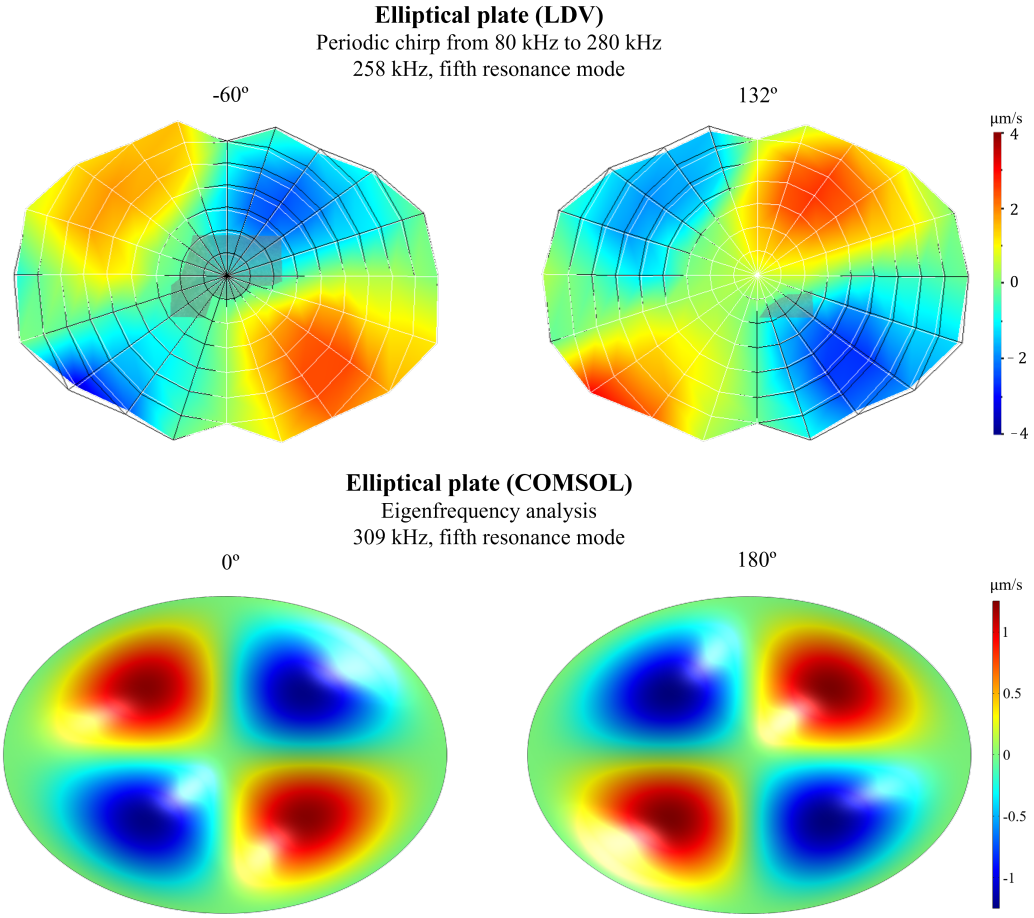

Figure 5.11: Comparison of LDV scans (top, 258 kHz) and COMSOL simulation with settings to match the 3D printed samples measured (bottom, 309 kHz) for the fifth resonant mode of an elliptical plate. Two stills of different phases are shown for each case to reflect the range of the eigenmode of the plate.

The resemblance of the fundamental and first harmonic are the clearest ones. There is an interesting effect in the mode thought to be the third one, and it is that it seems to show some overlap or superposition with what is expected for the fourth mode, with a big central maximum along the minor axis, at different phases for the same frequency. The frequencies at which each mode would be expected (228 kHz and 262 kHz respectively) are not so close to each other, so it is surprising to see this effect. At 258 kHz, the frequency that was initially believed to be the fourth resonance due to proximity to the expected value seems to better match the fifth mode, with two orthogonal nodal lines along the major and minor axes.

5.1.3 Elliptical double-thickness plates

Lastly, for the elliptical two-thickness plate, the frequency response extracted with the use of the piezoelectric chip and LDV can be seen in Figure 5.12, obtained from stimulation by a periodic chirp from 100 kHz up to 310 kHz. The first four resonant peaks found have been tagged in the graph. The experimental results fall within 3.5% of the eigenfrequencies predicted by COMSOL. The mode shapes now start resembling those observed and described for the moth tympanum and predicted by COMSOL, with the asymmetry from the two halves of different thicknesses displacing the nodal line found along the minor axis for the regular elliptical plate towards the thicker side. A comparison of the corresponding COMSOL eigenmodes can be side by side with the experimentally measured resonant modes in Figures 5.13 to 5.16.

5.2 Custom resin samples for directivity analysis

The setup for these experiments is the one detailed in section 3.5 and shown in Figures 3.13 and 3.14. Similarly to the previous section, Young's modulus of the custom mixed material was measured as explained in section 3.1.3 and found to be 46.3234 MPa (standard error 0.4769 GPa, sample size of 7). For the first sample, the plate has major and minor axes of 5.36 mm and 4 mm respectively; for the second, the dimensions are 6.55 mm across the major axis and 4.95 mm along the minor axis. Pictures of the 3D

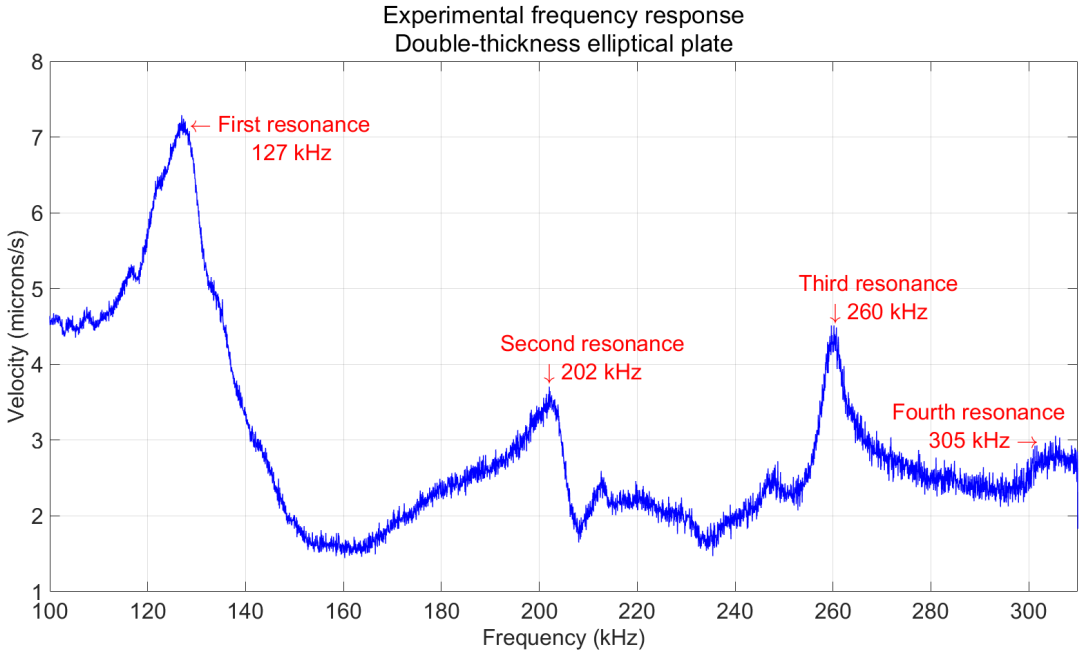

Figure 5.12: Frequency response for the double-thickness elliptical plate under periodic chirp excitation from 100 kHz up to 310 kHz. The peak amplitude voltage supplied to the piezoelectric chip is 5V, offset 5V, velocity setting for the LDV 20 mm/s. The maxima identified as resonant frequencies have been labelled.

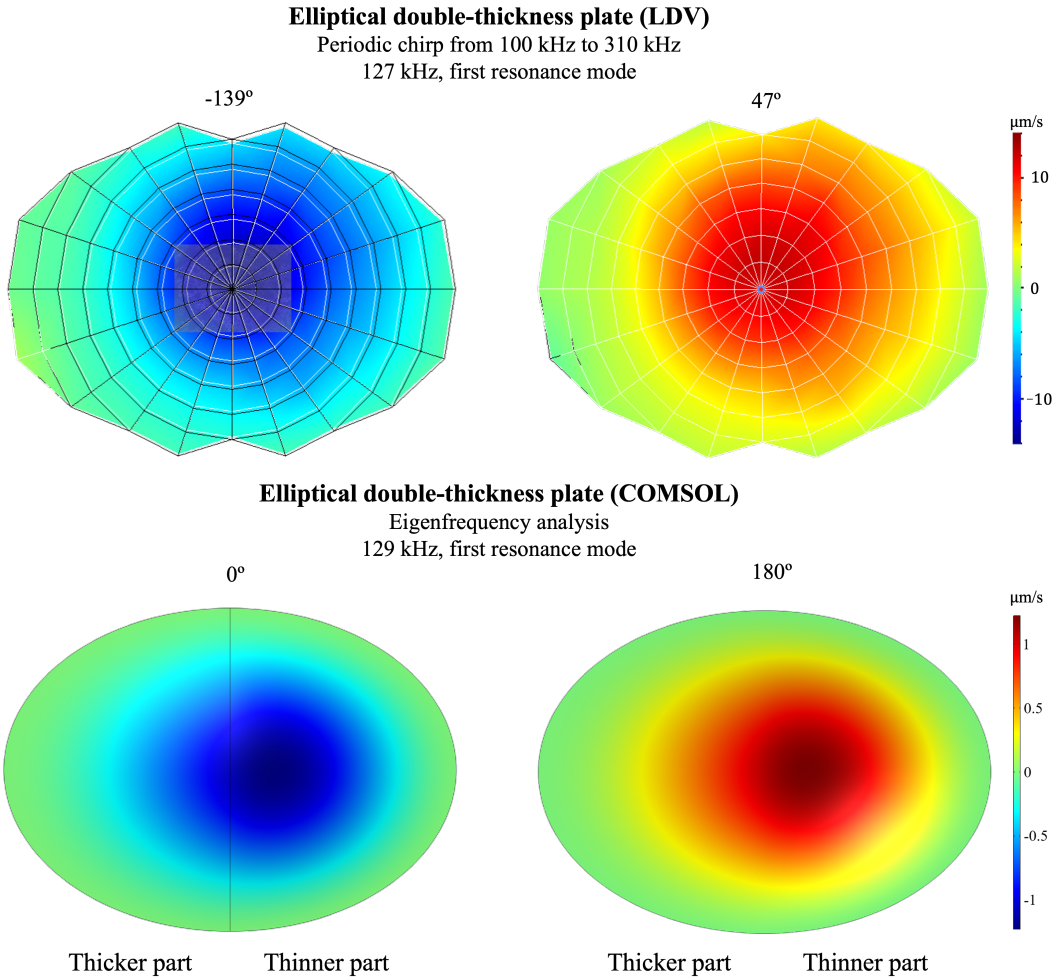

Figure 5.13: Comparison of LDV scans (top, 127 kHz) and COMSOL simulation with settings to match the 3D printed samples measured (bottom, 129 kHz) for the fundamental mode of an elliptical two-thickness plate. Two stills of different phases are shown for each case to reflect the range of the eigenmode of the plate.

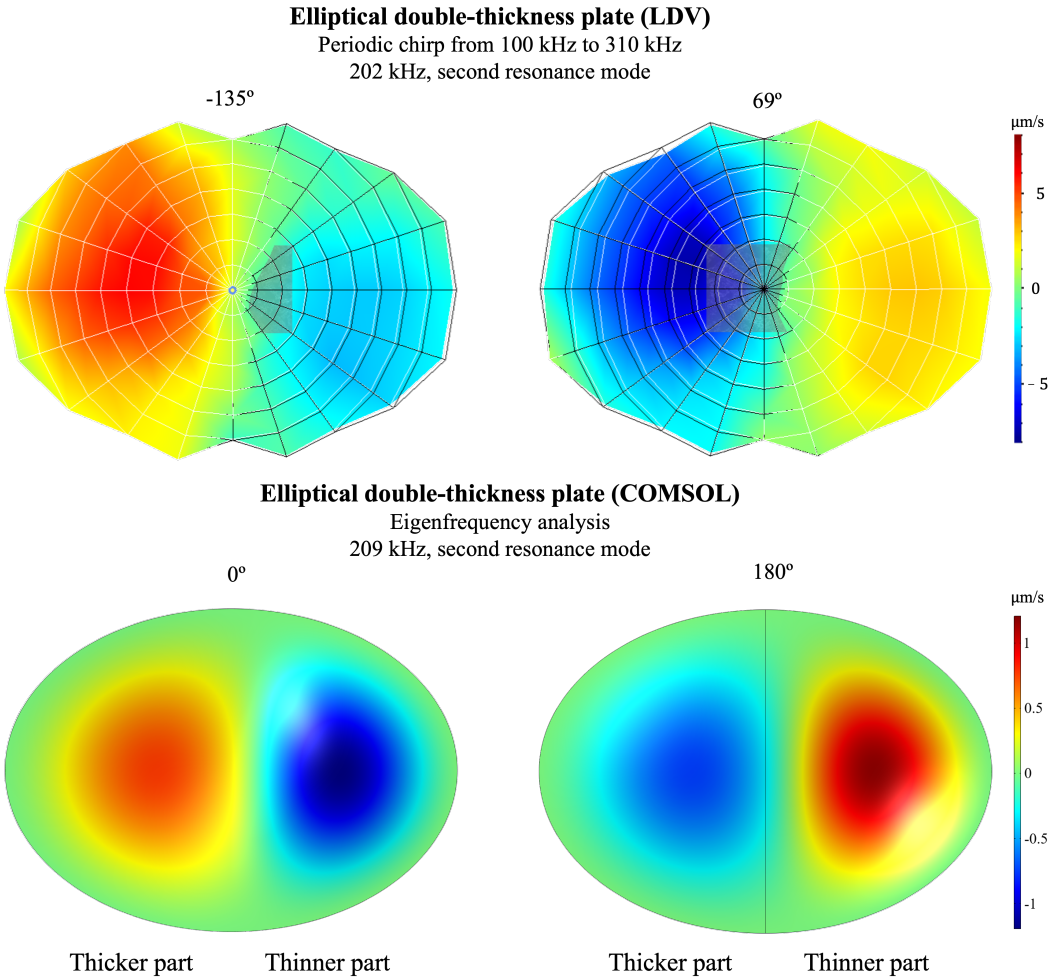

Figure 5.14: Comparison of LDV scans (top, 202 kHz) and COMSOL simulation with settings to match the 3D printed samples measured (bottom, 209 kHz) for the second resonant mode of an elliptical two-thickness plate. Two stills of different phases are shown for each case to reflect the range of the eigenmode of the plate.

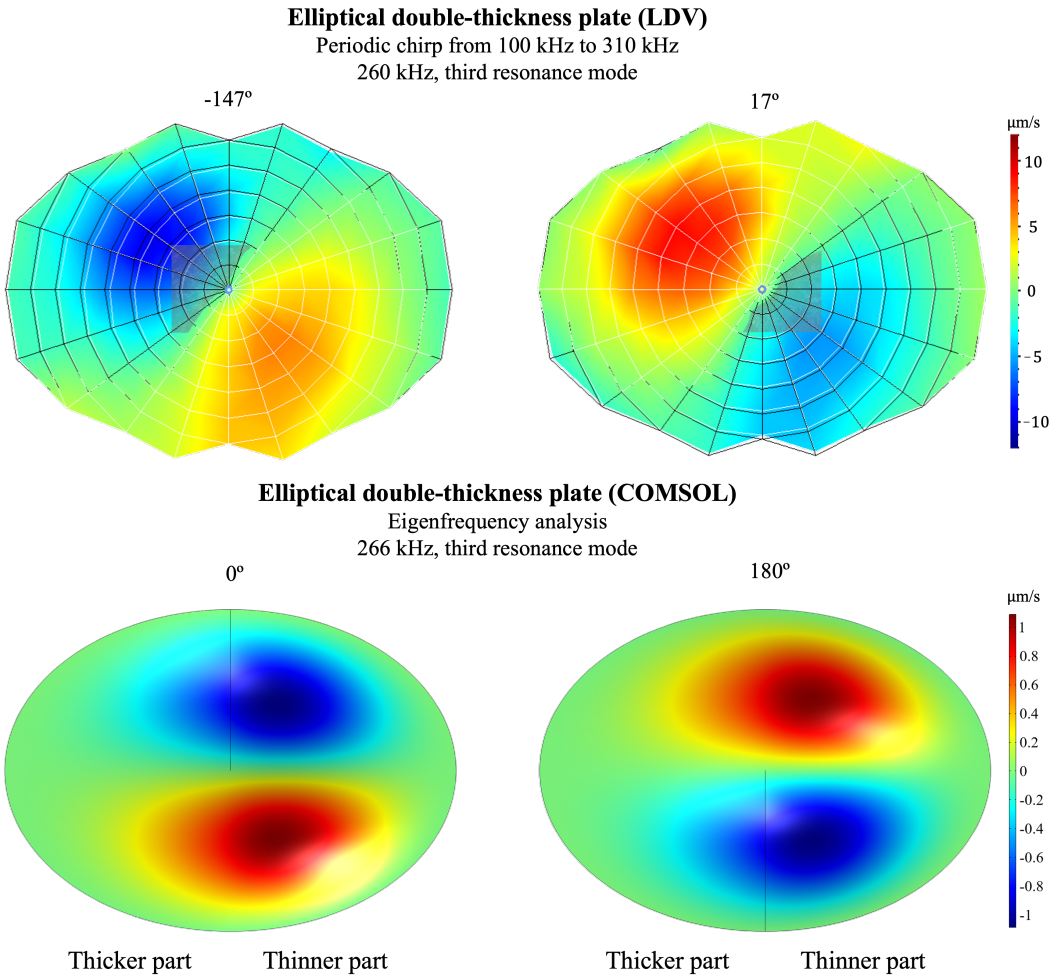

Figure 5.15: Comparison of LDV scans (top, 260 kHz) and COMSOL simulation with settings to match the 3D printed samples measured (bottom, 266 kHz) for the third resonant mode of an elliptical two-thickness plate. Two stills of different phases are shown for each case to reflect the range of the eigenmode of the plate.

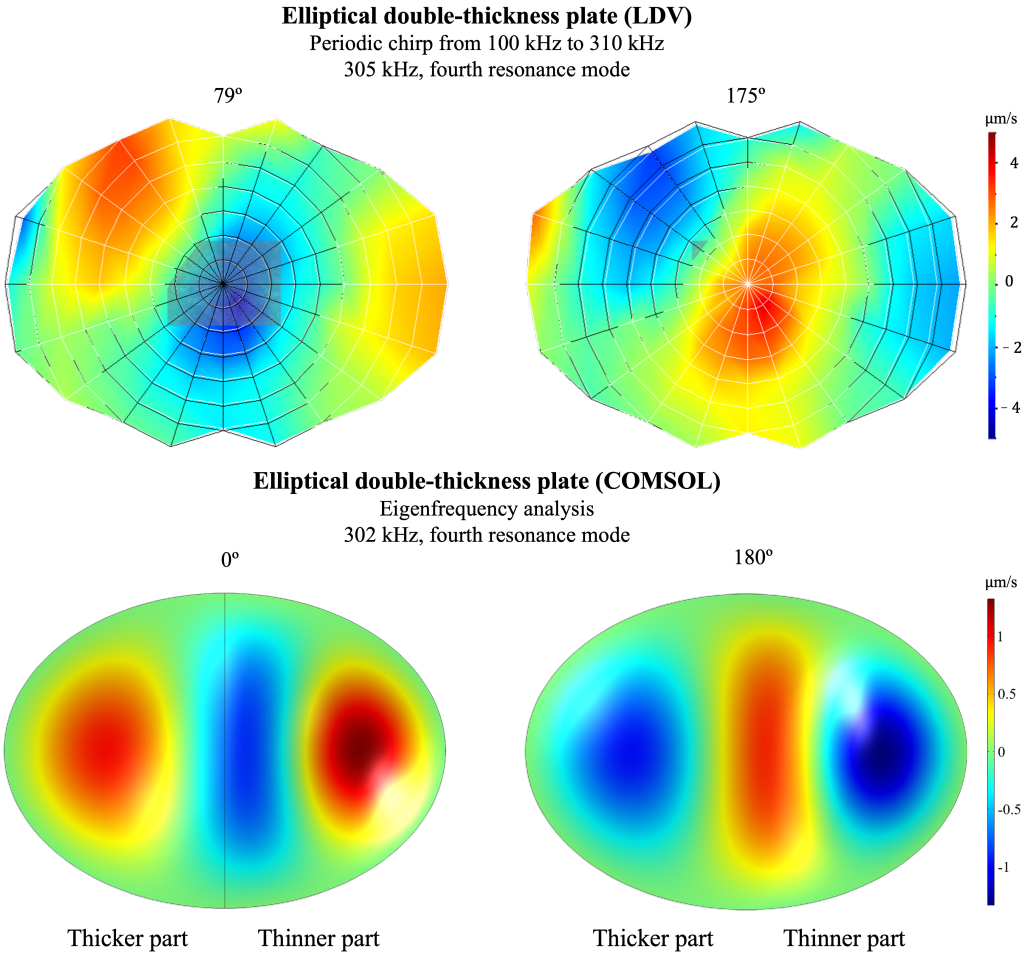

Figure 5.16: Comparison of LDV scans (top, 305 kHz) and COMSOL simulation with settings to match the 3D printed samples measured (bottom, 302 kHz) for the fourth resonant mode of an elliptical two-thickness plate. Two stills of different phases are shown for each case to reflect the range of the eigenmode of the plate.

printed samples can be seen in 5.1 C. The thicknesses of the custom resin plates were examined through μCT scanning and determined to be 122 microns for the single-layer half and 400 microns for the thick seven-layer half for the first sample, and 102 microns of thickness in the single-layer section and 259 microns of thickness in the triple-layer section for the second sample. Similarly to the commercial resin samples and for the same reasons, the layer thickness is larger than expected (50 microns and 25 microns respectively).

5.2.1 First iteration (lower resonances)

The piezoelectric chip was used initially to extract the frequency response of the plate printed with the new resin. A resulting spectrum is shown in Figure 5.17. With the LDV software, the resonant frequencies are identified by comparison with the mode shapes produced by COMSOL. The first two are found to be located at 3.01 kHz and 6.12 kHz respectively (tagged within the graph). COMSOL's prediction situates them at 4.65 kHz and 7.05 kHz, such that both are slightly higher in frequency.

Once the frequency response was obtained, the directionality response of the structures was measured. For this, the piezoelectric chip cannot be used to excite the plates, since the stimulus must be acoustic, at a distance and allow the structure (or stimulus) to be rotated. For this reason, the structures used a custom resin and slightly altered design, as explained in the methods. In this part of the work, only the elliptical two-thickness plates are considered, which is the model that is expected to provide the most directionality from simulations. The directivity patterns are produced by measuring displacement at the approximate attachment point, namely the centre of the thinner section. According to COMSOL, a switch in the directivity pattern is expected when exciting at the first and second resonant frequencies.

The resulting plots can be seen in a side-by-side comparison with the directivity plots produced by COMSOL. The shapes of the polar patterns are reasonably in agreement with the predictions by COMSOL. In the case of the first resonant frequency (Figure 5.18), a clear preference for the rear is seen; and in the case of the second frequency response (Figure 5.19), the preference seems to be towards the front, with a

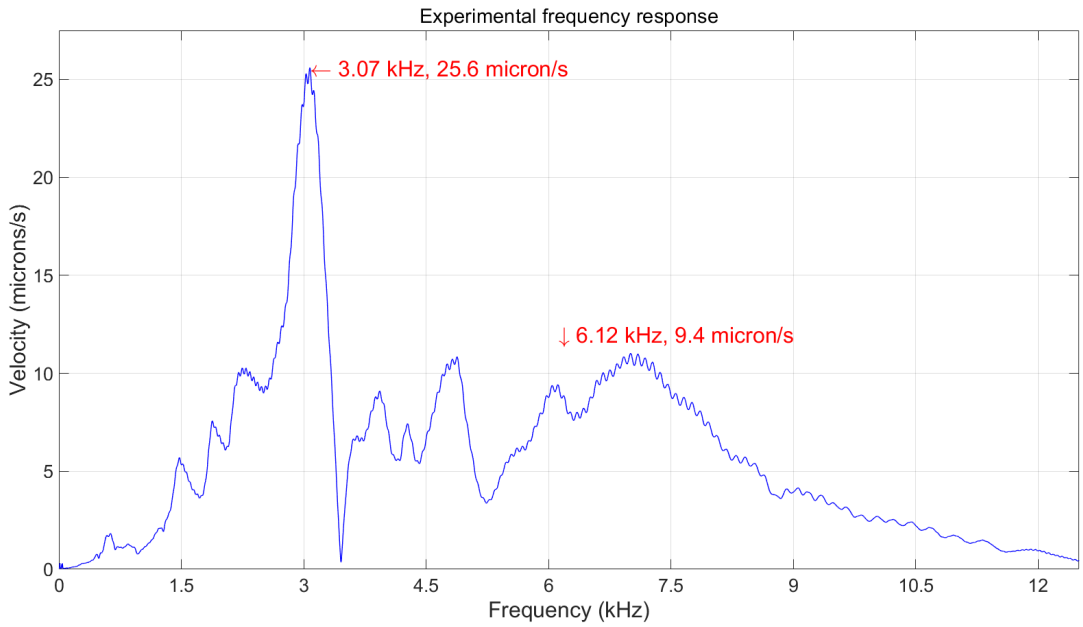

Figure 5.17: Frequency response for the double-thickness elliptical plate produced for the first iteration of directivity measurements, under periodic chirp excitation from 100 Hz up to 12.5 kHz. The maxima identified as resonant frequencies have been labelled.

slight narrowing that results in a small lobe pointing towards the back, such as the one present in the COMSOL simulation. The results prove that the elliptical two-thickness plates do show passive acoustic directionality due to their morphology and agree with the simulations set in COMSOL.

5.2.2 Second iteration (high-frequency resonance)

The results obtained with the Laser Doppler Vibrometer for the second sample can be seen in Figure 5.20. There is a large peak at approximately 1.7 kHz which is suspected to be a resonance of some element in the room; the reason for considering this point spurious is that this peak is present in many measurements of different setups and not just in this experiment. If the corresponding mode shape is observed, the whole structure can be seen vibrating up and down, as opposed to the actual relevant measurements where the edge remains significantly more fixed than the central part of the membrane. Such is the case of the maxima at 9.506 kHz and at 11.788 kHz.

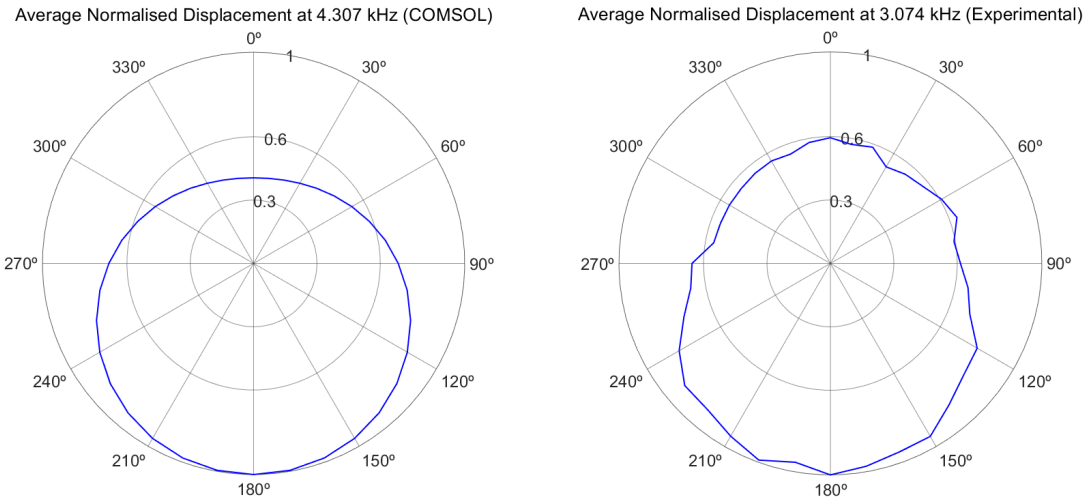

Figure 5.18: Directivity pattern of the two-thickness elliptical plate measuring at the approximate neuron attachment point at fundamental resonant frequency (left) simulated in COMSOL and (right) experimentally measured.

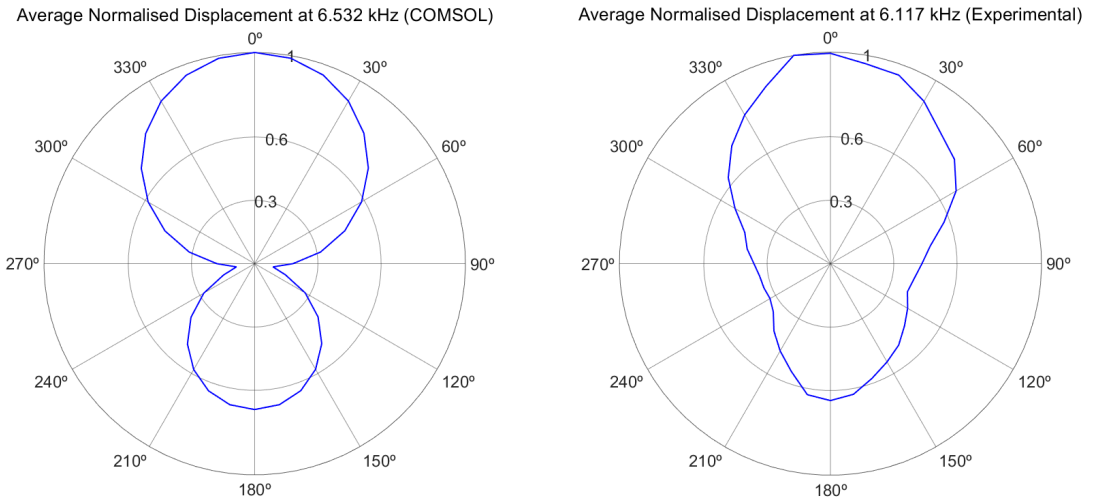

Figure 5.19: Directivity pattern of the two-thickness elliptical plate measuring at the approximate neuron attachment point at second resonant frequency (left) simulated in COMSOL and (right) experimentally measured.

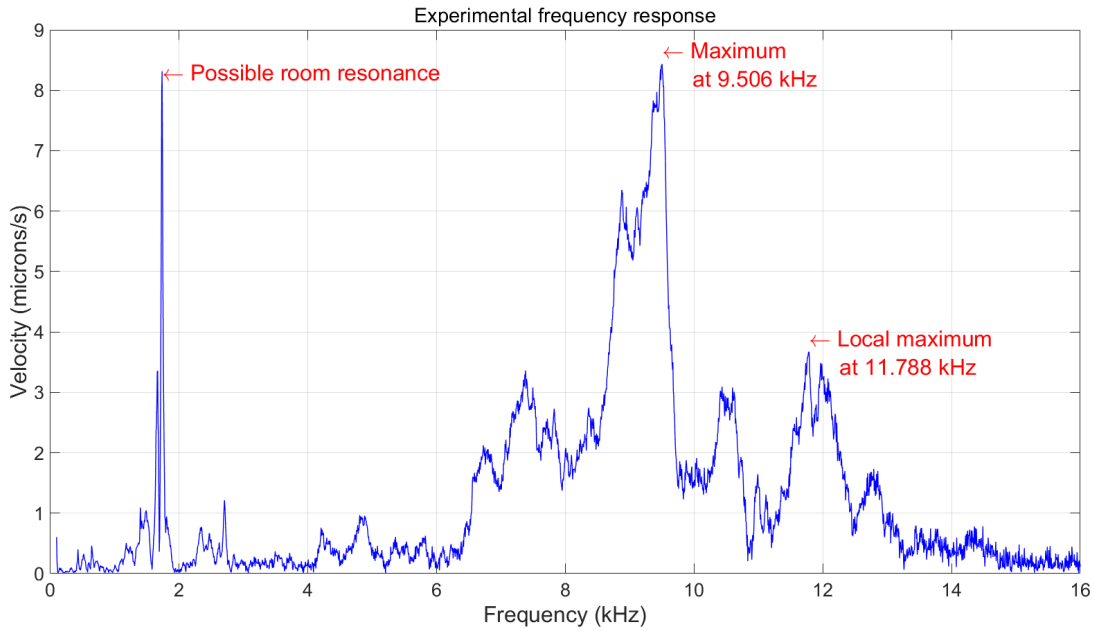

Figure 5.20: Frequency response of the second batch of elliptical two-thickness plates. A broadband periodic chirp from 100 Hz to 16 kHz produced by a speaker is used to excite the sample. The location of a spurious peak and the resonant frequencies for which directivity will be evaluated are tagged in red.

The COMSOL model is evaluated again with the parameters adjusted to fit the sample, in search of an eigenfrequency that is located close to the experimentally found resonant frequencies. In this case, the eigenfrequency 10.919 kHz is found. If the mode shapes for both resonant frequencies are examined and compared against the simulation, they are not found to agree in shape like those in the previous sections (see Figure 5.21). This can be due to the elements of the higher-order resonance not being adequately captured by the mesh of points for the LDV. Besides, the resonant peaks are both at a certain distance from the expected simulated eigenfrequency, one above and one below, so it can be the case that other resonances are filtering in and the mode is not so clearly identified. Lastly, local irregularities in the 3D printed sample, which are clearly seen under the microscope (see Figure 5.22) might affect the result too. An alternative manufacturing method might provide a more reliable result, but the cost and time of production would be higher.

The directivity responses for both 9.506 kHz and 11.788 kHz are examined in the way described in section 3.5. The simulated and experimentally obtained directivity patterns are then contrasted, a side-by-side comparison of the three can be seen in Figure 5.23. All patterns present lobes pointing to what corresponds to the sides of the moth (the setup is such that 0^{o} is where the head of the moth is pointing to and 180^{o} is the rear) and minimum response to sound coming from the front and back. The resulting patterns look like a sideways bi-directional or figure-8 pattern. The asymmetry and jagged edge on the experimental patterns can be due to misalignment of the setup and/or human error in the measurements. Nonetheless, the patterns show directionality and are in good agreement with each other.

The 3D printed sample shows passive acoustic directionality due to its asymmetrical morphology. It is seen that the experimentally measured directivity response reasonably agrees with what is expected from the simulations. Even though the pattern observed for the sample at this particular resonant frequency is not immediately advantageous for directional microphone manufacturing, it is positive to see such good agreement and a modification of the setup could potentially be suitable for directional microphone applications.

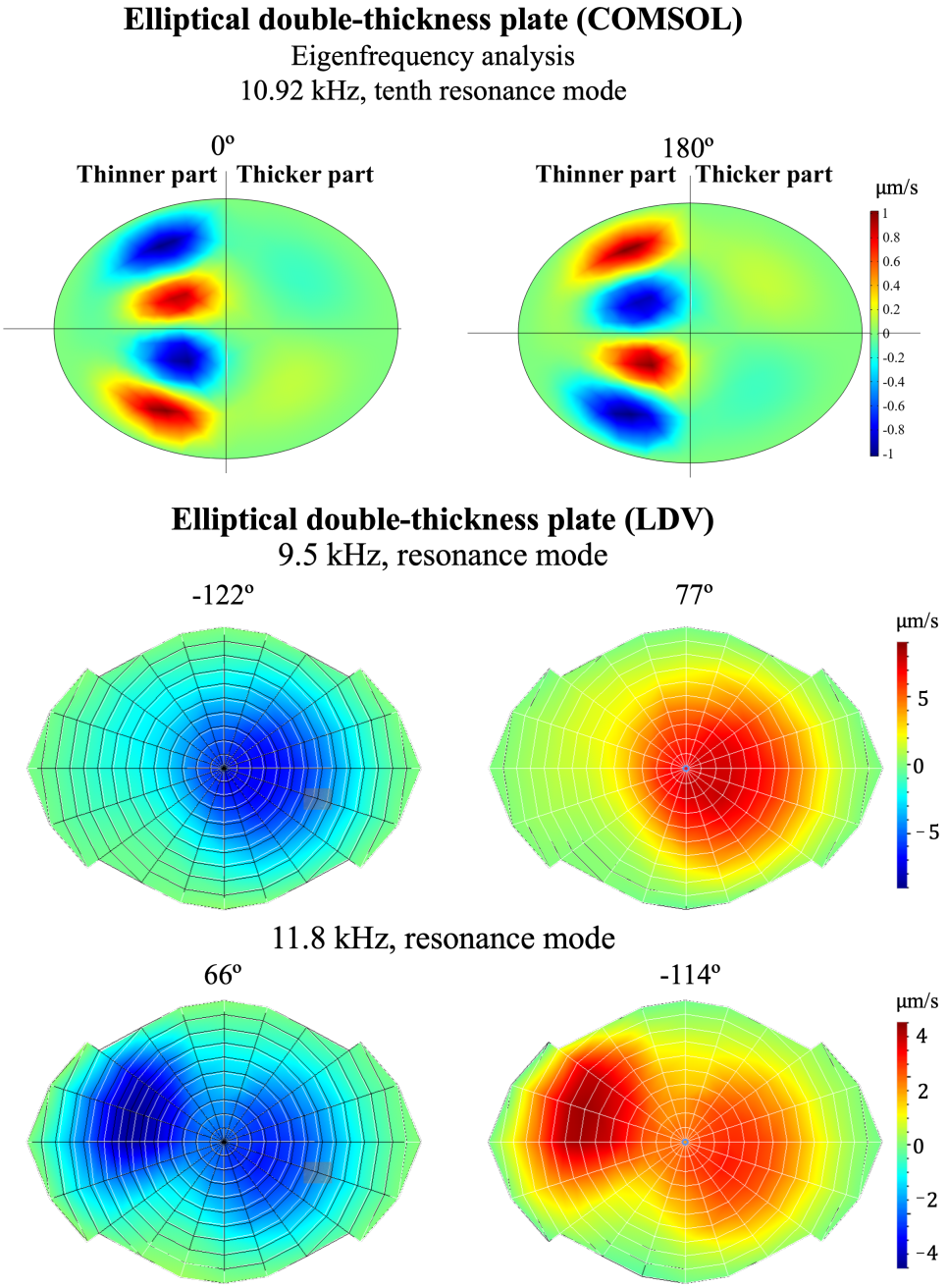

Figure 5.21: COMSOL and experimental comparison for the mode shapes found for the larger sample. The top two figures show two stills of opposite phases of the COMSOL-predicted eigenmode for 10.92 kHz. The bottom four figures show the resonant modes found in the 3D printed sample at 9.5 kHz and 11.8 kHz. For each frequency, two stills are shown to convey the range of the resonant mode. The mode shapes are not found to be in agreement.

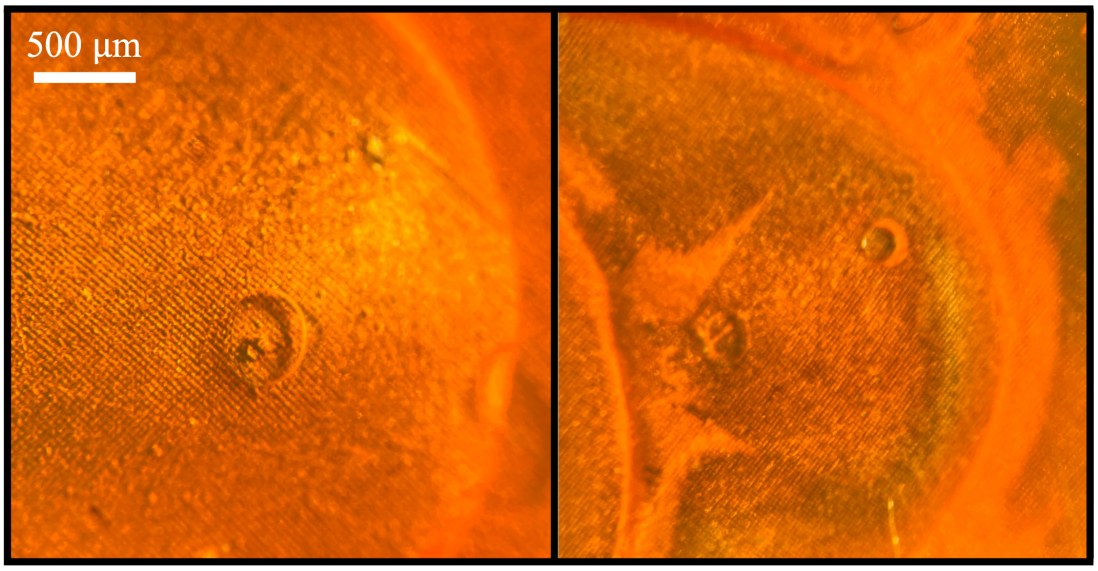

Figure 5.22: Local irregularities in two different samples as seen under the microscope.

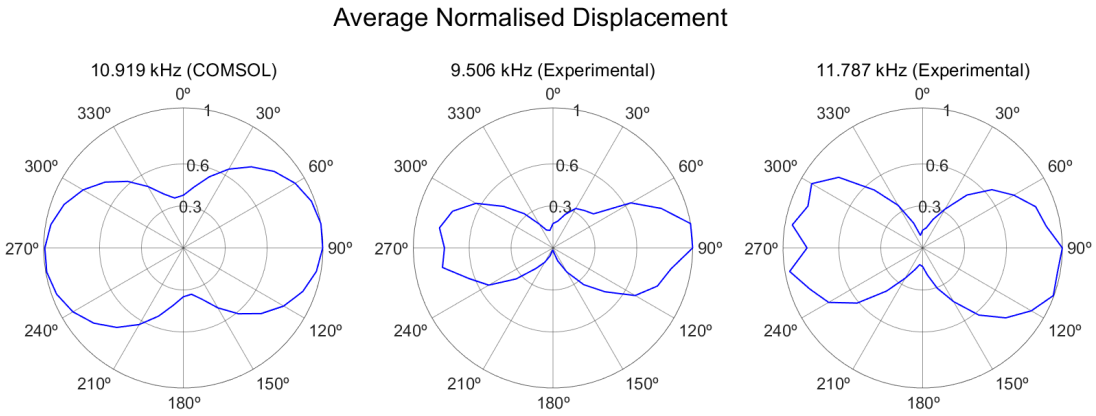

Figure 5.23: Directivity pattern of the two-thickness elliptical plate measuring at the approximate neuron attachment point (far left) simulated in COMSOL and (two on the right) experimentally measured. Higher-order resonant frequencies possibly correspond to the tenth resonant frequency.

5.3 Chapter summary

The results obtained from studying the frequency and directivity responses of different samples are discussed. The results are also compared to what was expected from simulations. The frequency responses match the simulations well. The two samples that are measured for directivity show directivity patterns that agree with those of simulations too. It is proved that elliptical asymmetric passive 3D printed structures show directionality at different frequencies.

Chapter 6

Conclusions and Future Work

6.1 Conclusions

Chapter 1 presented an introduction to the topic of the Thesis and discussed the motivation and objectives of the project. The objectives were described as developing a FEM simulation of the moth eardrum, investigating the directional response of the moth *Achroia grisella* and whether it can be due to the morphology of the eardrum, and applying the findings to 3D printing of parts that showed similar frequency and directivity response to those expected from simulation. All of these objectives have been accomplished and detailed in the rest of the Thesis.

Chapter 2 discussed the literature surrounding the topics relevant to this Thesis. General acoustics and microphones were reviewed, with a focus on MEMS technology. Vertebrate hearing, including human hearing, was discussed. Insect hearing and the main problems faced by insects, namely directional hearing, frequency discrimination, and low amplitude signals, were largely discussed. A detailed section on *Achroia grisella*, given that it is the main insect that this Thesis is concerned with, was also included. Bio-inspired sensors arising from the observation of insects were reviewed and contextualised according to what problem the solution that inspired them addresses.

Chapter 3 covered the methodology followed in this Thesis. The tools and techniques utilised are discussed at length, following the order in which the work took place. Firstly, the equations governing the simplest cases considered were detailed,

with a comprehensive resolution of the elliptical boundary for the model considered. The Finite Element Modelling software was described, as well as the steps followed to set up a model. The studies carried out in the FEM software were also detailed. 3D printing was discussed next, with a description of the different techniques employed and the materials used; it was followed by a brief description of micro-computed tomography, which allowed the examination of the samples produced. Lastly, a section on Laser Doppler Vibrometry was presented, where the principle of the technique is explained, and the laboratory setup is described.

Chapter 4 showed the results of the simulation model. It started with the simpler geometries, homogeneous, clamped all around, circular and elliptical plates, and compared them to the analytically predicted eigenfrequencies. Once the model was validated, it departed from the equations and into a greater similarity to the *Achroia grisella* eardrum. A novel model was then developed with an elliptical outline, clamped all around, with two sections of different thicknesses representing the *conjunctivum* and *tympanum proper*, and a mass-loaded point that at the same time accounts for the neural attachment and serves as measuring point for directivity plots. The eigenfrequencies and eigenmodes of the updated model were then studied, and one was identified as highly similar to the observations on live moths' eardrums.

The directivity of said eigenmode was evaluated and compared against measurements done on live *Achroia grisella* specimens and found to be in reasonable agreement too. The specimen's eardrum directionality showed a sharp response for sounds coming from the front, followed by a slightly lower response for sounds coming from the rear and a much lower response still for sounds coming from the sides. The simulation shows an almost bidirectional pattern, with a higher response to sounds coming from the front, slightly less from the rear, and a significantly lower response to sound coming from the sides (less so than measured in the specimen). Lastly, the model incorporated viscous damping through the modelling for the air domain and saw the likeness of the eigenmodes increase in comparison with the aforementioned measurements done on live moths.

Chapter 5 detailed the results of the experimental work carried out through the

3D printing of passive acoustic plates and the contrast against a COMSOL simulation altered to match the parameters corresponding to the 3D printing scale and physical characteristics of the 3D printable resins. Analogously to Chapter 4, the process started with the simplest geometries, contrasting homogeneous circular and elliptical 3D printed plates to the results from the analytical equations and COMSOL simulations. After a good agreement was found, the 3D printed parts and COMSOL model moved away from the equations and into a two-thickness elliptical plate, which was expected from simulations to show distinctive passive directionality patterns at the different resonant frequencies.

The eigenmodes were observed experimentally and compared against the simulations and then the directionality was measured at the approximate neural attachment point for the first two resonances. The patterns observed agree with those expected from simulation, the first one showing preference for the rear and minimal response towards the front, and the second showing a bidirectional pattern, with highest response to sounds coming from the front, minimum from the sides, and a smaller lobe pointing towards the back. A bigger sample was produced in an attempt to lower the resonant frequencies; a higher resonant mode was found and its directivity was examined, showing a sideways bidirectional pattern, with maximum response to sounds coming from the sides and minimum response to sounds coming from the front and back. The three resonant modes were found to agree with what was expected for the directivity from the simulations.

It is therefore concluded that *Achroia grisella* is conferred with some extent of directionality due to the morphology of their eardrum, as was proposed at the beginning of this Thesis. It is also concluded that passive structures can be 3D printed in the likeness of the moth eardrum and these show directionality in their acoustic responses.

6.2 Future Work

Both results Chapters (4 and 5) offer paths forward in their respective contexts. Several opportunities for future work arise from this Thesis:

- Chapter 4 sees a model of the moth eardrum come to life, and its eigenmodes, directivity and the effects of damping are examined. This model could be improved by including the body of the moth rather than considering the eardrum in isolation. The body could be approximated by a simplified shape (cylinder) or reconstructed from scans. Previous work with a simplified body morphology shows diffraction due to the ventral clefts in the moth's abdomen. This should be taken into account with the additional consideration of the upright position that the female moths adopt when walking, in which way they most commonly approach the male in the mating process (see Figure 6.1). Sound wavefronts are thus not perfectly perpendicular or parallel to the tympanum plane, and this is expected to have an impact on its response to sound.

- The COMSOL model would also greatly benefit from more precise values for the characterisation of insect cuticle. As it stands, the model uses values from the literature that are not specific for *Achroia grisella* and that provide a wide range of values. Characterisation of the moth's eardrum cuticle would allow to limit the values that are estimated and instead focus on other parameters that might affect the results.

- Regarding Chapter 5 and the 3D printed model, several advances could be made. In the first place, the passive plastic structures could incorporate a layer of piezoelectric material and be wired to provide an electrical response. That way, the passive model would be one step closer to becoming an acoustic sensor or transducer.

- Another element that could provide benefit would be the addition of a mass-load in the 3D printed design, accounting for the neural attachment, in what has been seen to affect the eigenmodes and directivity significantly.

- Another avenue of investigation is the superposition of two of these sensors, opening the possibilities to directional sensing in more than one axis, in a similar way to how some *Ormia ochracea*-inspired sensors have attempted the addition of diaphragms to consider an orthogonal axis for sound localisation.

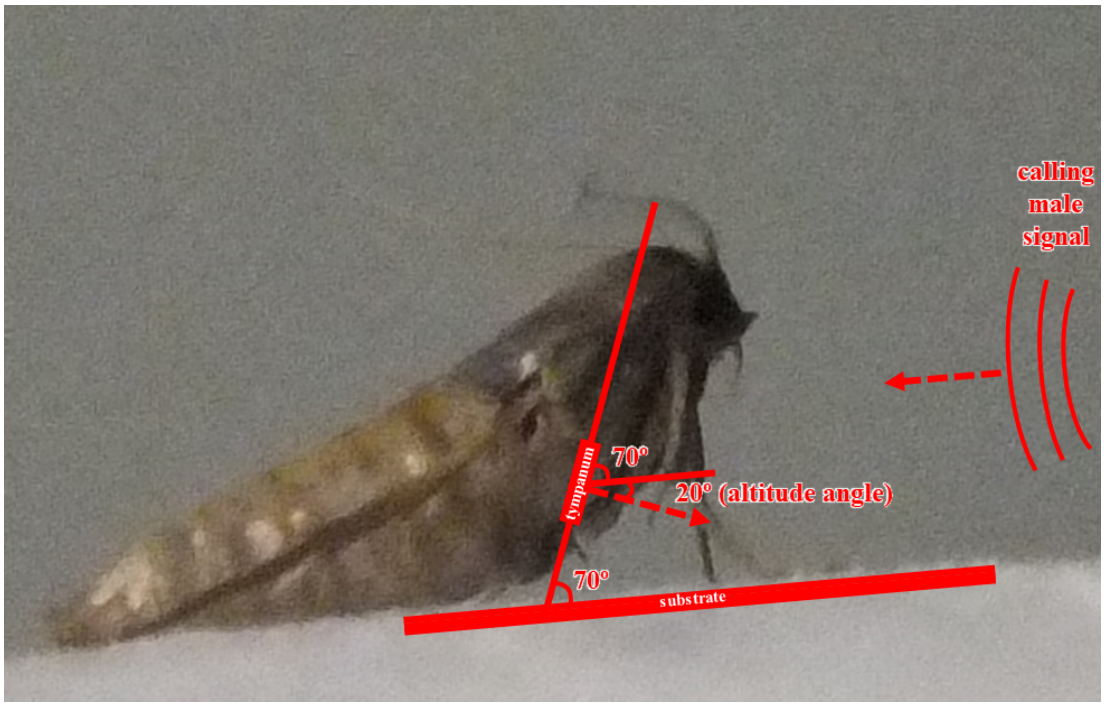

Figure 6.1: Female specimen of *Achroia grisella* standing on a substrate, showing the upright position adopted when walking. The approximate location of the tympanum is indicated, as well as the angle of incidence of the incoming male signal. Moth picture courtesy of Dr Andrew Reid.

Bio-inspiration has proved that basing new engineering solutions on nature provides innovative, outside-the-box ideas. In the current rapidly evolving world of small microphone technology, looking at insect hearing that has not been explored before could offer great rewards in terms of simplicity and effectiveness. 3D printing is an advantageous technique, both cheap and quick, for producing custom samples before committing to the development of a full product. All the improvements mentioned above in addition to the results presented in this Thesis could eventually lead to the moth *Achroia grisella* inspiring a novel miniature acoustic sensor for purposes such as smartphones or hearing aids.

Appendix A

IEEE Sensors 2021 proceedings paper

Towards a bio-inspired acoustic sensor: *Achroia grisella*'s ear

Lara Díaz-García*, *Student Member, IEEE*, Andrew Reid, Joseph Jackson, James F.C. Windmill, *Senior Member, IEEE*
Centre for Ultrasonic Engineering, University of Strathclyde, Glasgow, United Kingdom
* Corresponding author: lara.diaz-garcia@strath.ac.uk

***Abstract*— Bio-inspiration looks to nature to overcome challenges innovatively. Insects show many examples of efficient approaches to hearing considering the small sizes of their bodies. The nocturnal moth *Achroia grisella* is capable of directional hearing of wavelengths several times larger than the separation between its tympana. Directionality in this moth seems to be monoaural and dependent exclusively on morphology, so a model is developed to replicate the structure. We start from a simple circular model, progressively incorporating more complex elements to improve the resemblance to the natural system. The goal is to develop a model inspired by *Achroia*'s ear, that behaves similarly to it, and to 3D print devices that agree with the model. Equations, simulations, and 3D printed devices measured through Laser Doppler Vibrometry are compared.**

Keywords*— bio-inspiration; Achroia grisella; insect hearing; 3D printing; acoustic sensor

I. Introduction

Hearing is an important ability through which many animals interact with their environments. Localizing the stimuli source is key for tasks such as avoiding predators, locating preys, or finding a mating partner, some of the principal purposes for which hearing is used. Directional hearing is, therefore, a desirable trait. All animals that hear (except for mantids) present bilateral symmetry in their bodies, which means most of them have one ear (in the broader sense of the word) in each half of their bodies. Bigger animals can achieve directional hearing by comparing intensity, phase, or time of arrival between their two ears, but smaller animals, for which the inter-ear distance is too small for any of these differences to be meaningful, must resort to alternative, inventive methods to locate the origin of sounds [1].

Insects' bodies sizes are generally small. Not all of them possess a hearing sense that we know about, but some have found a way around the size limitation to hear frequencies with wavelengths of the same scale as their bodies. Some have different openings in their tracheal system to the outside in order to allow soundwaves to arrive to the outside and inside of their tympana, like grasshoppers [2] or field crickets [3]. Others, like the well-studied *Ormia ochracea*, have a stiff tissue bridge between their two tympana, making the whole system behave in a complex way with different resonances that allows them to land on their host with a 2º precision, even when the frequency of the host call is considerably larger than the fly's size [4]–[7].

Achroia grisella is a pyraloid moth that is uncommon in that its mating process involves the male calling the female through ultrasonic signals. Even though hearing is widespread in the *Pyraloidea* superfamily, interspecific acoustic communication is uncommon [8]. Their rudimentary hearing system is believed to have evolved to avoid their main predator, the bat, and later repurposed [9]. *Achroia*, when exposed to a bat's echolocation call, drops towards the ground if flying or stops moving completely if walking. On the other hand, during the mating process, male specimens produce a series of ultrasound pairs of pulses (main content of the signal of 100 kilohertz [10]) that the females orientate towards not optimally but efficiently enough to guarantee mating. The moths have only 3 neurons per tympanum, and they have been proven unable to discriminate frequencies. The threshold of the stimulus signal for different behavior (evasive or positive) in the moth is thus believed to be time-encoded [11]. *Achroia grisella*'s average size means that their tympana are separated less than 600 microns. This distance is insufficient to account for any phase, intensity, or time of arrival difference between their ears considering a 100 kilohertz signal has a wavelength of 3.8 millimeters. On the other hand, no connection has been detected between the tympana using X-ray scanning, no spiracles are found either [12], and the measurements of diffraction in the abdominal section of the moth do not provide enough intensity difference [13]. Furthermore, moths with one tympanum pierced and the other one in healthy condition were still able to locate the singing males, if only taking a longer time [14]. It is therefore believed that the directionality must be achieved monoaurally and purely through the geometry of the tympana themselves.

II. Analytical and Simulation Approach

Our working hypothesis is that the *Achroia grisella*'s tympanum must confer them with some degree of directionality. We start by posing a simple model and progressively increasing its complexity by adding new elements to it. The problem is considered through Finite Element Modelling (FEM) using COMSOL Multiphysics® and analytically.

Achroia grisella's tympana are roughly elliptic in shape, divided in two sections of different thicknesses (the thicker one called *conjunctivum* and the thinner one called tympanic membrane or *tympanum proper*), and have the *scolopidium*, a cluster of three periphery neurons, directly attached somewhere close to the center of the thinner region (Fig. 1). Through Laser Doppler Vibrometry, an *Achroia* tympanum is observed when exposed to a signal of 100 kilohertz. The displacement pattern of the membrane is complex and not drum-like. A large peak dominates the displacement close to the neuron attachment point; a series of secondary peaks

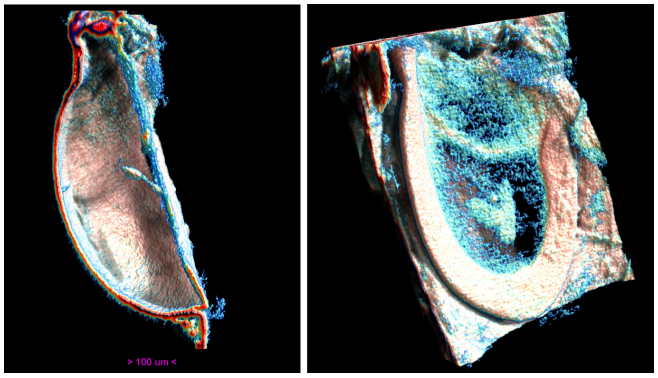

Fig. 1. Voxel reconstruction of Achroia grisella tympanum from X-ray microtomography. (Left) Side view cross section along major axis showing tympanal cavity and scolopidium. (Right) Tympanum face showing attachment point and ridge connecting upper and lower membranes.

appear in a ring formation around the main peak; and a very broad, low amplitude bump is seen in the *conjunctivum* [15].

To obtain an analytical solution, we consider the equation for transverse vibrations on a plate:

$$\nabla^2(\nabla^2 W) + \frac{1}{c^2} \cdot \frac{\delta^2 W}{\delta t^2} = 0 \qquad (1)$$

Where $\nabla^2\nabla^2 = \nabla^4$ is known as the biharmonic operator, $W = W(x, y, t)$ and describes displacement, and c is the velocity of the wave in the medium and is defined as:

$$c = \sqrt{\frac{E \cdot h^2}{12 \cdot \rho \cdot (1 - \nu^2)}} \qquad (2)$$

The parameters being Young's modulus (E), thickness (h), mass volume density (ρ), and Poisson's ratio (ν). The resolution of equation (1) gives us the eigenvalues for the problem which in turn are related to the natural frequencies of vibration of the plates. The reason we consider plates and not membranes is because stiffness is not negligible.

By assuming a periodical dependence on time, we can simplify the equation and solve for the specific boundary conditions of our problem. We consider plates clamped all around, such as is the case of the moth's tympana. The sizes considered both for the equations and simulations are approximated from measurements on actual specimens of *Achroia grisella* [15]. The values for Young's modulus, mass volume density, and Poisson's ratio are taken to be 1 gigapascal, 1180 kilograms per cubic meter and 0.35, all within the range of values for insect cuticle. Young's modulus is chosen in the lower end of the range of values for sclerotized cuticle. [16]

A. Circular plate

The first model is a circular plate in vacuum. This model is easily solved and simulated, and the first six eigenfrequencies and their corresponding mode shapes are obtained. The circular plate considered is 500 microns in diameter and 5 microns in thickness. We use polar coordinates, and the resolution involves Bessel functions. There is a good agreement between COMSOL and predicted eigenfrequencies, with differences below 1%.

B. Elliptical plate

The next step is considering an elliptical solid plate, which complicates the analytical solution significantly because elliptical coordinates and Mathieu functions need to be used [17], [18]. The elliptical plate has major and minor axes of 670 and 500 microns respectively, and a thickness of 5 microns. The resonance frequencies in the elliptical plates are related to the eigenvalues obtained from the application of the clamped boundary conditions at the perimeter of the ellipse:

$$f_{m,n} = \frac{2 \cdot q_{m,n} \cdot c}{\pi \cdot (a^2 - b^2)}, m = 0,1,2 \ldots, n = 1,2,3 \ldots \qquad (3)$$

Where the resonance frequencies ($f_{m,n}$) depend on the eigenvalues ($q_{m,n}$), the velocity of the wave in the medium (c) and the major and minor semi-axes of the ellipse (a and b respectively). There is also good agreement between COMSOL and predicted eigenfrequencies, with differences below 7%. The patterns of vibration of this and the previous model are still far from resembling the moth tympanum's movement.

C. Elliptical plate: double thickness and point mass

The next step is considering an elliptical plate divided in two different sections with thicknesses matching those of the thin and thick regions, and an attached point mass on the thinner region, to emulate the neuron attachment. The mass is estimated to be that of the whole plate concentrated on one point. At this point, with the increasing complexity of the model, analytical equations are no longer useful, but the good agreement in the previous two steps between analytical and simulation models is a reassurance that the COMSOL predicted eigenfrequencies are reliable. The division between regions in the model is 350 microns along the major axis for the thinner region and 320 microns for the thicker one, and the attachment point is located at the center of the thin region (175 microns from the center of the major axis of the ellipse). The thicknesses are 3 and 8 microns respectively.

The vibration pattern of this model has visibly changed and is more complex. The sixth mode shape (see Fig. 2) is a very good match for that described in *Achroia grisella*'s tympana [15]. The frequency response of the plate is extracted from a frequency analysis of the system on COMSOL and can be seen in Fig. 3.

III. Methods

3D printing is carried out using an Original Prusa SL1 3D printer and a commercial resin. This printer employs stereolithography technology, and the resin used is Prusa's own Orange Tough, modelled after Acrylonitrile-butadiene-styrene. The thickness of the printed layers in stereolithography depends on exposure time to UV light [19].

The physical properties of the resin are taken as a Poisson's ratio of 0.35 and volumetric mass density of 1180 kilograms per cubic meter [20]. Young's modulus is measured by printing a cantilevered beam of known dimensions and observing its frequency response. Considering beam theory [21], Young's modulus for the material can be extracted from:

$$E = \frac{48 \cdot \pi^2 \cdot \rho \cdot f_n^2 \cdot L^4}{\lambda_n^4 \cdot h^2}, n = 1,2,3 \ldots \qquad (4)$$

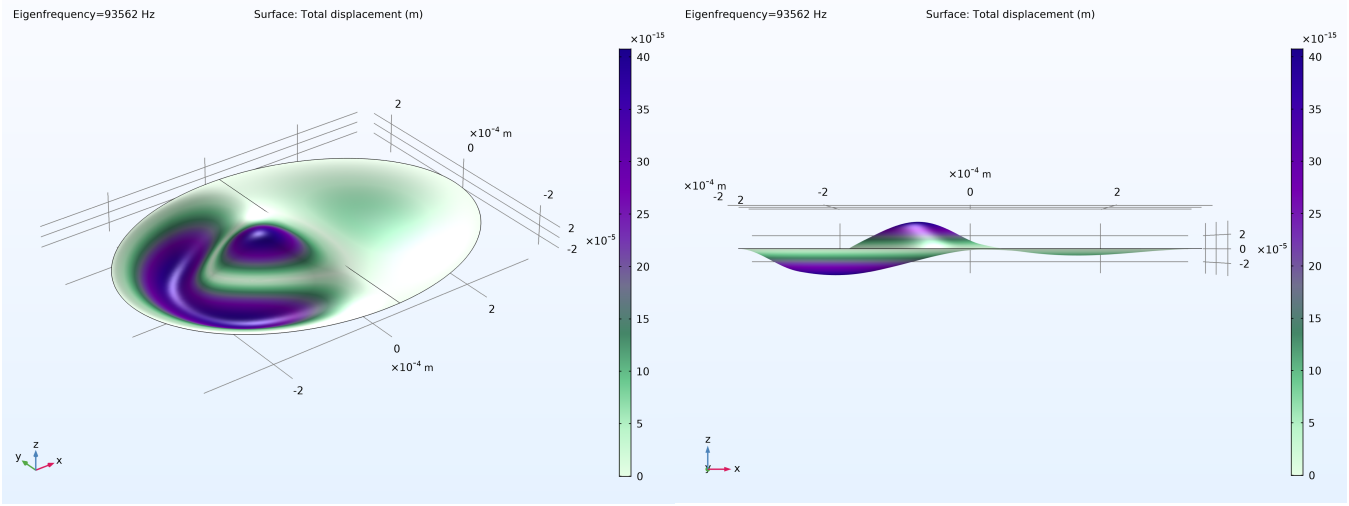

Fig. 2. COMSOL simulation of the sixth natural frequency of an elliptical plate divided in two sections of different thicknesses (thin one on the left half of the ellipse and thick one on the right) with an attached mass (perspective view on the left and XZ plane view on the right).

Where the parameters are Young's modulus (E), mass volume density (ρ), the eigenfrequencies (f_n), the length of the beam (L), the eigenvalues (λ_n) and the thickness (h), all of them known. The value experimentally estimated for Young's modulus is 1.327 gigapascals. The printing size is larger than that of the moth's tympanum. The plates produced have a diameter of 1.5 millimeters for the circular one and major and minor axes of 2.1 and 1.5 millimeters respectively for the elliptical ones. The thickness was measured through X-ray Computer Tomography using a Bruker Skyscan 1172 with SHT 11-megapixel camera and Mamamatsu 80 kilovolts (100 milliamps) source and found to be 162 microns for single layers and 270 microns for the thicker multi-layer regions. It is worth mentioning that 3D printing of small devices is complicated, with residual stress gradients severely affecting the result [22]–[25]. Repeatability and accuracy can be difficult to achieve.

The printed devices are examined in a 3D laser Doppler vibrometer (3D LDV) system with an MSA-100-3D scanning head (Polytec, Waldbrom, Germany). The devices are stimulated with a displacement piezo chip (75 volts, 2.8 microns, Thorlabs, Newton, New Jersey), with wideband periodic burst signals, and their frequency response is recorded. The resonances are found in the LDV scan and compared against the COMSOL simulation eigenfrequencies, re-run with parameters that match those of the 3D printed devices.

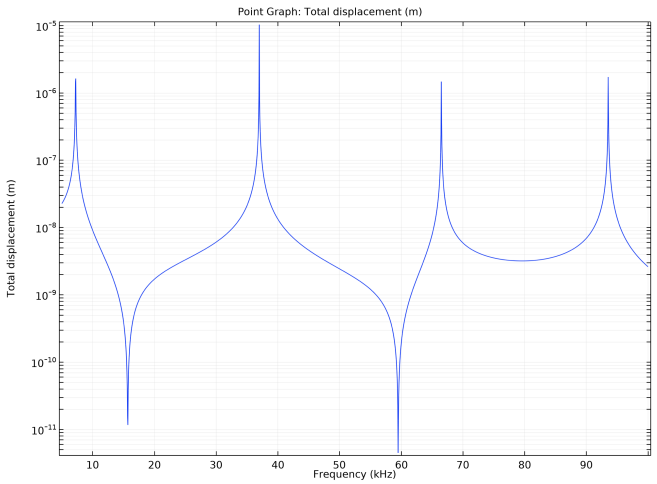

Fig. 3: Frequency response of the elliptical plate with two sections of different thicknesses and a point mass attached.

In Table 1, we can see a side-by-side comparison of the predicted eigenfrequencies and the actual eigenfrequencies of the printed plates. They are in good agreement and mode shapes are recognizable in the LDV scans. The 3D printing is successful, and the devices' behavior matches that predicted by simulation.

IV. Conclusions

Our aim was to develop a model that emulates the behavior of *Achroia grisella*'s tympanum. As we saw in Fig. 2, this objective was achieved satisfactorily. The secondary goal was to 3D print parts that agree with the models; parts were fruitfully produced, which is discussed in Table 1. Further work will delve into studying the directionality of the model in simulations and the directionality of 3D printed parts with experimental techniques.

TABLE I. Comparison between experimental 3D printed plates and COMSOL simulated plates.

	Resonance	COMSOL frequency	Experimental frequency
Circular	1st	135 kHz	137 kHz
	2nd	257 kHz	260 kHz
	3rd	257 kHz	260 kHz
Elliptical	1st	106 kHz	93 kHz
	2nd	174 kHz	167 kHz
	3rd	228 kHz	230 kHz
	4th	262 kHz	258 kHz
Elliptical (Two thicknesses)	1st	129 kHz	127 kHz
	2nd	209 kHz	202 kHz
	3rd	266 kHz	260 kHz
	4th	302 kHz	305 kHz

REFERENCES

[1] D. Robert, 'Directional Hearing in Insects', in *Sound Source Localization*, A. N. Popper and R. R. Fay, Eds. New York, NY: Springer, 2005, pp. 6–35, doi: https://doi.org/10.1007/0-387-28863-5_2

[2] J. Schul, M. Holderied, D. Von Helversen, and O. Von Helversen, 'Directional hearing in grasshoppers: neurophysiological testing of a bioacoustic model', *J. Exp. Biol.*, vol. 202, no. 2, p. 121, 1999.

[3] A. Michelsen, A. V. Popov, and B. Lewis, 'Physics of directional hearing in the cricket Gryllus bimaculatus', *J. Comp. Physiol. A*, vol. 175, no. 2, pp. 153–164, Aug. 1994, doi: 10.1007/BF00215111.

[4] R. S. Edgecomb, D. Robert, M. P. Read, and R. R. Hoy, 'The tympanal hearing organ of a fly: phylogenetic analysis of its morphological origins', *Cell Tissue Res.*, vol. 282, no. 2, pp. 251–268, Nov. 1995, doi: 10.1007/BF00319116.

[5] R. N. Miles, D. Robert, and R. R. Hoy, 'Mechanically coupled ears for directional hearing in the parasitoid fly Ormia ochracea', *J. Acoust. Soc. Am.*, vol. 98, no. 6, p. 3059, Jun. 1998, doi: 10.1121/1.413830.

[6] A. C. Mason, M. L. Oshinsky, and R. R. Hoy, 'Hyperacute directional hearing in a microscale auditory system', *Nature*, vol. 410, no. 6829, pp. 686–691, Apr. 2001, doi: 10.1038/35070564.

[7] W. H. Cade, M. Ciceran, and A.-M. Murray, 'Temporal patterns of parasitoid fly (Ormia ochracea) attraction to field cricket song (Gryllus integer)', *Can. J. Zool.*, Feb. 2011, doi: 10.1139/z96-046.

[8] M. D. Greenfield, 'Acoustic Communication in the Nocturnal Lepidoptera', in *Insect Hearing and Acoustic Communication*, B. Hedwig, Ed. Berlin, Heidelberg: Springer, 2014, pp. 81–100, doi: https://doi.org/10.1007/978-3-642-40462-7_6

[9] G. S. Pollack, A. C. Mason, A. N. Popper, and R. R. Fay, *Insect hearing*. Springer, 2016.

[10] L. Knopek and C. Hintze-Podufal, 'Uber den Bau der abdominalen Tympanalorgane der Kleinen Wachsmotte Achroia grisella (Fbr.)', *Zool. Jahrbuecher Abt. Fuer Anat. Ontog. Tiere*, vol. 1141, pp. 83–93, Jan. 1986.

[11] R. L. Rodríguez and M. D. Greenfield, 'Behavioural context regulates dual function of ultrasonic hearing in lesser waxmoths: bat avoidance and pair formation', *Physiol. Entomol.*, vol. 29, no. 2, pp. 159–168, 2004, doi: https://doi.org/10.1111/j.1365-3032.2004.00380.x.

[12] J. L. Eaton, *Lepidopteran anatomy*. New York; Chichester; Brisbane: J. Wiley & Sons, 1988.

[13] A. Reid, T. Marin-Cudraz, J. F. Windmill, and M. D. Greenfield, 'Evolution of directional hearing in moths via conversion of bat detection devices to asymmetric pressure gradient receivers', *Proc. Natl. Acad. Sci.*, vol. 113, no. 48, pp. E7740–E7748, 2016.

[14] H. G. Spangler and C. L. Hippenmeyer, 'Binaural phonotaxis in the lesser wax moth,Achroia grisella (F.) (Lepidoptera: Pyralidae)', *J. Insect Behav.*, vol. 1, no. 1, pp. 117–122, Jan. 1988, doi: 10.1007/BF01052508.

[15] A. Reid, 'Directional hearing at the micro-scale: bio-inspired sound localization', University of Strathclyde, 2017.

[16] J. F. V. Vincent and U. G. K. Wegst, 'Design and mechanical properties of insect cuticle', *Arthropod Struct. Dev.*, vol. 33, no. 3, pp. 187–199, Jul. 2004, doi: 10.1016/j.asd.2004.05.006.

[17] A. W. Leissa, *Vibration of Plates*. Scientific and Technical Information Division, National Aeronautics and Space Administration, 1969.

[18] J. C. Gutiérrez-Vega, R. M. Rodríguez-Dagnino, M. A. Meneses-Nava, and S. Chávez-Cerda, 'Mathieu functions, a visual approach', *Am. J. Phys.*, vol. 71, no. 3, pp. 233–242, Feb. 2003, doi: 10.1119/1.1522698.

[19] H. Gong, M. Beauchamp, S. Perry, A. T. Woolley, and G. P. Nordin, 'Optical approach to resin formulation for 3D printed microfluidics', *RSC Adv.*, vol. 5, no. 129, pp. 106621–106632, 2015.

[20] H. Mao *et al.*, 'Twist, tilt and stretch: From isometric Kelvin cells to anisotropic cellular materials', *Mater. Des.*, vol. 193, p. 108855, Aug. 2020, doi: 10.1016/j.matdes.2020.108855.

[21] J. M. Gere and S. P. Timoshenko, *Mechanics of materials*. Boston: PWS Publishing Company, 1997.

[22] D. Wu, Z. Zhao, Q. Zhang, H. Jerry Qi, and D. Fang, 'Mechanics of shape distortion of DLP 3D printed structures during UV post-curing', *Soft Matter*, vol. 15, no. 30, pp. 6151–6159, 2019, doi: 10.1039/C9SM00725C.

[23] J. Wu *et al.*, 'Evolution of material properties during free radical photopolymerization', *J. Mech. Phys. Solids*, vol. 112, pp. 25–49, Mar. 2018, doi: 10.1016/j.jmps.2017.11.018.

[24] P. S. Bychkov, V. M. Kozintsev, A. V. Manzhirov, and A. L. Popov, 'Determination of Residual Stresses in Products in Additive Production by the Layer-by-Layer Photopolymerization Method', *Mech. Solids*, vol. 52, no. 5, pp. 524–529, Sep. 2017, doi: 10.3103/S0025654417050077.

[25] A. Reid, J. C. Jackson, and J. F. C. Windmill, 'Voxel based method for predictive modelling of solidification and stress in digital light processing based additive manufacture', *Soft Matter*, vol. 17, no. 7, pp. 1881–1887, Feb. 2021, doi: 10.1039/D0SM01968B.

Appendix B

IEEE Sensors journal paper

Towards a bio-inspired acoustic sensor: *Achroia grisella*'s ear

Lara Díaz-García*, Student Member, IEEE, Andrew Reid, Joseph Jackson-Camargo, James F.C. Windmill, Senior Member, IEEE

***Abstract*— Gathering insight from nature to develop original solutions for engineering problems is known as bio-inspiration. The examples found in nature are often efficient and beautifully simple. For the particular issue of directional acoustic sensing at small scales, insects provide a myriad of clever adaptations to achieve hearing despite their small body size. *Achroia grisella* is a nocturnal moth capable of directional hearing of wavelengths significantly longer than its inter-tympanic distance. Previous studies have shown that directionality for this moth is monoaural and exclusively relies on the shape of the eardrum itself. The work developed a computer model that behaves similarly to the moth's ear, which is then 3D printed. The model starts from a simplified circular membrane and progresses until it reflects the moth's tympanum more closely. The approach followed consists of four steps: considering analytical equations, virtually simulating the model, manufacturing and performing experimental measurements, and finally comparing the outcomes of each. Equations are produced for the simplest geometries, and COMSOL Multiphysics is used for the simulations. The samples are manufactured via 3D printing and excited with a vibrating piezoelectric chip and a speaker while being measured with a 3D Laser Doppler Vibrometer to determine their frequency and directional responses.**

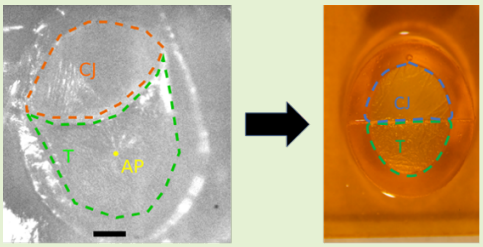

***Index Terms*—3D printing, Achroia grisella, acoustic sensor, bio-inspiration, insect hearing**

I. Introduction

HEARING is one of the ways in which animals interact with their surrounding environment. A few examples of useful applications of hearing in animals are escaping a predator, pursuing prey, communicating with conspecifics, or attracting a potential mate. In most of these cases, besides the detection of sound itself, it is particularly crucial to know the location of the sound source, hence why directional hearing is desirable for animals [1].

Hearing is commonly found in vertebrates, and intuitively identified in mammals, where we think of a pair of small flesh appendixes, the ears, that precede a subsequent pair of tympana, or eardrums. However, a hearing sense might not be as identifiable if we look at other animal classes, like arthropods, for which the hearing tools can be found all over the body and do not resemble human ears at all.

Except for mantids, animals that hear show bilateral symmetry, meaning there is an ear on each half of their bodies. Bigger animals use their two ears, separated by a certain distance, to compare the intensity, time of arrival and phase of incoming sound, locating the provenance of sound and consequently achieving directional hearing. On the other hand, smaller animals with hearing have an inter-ear distance that is not long enough for their brains to process any of these calculations, having to resort to other mechanisms instead.

Within arthropods we find the *Insecta* class, generally characterized by a small body size. Some insects have developed clever adaptations to overcome their size and perform directional hearing of sounds with wavelengths of the same scale as their body sizes. *Ormia ochracea*, for example, is a fly with tympana interconnected by a stiff tissue bridge, making the whole system move in a complex way. This grants the fly a precision of 2º when landing on their hosts, whose calls they listen for [2]–[5]. Other insects, like grasshoppers [6] and field crickets [7], have multiple openings to the outside in their tracheal systems, allowing sound to arrive to both sides of their tympana with different times and amplifications.

Lepidoptera are an order of insects composed of what are commonly called butterflies and moths. The latter, being mostly nocturnal, are predominantly predated by bats, which use echolocation for hunting. Therefore, it is believed that many moths have developed hearing in the ultrasonic range in order to anticipate the presence of hunting bats by their calls [8]. What is not so common is for moths to use their hearing sense for intraspecific communication [9].

Achroia grisella is a moth from the *Pyraloidea* superfamily. It is one of the many species that uses hearing for detecting bats. But *Achroia* are quite unique in that they use ultrasonic calling in their mating process, instead of just pheromones. The males fan their wings while remaining still, which produces a train of clicks (main content of the signal of 100 kHz [10]). The

Submitted for review on May 6th 2022.

All authors are affiliated with the Centre for Ultrasonic Engineering, University of Strathclyde, Glasgow, United Kingdom (e-mail corresponding author: lara.diaz-garcia@strath.ac.uk).

An earlier version of this paper was presented at the IEEE Sensors 2021 conference and was published in its Proceedings: https://ieeexplore.ieee.org/document/9639528.

females, upon listening to the signal, make their way to the males after some zigzagging.

These moths have just four auditory neurons per tympanum, and they are not capable of frequency discrimination. The way female moths differentiate a bat call from a male moth call, eliciting an evasive or positive behavior respectively, is thus believed to be time-encoded [11]. *Achroia*'s usual size is about 13 mm, which means their tympana are separated by less than 600 μm on average. This inter-ear distance is insufficient to discern any phase, intensity, or time of arrival difference for a signal of 100 kHz, which has a corresponding wavelength of 3.4 mm.

X-ray scans of moth specimens have discarded the suggestion of any existing connection between the tympana or spiracles in the body, ruling out systems like those previously mentioned [12]. Diffraction around the insect's abdominal section cannot account for a sufficient intensity difference either [13]. Moreover, experiments where female moths had one tympanum pierced showed that they were still able to find the calling males, albeit with more difficulty [14]. For all these reasons, it is believed that directionality in *Achroia grisella* is monoaural and exclusively dependent on tympanum morphology.

II. Methodology

The working hypothesis is, therefore, that the moth's tympanum geometry confers them with a certain extent of directionality. To test it, we have developed an approach where a simple model is proposed and examined analytically, in simulation, and with real 3D printed samples measured with Laser Doppler Vibrometry. The three are then compared against each other. The model is progressively revised to improve its complexity and its resemblance to the real moth tympanum.

Before considering the model, what the moth's actual tympanum looks and behaves like was explored. *Achroia*'s tympana are approximately elliptical and divided in two distinct sections of different thicknesses. The thicker part is called *conjunctivum* and the thinner part receives the name of *tympanum proper* or simply tympanic membrane. The *scolopidium*, a cluster of four auditory neurons, is attached directly to the latter, roughly in the center of the membrane (Fig. 1).

Under exposure to a 100 kHz signal, the tympanum moves in a complex, non-drum-like pattern, with the entirety of the surface vibrating and showing local maxima and minima. The main peak appears close to, but not exactly on, the neuron attachment point. Around it we see a half ring of lower-amplitude peaks. Lastly, a broader bump of low amplitude is seen on the thicker part. They are all slightly out of phase with each other [15].

A. Analytical Approach

In the first place, to find an analytical solution, the equations of motion that describe the system are observed. Transverse vibrations on a plate, which are ruled by different equations than membranes, were considered. The reason for considering a plate and not a membrane is because stiffness is not negligible. The plate equation is a fourth-degree differential one:

$$\nabla^2(\nabla^2 W) + \frac{1}{c^2}\cdot\frac{\delta^2 W}{\delta t^2} = 0 \quad (1)$$

Where the terms are $\nabla^2\nabla^2 = \nabla^4$, known as the biharmonic operator; $W = W(x, y, t)$, the function that describes displacement; and c, the velocity of the wave in the medium, itself defined as:

$$c = \sqrt{\frac{E\cdot h^2}{12\cdot\rho\cdot(1-\nu^2)}} \quad (2)$$

The physical characteristics, Young's modulus (E), mass volume density (ρ) and Poisson's ratio (ν), are taken as 1 GPa, 1180 kg/m^3 and 0.35 respectively. The particular values of these parameters for *Achroia grisella* are not known but are chosen here using the literature regarding insect cuticle. Young's modulus is taken towards the lower end of the spectrum of values for sclerotized cuticle, and Poisson's ratio is approximately in the middle of the range [15]. The thickness of the plate (h) will be measured directly on our samples or taken from the literature as needed [16].

To find the solutions, a periodical time dependence of the function is assumed. The boundary conditions of the problem, namely the shape and nature of the perimeter, are also considered. In this case the edge is clamped. As for the shape, the problem starts from an extreme simplification, a circular plate, and progressively increases complexity.

For the first case considered, a clamped circular plate, the solutions are easily obtained because the problem is a well-known one. Polar coordinates are used to suit the nature of the problem, and its resolution involves Bessel functions.

The next step is considering a clamped elliptical plate. The resolution becomes significantly more complicated as there is a need to use elliptical coordinates and Mathieu functions. The elliptical plates' resonance frequencies will be related to the eigenvalues obtained from the solution of the transversal wave equation in the following way:

$$f_{m,n} = \frac{2\cdot q_{m,n}\cdot c}{\pi\cdot(a^2-b^2)}, m = 0{,}1{,}2\ldots, n = 1{,}2{,}3\ldots \quad (3)$$

Where $f_{m,n}$ are the resonance frequencies, in turn dependent on the eigenvalues $q_{m,n}$, c is the velocity of the wave in the medium, and a and b are the major and minor semi-axes of the ellipse respectively.

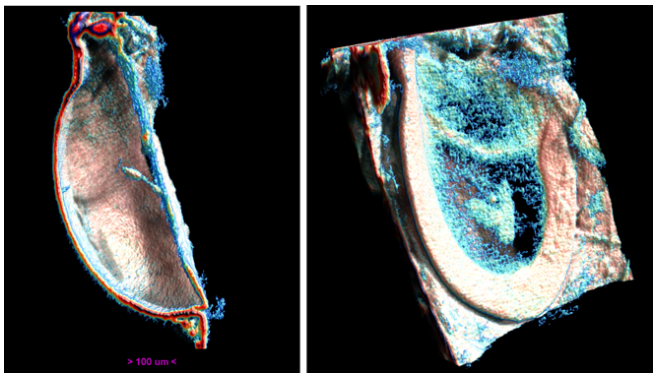

Fig. 1. Voxel reconstruction of the *Achroia grisella* tympanum from X-ray microtomography. (Left) Lateral view cross section along the major axis showing the tympanal cavity and the *scolopidium*. (Right) Front view of the tympanum showing the neuron attachment point and border between upper and lower membranes [17].

B. Simulation Approach

The simulation was carried out using the Finite Element Modelling (FEM) software COMSOL Multiphysics®. A Shell interface, from the Structural Mechanics module, is chosen for the tympanum. This interface is appropriate for considering a thin structure with considerable bending stiffness. For the resonant frequencies of the structure, a preset Eigenfrequency study is used.

For the directional response, a more general Frequency study is used. The stimulus used is in the shape of a spherical wave radiation, with an incident pressure field of 1 Pa. Two angles are set to characterize the provenance of the acoustic stimulus: polar and azimuthal. The azimuthal angle is fixed to 80º to suit our setup. A sweep of 360º over the polar angle is set, in intervals of 10º, to produce the directivity polar plots.

C. 3D Printing

3D printing was done using the digital light projection (DLP) technique. DLP has a layer-by-layer approach, creating a 2D pixel array of a slice of the design that selectively exposes the photosensitive resin to UV light, solidifying it. A printed layer will normally then fuse to the previously printed layer, however in the case of suspended regions or overhangs the layer thickness will be determined by the UV light exposure [18].

Structures were 3D printed with two different printers and materials. The structures used to initially determine the frequency responses were produced with an Original Prusa SL1 3D printer, which employs an LCD photomask to selectively pattern each material layer, and a commercial resin from the same manufacturer. The resin is Orange Tough, and it is modelled after Acrylonitrile-butadiene-styrene. The properties of the resin are obtained from the literature as a Poisson's ratio of 0.35 and volumetric mass density of 1180 kg/m^3 [19]. Young's modulus was measured in the printed samples using a 3D printed cantilever and beam theory.

The second 3D printer used was an Asiga Pico HD 3D printer and the resin chosen is a custom one composed of a base monomer, a photoinitiator, and a photo absorber. These are, respectively, Polyethylene glycol diacrylate (PEGDA) Mn 250, Phenylbis(2,4,6-trimethylbenzoyl)phosphine oxide at 0.5% weight percent, and Sudan I at 0.2% weight percent, all purchased from Merck Life Sciences and used without further modification. The resin is mixed in an ultrasonic bath (Decon FS250) for 20 minutes before use to ensure even distribution. From the literature, the Poisson's ratio and mass density of the resin are taken to be 0.32 and 1183 kg/m^3 respectively [20]. A value for Young's modulus of 52.9 MPa is also provided, but the 3D printed cantilever method, as well as compression testing, was used to determine it in these samples.

The reason for switching printing machines and moving to a custom resin was to achieve a lower Young's modulus, in turn producing lower resonant frequencies that can be excited through sound more comfortably with a common speaker for the directionality measurements. The size of the vibrating plates was increased slightly for the same reason. The aim was to produce the first three resonance frequencies under 20 kHz, reflecting the human hearing range.

The Orange Tough circular plates produced have a diameter of 1.5 mm, and the elliptical ones have major and minor axes of 2.1 mm and 1.5 mm respectively. The printed samples were examined by means of X-ray Computer Tomography using a Bruker Skyscan 1172 with SHT 11-megapixel camera and Mamamatsu 80 kV (100 milliamps) source to determine their thickness. The images generated were 1332 x 2000 pixels with a resolution of 4.98 µm per pixel. The images were collected, and a volumetric reconstruction of the sample generated by Bruker's CTvol software. The images produced are based on the level of attenuation through the sample, which is dependent on the thickness of the material and its absorption coefficient and is notably less near an object's extremities. The thickness measured is therefore dependent upon this manual thresholding. The thickness of the Orange tough samples is found to be 162 µm for single layers and 270 µm for the thicker multi-layer regions. For the custom resin, the plate has major and minor axes of 5.36 mm and 4 mm respectively. The thicknesses were examined in the same fashion and determined to be 122 µm for the single layer half and 400 µm for the thick multi-layer half. It must be noted that 3D printing of small devices is not straightforward, with residual stress gradients affecting the result significantly. Repeatability and accuracy can be difficult to achieve [21]–[24].

D. Laser Doppler Vibrometry

The printed structures were examined using 3D laser Doppler Vibrometry (3D LDV). The instrument used is an MSA-100-3D scanning head (Polytec, Waldbrom, Germany). The structures are stimulated first with a displacement piezo chip (75 V, 2.8 µm, Thorlabs, Newton, New Jersey), with wideband periodic burst signals. This allows examination of the frequency response recorded by the LDV. The resonances can be identified looking at out-of-plane vibrations and compared with the eigenfrequencies obtained from simulation, readjusted to the new parameters that match those of the 3D printed structures.

Once the resonant frequencies are found, the 3D printed plates are excited with a new setup to get the directionality measurements. Stimulation was with a Labo LB-PS1401D speaker (frequency response of 80 Hz to 20 kHz, maximum output power of 60W, sensitivity of 88 dB). The speaker was placed in an 80º angle so the normal of the speaker surface is not parallel to the ground (Fig. 2). The signals used consist of a series of sine tones at the resonant frequencies and the displacement at the middle point of the thin section recorded at

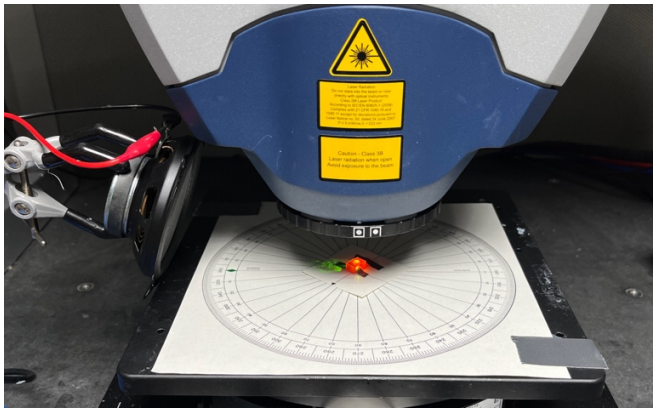

Fig. 2. Experimental setup of the directivity measurements showing the LDV, speaker, and sample being measured.

different angles. The sample is rotated in increments of 10° and the displacement is measured at the middle point of the thin half of the two-thickness sample. The experimental data are plotted using MATLAB. The direction taken for the polar plot is that on the same plane as the plate and aligned with the major axis, with the thick half being the front and corresponding to 0°. This corresponds to where the head of the moth would point to, as can be seen in Fig. 3.

III. Results

A. Young's Modulus

Two methods are used to determine the Young's modulus of the 3D printed resins. The first one uses a cantilever in the 3D print to measure the Young's modulus of the material from beam theory by observing the resonant frequencies in the LDV [25]. Young's modulus (E) can be obtained from the following equation:

$$E = \frac{48 \cdot \pi^2 \cdot \rho \cdot f_n^2 \cdot L^4}{\lambda_n^4 \cdot h^2}, n = 1,2,3 \ldots \quad (4)$$

The parameters being mass volume density (ρ), the eigenfrequencies (f_n), the length of the beam (L), the eigenvalues (λ_n) and the thickness (h). With all other values being known, the Young's moduli thus obtained are 1.327 GPa for the Orange Tough samples and 45.38 MPa for the custom resin samples.

The custom resin sample was also tested via compression test (Instron testing). The modulus is obtained from the linear part of the stress-strain curves, resulting in a value of approximately 53 MPa, which is within 15% of the results obtained with the cantilever method for the same material.

B. Frequency Response

The results obtained from evaluating the equations in MATLAB and an eigenfrequency study run in COMSOL with the same parameters are compared. For the circular plate, the diameter considered is of 500 µm and the thickness is 5 µm. These values are of the same scale as the moth's actual tympana [10]. The frequencies provided by COMSOL are within 1% of the analytical eigenfrequencies.

For the elliptical plate, the dimensions used are 670 µm for the major axis and 500 µm for the minor axis. The thickness considered is, again, 5 µm. Changing the geometry of the simulation to fit the new boundary conditions, the eigenfrequency study is run again, this time returning values within 7% of the frequencies predicted by the equations. It is worth noting that the vibrating patterns are still far from what is observed in the moth's tympanum for these two simple geometries. From this point onwards the equations are not considered, as they are no longer helpful in dealing with the more complex morphologies. Instead, the frequency responses of the COMSOL simulation are compared with those of the structures printed in Orange Tough. Regardless, the good agreement between COMSOL and the equations in the two previous cases is a reassurance of the validity of the eigenfrequencies predicted by COMSOL.

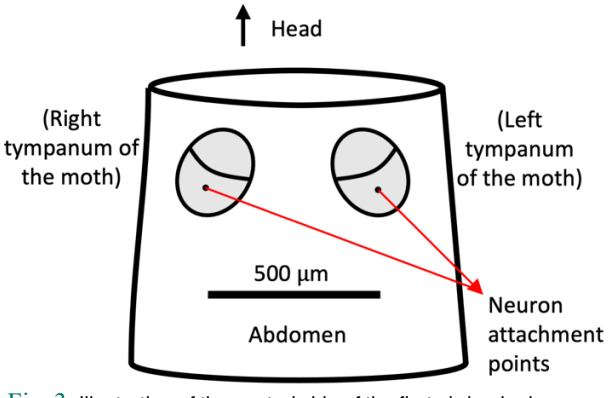

Fig. 3. Illustration of the ventral side of the first abdominal segment of *A. grisella* showing the general shape and position of the two tympana [13].

The next model considered includes two sections of different thicknesses, to reflect the two regions (thick and thin) of the moth's tympanum. The outline is, again, elliptical in shape. The circular, elliptical, and two-thickness elliptical plates printed with Orange Tough are examined in the LDV and the maxima of the frequency response are identified. The first few frequencies are found and compared with the COMSOL simulation, with parameters altered to match the physical properties of the printed plates. The results can be seen in Table 1. These are in good agreement with each other, as well as the mode shapes being recognizable in the LDV scans. The 3D printing is thus successful, and the structures behave as expected from the simulations.

Lastly, the simulation is taken one step further without a corresponding 3D printed structure. To approximate the design to the real moth's tympanum, damping is added by considering air as a viscous gas instead of an ideal one, and a point mass is added in the center of the thin section, to account for the neuron attachment. The mass chosen is one of an estimated biological relevance, equal to the mass of the whole plate but concentrated on one spot. Upon examination of the eigenfrequencies for this model, the sixth one (Fig. 4 c) is found to be quite an accurate reflection of the movement observed in the moth's tympanum, for which two scans can be seen in Fig. 4 a and b.

Table 1: Comparison between experimental 3D printed plates and COMSOL simulated plates [17].

	Resonance	COMSOL frequency	EXPERIMENTAL frequency
Circular	1st	135 kHz	137 kHz
	2nd	257 kHz	260 kHz
	3rd	257 kHz	260 kHz
Elliptical	1st	106 kHz	93 kHz
	2nd	174 kHz	167 kHz
	3rd	228 kHz	230 kHz
	4th	262 kHz	258 kHz
Two thickness	1st	129 kHz	127 kHz
	2nd	209 kHz	202 kHz
	3rd	266 kHz	260 kHz
	4th	302 kHz	305 kHz

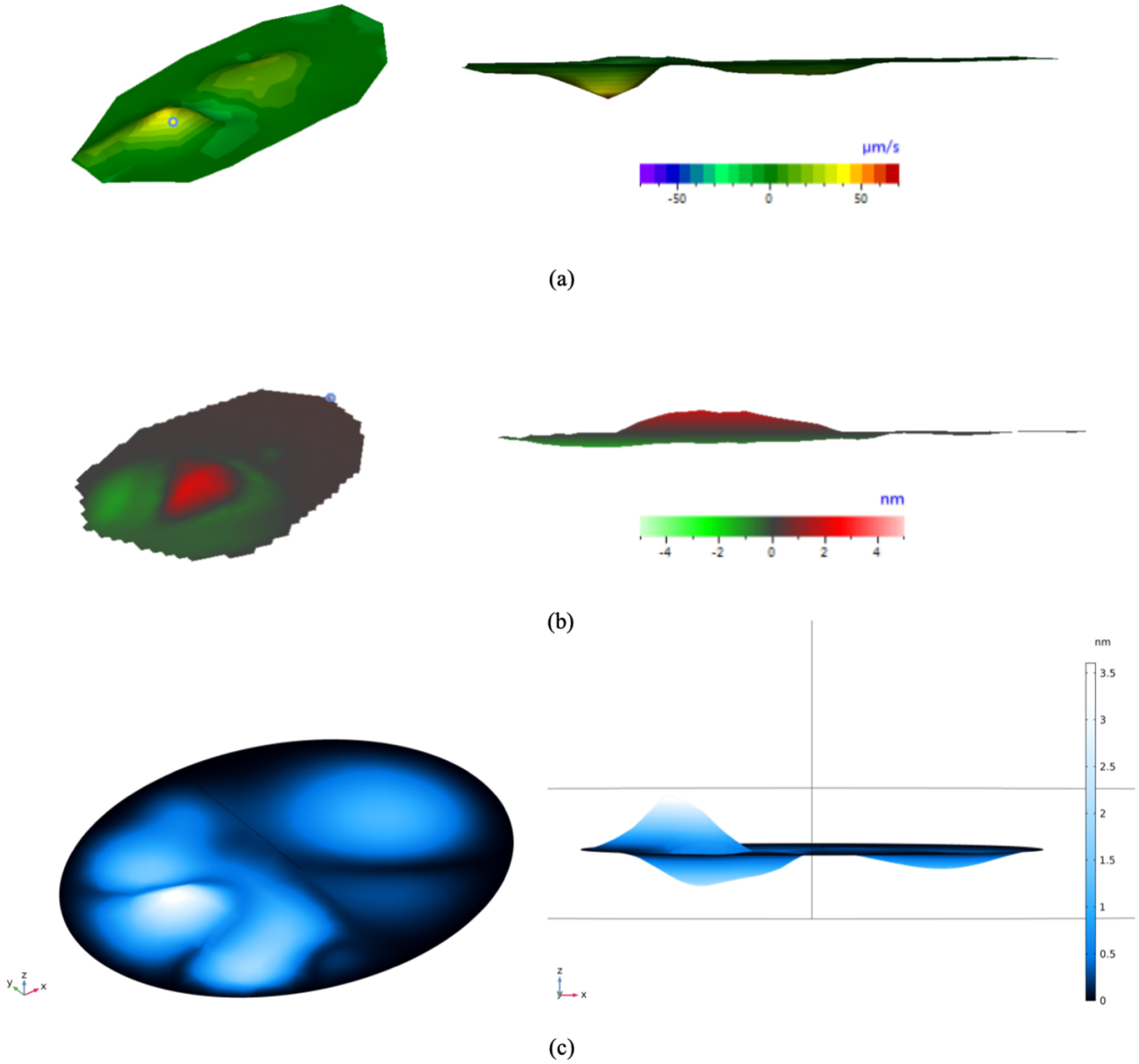

Fig. 4. (a) LDV measurement taken from a moth specimen showing the velocity at which the tympanum surface moves. (b) LDV measurement taken from a moth specimen showing displacement of the tympanum surface. (c) COMSOL simulation of the sixth natural frequency of an elliptical plate divided in two sections of different thicknesses (thin one on the left half of the ellipse and thick one on the right) with an attached mass (perspective view on the left and XZ plane view on the right).

C. Directivity Response

Once the method was validated, the directionality response of the structures was measured. For this the piezoelectric chip cannot be used to excite the plates, since the stimulus must be acoustic, at a distance and allow the structure (or stimulus) to be rotated. For this reason, the structures used the custom resin and slightly altered design, as explained in the methods. In this part of the work, only the elliptical, two-thickness, plates are considered, which is the model that is expected to provide the most directionality from simulations. According to COMSOL, a switch in the directivity pattern is expected when exciting at the first and second resonant frequencies.

The piezoelectric chip was used initially to extract the frequency response of the plate printed with the new resin. A resulting spectrum is shown in Fig. 5. With the LDV software, the resonant frequencies are identified by affinity with the mode shapes produced by COMSOL. The first two are found to be located at 3.074 kHz and 6.117 kHz respectively (tagged within the graph). COMSOL's prediction situates them at 4.6499 kHz and 7.053 kHz, such that both are slightly higher in frequency.

The resulting plots can be seen in Fig. 6 in a side-by-side comparison with the directivity plots produced by COMSOL. The shapes of the polar patterns are reasonably in agreement with the ideal version produced by COMSOL. In the case of the

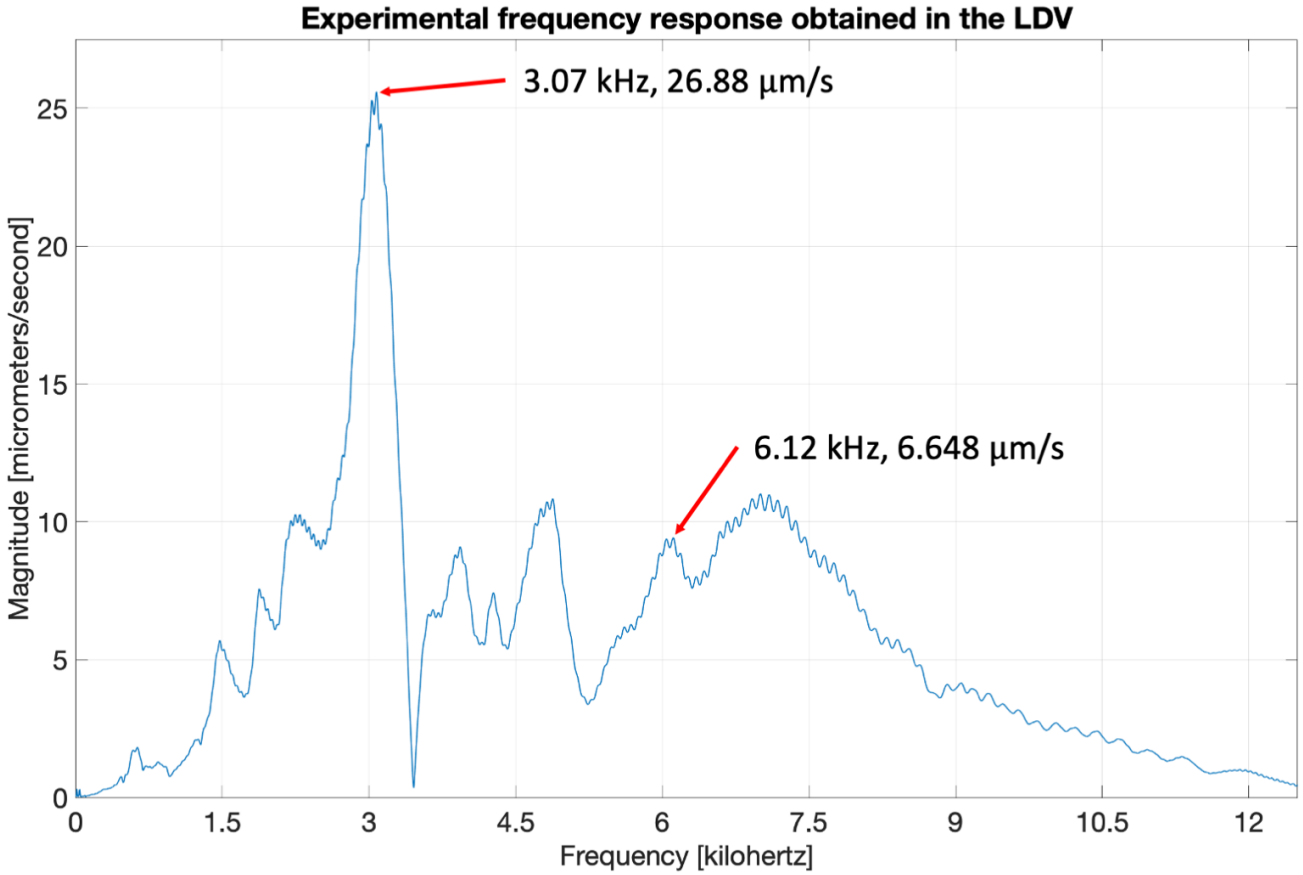

Fig. 5. Experimental frequency response of the two-thickness elliptical plate, with first and second resonances' location tagged.

first resonant frequency (images a and b), a clear preference for the rear is seen; and in the case of the second frequency response (c and d), the preference seems to be towards the front, with a slight narrowing that results in a small lob pointing towards the back, such as the one present in the COMSOL simulation.

IV. Conclusions

The discrepancy between experimental and simulated resonant frequencies for the printed structures can be at least partly attributed to the difficulties of the 3D printing process, as mentioned towards the end of section II. C. Irregularities on the surface of the plates can be seen in the LDV and a non-uniform thickness in the sections in the x-ray scans. There is also a source of human error in the process of locating the measuring point for the directionality measurements (there is a notch at the center of the thin section, but it must be located through the LDV vision system after each turn). A more trustworthy manufacturing process would palliate the irregularities of the surface, and a robotic automatization of the process of finding the measuring point or similar would also increase the precision. Nevertheless, the structures printed in this work reproduce the directivity patterns as expected from simulation results.

These promising results lead to future work including, but not limited to, adding a concentrated mass on the 3D printed plates to account for the moth's neuron attachment and taking the design forward to becoming an acoustic sensor by printing the model in piezoelectric materials to get an electric response when exposed to sound. Another path to explore is how to widen the sensitivity bandwidth of the plate, for it would be desirable to turn our system into a wideband sensor for applications like hearing aids.

Acknowledgment

The authors want to thank Lisa Asciak's help in mechanically testing the PEGDA samples to contrast the measurement of Young's modulus.

References

[1] D. Robert, 'Directional Hearing in Insects', in Sound Source Localization, A. N. Popper and R. R. Fay, Eds. New York, NY: Springer, 2005, pp. 6–35, doi: 10.1007/0-387-28863-5_2

[2] R. S. Edgecomb, D. Robert, M. P. Read, and R. R. Hoy, 'The tympanal hearing organ of a fly: phylogenetic analysis of its morphological origins', Cell Tissue Res., vol. 282, no. 2, pp. 251–268, Nov. 1995, doi: 10.1007/BF00319116.

[3] R. N. Miles, D. Robert, and R. R. Hoy, 'Mechanically coupled ears for directional hearing in the parasitoid fly Ormia ochracea', J. Acoust. Soc. Am., vol. 98, no. 6, p. 3059, Jun. 1998, doi: 10.1121/1.413830.

[4] A. C. Mason, M. L. Oshinsky, and R. R. Hoy, 'Hyperacute directional hearing in a microscale auditory system', Nature, vol. 410, no. 6829, pp. 686–691, Apr. 2001, doi: 10.1038/35070564

[5] W. H. Cade, M. Ciceran, and A. M. Murray, 'Temporal patterns of parasitoid fly (Ormia ochracea) attraction to field cricket song (Gryllus integer)', Can. J. Zool., Feb. 2011, doi: 10.1139/z96-046.

[6] J. Schul, M. Holderied, D. Von Helversen, and O. Von Helversen, 'Directional hearing in grasshoppers: neurophysiological testing of a

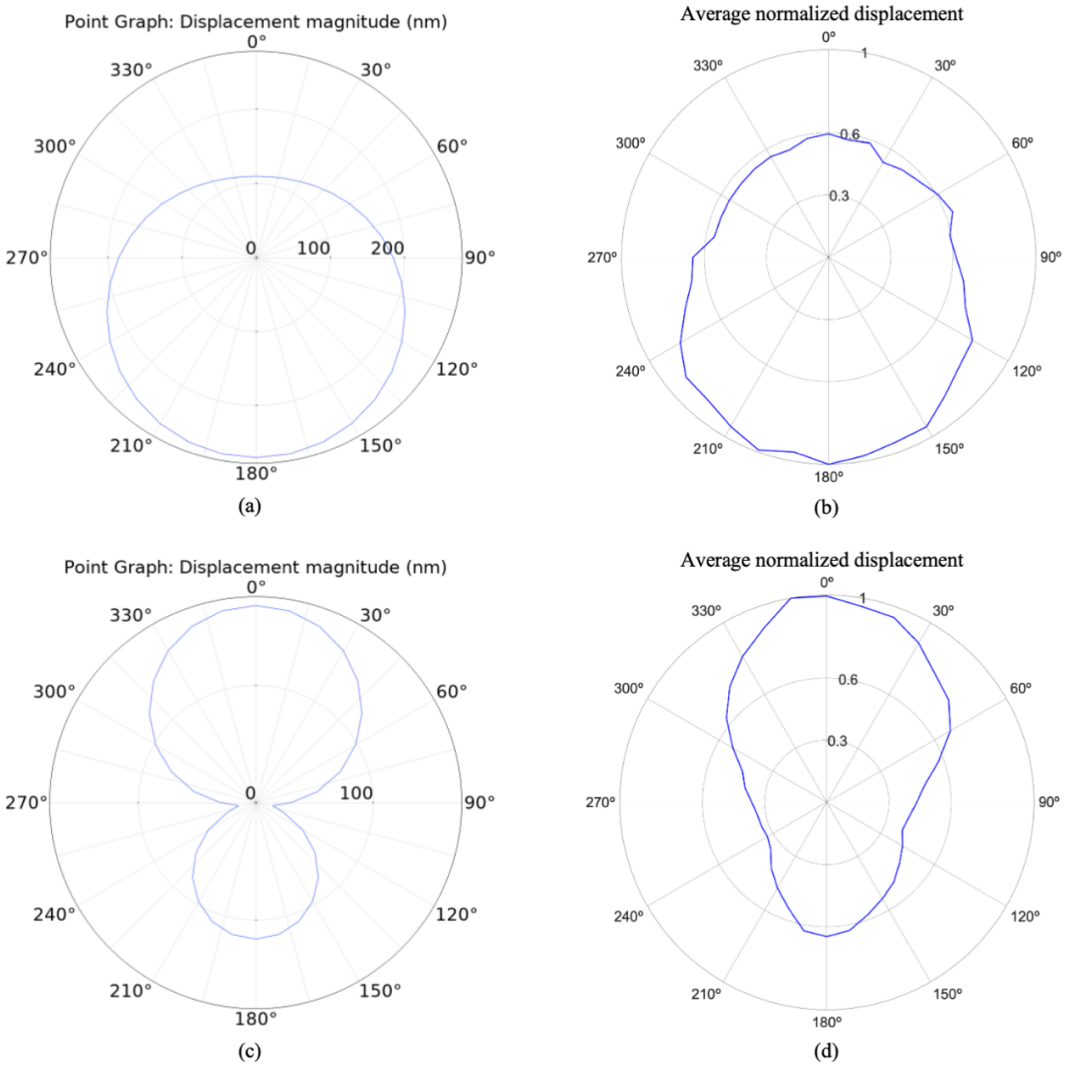

Fig. 6. COMSOL and experimental directivity plots for the two-thickness elliptical plate. Images a (simulated) and b (experimental) correspond to the first resonant frequency. Images c (simulated) and d (experimental) correspond to the second resonant frequency.

bioacoustic model', J. Exp. Biol., vol. 202, no. 2, p. 121, 1999, doi: 10.1242/jeb.202.2.121.

[7] A. Michelsen, A. V. Popov, and B. Lewis, 'Physics of directional hearing in the cricket Gryllus bimaculatus', J. Comp. Physiol. A, vol. 175, no. 2, pp. 153–164, Aug. 1994, doi: 10.1007/BF00215111.

[8] G. S. Pollack, A. C. Mason, A. N. Popper, and R. R. Fay, Insect hearing. Springer, 2016, doi: 10.1007/978-3-319-28890-1.

[9] M. D. Greenfield, 'Acoustic Communication in the Nocturnal Lepidoptera', in Insect Hearing and Acoustic Communication, B. Hedwig, Ed. Berlin, Heidelberg: Springer, 2014, pp. 81–100, doi: 10.1007/978-3-642-40462-7.

[10] L. Knopek and C. Hintze-Podufal, 'Uber den Bau der abdominalen Tympanalorgane der Kleinen Wachsmotte Achroia grisella (Fbr.)', Zool. Jahrbuecher Abt. Fuer Anat. Ontog. Tiere, vol. 1141, pp. 83–93, Jan. 1986.

[11] R. L. Rodríguez and M. D. Greenfield, 'Behavioural context regulates dual function of ultrasonic hearing in lesser waxmoths: bat avoidance and pair formation', Physiol. Entomol., vol. 29, no. 2, pp. 159–168, 2004, doi: 10.1111/j.1365-3032.2004.00380.x.

[12] J. L. Eaton, Lepidopteran anatomy. New York; Chichester; Brisbane: J. Wiley & Sons, 1988, doi: 10.1086/416282.

[13] A. Reid, T. Marin-Cudraz, J. F. Windmill, and M. D. Greenfield, 'Evolution of directional hearing in moths via conversion of bat detection devices to asymmetric pressure gradient receivers', Proc. Natl. Acad. Sci., vol. 113, no. 48, pp. E7740–E7748, 2016, doi: 10.1073/pnas.1615691113.

[14] H. G. Spangler and C. L. Hippenmeyer, 'Binaural phonotaxis in the lesser wax moth, Achroia grisella (F.) (Lepidoptera: Pyralidae)', J. Insect Behav., vol. 1, no. 1, pp. 117–122, Jan. 1988, doi: 10.1007/BF01052508.

[15] J. F. V. Vincent and U. G. K. Wegst, 'Design and mechanical properties of insect cuticle', Arthropod Struct. Dev., vol. 33, no. 3, pp. 187–199, Jul. 2004, doi: 10.1016/j.asd.2004.05.006.

[16] A. Reid, 'Directional hearing at the micro-scale: bio-inspired sound localization', University of Strathclyde thesis, 2017, doi: 10.48730/7r6d-aq98.

[17] L. Díaz-García, A. Reid, J. Jackson and J. F. C. Windmill, "Towards a bio-inspired acoustic sensor: Achroia grisella's ear," 2021 IEEE Sensors, 2021, pp. 1-4, doi: 10.1109/SENSORS47087.2021.9639528.

[18] H. Gong, M. Beauchamp, S. Perry, A. T. Woolley, and G. P. Nordin, 'Optical approach to resin formulation for 3D printed microfluidics', RSC Adv., vol. 5, no. 129, pp. 106621–106632, 2015, doi: 10.1039/C5RA23855B.
[19] H. Mao et al., 'Twist, tilt and stretch: From isometric Kelvin cells to anisotropic cellular materials', Mater. Des., vol. 193, p. 108855, Aug. 2020, doi: 10.1016/j.matdes.2020.108855.
[20] B. Tiller et al., 'Piezoelectric microphone via a digital light processing 3D printing process', Mater. Des., vol. 165, p. 107593, Mar. 2019, doi: 10.1016/j.matdes.2019.107593.
[21] D. Wu, Z. Zhao, Q. Zhang, H. Jerry Qi, and D. Fang, 'Mechanics of shape distortion of DLP 3D printed structures during UV post-curing', Soft Matter, vol. 15, no. 30, pp. 6151–6159, 2019, doi: 10.1039/C9SM00725C.
[22] J. Wu et al., 'Evolution of material properties during free radical photopolymerization', J. Mech. Phys. Solids, vol. 112, pp. 25–49, Mar. 2018, doi: 10.1016/j.jmps.2017.11.018.
[23] P. S. Bychkov, V. M. Kozintsev, A. V. Manzhirov, and A. L. Popov, 'Determination of Residual Stresses in Products in Additive Production by the Layer-by-Layer Photopolymerization Method', Mech. Solids, vol. 52, no. 5, pp. 524–529, Sep. 2017, doi: 10.3103/S0025654417050077.
[24] A. Reid, J. C. Jackson, and J. F. C. Windmill, 'Voxel based method for predictive modelling of solidification and stress in digital light processing based additive manufacture', Soft Matter, vol. 17, no. 7, pp. 1881–1887, Feb. 2021, doi: 10.1039/D0SM01968B.
[25] J. M. Gere and S. P. Timoshenko, Mechanics of materials. Boston: PWS Publishing Company, 1997, doi: 10.1007/978-1-4899-3124-5.

Lara Díaz-García received her bachelor's degree in physics from Universidad de La Laguna in 2016 and her master's degree in acoustics and music technology from the University of Edinburgh in 2017. She is currently pursuing her PhD in the Centre for Ultrasonic Engineering in the University of Strathclyde. Her research interests are varied, from biologically inspired acoustic sensors to the acoustics of musical instruments.

Andrew Reid is a Leverhulme Fellow at the Centre for Ultrasonic Engineering at Strathclyde. He received a B.Eng in Electrical and Mechanical Engineering in 2012 and a PhD degree in insect inspired acoustics from the same institution in 2016. His research interests are in soft and flexible sensors and actuators, spanning novel manufacuring methods and 3D printing techniques to systems design.

Joseph C. Jackson-Camargo received the MSc (Hons.) degree in physics from Imperial College London, London, in 2003, and the Ph.D. degree in bio- logical sciences from the University of Bristol in 2008. He is currently a Lecturer in electrical and electronic engineering with the Centre for Ultrasonic Engineering, University of Strathclyde. His research interests cover a wide range of subjects, such as the physical basis for hearing, sound production and reception in biology and engineering, and advanced bio-inspired transducer and signal design.

James F. C. Windmill (M'99-SM'18) is a Professor in the Department of Electronic and Electrical Engineering, University of Strathclyde, Glasgow, U.K. He received a B.Eng. degree in electronic engineering from the University of Plymouth, UK, in 1998 and a Ph.D. degree in magnetic microscopy from University of Plymouth, UK, in 2002. He has over 20 years of research and development experience in the areas of sensors and hearing systems. His research interests are in the field of biologically inspired acoustic systems, from the fundamental biology to various engineering application topics.

Appendix C

ASA 143rd meeting invited proceedings paper

Volume 50 http://acousticalsociety.org/

183rd Meeting of the Acoustical Society of America

Nashville, Tennessee

5-9 December 2022

*Interdisciplinary: Paper 2aSA1

Directional passive acoustic structures inspired by the ear of *Achroia grisella*

Lara Díaz-García
EEE, University Of Strathclyde, Glasgow, Glasgow City, G1 1RD, UNITED KINGDOM; lara.diaz-garcia@strath.ac.uk;laradiazgarcia@hotmail.com

Andrew Reid, Joseph Jackson-Camargo and James Windmill
University of Strathclyde, Glasgow, Lanarkshire, UNITED KINGDOM; andrew.reid@strath.ac.uk, joseph.jackson@strath.ac.uk, james.windmill@strath.ac.uk

The need for small directional microphones is patent in the current market. From smartphones to hearing aids, a small microphone capable of rejecting ambient noise is highly desirable. Most MEMS microphones are omnidirectional and have to resort to arrays to achieve directionality, effectively counteracting the reduced size that they offer in the first place. For this reason, we use bio-inspiration and turn to nature to find examples of solutions to this problem. The female specimens of the moth *Achroia grisella* are capable of monoaural directional hearing, which they use to track the males' mating calls. It is believed that they achieve directionality solely due to the morphology of their tympana. To test it, we first produce a multiphysics simulation of the structure that serves as a starting point. For experimental measurements, additive manufacturing is chosen for its ease and cost-efficiency. 3D-printed samples of the same model are examined through micro-CT scanning and then measured using laser-Doppler vibrometry to determine their frequency and directivity responses. The results of both approaches are compared, and it is found that the structure does indeed show directionality and the experimental and simulated results are in good agreement.

Nashville POMA Student Paper Competition Winner

Published by the Acoustical Society of America

 https://doi.org/10.1121/2.0001715

1. INTRODUCTION

There is currently a demand for microphones that are both small and directional. Their small size means they will be able to fit into portable applications like smartphones or hearing aids, providing ease of use and concealment to users; directionality implies that they are able not just to pick sound but also to favor sound coming from one direction and reject ambient noise coming from other directions. However, those two capacities are related through a trade-off. The way humans achieve directional hearing is by comparing the input received by each of our ears, different enough for our brain to perform the calculations and locate the source of the sound. If you reduce the space between the two ears, or microphones, too much, then sound will reach both at virtually the same time, with the difference not being enough to determine the origin of the stimulus. Classic microphone designs such as the condenser microphone are not suited for the task, which is why new, innovative models need to be considered.

Additive manufacturing, more commonly known as 3D-printing, has revolutionized engineering in the last few decades due to the ease and low cost of prototyping. With a Computer-Aided Design (CAD) software, one can quickly develop a personalized prototype with as much detail as one wishes. With materials, including the 3D-printer itself, being generally cheap, it is possible to produce an efficient prototype in any lab in a short time. With the current technology, it is possible to print thin membranes and diaphragms, which is a key component in microphone models.

A popular source of inspiration for such innovative microphones is the natural world, which received the name of bio-inspiration.[5,15,22,33] Insects are an example of living creature that face the very same challenge we described above. Directional hearing is desirable to find a potential mate or escape a predator, but insects' body size is usually small. The way insects overcome this challenge and achieve directional hearing is incredibly varied.[23] For example, *Ormia ochracea* is a parasitic fly with ultra-precise hearing known to have a complex inter-connected hearing system;[2,7,18] *Gryllus bimaculatus*, on the other hand, is a cricket with a tracheal system that connects to the outside of the body allowing sound to reach the inner side of their ears too.[17,24] These are just two examples, but different sorts of adaptations have been developed, and subsequently studied, to solve the issue of directional hearing at a small scale.

One such creature capable of directional hearing is the moth *Achroia grisella*.[3,10] *Achroia grisella* are also called lesser wax moth, and they are a small (average body size about 13 mm)[8] moth that parasites beehives. These moths belong to the *Arthropod* phylum, *Insecta* class, *Lepidoptera* order, and *Pyraloidea* superfamily. Like many nocturnal insects, the lesser wax moth is mainly preyed upon by bats, and are believed to have developed hearing in response to bat echolocation, to detect approaching bats and initiate evasive movements.[12,32] But for this end, *Achroia* does not need its hearing to be directional, it suffices to know that a bat is approaching and the moth will dive to the ground if flying or stop moving altogether if walking.

What is less common about *Achroia grisella* is that they further use their hearing for mating.[6,11] The male of the lesser wax moth emits a series of ultrasonic clicks with a structure at the base of their wings. The females are attracted by pheromones in the long distances, but in the close range, they listen for the song and zigzag until they reach it. Mechanisms like those of *Ormia* or *Gryllus* have been discarded in *Achroia grisella* through x-ray scans of their bodies.[19] Moreover, females with one ear pierced were still found able to track the artificial male calls,[27] which suggests that the moths' directional hearing is in fact monoaural and dependent exclusively on the morphology of the ear.

Achroia's hearing system consists of two ears that sit on the front of their abdomen next to each other. Each ear is comprised of an elliptical eardrum, with two sections of different thicknesses (the thicker one is called *conjuctivum* and the thinner one is called *tympanum proper* or tympanic membrane), and a *scolopidium*, a cluster of four auditory neurons that attach directly to the middle of the thin section.[13] When exposed to the mating call (main content of the signal approximately 100 kHz)[13,25,26], the eardrum moves in a complex, non-drum-like shape. There is a main amplitude peak close to, but not exactly on, the neuron attachment point. A ring of secondary peaks of lower amplitude surrounds the maximum. Lastly, there is a lower-amplitude, broader bump on the thicker section. All these sections move out of phase with each other, with the main peak almost in opposition to the other two regions.[19,21]

2. METHODS

The methodology followed combines different approaches and compares them between each other. Simultaneously, the model considered progressively increases its intricacy from a simplified version to a level of complexity closer to the real system. First, analytical equations were considered for the simpler cases that are not included in this paper; then, simulations were carried out with the Finite Element Modelling (FEM) software COMSOL Multiphysics; and lastly, samples were 3D-printed and measured in a 3D Laser Doppler Vibrometer. Good agreement was found between analytical results and simulation results for the simpler cases, thus validating the COMSOL model.

A. FINITE ELEMENT MODELLING

Finite Element Analysis was carried out in COMSOL Multiphysics®. A shell interface (Structural Mechanics module) is chosen to describe the system, accounting for a thin structure of significant bending stiffness. The physical characteristics of the system are parametrized to be easily changed to adapt the simulation to each considered case: values for the moth taken from the literature, measurements perfomed on 3D-printed samples, etc.

Two different kinds of study were performed: an eigenfrequency study and a general frequency study for directionality. The Eigenfrequency study is preset, and it is a straightforward way to obtain a number of natural resonances of a system.

For the directionality, a general frequency study is set, with an excitation stimulus consisting of a spherical wave of incident pressure field 1 Pa at one of the previously determined resonant frequencies. For producing polar plots, two angles were set, a polar angle and azimuthal angle. The azimuthal angle is the rise with respect of the ground and is set to 90 degrees to coincide with our setup (angle of the speaker surface with respect to the ground). The polar angle is swept over in intervals of 10 degrees, thus providing the points for the polar plot.

B. 3D-PRINTING

The 3D-printer used employs the Digital Light Projection (DLP) technique. DLP produces a 2D pixel array of each horizontal layer of the design, selectively exposing the photosensitive resin to UV light, which solidifies it. Each layer then attaches to the previous layers. If there is none, like in a suspended region or overhang, the exposure time will determine the thickness.[9] It is worth remarking that 3D-printing does present disadvantages, one of which is the difficulty of printing small samples due to residual stress gradients.[1,20,30,31] This can make it difficult to achieve repeatability and accuracy, which is why samples are measured individually to determine their size and thickness.

The material used is a custom mixed resin consisting of the base monomer, a photoinitiator, and a photo absorber. These are, in the same order, PEGDA (Polyethylene glycol diacrylate Mn 250), Phenylbis(2,4,6-trimethylbenzoyl)phosphine oxide at 0.5% weight percent, and Sudan I at 0.2% weight percent, purchased from Merck Life Sciences and used as bought. An ultrasonic bath (Decon FS250) was used to ensure even mixing of the three elements. From the literature, the Poisson's ratio and mass density of the resin are taken to be 0.32 and 1183 kg/m3 respectively.[28] The resin was calibrated in the following way: the UV light of the 3D-printer was shone directly onto the resin pool without a tray at different exposure times. The subsequent samples produced are stuck to the bottom of the resin pool, which are then carefully removed, washed in isopropyl alcohol, dried, and their thickness measured using a digital caliper. The relation of thicknesses and exposure times are adjusted using the model provided by Gong et al. [9]

C. X-RAY COMPUTER TOMOGRAPHY

To determine if the shape, size, and thickness of the 3D-printed samples is accurate, a Bruker Skyscan 1172 with SHT 11-megapixel camera and Mamamatsu 80 kV (100 mA) source is used. It generates images that are 1332 x 2000 px (resolution of 4.98 μm/px). Bruker's own CTvol software allows a volumetric reconstruction of the sample being scanned from the individual images.

Each image obtained is generated from the different attenuation across the sample. This is, likewise, dependent on the sample's absorption coefficient and thickness. The level of attenuation is significantly

less closer to an object's outer boundaries. The final measurement for the thickness will depend on this manual thresholding.

The sample for which results are presented was found to be 6.55 mm across the major axis, 4.95 mm along the minor axis, 102 μm of thickness in the thinner section and 259 μm of thickness in the thicker section. This agrees with the expected X-Y shrinkage and thicker curing of the Z layer thickness.

D. LASER DOPPLER VIBROMETRY

To measure the vibrations undergone by the structures printed, a 3D Laser Doppler Vibrometer (3D LDV) is employed. The machine is an MSA-1-3D scanning head (Polytec, Waldbrom, Germany), with sub-picometer amplitude resolution for in-plane and out-of-plane movements (provided by manufacturer). Measurements taken in the LDV are complex averaged five times.

For both frequency and directionality measurements, the plates are excited using a Labo LB-PS1401D speaker (frequency response of 80 Hz to 20 kHz, maximum output power of 60W, sensitivity of 88 dB, from manufacturer's specifications). The 3D LDV provides a visualizer software that shows out-of-plane vibrations over time, which are compared against theoretical resonances to identify them.

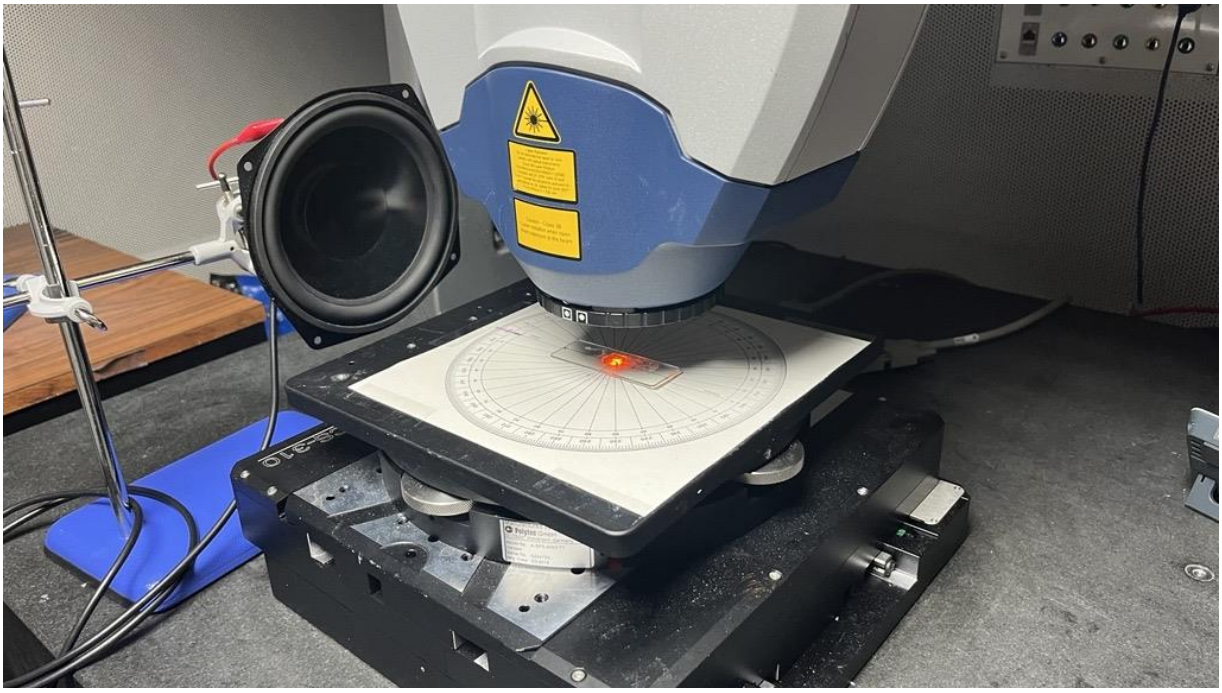

Fig 1. Experimental setup for the acquisition of the frequency and directivity responses. The sample is on a glass slide which can be rotated at measured intervals.

3. RESULTS

According to the analytical equations for a simple elliptical plate, resonant frequencies are proportional to Young's Modulus and thickness and inversely proportional to surface area. The resonant frequencies for a uniform elliptical plate are:

$$f_{m,n} = \frac{2 \cdot q_{m,n}}{\pi \cdot (a^2 - b^2)} \cdot \sqrt{\frac{D}{\rho \cdot h}}, m = 0,1,2 \dots, n = 1,2,3 \dots \quad (1)$$

Which depend on the eigenvalues ($q_{m,n}$), the major and minor semi-axes (a and b respectively), flexural rigidity (D), mass volume density (ρ), and thickness (h). The definition of D is the following:

$$D = \frac{E \cdot h^3}{12 \cdot (1 - \nu^2)} \quad (2)$$

Where the parameters not previously mentioned are as follows: Young's modulus (E), and Poisson's ratio (ν).[14] Although their exact values for *Achroia grisella* are not known with certainty, they are approximated as 1 GPa, 1180 kg/m^3 and 0.35 respectively. These values are obtained from literature values for insect cuticle.[29] Thickness is taken from literature or directly measured on the 3D-printed samples later on.[19] Even though the sample printed has two halves of different thicknesses, it is safe to assume we can expect a similar dependence with thickness and sizes of the axes.

Young's modulus was measured in two different ways for the custom material mix. The first one is through printing single layer cantilevers with our samples and examining their frequency response. The following equation from beam theory for a rectangular cantilever is used:

$$E = \frac{48 \cdot \pi^2 \cdot f_n^2 \cdot \rho \cdot L^4}{\lambda_n^4 \cdot h^2}, n = 1,2,3 \ldots \quad (3)$$

Where the parameters are mass volume density (ρ), the eigenfrequencies (f_n), the length of the beam (L), the eigenvalues (λ_n) and the thickness (h). [16] With all other values being known, Young's modulus is found to be 45.4 MPa. The second method used for measuring Young's modulus is compression testing, which provides the value of 53.0 MPa, obtained from the linear part of the stress-strain curves. Additionally, a value for the same custom resin's Young's modulus is also found in the literature as 52.9 MPa.[28] All values are found to be in reasonable agreement, and the value provided by the compression testing is chosen to be included in the COMSOL simulation.

A. FREQUENCY RESPONSE

The data obtained with the Laser Doppler Vibrometer for the sample mentioned in section 2.C was exported and plotted in MATLAB. The results can be seen in Figure 2. There is a large peak at approximately 1.7 kHz which is suspected to be a resonance of some element in the room; the reason for considering this point spurious is that this peak is present in all measurements of different setups and not just in this experiment. If the corresponding mode shape is observed, the whole structure can be seen vibrating up and down, as opposed to the actual relevant measurements where the edge remains clamped and only the central part of the membrane moves. Such is the case of the maxima at 9.506 kHz and at 11.788 kHz. The directivity response at these frequencies is evaluated in the next section.

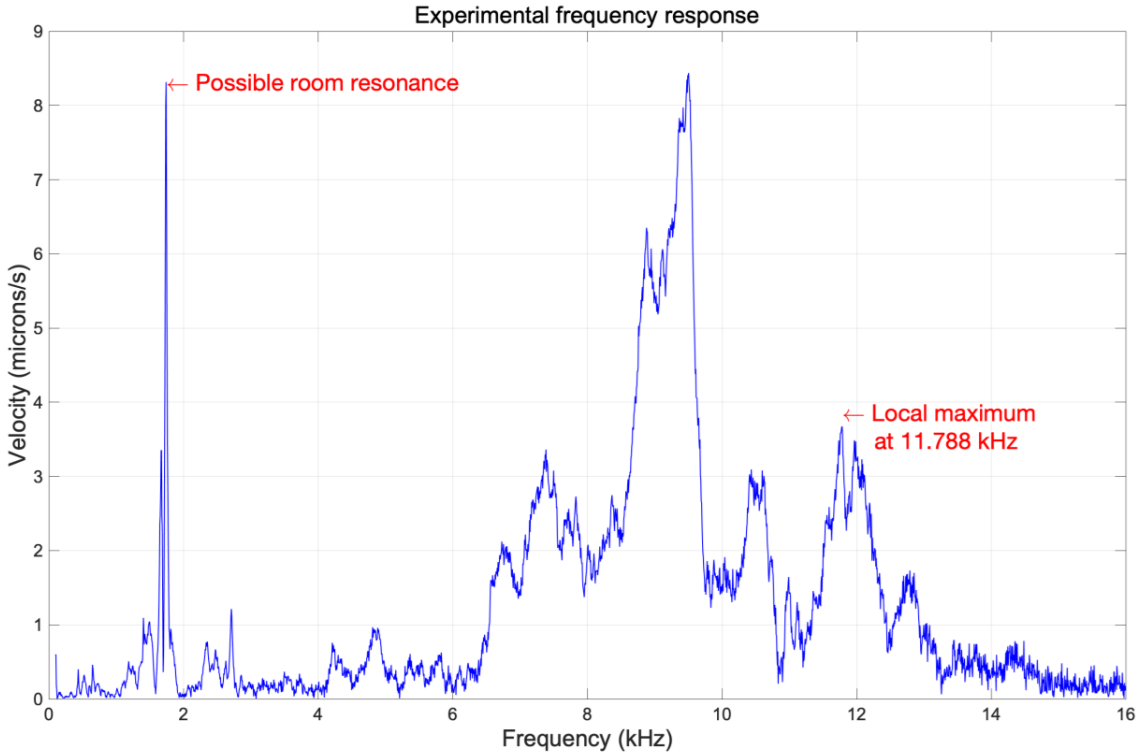

Fig 2. Frequency response obtained experimentally measuring at the approximate neuron attachment point. A broadband chirp produced by a speaker is used to excite the sample. The location of a spurious peak and the resonant frequency for which directivity will be evaluated are tagged in red.

B. DIRECTIVITY RESPONSE

The directivity responses for both 9.506 and 11.788 kHz are examined, and the one corresponding to 11.788 kHz is found to be a more recognizable shape to contrast against the simulation. Once a particular resonant frequency has been chosen from the frequency response, the COMSOL model is evaluated again with the parameters adjusted to fit the sample, in search of an eigenfrequency that is located close to the experimentally found resonant frequency. In this case, the eigenfrequency 10.026 kHz is found. The difference between resonant frequencies can be explained due to local irregularities in the 3D-printed sample, which are clearly seen under the microscope. An alternative manufacturing method might provide a more reliable result, but the cost and time of production would be higher. The simulated and experimentally obtained directivity patterns are then contrasted, a side-by-side comparison of the two can be seen in Figure 3. Both patterns present lobes pointing to what correspond to the sides of the moth (the setup is such that 0º is where the head of the moth is pointing to and 180º is the rear). The irregularities on the left side of the experimental pattern can be due to misalignment of the setup and/or human error in the measurements. Nonetheless, both patterns show directionality and are in good agreement with each other.

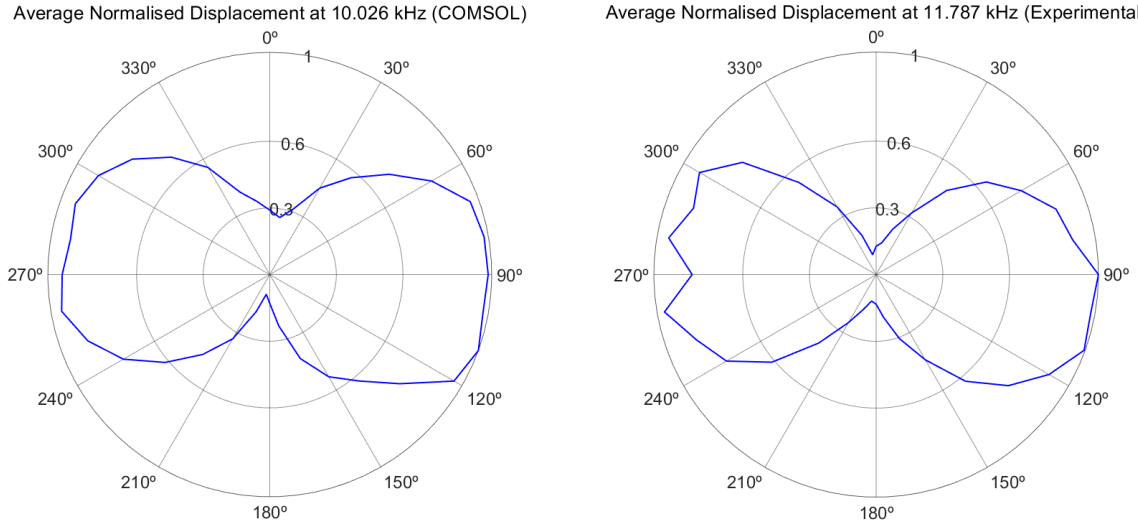

Fig 3. Directivity response obtained from COMSOL at 10.026 kHz (left) and experimentally at 11.788 kHz (right) for the sample described in section 2.C.

4. CONCLUSION

The 3D-printed sample shows clear passive acoustic directionality due to its asymmetrical morphology. It is seen that the experimentally measured directivity response agrees very well with what is expected from the simulations. Even though the pattern observed for the sample at this particular resonant frequency is not immediately advantageous for directional microphone manufacturing (a sideways bi-directional or figure-8 pattern), it is positive to see such good agreement and a modification of the setup could potentially be suitable for directional microphone applications. Previous studies of different patterns observed for lower resonant frequencies have been seen to possibly be helpful for the moth's directional hearing[4] and also show agreement with simulations.

Future work will look to produce the samples in piezoelectric materials to take the first step in the development of a novel bio-inspired transducer. Additionally, exploring different materials with other mechanical properties that bring down the resonant frequencies to the human audio range will also be investigated.

ACKNOWLEDGMENTS

The authors would like the acknowledge the help of Lisa Asciak in determining the Young's Modulus of the samples via compression testing.

REFERENCES

[1]P. S. Bychkov, V. M. Kozintsev, A. V. Manzhirov, and A. L. Popov, "Determination of Residual Stresses in Products in Additive Production by the Layer-by-Layer Photopolymerization Method," Mech. Solids **52**, 524–529 (2017). doi:10.3103/S0025654417050077

[2]W. H. Cade, M. Ciceran, and A. M. Murray, "Temporal patterns of parasitoid fly (Ormia ochracea) attraction to field cricket song (Gryllus integer)," , doi: 10.1139/z96-046. doi:10.1139/z96-046

[3]K. H. Dahm, D. Meyer, W. E. Finn, V. Reinhold, and H. Röller, "The olfactory and auditory mediated sex attraction in Achroia grisella (Fabr.)," Naturwissenschaften **58**, 265–266 (1971). doi:10.1007/BF00602990

[4]L. Díaz-García, A. Reid, J. Jackson-Camargo, and J. F. C. Windmill, "Towards a bio-inspired acoustic sensor: *Achroia grisella*'s ear," , doi: 10.1109/JSEN.2022.3197841. Presented at the IEEE Sensors Journal. doi:10.1109/JSEN.2022.3197841

[5]R. Domingo-Roca, B. Tiller, J. C. Jackson, and J. F. C. Windmill, "Bio-inspired 3D-printed piezoelectric device for acoustic frequency selection," Sens. Actuators Phys. **271**, 1–8 (2018).

[6]J. L. Eaton, *Lepidopteran anatomy*, (New York; Chichester; Brisbane, J. Wiley & Sons, 1988).
[7]R. S. Edgecomb, D. Robert, M. P. Read, and R. R. Hoy, "The tympanal hearing organ of a fly: phylogenetic analysis of its morphological origins," Cell Tissue Res. **282**, 251–268 (1995). doi:10.1007/BF00319116
[8]J. D. Ellis, J. R. Graham, and A. Mortensen, "Standard methods for wax moth research," J. Apic. Res. **52**, 1–17 (2013). doi:10.3896/IBRA.1.52.1.10
[9]H. Gong, M. Beauchamp, S. Perry, A. T. Woolley, and G. P. Nordin, "Optical approach to resin formulation for 3D printed microfluidics," RSC Adv. **5**, 106621–106632 (2015).
[10]M. Greenfield, and J. Coffelt, "Reproductive Behaviour of the Lesser Waxmoth, Achroia Grisella (Pyralidae: Galleriinae): Signalling, Pair Formation, Male Interactions, and Mate Guarding," Behaviour **84**, 287–314 (1983). doi:10.1163/156853983x00534
[11]M. D. Greenfield, "Acoustic Communication in the Nocturnal Lepidoptera," Animal Signals and Communication, in *Insect Hearing and Acoustic Communication*, edited by B. Hedwig (Berlin, Heidelberg, Springer, 2014) pp. 81–100.
[12]M. D. Greenfield, and M. Baker, "Bat Avoidance in Non-Aerial Insects: The Silence Response of Signaling Males in an Acoustic Moth," Ethology **109**, 427–442 (2003). doi:https://doi.org/10.1046/j.1439-0310.2003.00886.x
[13]L. Knopek, and C. Hintze-Podufal, "Uber den Bau der abdominalen Tympanalorgane der Kleinen Wachsmotte Achroia grisella (Fbr.)," Zool. Jahrbuecher Abt. Fuer Anat. Ontog. Tiere **1141**, 83–93 (1986).
[14]A. W. Leissa, *Vibration of Plates*, (Scientific and Technical Information Division, National Aeronautics and Space Administration, 1969).
[15]D. Mackie, J. Jackson, J. Brown, D. Uttamchandani, and J. Windmill, "Directional acoustic response of a silicon disc-based microelectromechanical systems structure," Micro Nano Lett. **9**, 276–279 (2014). doi:10.1049/mnl.2013.0677
[16]L. Meirovitch, *Analytical Methods in Vibrations*, (Macmillan, 1967).
[17]A. Michelsen, A. V. Popov, and B. Lewis, "Physics of directional hearing in the cricket Gryllus bimaculatus," J. Comp. Physiol. A **175**, 153–164 (1994). doi:10.1007/BF00215111
[18]R. N. Miles, D. Robert, and R. R. Hoy, "Mechanically coupled ears for directional hearing in the parasitoid fly Ormia ochracea," J. Acoust. Soc. Am. **98**, 3059 (1998). doi:10.1121/1.413830
[19]A. Reid, *Directional hearing at the micro-scale: bio-inspired sound localization*, (University of Strathclyde, 2017).
[20]A. Reid, J. C. Jackson, and J. F. C. Windmill, "Voxel based method for predictive modelling of solidification and stress in digital light processing based additive manufacture," Soft Matter **17**, 1881–1887 (2021). doi:10.1039/D0SM01968B
[21]A. Reid, T. Marin-Cudraz, J. F. Windmill, and M. D. Greenfield, "Evolution of directional hearing in moths via conversion of bat detection devices to asymmetric pressure gradient receivers," Proc. Natl. Acad. Sci. **113**, E7740–E7748 (2016).
[22]A. Reid, J. F. Windmill, and D. Uttamchandani, "Bio-inspired sound localization sensor with high directional sensitivity," Procedia Eng. **120**, 289–293 (2015).
[23]D. Robert, "Directional Hearing in Insects," Springer Handbook of Auditory Research, in *Sound Source Localization*, edited by A. N. Popper and R. R. Fay (New York, NY, Springer, 2005) pp. 6–35.
[24]J. Schul, M. Holderied, D. Von Helversen, and O. Von Helversen, "Directional hearing in grasshoppers: neurophysiological testing of a bioacoustic model," J. Exp. Biol. **202**, 121 (1999).
[25]H. G. Spangler, "Attraction of Female Lesser Wax Moths (Lepidoptera: Pyralidae) to Male-Produced and Artificial Sounds," J. Econ. Entomol. **77**, 346–349 (1984). doi:10.1093/jee/77.2.346
[26]H. G. Spangler, M. D. Greenfield, and A. Takessian, "Ultrasonic mate calling in the lesser wax moth," Physiol. Entomol. **9**, 87–95 (1984). doi:https://doi.org/10.1111/j.1365-3032.1984.tb00684.x
[27]H. G. Spangler, and C. L. Hippenmeyer, "Binaural phonotaxis in the lesser wax moth, Achroia grisella (F.) (Lepidoptera: Pyralidae)," J. Insect Behav. **1**, 117–122 (1988). doi:10.1007/BF01052508
[28]B. Tiller, A. Reid, B. Zhu, J. Guerreiro, R. Domingo-Roca, J. Curt Jackson, and J. F. C. Windmill, "Piezoelectric microphone via a digital light processing 3D printing process," Mater. Des. **165**, 107593 (2019). doi:10.1016/j.matdes.2019.107593
[29]J. F. V. Vincent, and U. G. K. Wegst, "Design and mechanical properties of insect cuticle," Arthropod Locomotion Systems: from Biological Materials and Systems to Robotics, Arthropod Struct. Dev. **33**, 187–199 (2004). doi:10.1016/j.asd.2004.05.006
[30]D. Wu, Z. Zhao, Q. Zhang, H. Jerry Qi, and D. Fang, "Mechanics of shape distortion of DLP 3D printed structures during UV post-curing," Soft Matter **15**, 6151–6159 (2019). doi:10.1039/C9SM00725C
[31]J. Wu, Z. Zhao, C. M. Hamel, X. Mu, X. Kuang, Z. Guo, and H. J. Qi, "Evolution of material properties during free radical photopolymerization," J. Mech. Phys. Solids **112**, 25–49 (2018). doi:10.1016/j.jmps.2017.11.018
[32]Y.-P. Zha, Q. Chen, and C. Lei, "Ultrasonic hearing in moths," Ann. Société Entomol. Fr. **45**, 145–156 (2009). doi:10.1080/00379271.2009.10697598
[33]Y. Zhang, R. Bauer, J. C. Jackson, W. M. Whitmer, J. F. Windmill, and D. Uttamchandani, "A low-frequency dual-band operational microphone mimicking the hearing property of Ormia ochracea," J. Microelectromechanical Syst. **27**, 667–676 (2018).

Appendix D

Bioinspiration & Biomimetics review paper

Reprinted from L. Díaz-García, B. Latham, A. Reid, and J. Windmill, "Review of the applications of principles of insect hearing to microscale acoustic engineering challenges," Bioinspiration & Biomimetics, vol. 18, p. 051002, Aug. 2023. Publisher: IOP Publishing. [218].

IOP Publishing Bioinspir. Biomim. 18 (2023) 051002 https://doi.org/10.1088/1748-3190/aceb29

Bioinspiration & Biomimetics

OPEN ACCESS

RECEIVED
31 January 2023

REVISED
23 May 2023

ACCEPTED FOR PUBLICATION
27 July 2023

PUBLISHED
14 August 2023

TOPICAL REVIEW

Review of the applications of principles of insect hearing to microscale acoustic engineering challenges

Lara Díaz-García*, Brendan Latham, Andrew Reid and James Windmill

Centre for Ultrasonic Engineering, University of Strathclyde, Glasgow, United Kingdom
* Author to whom any correspondence should be addressed.

E-mail: lara.diaz-garcia@strath.ac.uk

Keywords: bioacoustics, bioinspiration, insect hearing, acoustic sensors

Abstract

When looking for novel, simple, and energy-efficient solutions to engineering problems, nature has proved to be an incredibly valuable source of inspiration. The development of acoustic sensors has been a prolific field for bioinspired solutions. With a diverse array of evolutionary approaches to the problem of hearing at small scales (some widely different to the traditional concept of 'ear'), insects in particular have served as a starting point for several designs. From locusts to moths, through crickets and mosquitoes among many others, the mechanisms found in nature to deal with small-scale acoustic detection and the engineering solutions they have inspired are reviewed. The present article is comprised of three main sections corresponding to the principal problems faced by insects, namely frequency discrimination, which is addressed by tonotopy, whether performed by a specific organ or directly on the tympana; directionality, with solutions including diverse adaptations to tympanal structure; and detection of weak signals, through what is known as active hearing. The three aforementioned problems concern tiny animals as much as human-manufactured microphones and have therefore been widely investigated. Even though bioinspired systems may not always provide perfect performance, they are sure to give us solutions with clever use of resources and minimal post-processing, being serious contenders for the best alternative depending on the requisites of the problem.

1. Introduction

Bioinspired hearing requires a fundamentally different design paradigm. In nature, the peripheral sensory organs, the eyes, ears, or skin, are rarely passive recorders of their environment. They possess complex filtering, processing, and encoding functions that are built in to the material and structure at every level: from the atomic, through the cellular, to tissue structure, and organ structure. Such signal processing can be mechanical, such as the decomposition of sound into frequency bands that is famously performed by the mammalian cochlea [1], or the result of intercellular chemical or electrical communication [2], but a distinct characteristic is that the signal transduction and signal processing functions are integrated and inseparable. This necessity is enforced by the sparse, event-driven nature of signals transmitted to higher brain centres [3]. The signal complexity is limited to what may be encoded in the temporal pattern of a spike train [4].

In contrast, engineered sensors view transduction as a separate function. The transducer's output is a continuous in the time-domain, rather than event driven. This 'raw' signal must be appropriately filtered, encoded and efficiently transmitted in order to extract useful information. If we could borrow nature's trick of integrating this signal processing into the structure of the transducer we could unlock significant improvements in energy-efficiency, signal latency, bandwidth reduction, and device footprint. All of these areas are critical constraints on sensor networks [5], internet of things [6] and human wearable and implantable sensors [7].

Three of the most basic problems faced by animals and shared across species are the following [8–11]:

- Distinguishing conspecific communication from predator sounds.
- Localising the position of a potential prey, predator, or mate.
- Detecting weak sound signals that deteriorate as they propagate in their natural environment.

Body size compounds the complexity of these issues: sound emission and detection efficiency tend to decrease with the size of the acoustic sensor, the ability to locate sounds (and predators) when listening diminishes with diminishing space between the sensors, and that the frequency band available for communication is limited by predation and by the acoustic transmission properties of its environment [12]. The evolutionary adaptations to the physics of acoustic waves provide unique solutions to reducing the energy (and metabolic) cost of detection, to frequency decomposition, and to locating sound sources with miniscule available directional cues from the sound field. Acoustic systems at the micro-scale may draw particular inspiration from insect hearing and communication due to the constraint of insects' small body size.

Using sound to locate potential mates and to avoid predators is a common evolutionary tactic, with hearing in insects known to have evolved independently between 15 and 20 times [13]. The methods of detection can be grouped into pressure detection systems and particle velocity detection systems. In general, particle velocity detection systems are hair-like near-field, low-frequency mechano-receptors, reliant on light weight and high specific surface area in order to translate the velocity dependent viscous drag force into a detectible vibration [14]. They are often used to detect low frequency sound (less than 500 Hz) or reactive flow in the near field of an emitter, such as the mosquito antenna which is used to detect the flight disturbance from a nearby mate [15]. This paradigm has, however, been challenged recently by evidence that mosquitoes can in fact behaviourally react to sounds up to 10 m away [16]. Pressure receivers are exclusively tympanal systems, operating in the far field [17] and capable of detecting sound into the far ultrasound range [18].

Gathering inspiration from the way these problems are solved in nature has proved to be a successful path towards innovative engineering solutions. Thus, the motivation of this review is to provide a comprehensive compilation of the mechanical solutions implemented in technology that are inspired by insects and further encourage bio-inspiration as a source for innovative engineering solutions.

The body of this paper is structured in three distinct sections, each one referring to one of the three fundamental aforementioned problems. In addition, each section is divided in two subsections. The first one concerns some paradigmatic insect solutions for its corresponding problem and the second one covers engineering solutions arising from bio-inspiration of said insects.

The section 2.1 refers to spatial frequency decomposition and comprises some example cases of how insects deal with this problem and the technological solutions inspired by it. The section 3.1 verses on the direction of arrival estimation and it covers some of the most notable nature example solutions and the sensors inspired by them. Lastly, the section 4, active hearing, follows the same structure of natural examples and technology inspired by them. A section 5 finishes the manuscript.

2. Tonotopy

Frequency discrimination can be a matter of life and death for an organism. Sound communicates information. The purpose of all acoustic systems in biology is to get that information to the animal to elicit the appropriate behavioural response. One information component of sound is its frequency, and as much as the animal's survival and reproduction can depend on the organism's ability to distinguish key frequencies from its environment. Not doing so could mean a moth failing to evade the approaches of a predatory bat [19–21] or a female cricket failing to localise the position of a potential mate [22, 23].

2.1. Spatial frequency decomposition: cochlea and tympana

All ears must translate acoustic energy travelling through a medium, usually air, into mechanical motion, and then to electrical impulses. Electrical impulses are generated by neurons and, in acoustics specifically, by auditory mechanoreceptor cells, neurons with mechanically gated ion channels that require an acoustic-mechanical stimulus to fire an action potential [24]. Frequency selectivity is a difficult aspect of insect communication, since the spike train from a sensory neuron cannot encode frequency information in their signal. To have a means of discriminating frequencies, multiple such neurons must be individually tuned. A very simple ear, such as those of moths cannot passively distinguish between the frequencies of a predatory bat and the call of a potential mate, relying instead of differentiating the temporal structure of the mating call and the pulses of a bat's echolocation [25]. Individual tuning of multiple cells can be achieved by the arrangement of the neurons according to a morphological gradient. Morphological variation of a substrate—for example, some areas being thicker, thinner, wider, or narrower—in the cells' proximity can cause different points on the substrate to move differently according to the input frequency. This frequency-specific maximal displacement of the point, if coupled somehow to a sensory neuron, can in turn stimulate that neuron independently, thus tuning the cell to a single frequency. This place-based frequency decomposition is called *tonotopy*.

A second problem is that of the acoustic environment, since mating calls must compete with the potentially masking calls of other species without unnecessarily attracting the attention of predators

[26]. These mating calls are frequently pure tone signals, reflecting their reliance on resonant structures to transmit the necessary power to attract a mate as well as the need to seek unoccupied space in the locally available acoustic spectrum [27]. This places some constraints on the available communication bandwidth, since the resonant frequency is determined by the size of the radiator and, in order to transmit efficiently, the resonant structure should have a diameter approaching half of the signal wavelength [28]. There is a reproductive and survival advantage from the ability to distinguish the frequency composition of predators and competing species. In flagellar systems such as the mosquito [29], as well as some tympanal systems such as the tree cricket *Oecanthus henryi* [30] and the Noctuid moth [31], this frequency tuning is achieved by active amplification where the mechanosensory cells can produce sufficient power to drive the ear at the frequency of interest. This strategy is discussed in section 4. In this section, we discuss dispersive frequency decomposition, where sound travels and is localized to particular sites based on its frequency.

Dispersive frequency decomposition relies on a travelling wave, which is typically a flexural mode on the thin medium. The most well-known example of this is the travelling wave associated with the basilar membrane of the mammalian cochlea [32, 33]. An acoustic impulse applied to the narrow end of the wedge-shaped structure encounters a stiffness gradient. The wave shoals, increasing in amplitude whilst also slowing down until finally maximal vibration of the membrane is reached at a specific point along the membrane's length; afterwards, the wave rapidly decreases in amplitude. High-frequency stimuli terminate at a point near the narrow end, and those of lower frequency, near the wide end. Sensory neurons arranged linearly along the length of the substrate respond accordingly: a mechanoreceptor cell at a narrow region is activated only by a high frequency stimulus; a cell further along only responds to a lower frequency.

In contrast to vertebrates, among invertebrates, tonotopic systems are considerably rarer, and yet invertebrates also showcase the most diversity of system design. Moreover, invertebrate tonotopy is less understood and provides greater scope for novel discovery. Such ears can be categorised into two types, cochlea-type tonotopic systems and tympanal tonotopic systems. Both are exemplified by the bushcricket and the locust, respectively.

The bushcricket ear appears to possess the only insect cochlea yet identified [38], although some sort of cochlea analogue has been hypothesised for the cricket [39]. Bushcrickets (also known as katydids) are orthopterans, alongside crickets and grasshoppers, the latter including locusts. Their two ears (one on each of their two front legs) consist of two external tympanal membranes on either side of the leg, making four eardrums in total. Features of the bushcricket ear are reminiscent of the vertebrate peripheral auditory anatomy in terms of function. These include the tympanal plate, possibly functioning as a middle ear; and the *crista acustica*, the bushcricket's inner ear or cochlea [40] (see figure 1).

The most noticeable characteristic of the bushcricket *crista acustica* is its tapered shape and orderly arrangement of *sensilla* (figure 1(A)). The 25 or so sensory neurons are tonotopically arranged from high frequency tuned cells at the narrowest tip of the organ (up to and above around 50 kHz) to those tuned to lower frequencies its wider end (tuned from about 6 kHz) [41]. These sensors lie on a thin wall of a cuticular cavity, the anterior tracheal branch. Their dendrites project upwards dorsally, and each connects to a cap cell which is itself attached to a thin sheet that covers the entire organ, the tectorial membrane. Notably, the size gradient of these cap cells is correlated with the tonotopy. Nevertheless, the correlation is not strong enough to account for the full resolution of frequency representation. Rather, the tonotopy may require another morphological gradient such as features of the sensors themselves [35]. This arrangement appears to facilitate a travelling wave across the tectorial membrane, differentially stimulating the sensory cells according to frequency. The wave is initiated at the organ's narrow end and travels along the membrane towards the low frequency tuned sensors, terminating closer to the wider tip at low frequency impulses and closer to the point of initiation at higher frequencies [34].

The other type of tonotopic mechanism is not at all like a cochlea, and in fact has no comparison among the vertebrates. In tympanal tonotopic systems, known in the locust [37] and in the cicada [42], the tympanum, responsible for sound capture, is also responsible for frequency decomposition; both functions occur at the same substrate. This dual functionality requires the eardrums to be unusually complex, and indeed the locust tympanal membrane may be considered the most sophisticated tympanum yet identified.

Locusts have two tympana, one on each side of their abdomen. Around 70 mechanoreceptor cells attach to the underside of each tympanum, forming Müller's organ, a ganglion of *sensilla* divided into four groupings. Three of these are tuned to low-frequency bands (3.5–4, 4, and 5.5–6 kHz) and one to high frequencies (12–20 kHz) [36, 47]. Each sensory group is secured to its own specific morphologically unique tympanal feature (figure 1(C)). In addition, the locust eardrum exhibits further, larger-scale heterogeneity in the form of two parts to the tympanum, a thin membrane and a smallerthicker membrane (figure 1(D)). High-frequency mechanoreceptors attach to a point on the thin region, whereas the

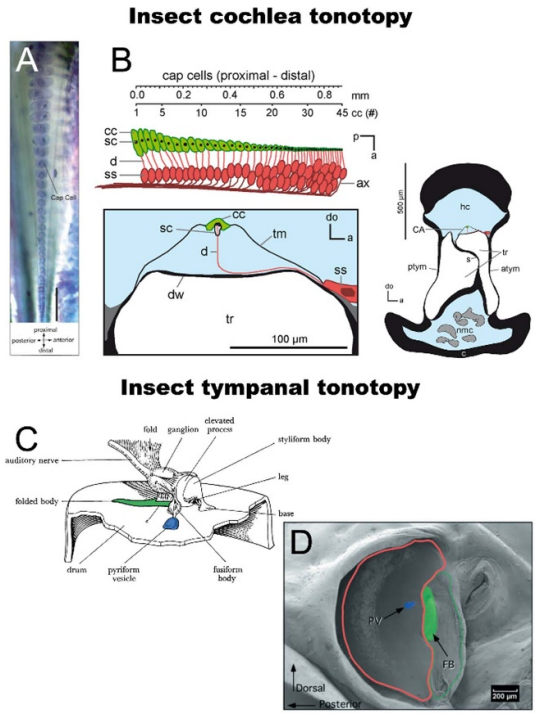

Figure 1. (A) Bushcricket crista acustica stained with methylene blue [34]. Reproduced from [34]. CC BY 4.0. (B) Anatomy of the crista acustica [35]. Used with permission of John Wiley & Sons - Books, from [35]; permission conveyed through Copyright Clearance Center, Inc. (C) Anatomy of the four locust mechanoreceptor attachment points on the underside of the tympanum [36]. Adapted to highlight the same points shown in the adjacent image, (D). Used with permission of The Royal Society (U.K.), from [36]; permission conveyed through Copyright Clearance Center, Inc. (D) SEM of the external surface of the locust tympanum [37]. Red outline: thin membrane; green outline: thick membrane; blue feature: attachment point of mechanoreceptors tuned to high frequencies; green highlight: attachment area of low frequency sensors. Used with permission of The Company of Biologists Ltd., from [37]; permission conveyed through Copyright Clearance Center, Inc.

others connect to fixtures of the much thicker membrane [37, 48]. Thus, a degree of morphological gradation is provided, enabling travelling waves. When stimulated with sound, a travelling wave is initiated in the thin membrane that maximally vibrates the tympanum at one of the four locations, depending on the stimulus frequency. At frequencies above 10 kHz, no movement of the thick membrane is detected. Rather, the travelling wave terminates at the high-frequency attachment point, rapidly attenuating when reaching the thicker cuticle. As such, there is a clear spatial frequency decomposition of high and low frequencies [37].

2.2. Bio-inspired frequency discriminating sensors

Engineered systems based on spatial frequency decomposition frequently target sub-Nyquist rate sampling as the value of their system [49]. An analogue to digital converter has a maximum sampling rate, and increasing this sampling rate lowers signal-to-noise ratios and increased power requirements [50]. A signal which is already filtered can be captured with lower sampling frequencies, and yet retain a higher effective sampling rate that can be significantly compressed by only retaining content when it is above a threshold. This strategy has been applied using electronic filter banks [51], and even converted to an output spike train to mimic the event-driven format of nerve conduction [52]. Mechanical filtering of the signal can be grouped into solutions using an array of resonators (figures 2(A) and (D)) [43, 46] or solutions using a tapered membrane [53].

Resonator arrays perhaps are the most obliquely connected to the natural inspiration, but they are simple to implement on silicon as arrays of cantilevers (figure 2(B)) [44] or clamped-clamped beams (figure 2(C)) [45]. The resonant frequency of each channel can be adjusted by changing the length of the beam; and transduction of the signal may be accomplished by piezoelectric [54, 55], triboelectric [45] or optical means [56]. While relatively easy to implement, using a beam as a method of acoustic capture is extremely inefficient for lower frequencies due to diffraction around the relatively narrow beam width. The pressure difference between the front and back sides of the cantilever is small, resulting in maximum displacements at resonance in the order of tens of nanometres [57]. The resultant electrical transduction and signal-to-noise level are also prohibitively small since the cantilevers may not rely on capacitive sensing through an electrical backplate, as in a traditional microphone, due to the impact of thin film damping on both the mechanical sensitivity of the device and the resonance frequency [58, 59]. Piezoelectric sensing can be used with the ceramic element implemented either on the upper surface with interdigitated electrodes [43], or by fabricating the cantilever as a bimorph [60]. However, both strategies produce piezoelectric charge sensitivities in the order of femto-Coulombs per nm. One strategy to overcome this limitation in micro-electromechanical system (MEMS) consists of using a thickened or disc-shaped central region in the arrays, maintaining a thin base region for the purposes of keeping a desired resonance frequency while maximising the surface area for acoustic capture (figure 2(E)) [61].

Frequency decomposition based on tapered membrane structures is closer to bio-inspired sources, consisting of a single membrane with significant acoustic dispersion to isolate the frequency bands. Such systems have two fundamental requirements: there must be a time-dependent pressure gradient along the membrane to support flexural wave propagation, and the wave velocity must change along the length of the membrane. The support of

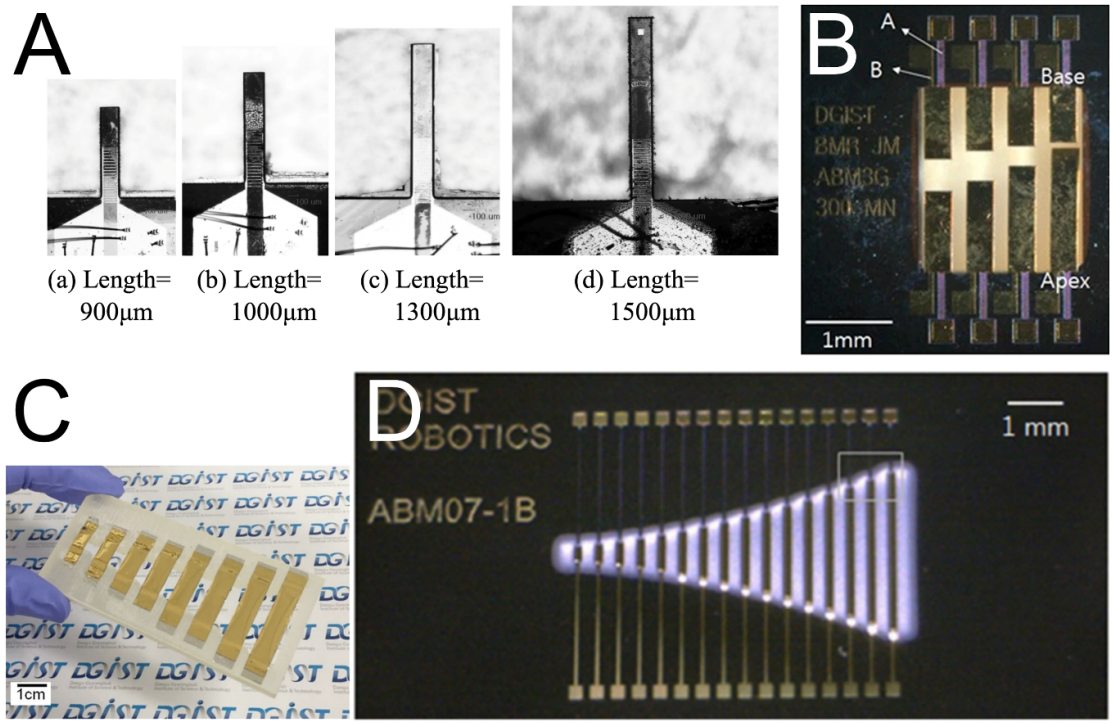

Figure 2. Array of resonator approaches to mechanical tonotopy (A) Single crystal PMN-PT cantilevers with interdigitated electrodes [43] Reproduced from [43], with permission from Springer Nature. (B) Dual sided cantilever array [44] Reproduced from [44]. CC BY 4.0. (C) Clamped-clamped array with triboelectric transduction [45]. Bottom row shows solutions to achieving desired frequency while maximising surface area for mechanical sensitivity. Used with permission of John Wiley & Sons - Books, from [45]; permission conveyed through Copyright Clearance Center, Inc. (D) Tapered clamped-clamped beam array [46]. Reproduced from [46]. © 2013 IOP Publishing. Reproduced with permission. All rights reserved.

a travelling flexural wave can be achieved by having a defined, highly localized sound input point, analogous to the oval window in the mammalian cochlea (figure 3(A)) [53, 62], or by ensuring the membrane length is between 1/6 and 1/4 of the frequency range of interest to ensure a phase difference across the membrane surface (figure 3(B)) [63, 64]. Both solutions have limitations, since restricting the sound input to a single point restrains the power that may be captured by the device, and tailoring the membrane length to the phase difference in the incoming sound wave either requires prohibitively large membranes or a highly restricted high-frequency range of interest.

The second requirement for acoustic dispersion is equally challenging to meet within the constraints of MEMS systems. The most obvious source of generating dispersion is through the tapering of the thickness of the membrane, based on an Euler–Bernoulli model of a thin plate where the bending wave speed may be given by [65]:

$$c_b = \left(\frac{Eh(x)^2 \omega^2}{12\rho(1-\nu^2)} \right)^{\frac{1}{4}}$$

where ρ is the density, ω is the angular frequency, E is the Young's modulus, ν is the Poisson's ratio, and $\boldsymbol{h}(\boldsymbol{x})$ is the thickness profile. In theory, for every frequency, there is a height below which the wave speed will drop to the point where it is no longer transmitted, or at least may be assumed to be sufficiently attenuated, analogous to the acoustic black hole effect described by Mironov and Pislyakov [66]. In practice, the variation in thickness would need to be two orders of magnitude over the length in order to separate frequency bands in the acoustic range using a common MEMS material such as single-crystal silicon.

The more commonly seen model varies the width of the membrane along its length, which should not result in variation of the phase velocity [67]. Instead, such systems rely on the membrane being placed on a closed channel, or either air or some fluid medium, such as water [68] or silicon oil [64]. The variation of the velocity of fluid flow in this channel generates a variation in the velocity potential [69], and hence the local pressure on the membrane; while the depth of the fluid channel increases, the fluid loading on the membrane reduces the resonance frequency (figure 3(C)) [70]. This, in combination with the slight spatial variation of the membrane's first-order resonance peak with frequency, results in some degree of tonotopy. Despite the size of these membranes, over 5 cm in length, they have extremely low mechanical responses at the resonance of less than a micron displacement and are only able to separate a few, widely separated frequency bands with poor spatial confinement compared to examples in nature.

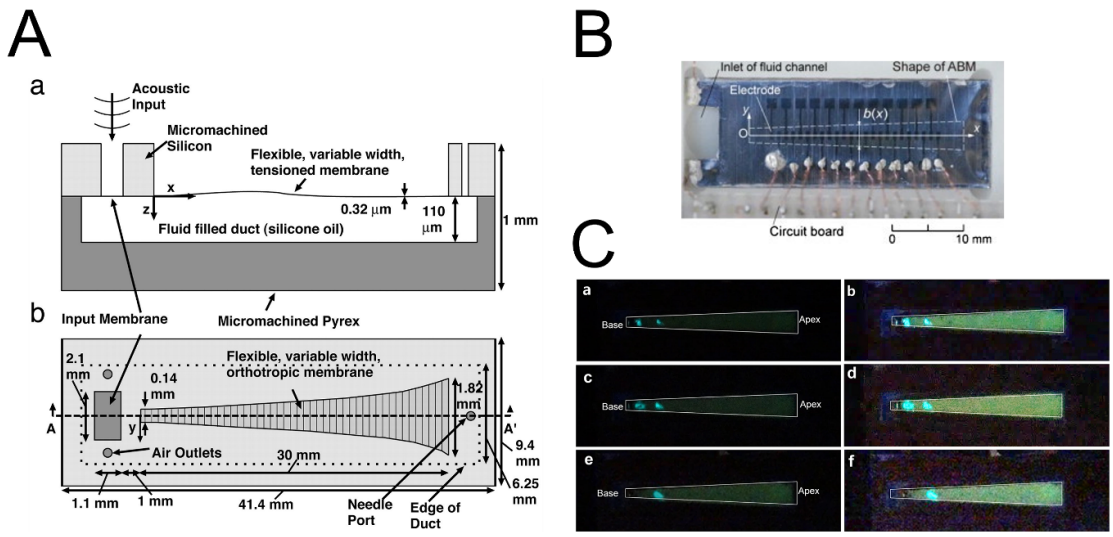

Figure 3. Continuous membrane approaches to tonotopy, which have one single graded sensing area with a localized transduction mechanism. (A) Hydromechanical model of the basilar membrane with silicon oil backing [53], [53] Copyright (2005) National Academy of Sciences, U.S.A. (B) Fluid backed tonotopic sensor using PVDF as the membrane with individual measurement points [64]. Reprinted [64], Copyright (2010), with permission from Elsevier. (C) Luminescent tapered membrane showing some frequency separation at very low frequencies (a), (b) 110 Hz; (c), (d) 80 Hz; (e), (f) 40 Hz [54]. Reproduced from [54]. CC BY 4.0.

3. Directionality

The localization of sound sources by small animals is a fundamental problem in bioacoustics. Where body size is diminutive and inter-ear distance is short, an animal cannot rely on comparison between the intensity difference or time delay of signals received at either ear. For many animals, the detection of a sound is sufficient. For example, all but one of the 10–12 independent origins of hearing in *Lepidoptera* occurred later than 65 Ma, the currently accepted date for the appearance of echolocation in bats [71]. The hearing that evolved in these moths is extremely simple, consisting of only 1–4 neurons per tympanum [72], minimum tuning over a broad frequency range [73], and limited or no directionality, yet it remains highly effective for escaping predatory bats [74]. Moths exposed to bat echolocation signals exhibit random evasive movement, diving towards the ground if in flight and freezing behaviour if running on the substrate [75]. Knowing exactly where the bat is coming from does not change the moth's response and it is not worth the evolutionary cost of developing directional hearing. For an insect on the other face of the prey-predator relationship, for parasites, or for finding the source of a conspecific mating call, it is necessary also to know the direction of the source of the sound.

Bilateral symmetry means that most animals have two ears, one for each half of their body (one notable exception is the praying mantis, which possesses only one ear [76]). Directional hearing in larger animals may be achieved by inter-aural intensity differences (IIDs), where sound shadowing from the body creates an appreciable level difference between the ears; or inter-aural time differences where the basis of comparison is the time difference of arrival between the ears. For an insect where the body length is a fraction of the wavelength of a relevant sound source, the acoustic shadow is minimal, and time differences of arrival may be measured in nanoseconds [77].

This section looks exclusively at tympanal hearing systems, as systems which have the closest analogy to the traditional microphone. Particle detection hearing systems are inherently directional, responding to the velocity vector of the sound field however such systems are far less sensitive to far-field sound and higher-frequency sound fields.

3.1. Direction of arrival estimation from tympanal structure

Ormia ochracea has undoubtedly inspired the greatest number of engineering designs which seek to mimic the unique coupling mechanism between its tympana. *O. ochracea* is a fly parasitoid of crickets, locating its host *Gryllus* by phonotaxis to the cricket's mating calls [78]. The auditory system of *O. ochracea* has long been of interest to researchers due to the uncanny accuracy with which it can locate the host call, a 5 kHz pure tone with a wavelength of over 10 times the body length of *O. ochracea* and 100 times the separation between the insect's tympana. This insect has directionality down to an accuracy of 2° in the azimuthal plane [77]. The system consists of two diaphragms mechanically connected by a bridge and pivot allowing the transfer of energy from the motion of one diaphragm to another (figures 4(A) and (D)) [79]. When the stiffness of this connecting bridge is

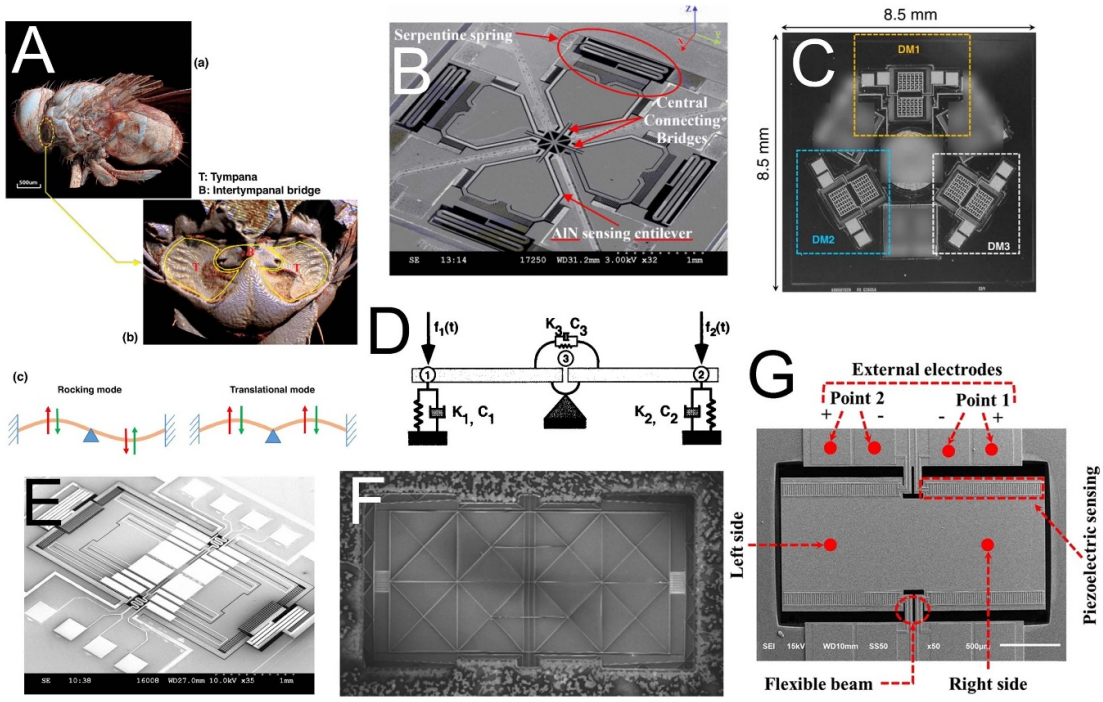

Figure 4. (A) Micro-CT images of tympanal system of *O. ochracea*. Arrays of Ormia inspired membranes [83]. Reproduced from [83]. CC BY 4.0. (B) four coupled membranes [81] © [2018] IEEE. Reprinted, with permission, from [81]. (C) Array of 3 see-saw style Ormia membranes [84]. Reproduced from [84]. CC BY 4.0. (D) Illustration of rocking and translational mode along with standard two degree of freedom model of the Ormia system [80]. Reproduced from [80], with permission from Springer Nature. SEM images of Ormia membranes targeting low acoustic frequencies using (E) silicon-on-insulator MEMS [83] Reproduced from [83]. CC BY 4.0. and (F) Silicon nitride patterning [85]. Reprinted with permission from [85]. Copyright [2009], Acoustic Society of America. (G) Transduction of membrane motion using capacitive comb sensing [86]. Reproduced from [86]. CC BY 4.0.

correctly tailored to the system, the signals from the stimulating sound wave and the linked companion diaphragm will constructively interfere with the ipsilateral sound source and destructively interfere with the contralateral sound source. The result is what was termed by Robert *et al* [80] mechanical interaural phase difference and mechanical IID which can be 40 times higher than the phase difference in the stimulating sound field. Much of the research into *Ormia*-inspired systems targets applications in hearing aids [81, 82]; however, there is an inherent conflict: the *Ormia*'s coupled ears are a resonant system and so single-frequency, while hearing aids, or teleconferencing applications require broadband sound source localization.

A potentially different tactic is employed by *Achroia grisella*. *A. grisella* is a moth of the *Pyralidae* family within the *Lepidoptera* order, known as the Lesser Wax Moth. It is less than 13 mm long and principally known as a parasite of unhealthy bee colonies, on which they deposit their eggs and on which their larvae feed. The unusual aspect of *Achroia* is the use of ultrasonic calling as a mating signal, and their use of phonotaxis rather than anemotaxis to track their preferred mate [87]. As discussed in the introduction to this section, simple hearing systems are widespread among nocturnal Lepidopters, but evidence of directional response is sparse save for some limited negative phonotaxis in Noctuids [88]. In contrast to hearing, acoustic communication in moths is rare and occurs only among isolated species and genera in the three major clades [71]. In many cases, acoustic communication is restricted to close-range courtship where directional hearing would not be critical [89]; however, *A. grisella* can transmit and track sound signals over distances over 2 m, making a sound localization capability expected. Unlike *O. ochracea*, whose acoustic perception of host crickets has probably evolved de novo, *A. grisella* already had an evolutionary ancient system for perceiving sound, and the mechanism for localization reflects an adaptation of the tympana as bat detectors to a new purpose [90, 91].

The tympana of *A. grisella* are located ventrally on the first abdominal segment (figure 5(A)). They are oval-shaped, between 500 μm and 550 μm long in the females and divided into an opaque anterior section and a transparent posterior section (figure 5(B)) [92]. These two sections of the tympana oscillate in anti-phase when there is no variation in the pressure field across the tympanum (i.e. when the sound wavefronts are planar), with a large peak in displacement near the neuronal attachment point [73, 93, 94]. This vibrational mode remains relatively stable with sound source angle until a 100 kHz sound source is located along the major axis of the

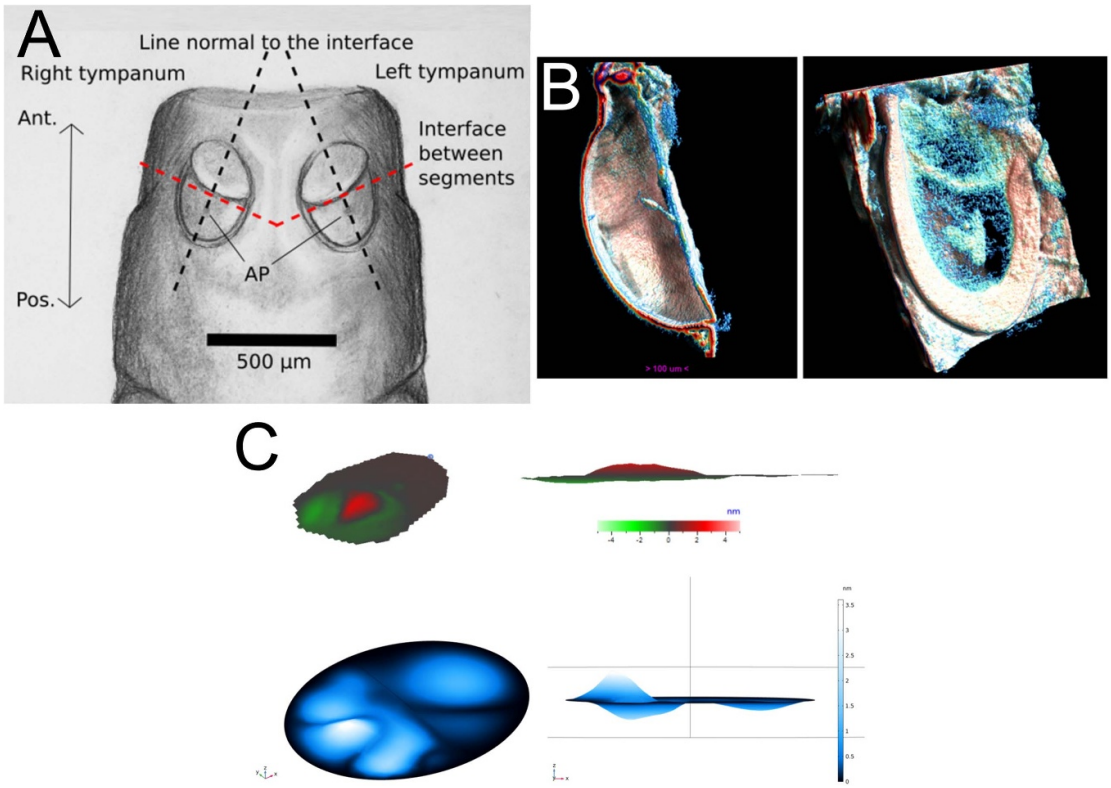

Figure 5. (A) Illustration of the ear location and orientation on the first abdominal segment of A. grisella [94]. Reproduced with permission from [94]. (B) x-ray CT voxel images of the structure of the tympanum showing the scolopale attachment point in the centre of the lower section of the tympanum [102]. © [2022] IEEE. Reprinted, with permission, from [102]. (C) Laser Doppler vibrometry measurement of A. grisella tympanal motion in response to a planar sound field and (top) and COMSOL reconstruction of the membrane (bottom) [102]. © [2022] IEEE. Reprinted, with permission, from [102].

tympanum at which point the peak in displacement near the attachment point grows sharply in magnitude [91].

3.2. Bio-inspired directional sensors

Ormia-inspired directional microphones are undoubtedly the largest class of bio-inspired hearing sensors and, consequently, have in themselves been subject to a number of dedicated reviews [83, 95]. The overwhelming direction of design has been towards a single-layer see-saw design realised in a silicon-on-insulator or related MEMS process, either as a single sensor (figures 4(E) and (F)) or an array (figures 4(B) and (C)) [85, 86, 96, 97]. This operates similarly to the *Ormiine* system, with each of the 'wings' of the device comparable to one tympanum, while the torsional stiffness of the bridge connecting the device to the substrate performs the equivalent function of the raised bridge and fulcrum in *O. ochracea*. The system is attractive to researchers as it is easily implemented in a multi-user MEMS process, and it can, with careful tailoring of the relative stiffness of the membrane wings and the torsional stiffness of the bridge, amplify directional cues in a similar manner to *O. ochracea*. This design path has several challenges which have not yet been overcome besides the inherent resonant nature of the device. The first is the signal-to-noise ratio achievable in this system. As the *Ormia*-inspired microphone relies on the interaction between the resonant modes, a traditional capacitive backplate is generally not used, at least partially because of the thin-film damping such a structure would introduce [84, 98]. Because the system works optimally at the frequency where the in-phase resonance and the out of phase resonance are the same power, increasing the bandwidth of these resonances necessarily means increasing the separation between the frequency peaks of the two modes. This has the effect of lowering the amplification of directional cues, but does broaden the frequency range over which this is possible [99]. Principally, designers avoid this issue entirely by incorporating optical [98] or capacitive comb-based sensing schemes (figure 4(G)) [97, 99]. The first of these adds significantly to the design complexity and cost, while both piezoelectric and capacitive comb-based methods in MEMS devices have low sensitivities [96, 100, 101].

The second obstacle to a good signal-to-noise ratio is more fundamental to the design—as the see-saw mechanism must be released from the periphery except at the anchor points, sound is free to diffract around the device. Since these devices are typically of a maximum size of 1 by 2 mm and the target sound field is in the acoustic range, the pressure difference across the membrane is minimal. This can

be solved by making a more direct model of *Ormia*'s hearing system, however so far all examples have been demonstrated at the mesoscale due to the complexity of fabricating a true 3D structure using lithographic methods [103, 104].

On the other hand, finite element modelling of *A. grisella*'s tympana and tests on 3D-printed models have shown that this single membrane directivity pattern can be replicated in a relatively simple stepped-thickness membrane (figure 5(C)) [102].

4. Active hearing

The third central problem for insect hearing is the inherently low energy of a propagating sound wave over the length scales that the insect can hope to capture. This problem is compounded for velocity sensing organs, such as the antenna in mosquitos and fruitflies, where the mechanism for energy capture is through the viscous drag losses in the antennal hairs [105]. In order to maximise the capture of these sounds and the transduction into neuronal signals, the mechanoreceptor neurons themselves add energy to the system, resulting in a non-linear response to sound [29]. The system is analogous to the active hearing contributions of hair cells in the cochlea; however, in insects, it can be directly observed in antennal systems. The existence of active hearing can be inferred from non-linear response characteristics in tympanal systems in insects, such as otoacoustic emissions or self-generated oscillations, in tree crickets [106] and Katydids [40]; nevertheless, the small scale of these systems and the relatively low number of congregated mechanoreceptors compared to Johnson's organ in the mosquito, make these systems harder to study.

4.1. Particle velocity sensors and active hearing

The champion species for active amplification in flagellar systems is the elephant mosquito, *Toxorhynchites brevipalpis*. The hearing organ consists of an antenna shaft which sits within a pedicel. Mechanically, it acts as a rotational spring, causing the antenna to oscillate in a rigid body motion with a resonant frequency of between 300 and 500 Hz [107]. Within the pedicel is Johnston's organ, a collection of some 16 000 mechanosensory cells arranged in a bowl shape along the base of the antenna. These consist of a scolopale rod which connects the antennal structure to the chordotonal neuron, which both senses the motion of the antenna and can inject additional energy into the antenna's oscillations [108]. If we model this system in a sound field as a passive oscillator, it can be approximated as a damped harmonic oscillator [109, 110]. Such a system will have a defined resonant frequency and a Q factor given by the ratio between resonant frequency and damping, which gives the half-power bandwidth of the resonant response.

Mosquitoes use their auditory receptors for mating purposes, detecting the acoustic signature of a female's wing beats. The female creates an extremely weak and brief sound signal, a sound particle displacement of around 3.5 nm at a distance of 10 cm [29]. As the sound intensity varies so sharply and so quickly with the change in distance between the male and the potential mate, the mosquito requires a sensor with an extremely fast temporal response. Mechanically, this would be a broadband, low Q factor, allowing the detection of higher frequency transients in the signal. Conversely, to successfully track the female, the male must filter out environmental noise for which a broadband sensor would be a poor choice and a sharply resonant, high Q factor sensor would be preferred. The antenna's frequency selectivity in passive hearing is principally determined by the resonance of the flagellum and spring base, which is well-damped and low Q factor [107]. The mosquito maximises its tracking efficiency by switching from the initial passive response to a sharply resonant response through the generation of force in the neurons at the base of the antenna [107]. These neurons fire at twice the frequency of the antenna's sound field-driven oscillation, sharpening the tuning of the resonant frequency (figure 6(A)) [111].

4.2. Bio-inspired active amplification sensors

The concept of active Q control has found applications in atomic force microscopy [112, 113] and in optical amplifiers, where it is referred to as parametric amplification. Rather than directly injecting energy, parametric amplification involves changing some property of the system with a specific phase timing, analogous to a child on a swing. In acoustic systems, the forcing mechanism is usually directly applied to either the membrane or the flagellum through electrostatic actuation, perhaps more analogous to someone pushing a swing. At root, this is a feedback system where the oscillations of the acoustic receiver are filtered through a leaky integrate and fire stage and recombined. In practice, this has meant generating a pulsed actuation signal controlled by a computational control mechanism, designed to fire in time with the oscillations of the incoming microphone signal. A MEMS microphone directly inspired by this principle was demonstrated by Guerreiro *et al* (figure 6(B)) [114, 115], using capacitive combs to inject the pulsed feedback signal. This was a unipolar signal, firing only once per oscillation of the membrane as opposed to the 2:1 mode of the mosquito [111]. The Q factor of the MEMS microphone is already high in the absence of strong damping sources such as thin film damping; however, the feedback mechanism demonstrated an increase of the Q factor from 30 to 66 with a consequent amplification of 2.19 [114].

The mechanism has also been used to lower the effective Q factor in *Ormia*-inspired devices.

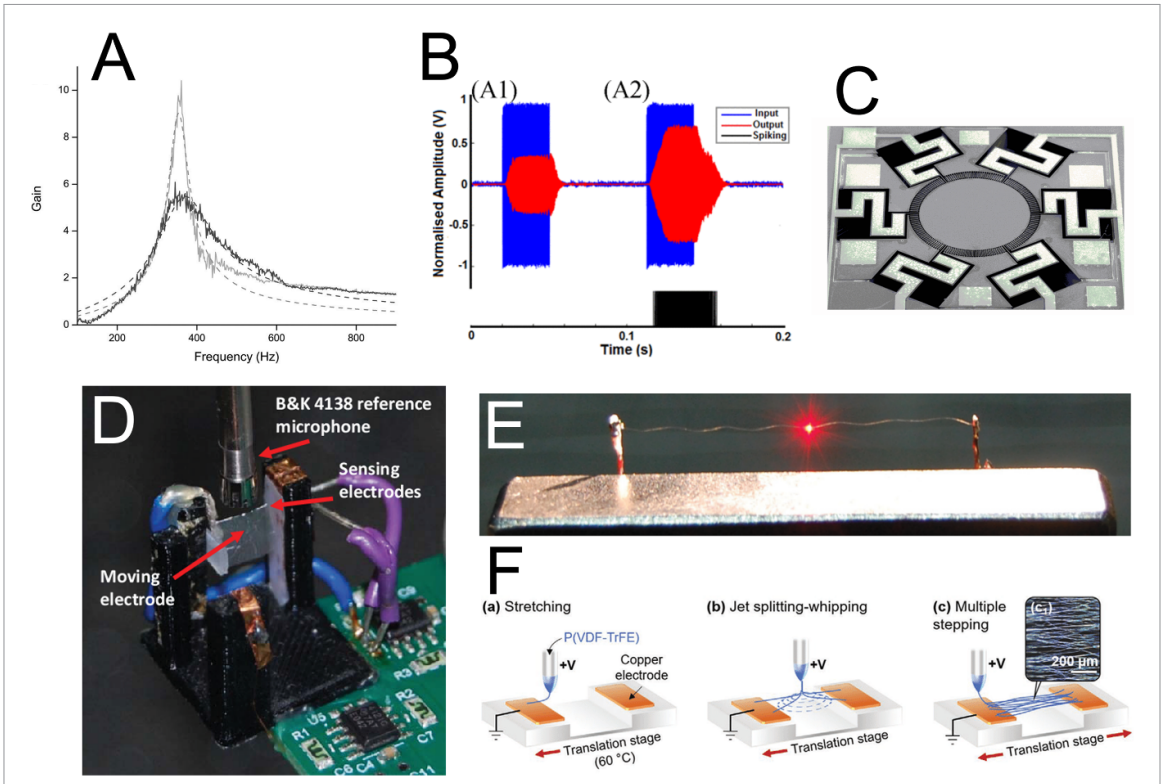

Figure 6. (A) Impact of twice frequency forcing in the mosquito antenna, changing the broadband response of the antenna into a sharp narrowband response [111]. Reprinted from [111] © 2009. Frequency forcing in a MEMS microphone using piezoelectric sensing and capacitive combs to inject the motile force, (B) resultant amplification with forcing [114], © 2018 IEEE. Reprinted, with permission, from [114]. (C) SEM of the membrane design [115]. © 2017 IEEE. Reprinted, with permission, from [115]. (D) Hair sensor microphone using electrostatic transduction [121] © 2019 IEEE. Reprinted, with permission, from [121], and (E) larger scale proof of concept of same using optical sensing [122]. Reproduced with permission from [122]. © 2018 by ASME. (F) Meshed hair sensing using electrospun PVDF [123]. Reproduced from [123]. CC BY 4.0.

As noted, MEMS devices without backplates will experience very light damping and therefore exhibit sharply resonant behaviour which can be a detriment to sound localization. The introduction of passive damping systems would increase thermal noise and reduce the microphone's fidelity. Miles *et al* [116] have demonstrated active Q control aimed to reduce damping, here using a proportional and differential gain and feedback scheme to an electrostatic mesh, successfully broadening the resonant response without noise gain. A similar effect can be achieved with pulse train stimulation, changing the phase timing of the pulse with respect to the diaphragm oscillations [117]. Active control over the damping in this manner relies on separate methods of measurement and feedback; for example, piezoelectric measurement of membrane motion and capacitive comb feedback [118], or laser diffraction-based measurement and actuation through a capacitive backplate [119, 120].

Particle velocity acoustic sensors are relatively rarer, with the majority of the bioinspired hair sensors being directed towards the detection of fluid flow [124], and we have few examples of hair or flagellum-based sensors that are directly mosquito inspired (for example [125]), although the claimed incorporation of active feedback appears in reality to be a simple directional response. A velocity feedback controller on a cantilever beam was demonstrated by Joyce and Tarazga [126], the device was constructed at scale being a 5 cm long aluminium beam with a resonance of 10.8 Hz. Antenna-inspired acoustic sensors should have large surface area relative to their mass (or moment of inertia) and stiffness [121, 122]. This can be achieved via sub-micron diameter thickness wires, either arranged individually (figures 6(D) and (E)) [127] or in a mesh via electrospinning (figure 6(F)) [123]. This leads to a significant challenge with signal transduction since a mechanical element that is sufficiently agile to respond to the drag forces from a sound field will also be driven more powerfully by any electrostatic or capacitive field [128]. Solutions based on electrospun meshes have the convenient electrical transduction mechanism of a piezoelectric polymer [129], in this case, P(VDF-TrFE) however, due to the random orientation of the fibres, the weak reverse piezoelectric effect and the clamped-clamped nature of the mesh the return pathway would be challenging to implement.

5. Conclusion

Insect hearing systems are diverse, but there are common sets of problems that all small animals must

deal with: size and energy. This tells us the type of problems we should be approaching with an insect-inspired solution. A system that uses a locust or bushcricket-inspired mechanical tonotopy will not outperform a well-designed digital filter in terms of frequency decomposition, but it will enable a low-power solution and reduce the data transmission needs by lowering the necessary sampling frequency. Directional sensors that make use of *Ormia* or *Achroia*-inspired directional membranes will not be more accurate than a well-spaced and sampled microphone array, but they will achieve the directionality in a fraction of the space. Only the active hearing processes are truly unique, having no digital equivalent that can change the response pattern of the sensor itself. There is great potential for this approach as we begin to consider autonomous sensors and remote 'fit-and-forget' networks for structural health monitoring, environmental monitoring or health monitoring purposes. The great difficulty thus far is in our ability to reproduce the mechanical functions of natural materials such as cuticle and resilin and to develop a reliable method of transducing the signal captured.

In summary, bio-inspired solutions are one of the most innovative and useful approaches to engineering design that prioritises energy and resource efficiency rather than the best performance possible, and have the potential to become even more so in the future as our knowledge of the principles behind biological solutions widen and our manufacturing capabilities improve.

Lara Díaz-García: Writing—Original Draft. Brendan Latham: Writing—Original Draft. Andrew Reid: Writing—Original Draft. James Windmill: Writing—Review & Editing and Supervision.

Data availability statement

No new data were created or analysed in this study.

ORCID iD

Lara Díaz-García https://orcid.org/0000-0002-0260-0312

References

[1] Robles L and Ruggero M A 2001 Mechanics of the mammalian cochlea *Physiol. Rev.* **81** 1305–52
[2] Nurse C A and Piskuric N A 2013 Signal processing at mammalian carotid body chemoreceptors *Semin. Cell Dev. Biol.* **24** 22–30
[3] Stensmyr M C, Dweck H K, Farhan A, Ibba I, Strutz A, Mukunda L, Linz J, Grabe V, Steck K and Lavista-Llanos S 2012 A conserved dedicated olfactory circuit for detecting harmful microbes in Drosophila *Cell* **151** 1345–57
[4] Strong S P, Koberle R, Van Steveninck R R D R and Bialek W 1998 Entropy and information in neural spike trains *Phys. Rev. Lett.* **80** 197
[5] Rault T, Bouabdallah A and Challal Y 2014 Energy efficiency in wireless sensor networks: a top-down survey *Comput. Netw.* **67** 104–22
[6] Yang W, Wang M, Zhang J, Zou J, Hua M, Xia T and You X 2017 Narrowband wireless access for low-power massive internet of things: a bandwidth perspective *IEEE Wirel. Commun.* **24** 138–45
[7] Jiang D, Shi B, Ouyang H, Fan Y, Wang Z L and Li Z 2020 Emerging implantable energy harvesters and self-powered implantable medical electronics *ACS Nano* **14** 6436–48
[8] Hoy R R and Fay R R 2012 *Comparative Hearing: Insects* vol 10 (Springer)
[9] Römer H 2020 Directional hearing in insects: biophysical, physiological and ecological challenges *J. Exp. Biol.* **223** jeb203224
[10] Pollack G S, Mason A C, Popper A N and Fay R R 2016 *Insect Hearing* (Springer) (https://doi.org/10.1007/978-3-319-28890-1)
[11] Robert D 2005 Directional hearing in insects *Sound Source Localization* ed A N Popper and R R Fay (Springer) pp 6–35
[12] Michelsen A 1992 Hearing and sound communication in small animals: evolutionary adaptations to the laws of physics *The Evolutionary Biology of Hearing* ed D B Webster, A N Popper and R R Fay (Springer) pp 61–77
[13] Yager D D 1999 Structure, development, and evolution of insect auditory systems *Microsc. Res. Tech.* **47** 380–400
[14] Clements A N 2013 *The Physiology of Mosquitoes* (*International Series of Monographs on Pure and Applied Biology: Zoology*) vol 17 (Pergamon) (https://doi.org/10.1016/C2013-0-07858-9)
[15] Gopfert M C, Briegel H and Robert D 1999 Mosquito hearing: sound-induced antennal vibrations in male and female Aedes aegypti *J. Exp. Biol.* **202** 2727–38
[16] Menda G, Nitzany E I, Shamble P S, Wells A, Harrington L C, Miles R N and Hoy R R 2019 The long and short of hearing in the mosquito Aedes aegypti *Curr. Biol.* **29** 709–14.e4
[17] Boyan G S 1993 Another look at insect audition: the tympanic receptors as an evolutionary specialization of the chordotonal system *J. Insect Physiol.* **39** 187–200
[18] Moir H M, Jackson J C and Windmill J F 2013 Extremely high frequency sensitivity in a 'simple'ear *Biol. Lett.* **9** 20130241
[19] Roeder K D and Treat A E 1961 The detection and evasion of bats by moths *Am. Sci.* **49** 168A—48 (available at: http://www.jstor.org/stable/27827782)
[20] Fullard J H 1988 The tuning of moth ears *Experientia* **44** 423–8
[21] Ter Hofstede H M and Ratcliffe J M 2016 Evolutionary escalation: the bat–moth arms race *J. Exp. Biol.* **219** 1589–602
[22] Popov A V, Shuvalov V F and Markovich A M 1975 Spectrum of the calling songs, phonotaxis and the auditory system in the cricket *Gryllus bimaculatus Zh. Evol. Biokhim. Fiziol.* **11** 453–60
[23] Kostarakos K, Hartbauer M and Römer H 2008 Matched filters, mate choice and the evolution of sexually selected traits *PLoS One* **3** e3005
[24] Yack J E 2004 The structure and function of auditory chordotonal organs in insects *Microsc. Res. Tech.* **63** 315–37
[25] Windmill J F C and Jackson J C 2016 ears *Insect Hearing* vol 55, ed G S Pollack, A C Mason, A N Popper and R R Fay (Springer) pp 125–57
[26] Greenfield M D 2016 Evolution of acoustic communication in insects *Insect Hearing* ed G S Pollack, A C Mason, A N Popper and R R Fay (Springer) pp 17–47
[27] Greenfield M D 2002 *Signalers and Receivers: Mechanisms and Evolution of Arthropod Communication* (Oxford University Press)
[28] Römer H 1992 Ecological constraints for the evolution of hearing and sound communication in insects *The Evolutionary Biology of Hearing* ed D B Webster, A N Popper and R R Fay (Springer) pp 79–93

[29] Gopfert M C and Robert D 2001 Active auditory mechanics in mosquitoes *Proc. R. Soc.* B **268** 333–9
[30] Mhatre N and Robert D 2013 A tympanal insect ear exploits a critical oscillator for active amplification and tuning *Curr. Biol.* **23** 1952–7
[31] Windmill J F C, Jackson J C, Tuck E J and Robert D 2006 Keeping up with bats: dynamic auditory tuning in a moth *Curr. Biol.* **16** 2418–23
[32] von Békésy G 1956 Simplified model to demonstrate the energy flow and formation of traveling waves similar to those found in the cochlea* *Proc. Natl Acad. Sci.* **42** 930–44
[33] Johnstone B M, Patuzzi R and Yates G K 1986 Basilar membrane measurements and the travelling wave *Hear. Res.* **22** 147–53
[34] Udayashankar A P, Kössl M and Nowotny M 2012 Tonotopically arranged traveling waves in the miniature hearing organ of bushcrickets *PLoS One* **7** e31008
[35] Hummel J, Kössl M and Nowotny M 2017 Morphological basis for a tonotopic design of an insect ear *J. Comp. Neurol.* **525** 2443–55
[36] Gray E G and Young J Z 1997 The fine structure of the insect ear *Phil. Trans. R. Soc.* B **243** 75–94
[37] Windmill J F C, Göpfert M C and Robert D 2005 Tympanal travelling waves in migratory locusts *J. Exp. Biol.* **208** 157–68
[38] Montealegre-Z F, Jonsson T, Robson-Brown K A, Postles M and Robert D 2012 Convergent evolution between insect and mammalian audition *Science* **338** 968–71
[39] Nishino H, Domae M, Takanashi T and Okajima T 2019 Cricket tympanal organ revisited: morphology, development and possible functions of the adult-specific chitin core beneath the anterior tympanal membrane *Cell Tissue Res.* **377** 193–214
[40] Montealegre-Z F and Robert D 2015 Biomechanics of hearing in katydids *J. Comp. Physiol.* A **201** 5–18
[41] Stölting H and Stumpner A 1998 Tonotopic organization of auditory receptors of the bushcricket Pholidoptera griseoaptera (Tettigoniidae, Decticinae) *Cell Tissue Res.* **294** 377–86
[42] Sueur J, Windmill J F C and Robert D 2006 Tuning the drum: the mechanical basis for frequency discrimination in a Mediterranean cicada *J. Exp. Biol.* **209** 4115–28
[43] Hur S, Lee S Q and Choi H S 2010 Fabrication and characterization of PMN-PT single crystal cantilever array for cochlear-like acoustic sensor *J. Mech. Sci. Technol.* **24** 181–4
[44] Jang J *et al* 2015 A microelectromechanical system artificial basilar membrane based on a piezoelectric cantilever array and its characterization using an animal model *Sci. Rep.* **5** 12447
[45] Jang J, Lee J, Jang J H and Choi H 2016 A triboelectric-based artificial basilar membrane to mimic cochlear tonotopy *Adv. Healthcare Mater.* **5** 2481–7
[46] Kim S, Song W J, Jang J, Jang J H and Choi H 2013 Mechanical frequency selectivity of an artificial basilar membrane using a beam array with narrow supports *J. Micromech. Microeng.* **23** 095018
[47] Römer H 1976 Die Informationsverarbeitung tympanaler Rezeptorelemente vonLocusta migratoria (Acrididae, Orthoptera) *J. Comp. Physiol.* **109** 101–22
[48] Stephen R O and Bennet-Clark H C 1982 The anatomical and mechanical basis of stimulation and frequency analysis in the locust ear *J. Exp. Biol.* **99** 279–314
[49] Joyce B, Dodson J and Wolfson J 2017 Beam array designs for a cochlea-inspired accelerometer for impact measurements *ASME 2017 Conf. on Smart Materials, Adaptive Structures and Intelligent Systems* (American Society of Mechanical Engineers Digital Collection) (https://doi.org/10.1115/SMASIS2017-3723)
[50] Tao S and Rusu A 2015 A power-efficient continuous-time incremental sigma-delta ADC for neural recording systems *IEEE Trans. Circuits Syst.* I **62** 1489–98
[51] Li C-h, Delbruck T and Liu S-C 2012 Real-time speaker identification using the AEREAR2 event-based silicon cochlea *2012 IEEE Int. Symp. on Circuits and Systems (ISCAS)* pp 1159–62
[52] Zai A T, Bhargava S, Mesgarani N and Liu S-C 2015 Reconstruction of audio waveforms from spike trains of artificial cochlea models *Front. Neurosci.* **9** 347
[53] White R D and Grosh K 2005 Microengineered hydromechanical cochlear model *Proc. Natl Acad. Sci.* **102** 1296–301
[54] Kim Y, Kim J-S and Kim G-W 2018 A novel frequency selectivity approach based on travelling wave propagation in mechanoluminescence basilar membrane for artificial cochlea *Sci. Rep.* **8** 12023
[55] Song W J, Jang J, Kim S and Choi H 2014 Piezoelectric performance of continuous beam and narrow supported beam arrays for artificial basilar membranes *Electron. Mater. Lett.* **10** 1011–8
[56] Bachman M, Zeng F-G, Xu T and Li G-P 2006 Micromechanical resonator array for an implantable bionic ear *Audiol. Neurotol.* **11** 95–103
[57] Zagabathuni A and Kanagaraj S 2020 Comparative analysis of mechanical characteristics of different topologies of the cantilever beam to mimic the function of the cochlea *Mater. Today* **33** 4927–32
[58] Neethu K and Suja K J 2016 Sensitivity analysis of rectangular microcantilever structure with piezoresistive detection technique using coventorware FEA *Proc. Comput. Sci.* **93** 146–52
[59] Ansari M Z, Cho C, Kim J and Bang B 2009 Comparison between deflection and vibration characteristics of rectangular and trapezoidal profile microcantilevers *Sensors* **9** 2706–18
[60] Wang H S *et al* 2021 Biomimetic and flexible piezoelectric mobile acoustic sensors with multiresonant ultrathin structures for machine learning biometrics *Sci. Adv.* **7** eabe5683
[61] Ngelayang T B, Majlis B Y and Latif R 2016 Straight bridge beams with centered diaphragm (SBBCD) design for MEMS cochlear biomodel *2016 IEEE Int. Conf. on Semiconductor Electronics (ICSE)* pp 13–16
[62] Chen F, Cohen H I, Bifano T G, Castle J, Fortin J, Kapusta C, Mountain D C, Zosuls A and Hubbard A E 2006 A hydromechanical biomimetic cochlea: experiments and models *J. Acoust. Soc. Am.* **119** 394–405
[63] Saadatzi M, Saadatzi M N and Banerjee S 2020 Modeling and fabrication of a piezoelectric artificial cochlea electrode array with longitudinal coupling *IEEE Sens. J.* **20** 11163–72
[64] Shintaku H, Nakagawa T, Kitagawa D, Tanujaya H, Kawano S and Ito J 2010 Development of piezoelectric acoustic sensor with frequency selectivity for artificial cochlea *Sens. Actuators* A **158** 183–92
[65] Karlos A, Elliott S J and Cheer J 2019 Higher-order WKB analysis of reflection from tapered elastic wedges *J. Sound Vib.* **449** 368–88
[66] Mironov M A and Pislyakov V V 2002 One-dimensional acoustic waves in retarding structures with propagation velocity tending to zero *Acoust. Phys.* **48** 347–52
[67] Hemmert W, Dürig U, Despont M, Drechsler U, Genolet G, Vettiger P and Freeman D M 2003 A life-sized, hydrodynamical, micromechanical inner ear *Biophysics of the Cochlea* (World Scientific) pp 409–16
[68] Lechner T P 1993 A hydromechanical model of the cochlea with nonlinear feedback using PVF_2 bending transducers *Hear. Res.* **66** 202–12
[69] Wittbrodt M J, Steele C R and Puria S 2004 Fluid–structure interaction in a physical model of the human cochlea *J. Acoust. Soc. Am.* **116** 2542–3
[70] Lüling H, Franosch J-M P and Leo van Hemmen J 2010 A two-dimensional cochlear fluid model based on conformal mapping *J. Acoust. Soc. Am.* **128** 3577–84
[71] Hoy R R 1992 The evolution of hearing in insects as an adaptation to predation from bats *The Evolutionary Biology*

of Hearing ed D B Webster, A N Popper and R R Fay (Springer) pp 115–29
[72] Cook M A and Scoble M J 1992 Tympanal organs of geometrid moths: a review of their morphology, function, and systematic importance *Syst. Entomol.* **17** 219–32
[73] Rodríguez R L, Schul J, Cocroft R B and Greenfield M D 2005 The contribution of tympanic transmission to fine temporal signal evaluation in an ultrasonic moth *J. Exp. Biol.* **208** 4159–65
[74] Greig E and Greenfield M D 2004 Sexual selection and predator avoidance in an acoustic moth: discriminating females take fewer risks *Behaviour* **141** 799–815
[75] Roeder K D 1962 The behaviour of free flying moths in the presence of artificial ultrasonic pulses *Anim. Behav.* **10** 300–4
[76] Yager D D and Hoy R R 1986 The cyclopean ear: a new sense for the praying mantis *Science* **231** 727–9
[77] Mason A C, Oshinsky M L and Hoy R R 2001 Hyperacute directional hearing in a microscale auditory system *Nature* **410** 686–90
[78] Walker T J 1993 Phonotaxis in femaleOrmia ochracea (Diptera: tachinidae), a parasitoid of field crickets *J. Insect Behav.* **6** 389–410
[79] Miles R N, Robert D and Hoy R R 1995 Mechanically coupled ears for directional hearing in the parasitoid fly Ormia ochracea *J. Acoust. Soc. Am.* **98** 3059–70
[80] Robert D, Miles R N and Hoy R R 1996 Directional hearing by mechanical coupling in the parasitoid fly Ormia ochracea *J. Comp. Physiol.* A **179** 29–44
[81] Zhang Y, Bauer R, Whitmer W M, Jackson J C, Windmill J F C and Uttamchandani D 2018 A MEMS microphone inspired by Ormia for spatial sound detection *2018 IEEE Micro Electro Mechanical Systems (MEMS)* pp 253–6
[82] Miles R 2017 Comparisons of the performance of commercially-available hearing aid microphones to that of the Binghamton Ormia-inspired gradient microphone *J. Acoust. Soc. Am.* **141** 3794
[83] Zhang Y, Reid A and Windmill J F C 2018 Insect-inspired acoustic micro-sensors *Curr. Opin. Insect Sci.* **30** 33–38
[84] Rahaman A and Kim B 2022 An mm-sized biomimetic directional microphone array for sound source localization in three dimensions *Microsyst. Nanoeng.* **8** 1–13
[85] Miles R N, Su Q, Cui W, Shetye M, Degertekin F L, Bicen B, Garcia C, Jones S and Hall N 2009 A low-noise differential microphone inspired by the ears of the parasitoid fly Ormia ochracea *J. Acoust. Soc. Am.* **125** 2013–26
[86] Rahaman A and Kim B 2020 Sound source localization by Ormia ochracea inspired low–noise piezoelectric MEMS directional microphone *Sci. Rep.* **10** 9545
[87] Spangler H G and Hippenmeyer C L 1988 Binaural phonotaxis in the lesser wax moth, Achroia grisella (F.) (Lepidoptera: pyralidae) *J. Insect Behav.* **1** 117–22
[88] Norman A P, Jones G and Arlettaz R 1999 Noctuid moths show neural and behavioural responses to sounds made by some bat-marking rings *Anim. Behav.* **57** 829–35
[89] Nakano R, Ishikawa Y, Tatsuki S, Surlykke A, Skals N and Takanashi T 2006 Ultrasonic courtship song in the Asian corn borer moth, Ostrinia furnacalis *Naturwissenschaften* **93** 292–6
[90] Greenfield M D and Hohendorf H 2009 Independence of sexual and anti-predator perceptual functions in an acoustic moth: implications for the receiver bias mechanism in signal evolution *Ethology* **115** 1137–49
[91] Reid A, Marin-Cudraz T, Windmill J F and Greenfield M D 2016 Evolution of directional hearing in moths via conversion of bat detection devices to asymmetric pressure gradient receivers *Proc. Natl Acad. Sci.* **113** E7740–8
[92] Hintze-Podufal C and Von Hermanni G 1996 Die Entwicklung der Tympanalorgane und ihrer invers gerichteten Skolopidien bei Wachsmotten (Lepidoptera: pyralidae: galleriinae) *Entomol. Gen.* **20** 195–201
[93] Rodríguez R L and Greenfield M D 2004 Behavioural context regulates dual function of ultrasonic hearing in lesser waxmoths: bat avoidance and pair formation *Physiol. Entomol.* **29** 159–68
[94] Reid A 2017 *Directional Hearing at the Micro-scale: Bio-inspired Sound Localization* (University of Strathclyde) (https://doi.org/10.48730/7r6d-aq98)
[95] Ishfaque A and Kim B 2018 Fly Ormia ochracea inspired MEMS directional microphone: a review *IEEE Sens. J.* **18** 1778–89
[96] Kuntzman M L, Hewa-Kasakarage N N, Rocha A, Kim D and Hall N A 2015 Micromachined in-plane pressure-gradient piezoelectric microphones *IEEE Sens. J.* **15** 1347–57
[97] Reid A, Windmill J F and Uttamchandani D 2015 Bio-inspired sound localization sensor with high directional sensitivity *Proc. Eng.* **120** 289–93
[98] Cui W, Bicen B, Hall N, Jones S A, Degertekin F L and Miles R N 2006 Optical sensing inadirectional memsmicrophone inspired by the ears of the parasitoid fly, *Ormia ochracea 19th IEEE Int. Conf. on Micro Electro Mechanical Systems* pp 614–7
[99] Kim T Y, Park S-H and Park K 2021 Development of functionally graded metamaterial using selective polymerization via digital light processing additive manufacturing *Addit. Manuf.* **47** 102254
[100] Touse M, Sinibaldi J, Simsek K, Catterlin J, Harrison S and Karunasiri G 2010 Fabrication of a microelectromechanical directional sound sensor with electronic readout using comb fingers *Appl. Phys. Lett.* **96** 173701
[101] Downey R H and Karunasiri G 2014 Reduced residual stress curvature and branched comb fingers increase sensitivity of MEMS acoustic sensor *J. Microelectromech. Syst.* **23** 417–23
[102] Díaz-García L, Reid A, Jackson-Camargo J and Windmill J F C 2022 Towards a bio-inspired acoustic sensor: Achroia grisella's ear *IEEE Sens. J.* **22** 17746–53
[103] Liu H J, Yu M and Zhang X M 2008 Biomimetic optical directional microphone with structurally coupled diaphragms *Appl. Phys. Lett.* **93** 243902
[104] Currano L J, Liu H, Gee D, Yang B and Yu M 2009 Microscale implementation of a bio-inspired acoustic localization device *Proc. SPIE* **7321** 97–104
[105] Albert J T and Kozlov A S 2016 Comparative aspects of hearing in vertebrates and insects with antennal ears *Curr. Biol.* **26** R1050–61
[106] Mhatre N, Pollack G and Mason A 2016 Stay tuned: active amplification tunes tree cricket ears to track temperature-dependent song frequency *Biol. Lett.* **12** 20160016
[107] Jackson J C and Robert D 2006 Nonlinear auditory mechanism enhances female sounds for male mosquitoes *Proc. Natl Acad. Sci. USA* **103** 16734–9
[108] Warren B, Lukashkin A N and Russell I J 2010 The dynein–tubulin motor powers active oscillations and amplification in the hearing organ of the mosquito *Proc. R. Soc.* B **277** 1761–9
[109] Avitabile D, Homer M, Champneys A R, Jackson J C and Robert D 2009 Mathematical modelling of the active hearing process in mosquitoes *J. R. Soc. Interface* **7** 105–22
[110] Windmill J F C, Jackson J C, Pook V G and Robert D 2018 Frequency doubling by active *in vivo* motility of mechanosensory neurons in the mosquito ear *R. Soc. Open Sci.* **5** 171082
[111] Jackson J C, Windmill J F C, Pook V G and Robert D 2009 Synchrony through twice-frequency forcing for sensitive and selective auditory processing *Proc. Natl Acad. Sci.* **106** 10177–82
[112] Rodríguez T R and García R 2003 Theory of Q control in atomic force microscopy *Appl. Phys. Lett.* **82** 4821–3
[113] Prakash G, Hu S, Raman A and Reifenberger R 2009 Theoretical basis of parametric-resonance-based atomic force microscopy *Phys. Rev.* B **79** 094304

[114] Guerreiro J, Reid A, Jackson J C and Windmill J F 2018 Active hearing mechanisms inspire adaptive amplification in an acoustic sensor system *IEEE Trans. Biomed. Circuits Syst.* **12** 655–64
[115] Guerreiro J, Reid A, Jackson J C and Windmill J F C 2017 Towards the development of a frequency agile MEMS acoustic sensor system *2017 IEEE SENSORS* pp 1–3
[116] Miles R N, Degertekin F L, Cui W, Su Q, Homentcovschi D and Banser F 2013 A biologically inspired silicon differential microphone with active Q control and optical sensing *Acoustical Society of America Biannual Meeting Proc. Meetings on Acoustics ICA2013* vol 19 (Acoustical Society of America) p 030031
[117] Guerreiro J, Reid A, Jackson J C and Windmill J F 2017 Bio-inspired active amplification in a MEMS microphone using feedback computation *2017 IEEE Biomedical Circuits and Systems Conf. (Biocas)* (IEEE) pp 1–4
[118] Guerreiro J, Jackson J C and Windmill J F 2017 Simple ears inspire frequency agility in an engineered acoustic sensor system *IEEE Sens. J.* **17** 7298–305
[119] Bicen B, Garcia C, Hall N A, Okandan M, Cui W, Su Q T, Miles R N and Degertekin L 2008 Diffraction based optical MEMS microphones and accelerometers with active electrostatic force feedback *J. Acoust. Soc. Am.* **123** 3230
[120] Bicen B 2010 *Micromachined Diffraction Based Optical Microphones and Intensity Probes with Electrostatic Force Feedback* (Georgia Institute of Technology) (available at: www.proquest.com/books/micromachined-diffraction-based-optical/docview/1136361303/se-2?accountid=14116)
[121] Miles R N, Farahikia M, Leahy S and Aziz A A 2019 A flow-sensing velocity microphone *2019 IEEE SENSORS* (IEEE) pp 1–4
[122] Miles R N and Zhou J 2018 Sound-induced motion of a nanoscale fiber *J. Vib. Acoust.* **140** 011009
[123] Wang W, Stipp P N, Ouaras K, Fathi S and Huang Y Y S 2020 Broad bandwidth, self-powered acoustic sensor created by dynamic near-field electrospinning of suspended, transparent piezoelectric nanofiber mesh *Small* **16** 2000581
[124] McConney M E, Schaber C F, Julian M D, Eberhardt W C, Humphrey J A, Barth F G and Tsukruk V V 2009 Surface force spectroscopic point load measurements and viscoelastic modelling of the micromechanical properties of air flow sensitive hairs of a spider (Cupiennius salei) *J. R. Soc. Interface* **6** 681–94
[125] Wang K, Gong S, Zhang Y, Yap L W and Cheng W 2022 Mosquito-inspired design of resistive antennae for ultrasensitive acoustic detection *Nanoscale* **14** 10108–17
[126] Joyce B S and Tarazaga P A 2014 Mimicking the cochlear amplifier in a cantilever beam using nonlinear velocity feedback control *Smart Mater. Struct.* **23** 075019
[127] Miles R N 2020 Effects of viscosity *Physical Approach to Engineering Acoustics* (*Mechanical Engineering*) (Springer) pp 189–231
[128] Miles R N 2018 A compliant capacitive sensor for acoustics: avoiding electrostatic forces at high bias voltages *IEEE Sens. J.* **18** 5691–8
[129] Zhou J, Li B, Liu J, Jones W E and Miles R N 2018 Highly-damped nanofiber mesh for ultrasensitive broadband acoustic flow detection *J. Micromech. Microeng.* **28** 095003

References

[1] W. A. Yost, ed., *Directional Hearing*. Springer-Verlag, 1987.

[2] J. Eargle, *The Microphone Book*. Taylor & Francis, 2004. Google-Books-ID: w8kXMVKOsY0C.

[3] R. N. Miles, "Acoustic Sensing," in *Physical Approach to Engineering Acoustics* (R. N. Miles, ed.), Mechanical Engineering Series, pp. 233–283, Cham: Springer International Publishing, 2020.

[4] J. L. LoPresti, "Evolution of miniature microphones in hearing instruments," *The Journal of the Acoustical Society of America*, vol. 148, pp. 2608–2608, Oct. 2020. Publisher: AIP Publishing.

[5] Y. Li, Y. Xu, Z. Wu, L. Ma, M. Guo, Z. Li, and Y. Li, "A comprehensive review on fish-inspired robots," *International Journal of Advanced Robotic Systems*, vol. 19, p. 17298806221103707, May 2022. Publisher: SAGE Publications.

[6] A. P. Lisiewski, H. J. Liu, M. Yu, L. Currano, and D. Gee, "Fly-ear inspired micro-sensor for sound source localization in two dimensions," *The Journal of the Acoustical Society of America*, vol. 129, pp. EL166–EL171, May 2011. Publisher: Acoustical Society of America.

[7] Z. Chen, Z. Zhang, Y. Wang, D. Xu, and Y. Zhao, "Butterfly inspired functional materials," *Materials Science and Engineering: R: Reports*, vol. 144, p. 100605, Apr. 2021.

[8] J. H. Fullard and J. E. Yack, "The evolutionary biology of insect hearing," *Trends in Ecology & Evolution*, vol. 8, pp. 248–252, July 1993.

[9] R. R. Hoy and D. Robert, "Tympanal hearing in insects," *Annual review of entomology*, vol. 41, no. 1, pp. 433–450, 1996.

[10] M. C. Göpfert and R. M. Hennig, "Hearing in Insects," *Annual Review of Entomology*, vol. 61, no. 1, pp. 257–276, 2016. _eprint: https://doi.org/10.1146/annurev-ento-010715-023631.

[11] D. D. Yager, "Structure, development, and evolution of insect auditory systems," *Microscopy Research and Technique*, vol. 47, pp. 380–400, Dec. 1999.

[12] B. Nadrowski, T. Effertz, P. R. Senthilan, and M. C. Göpfert, "Antennal hearing in insects – New findings, new questions," *Hearing Research*, vol. 273, pp. 7–13, Mar. 2011.

[13] J. Windmill, "Biologically inspired acoustic sensors: from insect ears to miniature microphones," in *AcousticalSociety of America*, Strathclyde University, 2018.

[14] H. G. Spangler, M. D. Greenfield, and A. Takessian, "Ultrasonic mate calling in the lesser wax moth," *Physiological Entomology*, vol. 9, no. 1, pp. 87–95, 1984.

[15] Y. Jang and M. D. Greenfield, "Ultrasonic communication and sexual selection in wax moths: female choice based on energy and asynchrony of male signals," *Animal Behaviour*, vol. 51, no. 5, pp. 1095–1106, 1996.

[16] R. L. Rodríguez and M. D. Greenfield, "Behavioural context regulates dual function of ultrasonic hearing in lesser waxmoths: bat avoidance and pair formation," *Physiological Entomology*, vol. 29, no. 2, pp. 159–168, 2004.

[17] M. Greenfield and J. Coffelt, "Reproductive Behaviour of the Lesser Waxmoth, Achroia Grisella (Pyralidae: Galleriinae): Signalling, Pair Formation, Male Interactions, and Mate Guarding," *Behaviour*, vol. 84, pp. 287–314, Jan. 1983.

[18] H. G. Spangler, "Attraction of Female Lesser Wax Moths (Lepidoptera: Pyralidae) to Male-Produced and Artificial Sounds," *Journal of Economic Entomology*, vol. 77, pp. 346–349, Apr. 1984.

[19] A. Reid, T. Marin-Cudraz, J. F. Windmill, and M. D. Greenfield, "Evolution of directional hearing in moths via conversion of bat detection devices to asymmetric pressure gradient receivers," *Proceedings of the National Academy of Sciences*, vol. 113, no. 48, pp. E7740–E7748, 2016.

[20] K. S. Boo and A. G. Richards, "Fine structure of the scolopidia in the johnston's organ of male Aedes aegypti (L.) (Diptera: Culicidae)," *International Journal of Insect Morphology and Embryology*, vol. 4, pp. 549–566, Dec. 1975.

[21] H. G. Spangler, "Sound and the Moths That Infest Beehives," *The Florida Entomologist*, vol. 71, no. 4, pp. 467–477, 1988. Publisher: Florida Entomological Society.

[22] P. Trematerra, "Some aspects of the sexual behaviour of the Lepidoptera Pyralidae infesting stored-products," *Anzeiger für Schädlingskunde, Pflanzenschutz, Umweltschutz*, vol. 70, pp. 87–91, July 1997.

[23] H. G. Spangler and C. L. Hippenmeyer, "Binaural phonotaxis in the lesser wax moth, Achroia grisella (F.) (Lepidoptera: Pyralidae)," *Journal of Insect Behavior*, vol. 1, pp. 117–122, Jan. 1988.

[24] R. L. Rodríguez, J. Schul, R. B. Cocroft, and M. D. Greenfield, "The contribution of tympanic transmission to fine temporal signal evaluation in an ultrasonic moth," *Journal of experimental biology*, vol. 208, no. 21, pp. 4159–4165, 2005.

[25] W. M. F. o. L. M. U. J. L. T. S. U. S. L. M. University, *University Physics Volume 1 by OpenStax*. XanEdu Publishing Inc, Sept. 2016.

[26] T. D. Rossing, D. M. Campbell, F. Dunn, N. H. Fletcher, and W. M. Hartmann, *Springer Handbook of Acoustics*. New York, NY: New York, NY: Springer New York, 2014.

[27] S. A. Gelfand, *Essentials of Audiology*. Thieme, Jan. 2011. Google-Books-ID: SGdR8uCuRHUC.

[28] C. Köppl, G. A. Manley, A. N. Popper, and R. R. Fay, *Insights from comparative hearing research*. Springer, 2014.

[29] N. Fletcher, *Acoustic Systems in Biology*. Oxford University Press, USA, 1992.

[30] G. von Békésy, "Simplified model to demonstrate the energy flow and formation of traveling waves similar to those found in the cochlea*," *Proceedings of the National Academy of Sciences*, vol. 42, pp. 930–944, Dec. 1956. Number: 12 Publisher: Proceedings of the National Academy of Sciences.

[31] B. M. Johnstone, R. Patuzzi, and G. K. Yates, "Basilar membrane measurements and the travelling wave," *Hearing Research*, vol. 22, pp. 147–153, Jan. 1986. Number: 1.

[32] Madhero88, "Normal tympanic membrane."

[33] G. Volandri, F. Di Puccio, P. Forte, and C. Carmignani, "Biomechanics of the tympanic membrane," *Journal of Biomechanics*, vol. 44, pp. 1219–1236, Apr. 2011.

[34] J. B. Sellon, R. Ghaffari, and D. M. Freeman, "The Tectorial Membrane: Mechanical Properties and Functions," *Cold Spring Harbor Perspectives in Medicine*, vol. 9, p. a033514, Jan. 2019. Publisher: Cold Spring Harbor Laboratory Press.

[35] L. Chittka and A. Brockmann, "Perception Space—The Final Frontier," *PLOS Biology*, vol. 3, no. 4, p. e137, 2005. Publisher: Public Library of Science.

[36] "Sensory Perception - Anatomy and Physiology | OpenStax."

[37] J. F. V. Vincent and U. G. K. Wegst, "Design and mechanical properties of insect cuticle," *Arthropod Structure & Development*, vol. 33, pp. 187–199, July 2004.

[38] R. R. Hoy, "The Evolution of Hearing in Insects as an Adaptation to Predation from Bats," in *The Evolutionary Biology of Hearing* (D. B. Webster, A. N. Popper, and R. R. Fay, eds.), pp. 115–129, New York, NY: Springer, 1992.

[39] R. R. Hoy and R. R. Fay, *Comparative hearing: insects*, vol. 10. Springer Science & Business Media, 2012.

[40] J. L. Eaton, *Lepidopteran anatomy*. New York; Chichester; Brisbane: J. Wiley & Sons, 1988.

[41] M. D. Greenfield, "Acoustic Communication in the Nocturnal Lepidoptera," in *Insect Hearing and Acoustic Communication* (B. Hedwig, ed.), Animal Signals and Communication, pp. 81–100, Berlin, Heidelberg: Springer, 2014.

[42] A. Y. Kawahara, D. Plotkin, M. Espeland, K. Meusemann, E. F. A. Toussaint, A. Donath, F. Gimnich, P. B. Frandsen, A. Zwick, M. dos Reis, J. R. Barber, R. S. Peters, S. Liu, X. Zhou, C. Mayer, L. Podsiadlowski, C. Storer, J. E. Yack, B. Misof, and J. W. Breinholt, "Phylogenomics reveals the evolutionary timing and pattern of butterflies and moths," *Proceedings of the National Academy of Sciences*, vol. 116, pp. 22657–22663, Nov. 2019. Publisher: Proceedings of the National Academy of Sciences.

[43] M. A. Cook and M. J. Scoble, "Tympanal organs of geometrid moths: a review of their morphology, function, and systematic importance," *Systematic Entomology*, vol. 17, no. 3, pp. 219–232, 1992.

[44] G. S. Pollack, A. C. Mason, A. N. Popper, and R. R. Fay, *Insect hearing*. Springer, 2016.

[45] H. M. Moir, J. C. Jackson, and J. F. Windmill, "Extremely high frequency sensitivity in a 'simple'ear," *Biology letters*, vol. 9, no. 4, p. 20130241, 2013.

[46] E. Greig and M. D. Greenfield, "Sexual selection and predator avoidance in an acoustic moth: discriminating females take fewer risks," *Behaviour*, vol. 141, pp. 799–815, Jan. 2004.

[47] K. D. Roeder, "The behaviour of free flying moths in the presence of artificial ultrasonic pulses," *Animal Behaviour*, vol. 10, pp. 300–304, July 1962. Number: 3.

[48] K. H. Dahm, D. Meyer, W. E. Finn, V. Reinhold, and H. Röller, "The olfactory and auditory mediated sex attraction in Achroia grisella (Fabr.)," *Naturwissenschaften*, vol. 58, pp. 265–266, May 1971.

[49] L. Knopek and C. Hintze-Podufal, "Uber den Bau der abdominalen Tympanalorgane der Kleinen Wachsmotte Achroia grisella (Fbr.)," *Zoologische Jahrbuecher Abteilung fuer Anatomie und Ontogenie der Tiere*, vol. 1141, pp. 83–93, Jan. 1986.

[50] R. Nakano, T. Takanashi, and A. Surlykke, "Moth hearing and sound communication," *Journal of Comparative Physiology A*, vol. 201, pp. 111–121, Jan. 2015.

[51] D. Robert, "Directional Hearing in Insects," in *Sound Source Localization* (A. N. Popper and R. R. Fay, eds.), Springer Handbook of Auditory Research, pp. 6–35, New York, NY: Springer, 2005.

[52] H. G. Spangler and A. Takessian, "Further Observations on Sound Production by the Lesser Wax Moth, Achroia grisella (F.) (Lepidoptera: Pyralidae)," *Journal of the Kansas Entomological Society*, vol. 59, no. 3, pp. 555–557, 1986. Publisher: Kansas (Central States) Entomological Society.

[53] H. G. Spangler and A. Takessian, "Sound Perception by Two Species of Wax Moths (Lepidoptera: Pyralidae)," *Annals of the Entomological Society of America*, vol. 76, pp. 94–97, Jan. 1983.

[54] J. D. Ellis, J. R. Graham, and A. Mortensen, "Standard methods for wax moth research," *Journal of Apicultural Research*, vol. 52, pp. 1–17, Jan. 2013.

[55] C. Hintze-Podufal and G. Von Hermanni, "Die Entwicklung der Tympanalorgane und ihrer invers gerichteten Skolopidien bei Wachsmotten (Lepidoptera: Pyral-

idae: Galleriinae)," *Entomologia Generalis*, pp. 195–201, Jan. 1996. Publisher: Schweizerbart'sche Verlagsbuchhandlung.

[56] A. Reid, *Directional hearing at the micro-scale: bio-inspired sound localization.* PhD thesis, University of Strathclyde, 2017.

[57] L. Díaz-García, A. Reid, J. C. Jackson-Camargo, and J. F. C. Windmill, "Toward a Bio-Inspired Acoustic Sensor: Achroia grisella's Ear," *IEEE Sensors Journal*, vol. 22, pp. 17746–17753, Sept. 2022.

[58] D. D. Yager and R. R. Hoy, "The Cyclopean Ear: A New Sense for the Praying Mantis," *Science*, vol. 231, pp. 727–729, Feb. 1986. Publisher: American Association for the Advancement of Science.

[59] R. A. Norberg and B. B. Boycott, "Skull asymmetry, ear structure and function, and auditory localization in Tengmalm's owl, Aegolius funereus (Linné)," *Philosophical Transactions of the Royal Society of London. B, Biological Sciences*, vol. 282, pp. 325–410, Jan. 1997. Publisher: Royal Society.

[60] A. P. Vedurmudi, J. Goulet, J. Christensen-Dalsgaard, B. A. Young, R. Williams, and J. L. van Hemmen, "How Internally Coupled Ears Generate Temporal and Amplitude Cues for Sound Localization," *Physical Review Letters*, vol. 116, p. 028101, Jan. 2016.

[61] A. P. Vedurmudi, B. A. Young, and J. L. van Hemmen, "Active tympanic tuning facilitates sound localization in animals with internally coupled ears," *Hearing Research*, vol. 387, p. 107861, Mar. 2020.

[62] D. L. Jones and R. Ratnam, "Are frog calls relatively difficult to locate by mammalian predators?," *Journal of Comparative Physiology A*, vol. 209, no. 1, pp. 11–30, 2023.

[63] R. N. Miles, "Acoustically Coupled Microphone Arrays," *Journal of Vibration and Acoustics*, vol. 138, Sept. 2016.

[64] Q. Dong, X. Song, J. S.-J. Chen, A. Kim, and H. Liu, "A bio-inspired optical directional microphone with cavity-coupled diaphragms," *JASA Express Letters*, vol. 1, p. 072802, July 2021. Publisher: Acoustical Society of America.

[65] L. Zhang, J. Hallam, and J. Christensen-Dalsgaard, "Effects of asymmetry and learning on phonotaxis in a robot based on the lizard auditory system," *Adaptive Behavior*, vol. 20, pp. 159–171, June 2012. Publisher: SAGE Publications Ltd STM.

[66] H. Nishino, M. Domae, T. Takanashi, and T. Okajima, "Cricket tympanal organ revisited: morphology, development and possible functions of the adult-specific chitin core beneath the anterior tympanal membrane," *Cell and Tissue Research*, vol. 377, pp. 193–214, Aug. 2019.

[67] A. Michelsen and O. N. Larsen, "Biophysics of the ensiferan ear," *Journal of comparative physiology*, vol. 123, pp. 193–203, Sept. 1978.

[68] E. Celiker, T. Jonsson, and F. Montealegre-Z, "The Auditory Mechanics of the Outer Ear of the Bush Cricket: A Numerical Approach," *Biophysical Journal*, vol. 118, pp. 464–475, Jan. 2020.

[69] T. Jonsson, F. Montealegre-Z, C. D. Soulsbury, K. A. Robson Brown, and D. Robert, "Auditory mechanics in a bush-cricket: direct evidence of dual sound inputs in the pressure difference receiver," *Journal of The Royal Society Interface*, vol. 13, p. 20160560, Sept. 2016. Publisher: Royal Society.

[70] A. Michelsen, A. V. Popov, and B. Lewis, "Physics of directional hearing in the cricket Gryllus bimaculatus," *Journal of Comparative Physiology A*, vol. 175, pp. 153–164, Aug. 1994.

[71] B. Schmitz, H. Scharstein, and G. Wendler, "Phonotaxis in gryllus campestris l.(orthoptera, gryllidae) i. mechanism of acoustic orientation in intact female crickets," *Journal of comparative physiology*, vol. 148, pp. 431–444, 1982.

[72] B. Schmitz, H. Scharstein, and G. Wendler, "Phonotaxis in gryllus campestris l.(orthoptera, gryllidae) ii. acoustic orientation of female crickets after occlusion of single sound entrances," *Journal of comparative physiology*, vol. 152, pp. 257–264, 1983.

[73] B. Schmitz, "Phonotaxis in gryllus campestris l.(orthoptera, gryllidae) iii. intensity dependence of the behavioural performance and relative importance of tympana and spiracles in directional hearing," *Journal of Comparative Physiology A*, vol. 156, pp. 165–180, 1985.

[74] B. Schmitz, H. U. Kleindienst, K. Schildberger, and F. Huber, "Acoustic orientation in adult, female crickets (gryllus bimaculatus de geer) after unilateral foreleg amputation in the larva," *Journal of Comparative Physiology A*, vol. 162, pp. 715–728, 1988.

[75] F. Huber, H. U. Kleindienst, T. Weber, and J. Thorson, "Auditory behavior of the cricket," *Journal of Comparative Physiology A*, vol. 155, pp. 725–738, Nov. 1984.

[76] T. J. Walker, "Phonotaxis in femaleOrmia ochracea (Diptera: Tachinidae), a parasitoid of field crickets," *Journal of Insect Behavior*, vol. 6, pp. 389–410, May 1993. Number: 3.

[77] A. C. Mason, M. L. Oshinsky, and R. R. Hoy, "Hyperacute directional hearing in a microscale auditory system," *Nature*, vol. 410, pp. 686–691, Apr. 2001.

[78] D. Robert, R. N. Miles, and R. R. Hoy, "Directional hearing by mechanical coupling in the parasitoid fly Ormia ochracea," *Journal of Comparative Physiology A*, vol. 179, pp. 29–44, July 1996. Number: 1.

[79] Y. Zhang, R. Bauer, W. M. Whitmer, J. C. Jackson, J. F. C. Windmill, and D. Uttamchandani, "A MEMS microphone inspired by Ormia for spatial sound detection," in *2018 IEEE Micro Electro Mechanical Systems (MEMS)*, pp. 253–256, Jan. 2018. ISSN: 2160-1968.

[80] J. E. Yack, "The structure and function of auditory chordotonal organs in insects," *Microscopy Research and Technique*, vol. 63, no. 6, pp. 315–337, 2004.

[81] M. D. Greenfield, "Evolution of Acoustic Communication in Insects," in *Insect Hearing* (G. S. Pollack, A. C. Mason, A. N. Popper, and R. R. Fay, eds.), Springer Handbook of Auditory Research, pp. 17–47, Cham: Springer International Publishing, 2016.

[82] M. D. Greenfield, *Signalers and Receivers: Mechanisms and Evolution of Arthropod Communication*. Oxford University Press, Feb. 2002. Google-Books-ID: qUkt1lqAW4IC.

[83] H. Römer, "Ecological Constraints for the Evolution of Hearing and Sound Communication in Insects," in *The Evolutionary Biology of Hearing* (D. B. Webster, A. N. Popper, and R. R. Fay, eds.), pp. 79–93, New York, NY: Springer, 1992.

[84] F. Montealegre-Z., T. Jonsson, K. A. Robson-Brown, M. Postles, and D. Robert, "Convergent Evolution Between Insect and Mammalian Audition," *Science*, vol. 338, pp. 968–971, Nov. 2012. Number: 6109 Publisher: American Association for the Advancement of Science.

[85] C. Woodrow, C. Pulver, H. Song, and F. Montealegre-Z, "Auditory mechanics in the grig (cyphoderris monstrosa): tympanal travelling waves and frequency discrimination as a precursor to inner ear tonotopy," *Proceedings of the Royal Society B*, vol. 289, no. 1973, p. 20220398, 2022.

[86] F. Montealegre-Z and D. Robert, "Biomechanics of hearing in katydids," *Journal of Comparative Physiology A*, vol. 201, pp. 5–18, Jan. 2015. Number: 1.

[87] A. P. Udayashankar, M. Kössl, and M. Nowotny, "Tonotopically Arranged Traveling Waves in the Miniature Hearing Organ of Bushcrickets," *PLOS ONE*, vol. 7, p. e31008, Feb. 2012. Number: 2 Publisher: Public Library of Science.

[88] J. Hummel, M. Kössl, and M. Nowotny, "Morphological basis for a tonotopic design of an insect ear," *Journal of Comparative Neurol-*

ogy, vol. 525, no. 10, pp. 2443–2455, 2017. Number: 10 _eprint: https://onlinelibrary.wiley.com/doi/pdf/10.1002/cne.24218.

[89] E. G. Gray and J. Z. Young, "The fine structure of the insect ear," *Philosophical Transactions of the Royal Society of London. Series B, Biological Sciences*, vol. 243, pp. 75–94, Jan. 1997. Number: 700 Publisher: Royal Society.

[90] J. F. C. Windmill, M. C. Göpfert, and D. Robert, "Tympanal travelling waves in migratory locusts," *Journal of Experimental Biology*, vol. 208, pp. 157–168, Jan. 2005. Number: 1.

[91] J. Strauß, "What determines the number of auditory sensilla in the tympanal hearing organs of tettigoniidae? perspectives from comparative neuroanatomy and evolutionary forces," *Journal of Orthoptera Research*, vol. 28, no. 2, pp. 205–219, 2019.

[92] H. Stölting and A. Stumpner, "Tonotopic organization of auditory receptors of the bushcricket Pholidoptera griseoaptera (Tettigoniidae, Decticinae)," *Cell and Tissue Research*, vol. 294, pp. 377–386, Oct. 1998. Number: 2.

[93] J. Sueur, J. F. C. Windmill, and D. Robert, "Tuning the drum: the mechanical basis for frequency discrimination in a Mediterranean cicada," *Journal of Experimental Biology*, vol. 209, pp. 4115–4128, Oct. 2006. Number: 20.

[94] H. Römer, "Die Informationsverarbeitung tympanaler Rezeptorelemente vonLocusta migratoria (Acrididae, Orthoptera)," *Journal of comparative physiology*, vol. 109, pp. 101–122, Jan. 1976.

[95] R. O. Stephen and H. C. Bennet-Clark, "The Anatomical and Mechanical Basis of Stimulation and Frequency Analysis in the Locust Ear," *Journal of Experimental Biology*, vol. 99, pp. 279–314, Aug. 1982. Number: 1.

[96] J. T. Albert and A. S. Kozlov, "Comparative Aspects of Hearing in Vertebrates and Insects with Antennal Ears," *Current Biology*, vol. 26, pp. R1050–R1061, Oct. 2016. Number: 20.

[97] Y. Zhu, C. Liang, J. Chen, L. Zong, G.-D. Chen, and H.-B. Zhao, "Active cochlear amplification is dependent on supporting cell gap junctions," *Nature Communications*, vol. 4, p. 1786, Apr. 2013. Number: 1 Publisher: Nature Publishing Group.

[98] M. C. Gopfert and D. Robert, "Active auditory mechanics in mosquitoes," *Proceedings of the Royal Society of London. Series B: Biological Sciences*, vol. 268, pp. 333–339, Feb. 2001. Number: 1465 Publisher: Royal Society.

[99] N. Mhatre and D. Robert, "A Tympanal Insect Ear Exploits a Critical Oscillator for Active Amplification and Tuning," *Current Biology*, vol. 23, pp. 1952–1957, Oct. 2013. Number: 19.

[100] J. C. Jackson and D. Robert, "Nonlinear auditory mechanism enhances female sounds for male mosquitoes," *Proceedings of the National Academy of Sciences*, vol. 103, pp. 16734–16739, Nov. 2006. Publisher: Proceedings of the National Academy of Sciences.

[101] B. Warren, A. N. Lukashkin, and I. J. Russell, "The dynein–tubulin motor powers active oscillations and amplification in the hearing organ of the mosquito," *Proceedings of the Royal Society B: Biological Sciences*, vol. 277, pp. 1761–1769, June 2010. Number: 1688.

[102] J. F. Windmill, J. C. Jackson, V. G. Pook, and D. Robert, "Frequency doubling by active in vivo motility of mechanosensory neurons in the mosquito ear," *Royal Society open science*, vol. 5, no. 1, p. 171082, 2018.

[103] D. Avitabile, M. Homer, A. R. Champneys, J. C. Jackson, and D. Robert, "Mathematical modelling of the active hearing process in mosquitoes," *Journal of The Royal Society Interface*, vol. 7, pp. 105–122, May 2009. Publisher: Royal Society.

[104] J. C. Jackson, *Experimental and theoretical investigations into the active nonlinear processes of mosquito audition.* Ph.D., University of Bristol, 2012. Accepted: 2012.

[105] J. C. Jackson, J. F. C. Windmill, V. G. Pook, and D. Robert, "Synchrony through twice-frequency forcing for sensitive and selective auditory processing," *Proceedings of the National Academy of Sciences*, vol. 106, pp. 10177–10182, June 2009. Publisher: Proceedings of the National Academy of Sciences.

[106] D. Avitabile, M. Homer, A. Champneys, J. Jackson, and D. Robert, "Mathematical modelling of the active hearing process in mosquitoes," *Journal of the Royal Society Interface*, vol. 7, no. 42, pp. 105–122, 2010.

[107] G. W. Elko and K. P. Harney, "A History of Consumer Microphones: The Electret Condenser Microphone Meets Micro-Electro-Mechanical-Systems," *Acoustics Today*, Apr. 2009.

[108] G. M. Sessler and J. E. West, "Self-biased condenser microphone with high capacitance," *The Journal of the Acoustical Society of America*, vol. 34, no. 11, pp. 1787–1788, 1962. Publisher: Acoustical Society of America.

[109] H. Jaffe and D. Berlincourt, "Piezoelectric transducer materials," *Proceedings of the IEEE*, vol. 53, no. 10, pp. 1372–1386, 1965.

[110] M. Henshall, "Shure Unidyne, 75 Years of the World's Most Recognisable Mic," 2014.

[111] L. L. Beranek and T. J. Mellow, "Chapter 5 - Microphones," in *Acoustics: Sound Fields and Transducers* (L. L. Beranek and T. J. Mellow, eds.), pp. 199–240, Academic Press, Jan. 2012.

[112] Omegatron, "Microphone patterns," Sept. 2005.

[113] P. R. Scheeper, A. G. H. van der Donk, W. Olthuis, and P. Bergveld, "A review of silicon microphones," *Sensors and Actuators A: Physical*, vol. 44, pp. 1–11, July 1994.

[114] K. Gabriel, J. Jarvis, and W. Trimmer, "Small machines, large opportunities: A report on the emerging field of microdynamics," in *Micromechanics and MEMS: Classic and Seminal Papers to 1990*, pp. 117–143, Wiley - IEEE Press, 1997.

[115] P. Scheeper, B. Nordstrand, J. Gullv, B. Liu, T. Clausen, L. Midjord, and T. Storgaard-Larsen, "A new measurement microphone based on MEMS technology," *Journal of Microelectromechanical Systems*, vol. 12, pp. 880–891, Dec. 2003. Conference Name: Journal of Microelectromechanical Systems.

[116] C. Liu, *Foundations of MEMS*. Upper Saddle River, [N.J.] ; London: Prentice Hall, 2nd ed., international ed.. ed., 2012.

[117] J. Iannacci, "Introduction to MEMS and RF-MEMS: From the early days of microsystems to modern RF-MEMS passives," in *RF-MEMS Technology for High-Performance Passives: The challenge of 5G mobile applications*, IOP Publishing, Nov. 2017.

[118] R. Bogue, "Non-silicon mems–the hard and soft alternatives," *Sensor Review*, vol. 36, no. 3, pp. 225–230, 2016.

[119] C. Rusch, M. Börner, J. Mohr, T. Zwick, Y. Chen, and J. Héctor, "Electrical tuning of dielectric resonators with liga-mems," in *2013 European Microwave Integrated Circuit Conference*, pp. 316–319, IEEE, 2013.

[120] H. Li, D. Li, Y. Hu, P. Pan, T. Li, and J. Feng, "Uv-liga microfabrication for high frequency structures of a 220ghz twt amplifier," in *2016 IEEE International Vacuum Electronics Conference (IVEC)*, pp. 1–3, IEEE, 2016.

[121] A. Industries, "Adafruit I2S MEMS Microphone Breakout - SPH0645LM4H," Nov. 2022.

[122] S. A. Zawawi, A. A. Hamzah, B. Y. Majlis, and F. Mohd-Yasin, "A Review of MEMS Capacitive Microphones," *Micromachines*, vol. 11, p. 484, May 2020. Number: 5 Publisher: Multidisciplinary Digital Publishing Institute.

[123] M. Royer, J. O. Holmen, M. A. Wurm, O. S. Aadland, and M. Glenn, "ZnO on Si integrated acoustic sensor," *Sensors and Actuators*, vol. 4, pp. 357–362, Jan. 1983.

[124] R. J. Baken, *Clinical measurement of speech and voice*. San Diego: Singular Thomson Learning, 2nd ed.. ed., 2000.

[125] A. Ishfaque and B. Kim, "Fly Ormia Ochracea Inspired MEMS Directional Microphone: A Review," *IEEE Sensors Journal*, vol. 18, pp. 1778–1789, Mar. 2018. Conference Name: IEEE Sensors Journal.

[126] Y. Zhang, A. Reid, and J. F. C. Windmill, "Insect-inspired acoustic microsensors," *Current opinion in insect science*, vol. 30, pp. 33–38, 2018.

[127] A. Rahaman and B. Kim, "Sound source localization by Ormia ochracea inspired low–noise piezoelectric MEMS directional microphone," *Scientific Reports*, vol. 10, p. 9545, June 2020. Number: 1 Publisher: Nature Publishing Group.

[128] J. Jang, J. Lee, S. Woo, D. J. Sly, L. J. Campbell, J.-H. Cho, S. J. O'Leary, M.-H. Park, S. Han, J.-W. Choi, J. Hun Jang, and H. Choi, "A microelectromechanical system artificial basilar membrane based on a piezoelectric cantilever array and its characterization using an animal model," *Scientific Reports*, vol. 5, p. 12447, July 2015. Number: 1 Publisher: Nature Publishing Group.

[129] J. Guerreiro, A. Reid, J. C. Jackson, and J. F. Windmill, "Bio-inspired active amplification in a MEMS microphone using feedback computation," in *2017 IEEE Biomedical Circuits and Systems Conference (BioCAS)*, pp. 1–4, IEEE, 2017.

[130] R. N. Miles, Q. Su, W. Cui, M. Shetye, F. L. Degertekin, B. Bicen, C. Garcia, S. Jones, and N. Hall, "A low-noise differential microphone inspired by the ears of the parasitoid fly Ormia ochracea," *The Journal of the Acoustical Society of America*, vol. 125, pp. 2013–2026, Apr. 2009. Number: 4 Publisher: Acoustical Society of America.

[131] M. L. Kuntzman, N. N. Hewa-Kasakarage, A. Rocha, D. Kim, and N. A. Hall, "Micromachined In-Plane Pressure-Gradient Piezoelectric Microphones," *IEEE Sensors Journal*, vol. 15, pp. 1347–1357, Mar. 2015. Number: 3 Conference Name: IEEE Sensors Journal.

[132] A. Reid, J. F. Windmill, and D. Uttamchandani, "Bio-inspired sound localization sensor with high directional sensitivity," *Procedia engineering*, vol. 120, pp. 289–293, 2015.

[133] W. Cui, B. Bicen, N. Hall, S. Jones, F. Degertekin, and R. Miles, "Optical Sensing Inadirectional Memsmicrophone Inspired by the Ears of the Parasitoid Fly, Ormia Ochracea," in *19th IEEE International Conference on Micro Electro Mechanical Systems*, pp. 614–617, Jan. 2006. ISSN: 1084-6999.

[134] A. Rahaman and B. Kim, "An mm-sized biomimetic directional microphone array for sound source localization in three dimensions," *Microsystems & Nanoengineering*, vol. 8, pp. 1–13, June 2022. Number: 1 Publisher: Nature Publishing Group.

[135] T. Y. Kim, S.-H. Park, and K. Park, "Development of functionally graded metamaterial using selective polymerization via digital light processing additive manufacturing," *Additive Manufacturing*, vol. 47, p. 102254, Nov. 2021.

[136] M. L. Kuntzman and N. A. Hall, "Sound source localization inspired by the ears of the Ormia ochracea," *Applied Physics Letters*, vol. 105, p. 033701, July 2014. Number: 3 Publisher: American Institute of Physics.

[137] M. Touse, J. Sinibaldi, K. Simsek, J. Catterlin, S. Harrison, and G. Karunasiri, "Fabrication of a microelectromechanical directional sound sensor with electronic readout using comb fingers," *Applied Physics Letters*, vol. 96, p. 173701, Apr. 2010. Number: 17 Publisher: American Institute of Physics.

[138] R. H. Downey and G. Karunasiri, "Reduced Residual Stress Curvature and Branched Comb Fingers Increase Sensitivity of MEMS Acoustic Sensor," *Journal of Microelectromechanical Systems*, vol. 23, pp. 417–423, Apr. 2014. Number: 2 Conference Name: Journal of Microelectromechanical Systems.

[139] H. J. Liu, M. Yu, and X. M. Zhang, "Biomimetic optical directional microphone with structurally coupled diaphragms," *Applied Physics Letters*, vol. 93, p. 243902, Dec. 2008. Publisher: American Institute of Physics.

[140] L. J. Currano, H. Liu, D. Gee, B. Yang, and M. Yu, "Microscale implementation of a bio-inspired acoustic localization device," in *Bio-Inspired/Biomimetic Sensor Technologies and Applications*, vol. 7321, pp. 97–104, SPIE, May 2009.

[141] B. Joyce, J. Dodson, and J. Wolfson, "Beam Array Designs for a Cochlea-Inspired Accelerometer for Impact Measurements," in *SMASIS 2017*, American Society of Mechanical Engineers Digital Collection, Nov. 2017.

[142] S. Tao and A. Rusu, "A Power-Efficient Continuous-Time Incremental Sigma-Delta ADC for Neural Recording Systems," *IEEE Transactions on Circuits and Systems I: Regular Papers*, vol. 62, pp. 1489–1498, June 2015. Number: 6 Conference Name: IEEE Transactions on Circuits and Systems I: Regular Papers.

[143] C.-H. Li, T. Delbruck, and S.-C. Liu, "Real-time speaker identification using the AEREAR2 event-based silicon cochlea," in *2012 IEEE International Symposium on Circuits and Systems (ISCAS)*, pp. 1159–1162, May 2012. ISSN: 2158-1525.

[144] A. T. Zai, S. Bhargava, N. Mesgarani, and S.-C. Liu, "Reconstruction of audio waveforms from spike trains of artificial cochlea models," *Frontiers in Neuroscience*, vol. 9, 2015.

[145] S. Hur, S. Q. Lee, and H. S. Choi, "Fabrication and characterization of PMN-PT single crystal cantilever array for cochlear-like acoustic sensor," *Journal of Mechanical Science and Technology*, vol. 24, pp. 181–184, Jan. 2010. Number: 1.

[146] S. Kim, W. J. Song, J. Jang, J. H. Jang, and H. Choi, "Mechanical frequency selectivity of an artificial basilar membrane using a beam array with narrow supports," *Journal of Micromechanics and Microengineering*, vol. 23, p. 095018, Aug. 2013. Number: 9 Publisher: IOP Publishing.

[147] R. D. White and K. Grosh, "Microengineered hydromechanical cochlear model," *Proceedings of the National Academy of Sciences*, vol. 102, pp. 1296–1301, Feb. 2005. Number: 5 Publisher: Proceedings of the National Academy of Sciences.

[148] J. Jang, J. Lee, J. H. Jang, and H. Choi, "A Triboelectric-Based Artificial Basilar Membrane to Mimic Cochlear Tonotopy," *Advanced Healthcare Materials*, vol. 5, no. 19, pp. 2481–2487, 2016. Number: 19 _eprint: https://onlinelibrary.wiley.com/doi/pdf/10.1002/adhm.201600232.

[149] T. B. Ngelayang, B. Y. Majlis, and R. Latif, "Straight Bridge Beams with Centered Diaphragm (SBBCD) design for MEMS cochlear biomodel," in *2016 IEEE International Conference on Semiconductor Electronics (ICSE)*, pp. 13–16, Aug. 2016.

[150] Y. Kim, J.-S. Kim, and G.-W. Kim, "A Novel Frequency Selectivity Approach Based on Travelling Wave Propagation in Mechanoluminescence Basilar Membrane for Artificial Cochlea," *Scientific Reports*, vol. 8, p. 12023, Aug. 2018. Number: 1 Publisher: Nature Publishing Group.

[151] W. J. Song, J. Jang, S. Kim, and H. Choi, "Piezoelectric performance of continuous beam and narrow supported beam arrays for artificial basilar membranes," *Electronic Materials Letters*, vol. 10, pp. 1011–1018, Sept. 2014. Number: 5.

[152] M. Bachman, F.-G. Zeng, T. Xu, and G.-P. Li, "Micromechanical Resonator Array for an Implantable Bionic Ear," *Audiology and Neurotology*, vol. 11, no. 2, pp. 95–103, 2006. Number: 2 Publisher: Karger Publishers.

[153] A. Zagabathuni and S. Kanagaraj, "Comparative analysis of mechanical characteristics of different topologies of the cantilever beam to mimic the function of the cochlea," *Materials Today: Proceedings*, vol. 33, pp. 4927–4932, Jan. 2020.

[154] K. Neethu and K. J. Suja, "Sensitivity Analysis of Rectangular Microcantilever Structure with Piezoresistive Detection Technique Using Coventorware FEA," *Procedia Computer Science*, vol. 93, pp. 146–152, Jan. 2016.

[155] M. Z. Ansari, C. Cho, J. Kim, and B. Bang, "Comparison between Deflection and Vibration Characteristics of Rectangular and Trapezoidal profile Microcantilevers," *Sensors*, vol. 9, pp. 2706–2718, Apr. 2009. Number: 4 Publisher: Molecular Diversity Preservation International.

[156] H. S. Wang, S. K. Hong, J. H. Han, Y. H. Jung, H. K. Jeong, T. H. Im, C. K. Jeong, B.-Y. Lee, G. Kim, C. D. Yoo, and K. J. Lee, "Biomimetic and flexible piezoelectric mobile acoustic sensors with multiresonant ultrathin structures for machine learning biometrics," *Science Advances*, vol. 7, p. eabe5683, Feb. 2021. Number: 7 Publisher: American Association for the Advancement of Science.

[157] F. Chen, H. I. Cohen, T. G. Bifano, J. Castle, J. Fortin, C. Kapusta, D. C. Mountain, A. Zosuls, and A. E. Hubbard, "A hydromechanical biomimetic cochlea: Experiments and models," *The Journal of the Acoustical Society of America*, vol. 119, pp. 394–405, Jan. 2006. Number: 1 Publisher: Acoustical Society of America.

[158] M. Saadatzi, M. N. Saadatzi, and S. Banerjee, "Modeling and Fabrication of a Piezoelectric Artificial Cochlea Electrode Array With Longitudinal Coupling," *IEEE Sensors Journal*, vol. 20, pp. 11163–11172, Oct. 2020. Number: 19 Conference Name: IEEE Sensors Journal.

[159] H. Shintaku, T. Nakagawa, D. Kitagawa, H. Tanujaya, S. Kawano, and J. Ito, "Development of piezoelectric acoustic sensor with frequency selectivity for artificial cochlea," *Sensors and Actuators A: Physical*, vol. 158, pp. 183–192, Mar. 2010. Number: 2.

[160] A. Karlos, S. J. Elliott, and J. Cheer, "Higher-order WKB analysis of reflection from tapered elastic wedges," *Journal of Sound and Vibration*, vol. 449, pp. 368–388, June 2019.

[161] M. A. Mironov and V. V. Pislyakov, "One-dimensional acoustic waves in retarding structures with propagation velocity tending to zero," *Acoustical Physics*, vol. 48, pp. 347–352, May 2002. Number: 3.

[162] W. Hemmert, U. Dürig, M. Despont, U. Drechsler, G. Genolet, P. Vettiger, and D. Freeman, "A life-sized, hydrodynamical, micromechanical inner ear," in *Biophysics of the Cochlea*, pp. 409–416, WORLD SCIENTIFIC, Feb. 2003.

[163] T. P. Lechner, "A hydromechanical model of the cochlea with nonlinear feedback using PVF2 bending transducers," *Hearing Research*, vol. 66, pp. 202–212, Apr. 1993. Number: 2.

[164] M. J. Wittbrodt, C. R. Steele, and S. Puria, "Fluid–structure interaction in a physical model of the human cochlea," *The Journal of the Acoustical Society of America*, vol. 116, pp. 2542–2543, Oct. 2004. Number: 4 Publisher: Acoustical Society of America.

[165] H. Lüling, J.-M. P. Franosch, and J. Leo van Hemmen, "A two-dimensional cochlear fluid model based on conformal mapping," *The Journal of the Acoustical Society of America*, vol. 128, pp. 3577–3584, Dec. 2010. Number: 6 Publisher: Acoustical Society of America.

[166] T. R. Rodríguez and R. García, "Theory of Q control in atomic force microscopy," *Applied Physics Letters*, vol. 82, pp. 4821–4823, June 2003. Number: 26 Publisher: American Institute of Physics.

[167] G. Prakash, S. Hu, A. Raman, and R. Reifenberger, "Theoretical basis of parametric-resonance-based atomic force microscopy," *Physical Review B*, vol. 79, p. 094304, Mar. 2009. Number: 9 Publisher: American Physical Society.

[168] J. Guerreiro, A. Reid, J. C. Jackson, J. F. Windmill, and systems, "Active hearing mechanisms inspire adaptive amplification in an acoustic sensor system," *IEEE transactions on biomedical circuits*, vol. 12, no. 3, pp. 655–664, 2018.

[169] J. Guerreiro, A. Reid, J. C. Jackson, and J. F. Windmill, "Towards the development of a frequency agile MEMS acoustic sensor system," in *2017 IEEE SENSORS*, pp. 1–3, Oct. 2017.

[170] R. N. Miles, M. Farahikia, S. Leahy, and A. A. Aziz, "A flow-sensing velocity microphone," in *2019 IEEE SENSORS*, pp. 1–4, IEEE, 2019.

[171] R. N. Miles and J. Zhou, "Sound-induced motion of a nanoscale fiber," *Journal of Vibration and Acoustics*, vol. 140, no. 1, 2018. Number: 1 ISBN: 1048-9002 Publisher: American Society of Mechanical Engineers Digital Collection.

[172] W. Wang, P. N. Stipp, K. Ouaras, S. Fathi, and Y. Y. S. Huang, "Broad bandwidth, self-powered acoustic sensor created by dynamic near-field electrospinning of suspended, transparent piezoelectric nanofiber mesh," *Small*, vol. 16, no. 28, p. 2000581, 2020. Number: 28 ISBN: 1613-6810 Publisher: Wiley Online Library.

[173] R. N. Miles, F. L. Degertekin, W. Cui, Q. Su, D. Homentcovschi, and F. Banser, "A biologically inspired silicon differential microphone with active Q control and optical sensing," in *Proceedings of Meetings on Acoustics ICA2013*, vol. 19, p. 030031, Acoustical Society of America, 2013. Issue: 1.

[174] J. Guerreiro, J. C. Jackson, and J. F. Windmill, "Simple ears inspire frequency agility in an engineered acoustic sensor system," *IEEE Sensors Journal*, vol. 17, no. 22, pp. 7298–7305, 2017.

[175] B. Bicen, C. Garcia, N. A. Hall, M. Okandan, W. Cui, Q. T. Su, R. N. Miles, and L. Degertekin, "Diffraction based optical MEMS microphones and accelerometers with active electrostatic force feedback," *The Journal of the Acoustical Society of America*, vol. 123, no. 5, pp. 3230–3230, 2008. Number: 5 ISBN: 0001-4966 Publisher: Acoustical Society of America.

[176] B. Bicen, *Micromachined diffraction based optical microphones and intensity probes with electrostatic force feedback*. Georgia Institute of Technology, 2010.

[177] M. E. McConney, C. F. Schaber, M. D. Julian, W. C. Eberhardt, J. A. Humphrey, F. G. Barth, and V. V. Tsukruk, "Surface force spectroscopic point load measurements and viscoelastic modelling of the micromechanical properties of air flow sensitive hairs of a spider (Cupiennius salei)," *Journal of the Royal Society Interface*, vol. 6, no. 37, pp. 681–694, 2009. Number: 37 ISBN: 1742-5689 Publisher: The Royal Society.

[178] K. Wang, S. Gong, Y. Zhang, L. W. Yap, and W. Cheng, "Mosquito-inspired design of resistive antennae for ultrasensitive acoustic detection," *Nanoscale*, vol. 14, no. 28, pp. 10108–10117, 2022. Number: 28 Publisher: Royal Society of Chemistry.

[179] B. S. Joyce and P. A. Tarazaga, "Mimicking the cochlear amplifier in a cantilever beam using nonlinear velocity feedback control," *Smart Materials and Structures*, vol. 23, p. 075019, June 2014. Number: 7 Publisher: IOP Publishing.

[180] R. N. Miles and R. N. Miles, "Effects of Viscosity," *Physical Approach to Engineering Acoustics*, pp. 189–231, 2020. ISBN: 3030226751 Publisher: Springer.

[181] R. N. Miles, "A compliant capacitive sensor for acoustics: Avoiding electrostatic forces at high bias voltages," *IEEE Sensors Journal*, vol. 18, no. 14, pp. 5691–5698, 2018. Number: 14 ISBN: 1530-437X Publisher: IEEE.

[182] J. Zhou, B. Li, J. Liu, W. E. Jones, and R. N. Miles, "Highly-damped nanofiber mesh for ultrasensitive broadband acoustic flow detection," *Journal of Micromechanics and Microengineering*, vol. 28, no. 9, p. 095003, 2018. Number: 9 ISBN: 0960-1317 Publisher: IOP Publishing.

[183] K. C. e. Zhou, *Additive manufacturing: materials, functionalities and applications*. Cham, Switzerland: Springer, 2023.

[184] G. Wypych, *Handbook of Polymers*. Elsevier, Feb. 2016.

[185] P. J. Bártolo, ed., *Stereolithography: Materials, Processes and Applications*. Boston, MA: Springer US, 2011.

[186] A. Bagheri and J. Jin, "Photopolymerization in 3D Printing," *ACS Applied Polymer Materials*, vol. 1, pp. 593–611, Apr. 2019. Publisher: American Chemical Society.

[187] J. Průša, "Introducing Original Prusa SL1 - Open Source SLA 3D Printer by Josef Prusa," Sept. 2018.

[188] Dsazer25, "Three unique methods of spatial light modulation, which control light pattern positions in 3D space over time," May 2020.

[189] J. Wu, Z. Zhao, C. M. Hamel, X. Mu, X. Kuang, Z. Guo, and H. J. Qi, "Evolution of material properties during free radical photopolymerization," *Journal of the Mechanics and Physics of Solids*, vol. 112, pp. 25–49, Mar. 2018.

[190] D. Wu, Z. Zhao, Q. Zhang, H. Jerry Qi, and D. Fang, "Mechanics of shape distortion of DLP 3D printed structures during UV post-curing," *Soft Matter*, vol. 15, no. 30, pp. 6151–6159, 2019.

[191] P. S. Bychkov, V. M. Kozintsev, A. V. Manzhirov, and A. L. Popov, "Determination of Residual Stresses in Products in Additive Production by the Layer-by-Layer Photopolymerization Method," *Mechanics of Solids*, vol. 52, pp. 524–529, Sept. 2017.

[192] A. Reid, J. C. Jackson, and J. F. C. Windmill, "Voxel based method for predictive modelling of solidification and stress in digital light processing based additive manufacture," *Soft Matter*, vol. 17, pp. 1881–1887, Feb. 2021.

[193] C. Arnold, D. Monsees, J. Hey, and R. Schweyen, "Surface Quality of 3D-Printed Models as a Function of Various Printing Parameters," *Materials*, vol. 12, p. 1970, June 2019.

[194] J. Mrázek, "Cross-layer Curing and Layer Bulging on Resin Printers: Enemy of Overall Dimensional Accuracy and Printed Threads," Nov. 2022.

[195] W. H. Goh and M. Hashimoto, "Dual Sacrificial Molding: Fabricating 3D Microchannels with Overhang and Helical Features," *Micromachines*, vol. 9, p. 523, Oct. 2018. Number: 10 Publisher: Multidisciplinary Digital Publishing Institute.

[196] P. F. O'Neill, N. Kent, and D. Brabazon, "Mitigation and control of the overcuring effect in mask projection micro-stereolithography," *AIP Conference Proceedings*, vol. 1896, p. 200012, Oct. 2017.

[197] R. Domingo-Roca, *3D-printing technology applied to the development of bio-inspired functional acoustic systems.* PhD thesis, Thesis [Ph. D.] –University of Strathclyde, 2018, 2018.

[198] B. Zhu, *Additive manufacturing (3D print) of air-coupled diaphragm ultrasonic transdrucers.* PhD thesis, University of Strathclyde, 2019.

[199] S. S. Rao, *Vibration of Continuous Systems.* New York: Wiley, 2007.

[200] J. N. Reddy, *Theory and Analysis of Elastic Plates and Shells.* CRC press, 2nd ed., 2007.

[201] A. Brugnoli, D. Alazard, V. Pommier-Budinger, and D. Matignon, "Port-Hamiltonian formulation and symplectic discretization of plate models Part II: Kirchhoff model for thin plates," *Applied Mathematical Modelling*, vol. 75, pp. 961–981, Nov. 2019.

[202] A. W. Leissa, *Vibration of Plates.* Scientific and Technical Information Division, National Aeronautics and Space Administration, 1969.

[203] T. Rossing and N. Fletcher, *Principles of Vibration and Sound.* Springer New York, 2013.

[204] H. Carrington, "The frequencies of vibration of flat circular plates fixed at the circumference," *The London, Edinburgh, and Dublin Philosophical Magazine and Journal of Science*, vol. 50, pp. 1261–1264, Dec. 1925.

[205] J. C. Gutiérrez-Vega, R. M. Rodríguez-Dagnino, M. A. Meneses-Nava, and S. Chávez-Cerda, "Mathieu functions, a visual approach," *American Journal of Physics*, vol. 71, pp. 233–242, Feb. 2003.

[206] A. W. Leissa, "Vibration of a simply-supported elliptical plate," *Journal of Sound and Vibration*, vol. 6, pp. 145–148, July 1967.

[207] Y. Shibaoka, "On the Transverse Vibration of an Elliptic Plate with Clamped Edge," *Journal of the Physical Society of Japan*, vol. 11, pp. 797–803, July 1956.

[208] N. W. McLachlan, *Theory and application of Mathieu Functions*. Oxford University Press, 1951.

[209] T. L. Reddy, P. V. P. Kumar, and A. Prajapati, "Modal analysis of an elliptical plate clamped along its boundary," *International Research Journal of Engineering and Technology*, vol. 02, Dec. 2015.

[210] J. M. Gere and S. P. Timoshenko, *Mechanics of materials*. Boston: PWS Publishing Company, 1997.

[211] J. N. Reddy, *Introduction to the finite element method*. McGraw-Hill Education, 2019.

[212] H. Mao, R. Rumpler, M. Gaborit, P. Göransson, J. Kennedy, D. O'Connor, D. Trimble, and H. Rice, "Twist, tilt and stretch: From isometric Kelvin cells to anisotropic cellular materials," *Materials & Design*, vol. 193, p. 108855, Aug. 2020.

[213] B. Tiller, A. Reid, B. Zhu, J. Guerreiro, R. Domingo-Roca, J. Curt Jackson, and J. Windmill, "Piezoelectric microphone via a digital light processing 3D printing process," *Materials & Design*, vol. 165, p. 107593, Mar. 2019.

[214] H. Gong, B. P. Bickham, A. T. Woolley, and G. P. Nordin, "Custom 3D printer and resin for 18 μm $\times$ 20 μm microfluidic flow channels," *Lab on a Chip*, vol. 17, no. 17, pp. 2899–2909, 2017. Number: 17 Publisher: Royal Society of Chemistry.

[215] E. L. Ritman, "Micro-computed tomography—current status and developments," *Annu. Rev. Biomed. Eng.*, vol. 6, pp. 185–208, 2004.

[216] B. Leszczyński, J. Skrzat, M. Kozerska, A. Wróbel, and J. Walocha, "Three dimensional visualisation and morphometry of bone samples studied in microcomputed tomography (micro-ct)," *Folia morphologica*, vol. 73, no. 4, pp. 422–428, 2014.

[217] L. Díaz-García, A. Reid, J. Jackson-Camargo, and J. Windmill, "Directional passive acoustic structures inspired by the ear of Achroia grisella," *Proceedings of Meetings on Acoustics*, vol. 50, p. 032001, Mar. 2023.

[218] L. Díaz-García, B. Latham, A. Reid, and J. Windmill, "Review of the applications of principles of insect hearing to microscale acoustic engineering challenges," *Bioinspiration & Biomimetics*, vol. 18, p. 051002, Aug. 2023. Publisher: IOP Publishing.